# Design, Fabrication and Characterization of MEMS Gyroscopes Based on Frequency Modulation

by

Dawit Effa

A thesis

presented to the University of Waterloo

in fulfillment of the

thesis requirement for the degree of

Doctor of Philosophy

in

Mechanical and Mechatronics Engineering (Nanotechnology)

Waterloo, Ontario, Canada, 2018

© Dawit Effa 2018

## Examining Committee Membership

The following served on the Examining Committee for this thesis. The decision of the Examining Committee is by majority vote.

| | |
|---|---|
| External Examiner | Professor Edmond Cretu<br>Electrical and Computer Engineering |
| Supervisors | Professor Eihab Abdel-Rahman<br>System Design Engineering |
| | Professor Mustafa Yavuz<br>Mechanical and Mechatronics Engineering |
| Internal Member | Professor Baris Fidan<br>Mechanical and Mechatronics Engineering |
| | Professor Amir Khajepour<br>Mechanical and Mechatronics Engineering |
| | Professor Raafat Mansour<br>Electrical and Computer Engineering |
| | Professor Gregory Glinka<br>Mechanical and Mechatronics Engineering |
| Other Member(s) | Professor Siva Sivoththaman<br>Electrical and Computer Engineering |

## Author's Declaration

I hereby declare that I am the sole author of this thesis. This is a true copy of the thesis, including any required final revisions, as accepted by my examiners.

I understand that my thesis may be made electronically available to the public.

## Abstract

Conventional amplitude modulated (AM) open loop MEMS gyroscopes experience a significant performance trade-off between having a large bandwidth or high sensitivity. It is impossible to improve both metrics at the same time without increasing the mass of the gyroscope or introducing a closed loop (force feedback) system into the device design. Introducing a closed loop system or increasing the proof mass on the other hand will surge power consumption. Consequently, it is difficult to maintain consistently high performance while scaling down the device size. Furthermore, bias stability, bias repeatability, reliability, nonlinearity and other performance metrics remain primary concerns as designers look to expand MEMS gyroscopes into areas like space, military and navigation applications. Industries and academics carried out extensive research to address these limitations in conventional AM MEMS gyroscope design.

This research primarily aims to improve MEMS gyroscope performance by integrating a frequency modulated (FM) readout system into the design using a cantilever beam and microplate design. The FM resonance sensing approach has been demonstrated to provide better performance than the traditional AM sensing method in similar applications (e.g., Atomic Force Microscope). The cantilever beam MEMS gyroscope is specifically designed to minimize error sources that corrupt the Coriolis signal such as operating temperature, vibration and packaging stress. Operating temperature imposes enormous challenges to gyroscope design, introducing a thermal noise and drift that degrades device performance. The cantilever beam mass gyroscope system is free on one side and can therefore minimize noise caused by both thermal effects and packaging stress. The cantilever beam design is also robust to vibrations (it can reject vibrations by sensing the orthogonally arranged secondary gyroscope) and minimizes cross-axis sensitivity. By alleviating the negative impacts of operating environment in MEMS gyroscope design, reliable, robust and high-performance angular rate measurements can be realized, leading to a wide range of applications including dynamic vehicle control, navigation/guidance systems, and IOT applications. The FM sensing approach was also investigated using a traditional crab-leg design. Tested under the same conditions, the crab-leg design provided a direct point of comparison for assessing the performance of the cantilever beam gyroscope.

To verify the feasibility of the FM detection method, these gyroscopes were fabricated using commercially available MIDIS™ process (Teledyne Dalsa Inc.), which provides 2 μm capacitive gaps and 30 μm structural layer thickness. The process employs 12 masks and hermetically sealed (10mTorr) packaging to ensure a higher quality factor. The cantilever beam gyroscope is designed such that the driving and sensing mode resonant frequency is 40.8 KHz with 0.01% mismatch.

Experimental results demonstrated that the natural frequency of the first two modes shift linearly with the angular speed and demonstrate high transducer sensitivity. Both the cantilever beam and crab-leg gyroscopes showed a linear dynamic range up to 1500 deg/s, which was limited by the experimental test setup. However, we also noted that the cantilever beam design has several advantages over traditional crab-leg devices, including simpler dynamics and control, bias stability and bias repeatability. Furthermore, the single-port sensing method implemented in this research improves the electronic performance and therefore enhances sensitivity by eliminating the need to measure vibrations via a secondary mode. The single-port detection mechanism could also simplify the IC architecture.

Rate table characterization at both high (110 ºC) and low (22 ºC) temperatures showed minimal changes in sensitivity performance even in the absence of temperature compensation mechanism and active control, verifying the improved robustness of the design concept. Due to significant die area reduction, the cantilever design can feasibly address high-volume consumer market demand for low cost, and high-volume production using a silicon wafer for the structural part. The results of this work introduce and demonstrate a new paradigm in MEMS gyroscope design, where thermal and vibration rejection capability is achieved solely by the mechanical system, negating the need for active control and compensation strategies.

## Acknowledgements

First, I would like to express my sincere gratitude to my advisor, Prof. Eihab Abdel-Rahman and Prof. Mustafa Yavuz. Thank you for your guidance and support throughout the various stages of the dissertation. Thanks are due to my friends and members of the entire Advanced Micro and Nano Device Lab group, for valuable insights that enriched my work over the last few years. Very special thanks go to Dr. Sangtak Park and Mahmoud Khater for providing with invaluable advice and comments on my study and research.

I would also like to thank CMC Microsystems for supporting this work and providing us with the necessary device fabrication and packaging resource, without which my research progress in this subject would not have been possible. I would like to also acknowledge the extensive test equipment supports provided by CMC Microsystems including rate table and other signal measurement equipment's.

I would like also to thank Prof. Raafat Mansour and his team from Center for Integrated RF Engineering lab for allowing the use of additional test equipment. I whole heartily thank Prof. Steve Lambert and Oscar Nespoli for making my study possible while I was working at the University of Waterloo.

I would like to extend my gratitude to my committee members Prof. Edmond Cretu, Prof. Baris Fidan, Prof. Amir Khajepour, Prof. Raafat Mansour, Prof. Gregory Glinka, for making time in their busy schedules to serve on my dissertation committee. Thank you for taking an interest in my work and serving on my PhD defense committee.

I would like to express my gratitude to Page Burton for their invaluable help with the editing of this Thesis.

## Dedication

To Isabel, Michaela and Nathaniel!

# Table of Contents


Examining Committee Membership ..... ii
Author's Declaration ..... iii
Abstract ..... iv
Acknowledgements ..... vi
Dedication ..... vii
Table of Contents ..... viii
List of Figures ..... xii
Nomenclature ..... xvi
List of Abbreviations ..... xix
Chapter I ..... 1
Introduction ..... 1
1.1 Overview of MEMS Gyroscope ..... 2
1.2 Gyroscope Performance Metrics ..... 4
1.2.1 Angular Random Walk (deg/Hz) ..... 5
1.2.2 Rate Random Walk (deg/s/Hz) ..... 5
1.2.3 Bias (deg/s) ..... 6
1.2.4 Power on Bias Drift (deg/s) ..... 6
1.2.5 Bias Stability (deg/s) ..... 7
1.2.6 Nonlinearity (ppm) ..... 7
1.2.7 Resolution (deg/sHz) ..... 7
1.2.8 Sensitivity (mV/(deg/s) or LSB/ (deg/s)) ..... 7

Hysteresis (deg/s) ........................................................................................8
1.2.10 Bandwidth (Hz) ........................................................................................9
1.2.13 Operating Temperature Range (˚C)............................................................9
1.2.14 Shock Survivability ....................................................................................10
1.3 Review of MEMS Gyroscope ..........................................................................10
1.4. Current State of the Art ....................................................................................11
1.5 Motivation and Objectives of the Thesis..........................................................16
1.5.1 Research Contribution.................................................................................18
1.6 Research Outline .................................................................................................18
Chapter II ...............................................................................................................20
Frequency Modulated MEMS Gyroscope ..........................................................20
2.1 Resonance and Resonant Sensing ....................................................................20
2.2 Frequency-Based Detection of Angular Rate....................................................21
2.3 Kinematics Analysis of the Cantilever Beam MEMS gyroscope .....................23
2.3.1 MEMS Gyroscope Frequency Modulation Detection Approach ..................30
2.4 Electrical Excitation and Detection ....................................................................31
2.4.1 Primary Mode Excitation Method.....................................................................33
2.4.2 Drive and Sense Motion Detection ..........................................................38
2.4.2.1 Single port actuation and detection with DC bias ..................................40
2.5 Effects of Capacitive Excitation and Detection ...............................................44
2.5.1 Spring Softening............................................................................................44
Chapter III..............................................................................................................46
MEMS Gyroscope Dynamic Behavior Modeling and Analysis..........................46
3.1 Kinetics Modeling and Assumptions ...............................................................48

3.1.2 Strain-Curvature Relations ....53
3.2 Equations of Motion and Boundary Conditions ....54
3.2.1 Kinetic Energy of the System ....55
3.2.2 Potential Energy ....58
3.3 Extended Hamilton's Principle ....61
3.6 Finite Element Simulations and Results ....80
3.6.1 Cantilever Beam Gyroscope FEA Analysis ....80
3.6.2 Crab Leg FEA Analysis (Device 2) ....86
Chapter IV ....92
Analysis of Thermal Noise in Frequency-Modulated Gyroscopes ....92
4.1 Thermal Noise in MEMS Gyroscope ....93
4.2 Thermal Noise in Frequency-Modulated Gyroscopes ....95
4.2 Analysis of Stability and Device Performance of the Cantilever Gyroscopes ....97
4.2.1 Allan variance ....97
Chapter V ....100
Prototypes Fabrication and Device Characterization ....100
5.1 Prototypes Fabrication MIDIS™ Process ....102
5.2 Experimental Characterization ....112
5.2.1 Single port Actuation and Detection ....114
5.2.2 Crab-Leg Characterization ....119
5.4 Temperature Effects on Cantilever vs Crab Leg ....125
5.5 Noise Analysis ....128
Chapter VI ....132

Summary and Conclusions ....................................................................................... 132

6.1 Contributions and Outcome of This Work ........................................................... 133

6.2 Recommendations for Future Work ..................................................................... 134

References ....................................................................................................... 136

Appendix A: MEMS Gyroscope Model Using MATLAB / Simulink .......................... 142

Appendix B: Fabrication process flow ........................................................................ 145

Appendix C: Mask Design Layouts of MIDIS™ ......................................................... 147

Appendix D: Device Design Parameter and Test Results ............................................ 148

# List of Figures

Figure 1.1: Comparison of the optical vs. mechanical gyroscope ........................................2
Figure 1.2: A typical crab leg MEMS gyroscope 3D model .................................................3
Figure 1.3: Sample Plot of Allan Variance Analysis Results [6] ..........................................5
Figure 1.4: Bias error output for zero input rate ....................................................................6
Figure 1.5: Thermal Hysteresis of gyroscope ........................................................................8
Figure 1.6: Frequency response curve of a resonator ............................................................9
Figure 1.7: AM vibrating MEMS gyroscope block diagram ................................................12
Figure 1.9: Isometric view of (a) cantilever beam (b) crab leg gyroscope ..........................17
Figure 2.1: Functional block diagram of resonant sensing ...................................................20
Figure 2.2: Functional block diagram of FM MEMS gyroscope..........................................21
Figure 2.3: Perspective view of the cantilever beam MEMS gyroscope .............................22
Figure 2.4: Perspective view of the crab leg flexures ..........................................................23
Figure 2.5: Cantilever flexural- flexural displacements .......................................................24
Figure 2.6: Particle O moving in non-inertial Frame B with respect to inertial Frame A. ...25
Figure 2.7: Simplified lumped-mass model of a vibrating MEMS gyroscope .....................28
Figure 2.8: A parallel-plate electrostatic actuator and detection electrodes .........................32
Figure 2.9: A parallel plate electrostatic actuator ................................................................34
Figure 2.10: Crab leg comb finger actuator and sensor electrodes ......................................35
Figure 2.11: Single Port actuation and sensing.....................................................................37
Figure 2.12: Cantilever beam MEMS gyroscope actuation circuit.......................................38
Figure 2.13: Comb finger model for 3D electrostatic force analysis...................................39
Figure 2.14: Cantilever beam MEMS gyroscope sensing circuit ........................................40
Figure 3.1: Schematic of the cantilever beam......................................................................46
Figure 3.2: Cantilever 1 design parameter ...........................................................................47
Figure 3.3: Cantilever beam flexural-flexural deflection ....................................................49

Figure 3.4: Rigid body rotations of beam ....................................................................50
Figure 3.5: A segment of the neutral axis local coordinate system ....................................52
Figure 3.6: Initial and deformed positions of an arbitrary point P.....................................53
Figure 3.7: Load acting on the cantilever beam.................................................................55
Figure 3.8: Variation of the static deflection in the drive with the DC voltage...................70
Figure 3.9: Variation of the static deflection in the sense direction with the DC voltage ....71
Figure 3.10: Variation of the first natural frequency with the DC voltage for cantilever 1 gyroscope (drive) ..........................................................................................................75
Figure 3.11: Variation of the first natural frequency with the DC voltage for Cantilever 1 gyroscope (sense)...........................................................................................................75
Figure 3.12: System output response plot for the drive mode ............................................79
Figure 3.13: System output response plot for the Sense mode ............................................79
Figure 3.14: Meshed element of the cantilever beam gyroscope.........................................81
Figure 3.15: Variation of the static deflection with the DC voltage ....................................82
Figure 3.16: Deformed shape of the cantilever beam gyroscope.........................................83
Figure 3.17: First mode shape of the cantilever beam .........................................................85
Figure 3.18. Second mode shape of the cantilevered beam. ................................................85
Figure 3.19. Third mode shape of the cantilevered beam. ...................................................86
Figure 3.20: Crab leg gyroscope design parameter .............................................................87
Figure 3.21: Meshed crab leg gyroscope .............................................................................88
Figure 3.22: Static deflection and deformed shape of the crab-leg gyroscope .....................89
Figure 3.23: The first mode shape of crab-leg gyroscope (z-axis) ......................................90
Figure 3.24: The second mode shape of crab-leg gyroscope (x-axis) .................................90
Figure 3.25: The third mode shape of crab-leg gyroscope (y-axis).....................................91
Figure 4.1: Allan Variance flow chart .................................................................................98
Figure 4.2: Sample Plot of Allan Variance Analysis Results [5] ........................................99
Figure 5.1: A 3D model of the structure of the cantilever beam element..........................101

Figure 5.2: A comb finger electrode and other structural parts for the crab leg beam element....102
Figure 5.3: Substrates assembly process....103
Figure 5.4: Handle wafer patterning to a depth of 20µm using mask 95 cavity....105
Figure 5.5: Device layer is patterned using a combination of mask 32 and 37....106
Figure 5.6: crab-leg sense and drive electrodes defined using mask 32 and 37....106
Figure 5.7: Second bonding plane definition using mask 34 to creates a 2µm deep spacer between device TSV wafers....107
Figure 5.8: Second bonding plane definition using mask 34....107
Figure 5.9: Cross-section view of final stack....108
Figure 5.10: Second bonding plane definition using mask 34....108
Figure 5.11: Second bonding plane definition using mask 34....109
Figure 5.12: Process cross-section with substrates and masks identification....109
Figure 5.13: Photograph of vacuum packaged test chip along with a 1 cent coin....112
Figure 5.14: Sensing circuit to detect the frequency difference between driving and sensing side resonance....113
Figure 5.15: Illustration of the device characterization setup....114
Figure 5.16: The experimental setup for device characterization using SR850c lock amplifier....115
Figure 5.17: Actuation and Sensing circuit for device characterization in the in-plan direction (x-axis)....116
Figure 5.18: Measured frequency response for Cantilever 1 gyroscope in the drive direction....117
Figure 5.19: zicontrol screen shot for the cantilever beam design 3....119
Figure 5.20: Electrical connection for frequency response test for Device #2....120
Figure 5.21: Measured frequency response for Crab leg (Device #2) drive mode....121
Figure 5.22: zicontrol screen shot of the test device #2....122

Figure 5.23: The experimental illustration for rate table (rate table not shown here) ........123
Figure 5.24: The experimental setup for rate-table characterization ..................................124
Figure 5.25: Measured frequency response for Cantilever beam (Device #1) ...................125
Figure 5.28: Measured frequency shift as a function of time for the cantilever beam gyroscopes..........................................................................................................................128
Figure 5.29: Measured frequency shift as a function of time for the crab leg gyroscopes .129
Figure 5:30: Measured Allan variance comparison between cantilever beam FM gyroscopes..........................................................................................................................130
Figure 5.31: Measured Allan variance comparison between crab leg FM gyroscopes ......131

# Nomenclature

| Symbol | Quantity Description | Units |
|---|---|---|
| $\vec{F}_c$ | Coriolis force | N |
| $m$ | Mass per unit length cantilever beam gyroscope | Kg/m |
| $\vec{\Omega}$ | Input angular rate | $^{O}$/sec (DPS) |
| $\vec{\theta}$ | Angular displacement | Deg. ($^{O}$) |
| $\vec{v}_d$ | Actuation velocity of the proof mass | m/s |
| $R_m$ | Motional impedance | |
| $g_o$ | Initial capacitor gap | $\mu m$ |
| $L_{sm}$ | Suspended mass length | $\mu m$ |
| $b_{sm}$ | Suspended mass width | $\mu m$ |
| $\rho$ | Density | Kg/m$^3$ |
| E | Young's modules | Pascal |
| | Poisson's ratio | - |
| $\mathcal{M}$ | Suspended microplate mass | Kg |
| $w_b$ | Cantilever beam width | $\mu m$ |
| $t_b$ | Cantilever beam thickness | $\mu m$ |
| L | Cantilever beam length | $\mu m$ |
| $V_{AC}$ | AC voltage | Voltage |
| $V_{DC}$ | DC voltage | Voltage |
| $F_{es}$ | Electrostatic actuation force | N |
| $\delta_x(y,t)$ | Sense direction deflection of the microplate | $\mu m$ |
| $\delta_z(y,t)$ | Drive direction deflection of the microplate | $\mu m$ |
| $\vec{r}_A$ | Position vector relative to inertial frame A | $\mu m$ |
| $\vec{r}_B$ | Position vector relative to base frame B | $\mu m$ |
| $\vec{r}_{A/B}$ | Position vector relative to rotating frame | $\mu m$ |
| $\dot{\vec{r}}_A$ | Absolute velocity of particle with respect to the inertial reference | $\mu m/s$ |

| | | |
|---|---|---|
| $\ddot{\vec{r}}_A$ | Acceleration of particle with respect to the inertial reference | $\mu m/s^2$ |
| $F_{fict}$ | Fictitious force | N |
| $\zeta_d$ | Damping ratio of the drive direction | - |
| $\zeta_s$ | Damping ratio of the sense direction | - |
| $\omega_{nd}$ | Natural frequencies of the drive direction | KHz |
| $\omega_{ns}$ | Natural frequencies of the sense direction | KHz |
| $\dot{\Omega}$ | Angular acceleration | $deg./s^2$ |
| $\Delta\omega_{\Omega}$ | Difference between the drive and sense natural frequencies | $deg./s$ |
| $V_{exc}(t)$ | Excitation voltage | V |
| $C$ | Capacitance | F |
| $A$ | Electrode area | $\mu m^2$ |
| $\varepsilon_o$ | Permittivity of vacuum | F/m |
| $\varepsilon_r$ | Relative permittivity of the insulator between the plates | F/m |
| Q | Quality factor | - |
| $E_{es}$ | Total energy | J |
| $\omega_{exc}$ | Excitation frequency | Hz. |
| $C_p$ | Parasitic capacitance | F |
| $C_m\ (t)$ | Capacitance of the electrostatic transducer | F |
| $i(t)$ | Electric current | A |
| $V_{pi}$ | Pull-in voltage | V |
| $k$ | Spring stiffness | $N/m$ |
| A | Peak amplitude of the harmonic signal | |
| $k_{eff}$ | Effective spring constant | $N/m$ |
| $k_{es}$ | Electrostatic spring constant | $N/m$ |
| $[T]$ | Transformation matrix | - |
| $\psi$ | Transformation angle | $deg$ |
| $\theta$ | Transformation angle | $deg$ |
| $\phi$ | Transformation angle | $deg$ |

| | | |
|---|---|---|
| $\rho(s,t)$ | Curvature vector | - |
| $e$ | Strain | - |
| $T_{tr}$ | Kinetic energy due to translation displacement | J |
| $T_{rot}$ | Kinetic energy due to rotation | J |
| T | Total Kinetic energy | J |
| U | Total Potential energy | J |
| $\dot{\delta}_x(L,t)_y$ | Angular speed of the suspended mass in the sense direction (x-axis) | $deg./s$ |
| $\dot{\delta}_z(L,t)_y$ | Angular speed of the suspended mass in the drive direction (z-axis) | $deg./s$ |
| $\sigma_{\mathrm{ij}}$ | Stress | Pa |
| $\varepsilon_{\mathrm{ij}}$ | Strain | - |
| $\delta\mathcal{L}$ | Lagrangian density | - |
| $\delta W_{NC}$ | Virtual work done by non-conservative forces | J |
| $L_1$ | Crab leg beam length 1 | $\mu m$ |
| $L_2$ | Crab leg beam length 2 | $\mu m$ |
| $w_{bw}$ | Crab leg beam width | $\mu m$ |
| $t_b\ (t_p)$ | Crab leg beam thickness | $\mu m$ |
| $L_{cp}$ | Crab leg microplate length | $\mu m$ |
| $w_p$ | Crab leg microplate width | $\mu m$ |
| E | Young’s modules | MPa |
| T | Time constant | |

# List of Abbreviations

| Symbol | Description |
|---|---|
| $BW$ | Bandwidth |
| SF | Scale factor |
| FR | Full-scale range |
| AFM | Atomic force Microscope |
| FM | Frequency modulation |
| DSP | Digital signal processing |
| SNR | Signal to noise ratio |
| LPF | Law pass filter |
| ARW | Angular Radom Walk |
| RRW | Rate Random Walk |
| PLL | Phase locked loop |
| AGC | Automatic gain control |
| PID | Proportional integral derivative |
| TIA | Transimpedance amplifiers |
| VCO | Voltage controlled oscillator |
| MIDIS | MEMS Integrated Design for Inertial Sensors |
| TSV | Through-Silicon Via |
| DRIE | Deep Reactive Ion Etching |
| SOIMUMPS | Silicon-On-Insulato Multiple User Platform |
| AVAR | Allan variance |
| FEM | Finite Element Method |
| APDL | Parametric Design Language of ANSYS |
| PDE | Partial Differential Equation |
| ODE | Ordinary Differential Equation |
| DPS | Degree per second |

# CHAPTER I

# Introduction

Micro-Electromechanical Systems (MEMS) are miniaturized devices that combine integrated electrical circuit and micromechanical components through microfabrication technology. The advent of MEMS technology has directly enabled the development of low-cost, low-power sensors and actuators, which are rapidly replacing their macroscopic scale equivalents in many traditional applications most notably, inertial measurement units (IMU). MEMS inertial sensors, comprised of gyroscopes and accelerometers, are used to measure the rotation rate, angle or acceleration of a body with respect to an inertial reference frame. In recent years, the MEMS inertial sensor market has benefitted significantly from the rise of mobile communication platforms, the Internet of Things (IOT), automotive, augmented reality (AR) and gaming [1-3]. Consequently, MEMS gyroscopes now comprise one of the fastest growing segments of the MEMS sensor market [4].

Conventional vibratory MEMS gyroscope designs have a proof mass suspended above the substrate by a suspension system consisting of flexible beams, typically formed in the same structural layer as the proof mass. A rotational motion perpendicular to the sensor's drive axis produces a DC voltage proportional to the rate of rotation due to the Coriolis forces acting on the sense direction. However, the Coriolis force detection method is very sensitive to change in the environment (such as temperature and stress due to package) and asymmetries in the mechanical transducer because the rate signal is derived from the sense axis. Furthermore, parasitic coupling between the drive and sense axes introduces unwanted bias (offset) errors due to deterministic or stochastic noise sources.

In this study, we focused on vibratory MEMS gyroscopes designed to measure the Coriolis Effect induced by rotation using the frequency modulation (FM) detection technique. Moreover, we investigated the first implementation of a cantilever beam MEMS gyroscope. An introduction to vibratory MEMS gyroscope technology is presented in this chapter including device classification and performance metrics. A detailed review of prior research carried out by the academic and industrial research communities in the conventional MEMS gyroscope design is presented, while emerging, non-

conventional MEMS gyroscope technologies are briefly covered. The chapter concludes with the motivation, objectives and general layout of the thesis research.

## 1.1 Overview of MEMS Gyroscope

Gyroscope devices are typically categorized by the actuation and sensing method employed, either mechanical or optical. Mechanical gyroscopes apply the conservation of angular momentum stored in a vibrating system, whereas optical gyroscopes use the Sagnac effect experienced by counter-propagating laser beams in a ring cavity or a fiber optic coil [5-7]. The Sagnac effect is a special relativistic phenomenon that manifests itself as a phase shift proportional to the rotation rate in a closed-loop interferometer. Optical gyroscopes are typically used for industrial, military and high-tactical grade applications and generally provide good performance. A summary of the comparison between mechanical and optic sensing approaches is presented in Figure 1.1.

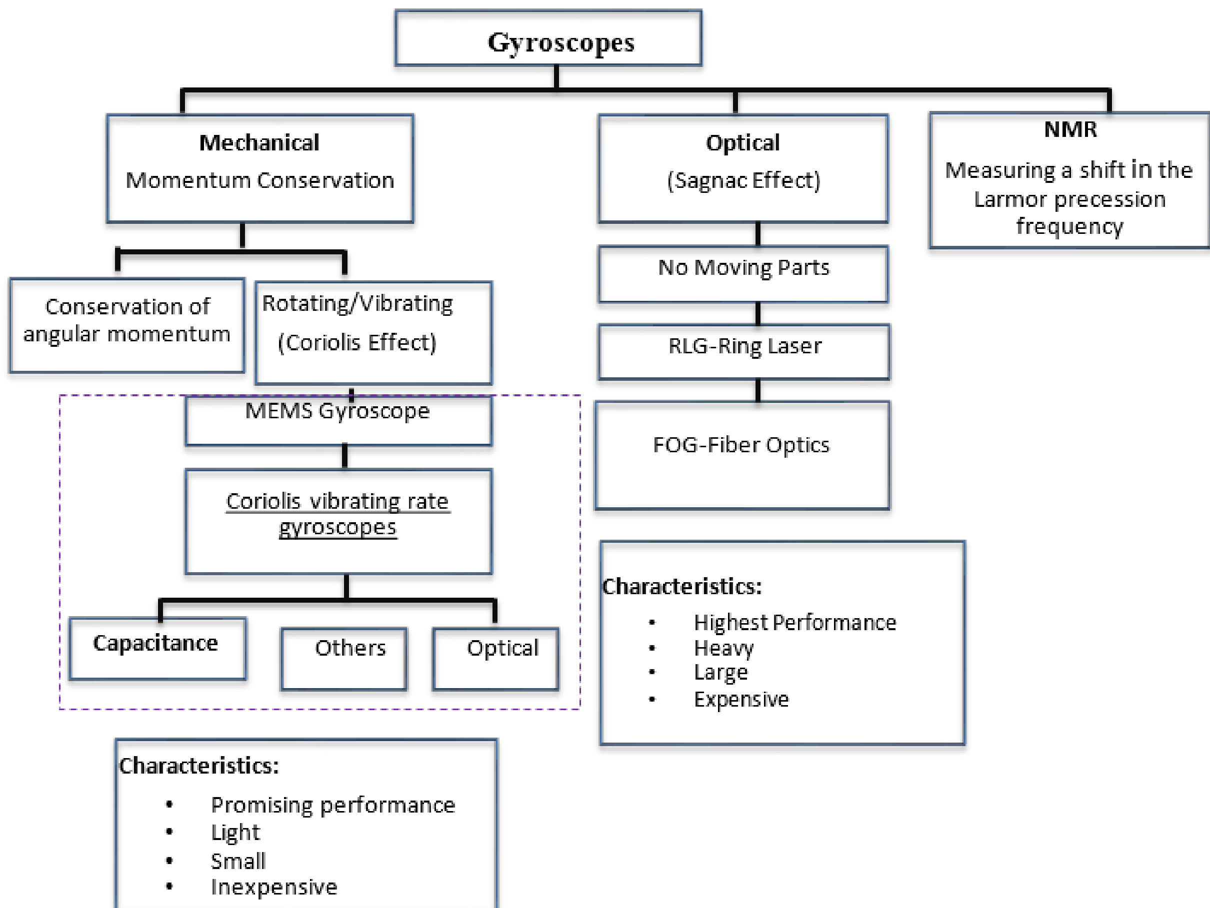


**Figure 1.1: Comparison of the optical vs. mechanical gyroscope**

MEMS vibratory gyroscopes measure angular rotations about specific axes with respect to an inertial reference frame and have found broad application in automotive (rollover detection, anti-sliding control, and GPS), consumer electronics (game consoles, camera image stabilization, cell phone, and 3-D mouse) and medical device applications. Rate gyroscopes measure angular velocity while whole angle gyroscopes measure the rotation angle.

Currently, MEMS gyroscope lag behind optical gyroscope technology in critical performance metrics such angle random walk (ARW) and bias stability, which are extremely important performance criteria for stabilization and positioning systems required for navigation and tactical applications. MEMS entry into these markets is also hampered by the thermal sensitivity of MEMS gyroscopes and inertial systems, which directly impacts their bias and sensitivity [6]. This research aimed to improve these critical performance barriers - specifically bias stability and thermal sensitivity - by implementing the FM detection method and innovative cantilever beam MEMS gyroscope design.

MEMS gyroscopes are mainly vibratory gyroscopes that detect the transfer of energy between two oscillatory modes. A typical two degree of freedom (2-DOF) mechanical resonator design is shown in Figure 1.2. A classical implementation of vibratory gyroscopes consists of a single vibrating proof mass. The proof mass is suspended above the substrate using flexible beams that act as a suspension to isolate the mass from the gyroscope support structure and allow it to vibrate freely.

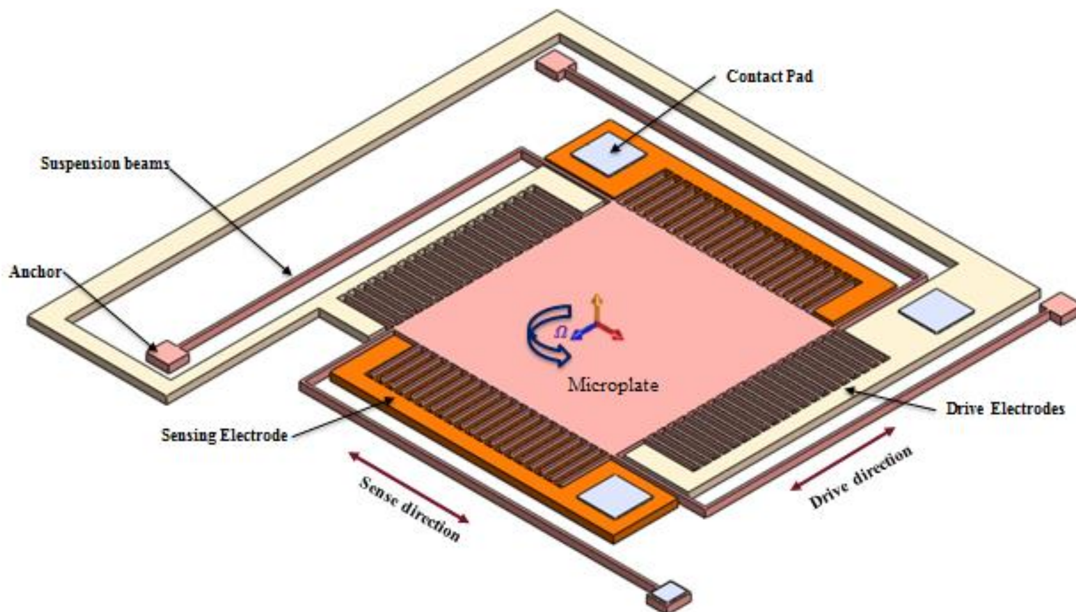


**Figure 1.2: A typical crab leg MEMS gyroscope 3D model**

The proof mass is driven into resonance along the drive axis using drive electrodes. When the sensor rotates in the orthogonal direction of the drive axis, a Coriolis force perpendicular to the drive axis and the angular rotation axis is induced on the proof mass. In the sense direction, the displacement of the proof mass is detected using sense electrodes.

The Coriolis force is oscillatory in nature since it's coupled with the drive motion, and thus the driving frequency of the gyroscope will ideally match with the sensing resonant frequency. If the proof mass is not excited at the right frequency, then the displacement in the sensing direction will be significantly reduced there by affecting its sensitivity. However, slight shifts in the resonant frequencies can improve the gyroscope bandwidth [8]. Hence, there is always a trade-off between the bandwidth and the sensitivity for conventional open-loop MEMS gyroscope technologies. The design can be optimized, however, depending on the application requirements.

Drive mode oscillations are typically range from 5 to 40 kHz with a typical amplitude of about 0.5 to 1.5 $\mu m$, depending on the application. Therefore, the peak oscillation velocity ($\vec{v}_d$) is about 0.06 m/s. The Coriolis force is proportional to the vibrating mass, the drive velocity, and the input angular speed. For MEMS gyroscopes, typical values are used to estimate the Coriolis force in Eq. (1.1), which is on the order of a pico-Newton. Assuming a spring stiffness for the sensing mode of 1 N/m, the sensed displacement is about 10 pm. Thus, capacitive sensing methods are required to detect very small forces (motion).

$$\vec{F}_c = -2m(\vec{\Omega} \times \vec{v}_d) \propto 10^{-12} \times 10^{2} \times 10^{-2} \sim pN \quad (1.1)$$

where $\vec{F}_c$, $m$, $\Omega$, and $\vec{v}_d$ represent the Coriolis force, the mass, the angular speed and the velocity of a proof mass, respectively.

## 1.2 Gyroscope Performance Metrics

MEMS gyroscope performance, particularly with respect to Angular Random Walk (ARW), bias stability and drift metrics, are crucial to their real-world application. This section briefly covers the most basic performance metrics for MEMS gyroscopes.

### 1.2.1 Angular Random Walk (deg/$\sqrt{Hz}$)

Angular Random Walk (ARW) is a measure of noise (i.e., broadband and random noise) in the angle signal as a result of integrating the output of a stationary gyroscope rate over time. For a stationary gyroscope, the ideal output value should be zero. Too much noise critically reduces measurement precision and accuracy in the position measurement. ARW describes the average deviation or error that will occur as a result of this noise element and can be obtained from the Allan Variance value at the 1-sec crossing time, Figure 1.3 [5]. A gyroscope with 0.25 $\frac{\text{deg}}{\sqrt{Hz}}$ ARW will have a standard deviation of the orientation error of 0.25 deg. after one hour and a standard deviation of the orientation error of $\sqrt{2} \cdot 0.25$ deg. = 0.35 deg.

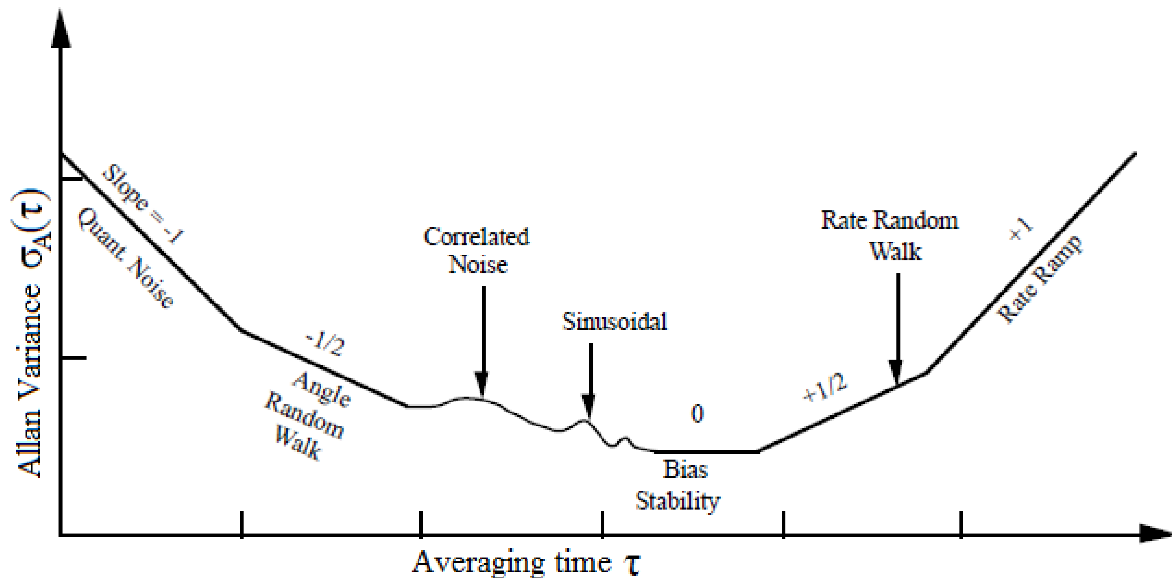


**Figure 1.3: Sample Plot of Allan Variance Analysis Results [5]**

### 1.2.2 Rate Random Walk (deg/s/$\sqrt{Hz}$)

The Rate Random Walk (RRW) is a noise component in the gyroscope rate output signal due to accumulated errors in the mechanical dynamics of the sensor. This component has a very small coefficient and therefore dynamic in the low-frequency band. Therefore, it cannot be removed by classical filtering on the board of the sensor.

### 1.2.3 Bias (deg/s)

MEMS sensor bias, also known as offset, is the average output rate signal when the input is zero. Bias can be expressed as a voltage or a percentage of full-scale output, but it essentially represents an angular rate. The bias error of a gyroscope can be caused by several factors, including deterministic or stochastic noise. The gyroscope bias can be determined and compensated by calibration, while bias drift is random in nature and can be modeled as a stochastic process. Figure 1.4 illustrate a simulated MEMS gyro signal output for zero input rate using Matlab Simulink with zero offset, Appendix A. A change in any physical property such as pressure, temperature or height can induce bias. For MEMS gyroscope, temperature variation, weather it is due to the environment or to the heating of the sensor itself, is the main cause of bias. Because of the many physical properties depending on the temperature, the bias caused by temperature fluctuation is nonlinear to the temperature change itself [9].

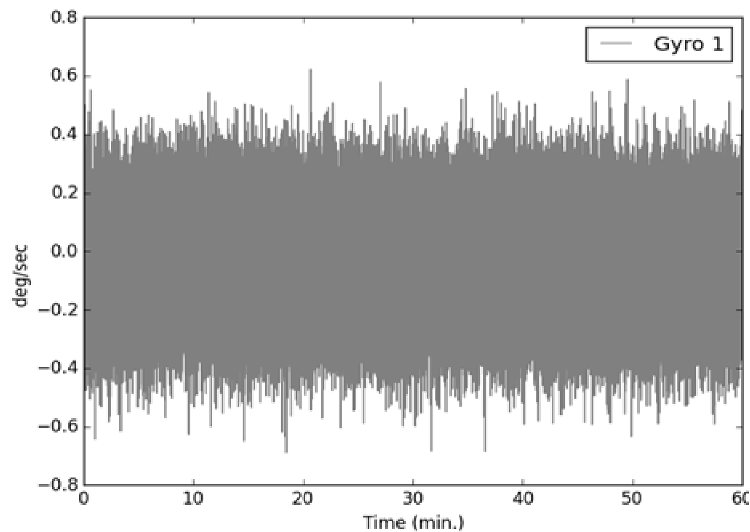


**Figure 1.4: Bias error output for zero input rate**

### 1.2.4 Power on Bias Drift (deg/s)

Power on bias drift is a measure of output measured rate every time the gyroscope is turned on, and should ideally be the same each time. Turning the device on and off many times and achieving good repeatability requires very stable devices and good control over the thermal, mechanical and electrical characteristics of the device.

### 1.2.5 Bias Stability ($\mathbf{deg}/\boldsymbol{s}$)

Bias stability is a measure of the gyroscope's output stability over a length of time, and is a fundamental performance metric for all gyroscopes types including fibre optic gyroscope (FOG), ring laser gyroscope (RLG), and MEMS. Bias stability is measured after the device is turned on and for a particular length of time. This variable provides a measure of the drift of the output offset value over time. Bias instability is best measured using the Allan Variance measurement technique, Figure 1.3. Many applications, including autonomous vehicle navigation, require higher bias stability for excellent performance.

### 1.2.6 Nonlinearity (ppm)

Gyroscopes output a voltage proportional to the input angular rate. Nonlinearity measures how the outputted voltage close to linearity to the actual angular rate. Nonlinearity measured as a percentage error from a linear fit over the full-scale range or an error in parts per million (ppm). For MEMS gyroscope, the output linearity affected by physical property such as pressure or temperature. Additionally, packaging stress play a critical role in nonlinearity.

### 1.2.7 Resolution ($\frac{\mathbf{deg/s}}{\sqrt{\boldsymbol{Hz}}}$)

Gyroscope resolution defines the minimum change in input required to produce a measurable change in output. The white noise of the device limits the resolution; therefore, the resolution can be determined by measuring the standard deviation of the white noise.

### 1.2.8 Sensitivity (mV/($\mathbf{deg}/\boldsymbol{s}$) or LSB/ ($\mathbf{deg}/\boldsymbol{s}$))

Sensitivity defines the relationship between the input rotation rate, in degree per second ($\frac{\text{deg}}{\sqrt{Hz}}$), and the gyroscope's output voltage change. A device's sensitivity can vary due to many factors as the output signal may be sensitive to environmental conditions and other undesirable inputs. Some common secondary inputs include temperature, pressure, and humidity. Sensitivity can be used to convert the gyroscope's output voltage signal into angular velocity.

$$S_f = \frac{(\Omega + \Omega_0)}{\hat{\Omega}} \tag{1.2}$$

where $\hat{\Omega}$ is the output signal,

$S_f$ is the sensitivity,

$\Omega$ is the applied rate and

$\Omega_0$ is the Zero-rate offset (ZRO).

The ZRO is the gyroscope measured rate when no rate is applied.

### Hysteresis $(\mathbf{deg}/\boldsymbol{s})$

A gyroscope exhibit hysteresis when a characteristic looping behaviour of the input-output graph is displayed. These loops can be due to a variety of causes including temperature, pressure or other environmental factors. The Thermal hysteresis of the zero offset is the maximum deviation of the zero offset at any temperature within the operating temperature range after the temperature is cycled between the minimum and maximum operating temperature points. In other words: Thermal hysteresis describes a phenomenon whereby the same applied temperature results in different output signals depending upon whether the temperature is approached from a lower or higher temperature. The temperature hysteresis strongly depends on the measurement conditions, e.g. dwell times, and the chosen temperature range.

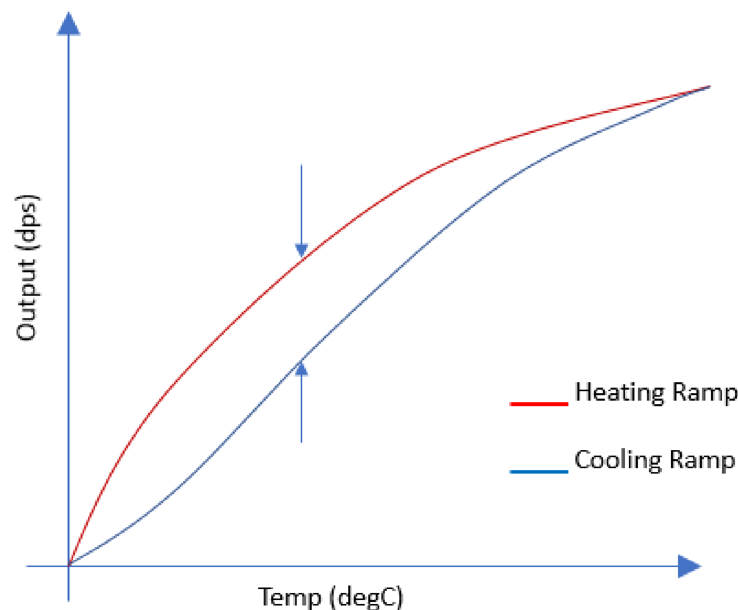


**Figure 1.5: Thermal Hysteresis of gyroscope**

## 1.2.10 Bandwidth (Hz)

The bandwidth of a gyroscope typically measures how many measurements can be made per second. the range of frequency of the angular rate input that the gyroscope can detect. It indicates the range of input frequencies for which the output-input relation is preserved. Traditionally, a 3-dB variation in the scale is tolerated at the edge of the bandwidth. Figure 1.5 illustrate the bandwidth of a signal in the frequency response curve. The bandwidth of a MEMS vibratory structure can be expressed:

$$BW = \frac{(f_1 - f_2)}{Q} \quad (1.4)$$

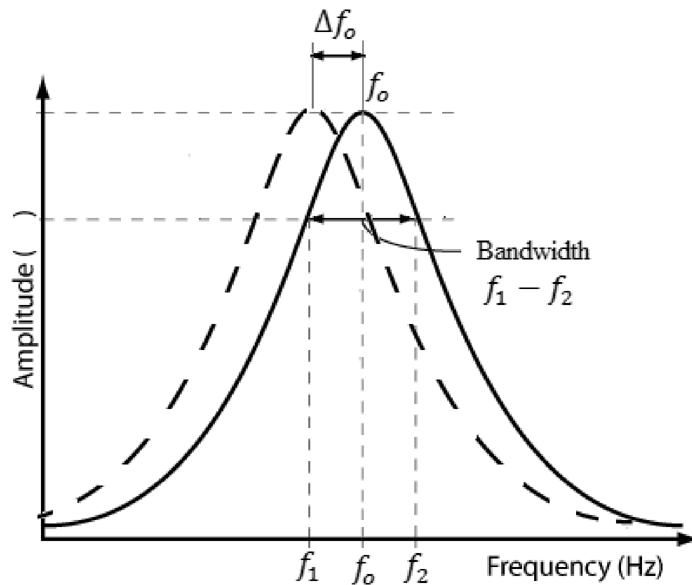


**Figure 1.6: Frequency response curve of a resonator**

## 1.2.13 Operating Temperature Range (˚C)

MEMS gyroscope performance degrades over temperature. Many gyroscopes are available with an onboard temperature sensor, so the output of the gyroscope compensated (calibrations) based on the temperature sensor reading. Hence, the range of operating temperatures for MEMS gyroscopes is spanning from roughly -40˚C to 200˚C.

### 1.2.14 Shock Survivability

In systems where both linear acceleration and angular rotation rate are measured, it is important to know how much force the gyroscope can withstand without failing. This is typically measured in g's (1g = earth's acceleration due to gravity), and occasionally the time with which the maximum g-force can be applied before the unit fails is also given.

## 1.3 Review of MEMS Gyroscope

A wide range of MEMS gyroscope designs, fabrication methods, and control systems have been developed over the last two decades. This section highlights major progress made during this period. Draper Labs demonstrated the first MEMS gyroscope in 1991, utilizing a double-gimbal single crystal silicon structure suspended by torsional flexures with a resolution of 4 $\frac{\text{deg/s}}{\sqrt{Hz}}$ over 60Hz bandwidth [9]. Since then, various MEMS gyroscopes designs fabricated with a wide range of topologies, fabrication process, integration approaches, and detection techniques have emerged [10].

In 1993, Draper Labs reported tuning fork gyroscopes with 1 $\frac{\text{deg/s}}{\sqrt{Hz}}$ resolution at 60Hz bandwidth using a silicon-on-glass fabrication technique to reduce parasitic capacitances. In 1996, the Berkeley Sensor and Actuator Center (BSAC) developed an integrated z-axis vibratory rate gyroscope with a resolution of 1 $\frac{\text{deg/s}}{\sqrt{Hz}}$ using a surface micromachining process. This z-axis gyroscope had a single proof mass driven in-plane at resonance. Electrostatic frequency tuning of sense-modes was successfully demonstrated to enhance sensitivity by minimizing mode mismatching. Furthermore, the quadrature error nullifying technique was employed to compensate for structural imperfections caused by fabrication tolerances.

In 1997, BSAC developed an x-y dual input axis gyroscope with a 2μm quad symmetric circular oscillating polysilicon rotor disc. This gyroscope utilizes torsional drive-mode excitation and two orthogonal torsional sense-modes to achieve a resolution of 0.24 $\frac{\text{deg/s}}{\sqrt{Hz}}$. Subsequent electrostatic tuning of the device resulted in higher performance, at 0.05 $\frac{\text{deg/s}}{\sqrt{Hz}}$ resolution, but at the expense of high cross axis sensitivity [9-10].

In 2000, Seoul National University reported a hybrid surface-bulk micromachining (SBM) process with deep reactive ion etching (DRIE) to fabricate high aspect ratio structures with large sacrificial gaps in a single wafer. A new isolation method using sandwiched oxide, polysilicon and metal films was

developed for electrostatic actuation and capacitive sensing. This 40µm thick single crystal silicon MEMS gyroscope demonstrated a resolution of 0.0025 $\frac{deg/s}{\sqrt{Hz}}$ at 100Hz bandwidth [11].

In 2001, Carnegie-Mellon University (CMU) employed a mask-less post-CMOS micromachining process to develop a lateral-axis integrated gyroscope with a resolution of about 0.5 $\frac{deg/s}{\sqrt{Hz}}$ [12]. The lateral-axis gyroscope had a 5µm thick structure with out of plane actuation and was fabricated using Agilent's three-metal 0.5µm CMOS process. CMU also fabricated an 8µm thick z-axis integrated gyroscope with dimensions 410×330µm$^2$ using a six-copper layer and 0.18µm CMOS process [13]. This device showed a sensitivity of 0.8µV/o/s and a resolution of 0.5 $\frac{deg/s}{\sqrt{Hz}}$.

In 2003, CMU demonstrated a DRIE CMOS-MEMS lateral axis gyroscope with dimensions 1×1 mm2 and a measured resolution of 0.02 $\frac{deg/s}{\sqrt{Hz}}$ at 5Hz. This device was fabricated by post-CMOS micromachining using interconnect metal layers to mask the structural etch steps. The device was built with on-chip CMOS circuitry and demonstrated in-plane vibration and out of plane Coriolis acceleration detection [14].

In 2004, Middle East Technical University (METU), Turkey, presented a symmetrical and decoupled surface MEMS gyroscope fabricated by electroforming thick Nickel on a glass substrate. A capacitive interface circuit, which was fabricated using a 0.8µm CMOS process, was hybrid connected to the gyroscope, where the circuit had an input capacitance lower than 50fF and a sensitivity of 33mV/fF. Calculations on measured resonance values suggested that the fabricated gyroscope, which had a 16µm thick structural layer, provides a resolution of 0.004 $\frac{deg/s}{\sqrt{Hz}}$ [15].

There are still active research and development from other key player to address the market need for emerging new application such as IOT and augmented reality. Various design methods and fabrication processes have been explored to improve the certain performance metrics especially bias instability and ARW to increase MEMS gyroscopes robustness.

## 1.4. Current State of the Art

Gyroscopes are classified into three different categories based on their performance: rate-grade, tactical-grade, and inertial grade devices. Table 1.2 summarizes the performance metrics for each category. Over the past decade, much of the effort in developing MEMS gyroscopes has concentrated on rate grade

devices, primarily because of their use in consumer electronics and automotive applications. Depending on the application, automotive systems generally require a full-scale range of at least 50 - 300 deg/s and a resolution of about 0.5 - 0.05 deg/s in a bandwidth of less than 100 Hz [22].

**Table 1.1: Main Classes of gyroscopes**

| **Parameter** | **Rate Grade** | **Tactical Grade** | **Inertial Grade (Strategic and Navigational)** |
|---|---|---|---|
| Angle random walk [$deg/\sqrt{h}$] | $> 0.5$ | 0.5– 0.05 | <0.001 |
| Bias Stability [deg/hr] | 1 - 30 | 0. 1 - 30 | 0.0001 - 0.1 |
| Bias drift [deg/h] | 10– 1000 | 0.1– 10 | $< 0.01$ |
| Scale factor accuracy [%] | 0.1– 1 | 0.01– 0.1 | $< 0.001$ |

Current MEMS gyroscopes operate as amplitude modulation (AM) systems, illustrated in Figure 1.6, where the mechanical sense-mode response is excited by the input angular velocity. Existing optical gyroscopes are high-performance sensors, but they are heavy, large and are not suitable for most consumer electronics and emerging IOT applications. For a vibratory MEMS gyroscope to achieve performance levels equivalent to current optical gyroscope technologies, their mechanical and electronic components, as well as their sensing mechanisms, must be analyzed in detail and new approaches are required to minimize error while increasing sensitivity. This means care must be taken in achieving material uniformity, and in combining mixed micromachining fabrication processes on silicon and deep etching techniques to ensure the structures maintain a high-quality. Robust vacuum packaging techniques and frequency tuning are also important to compensate for sensor drifts and long-term effects.

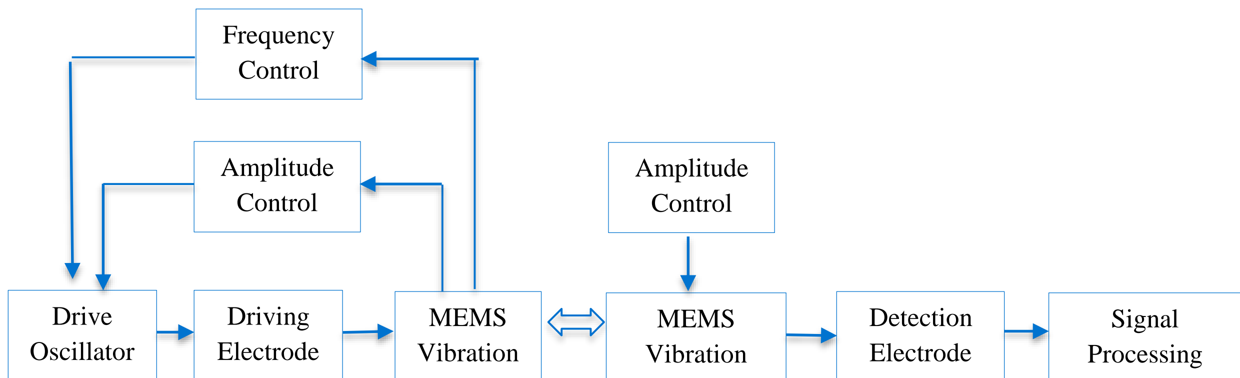


**Figure 1.7: AM vibrating MEMS gyroscope block diagram**

All conventional MEMS gyroscopes are based on Coriolis Effect amplitude modulation (AM) gyroscopes. In this case, the input angular rate is amplitude-modulated by the drive mode velocity signal. They need high quality factors (Q) to improve the sensitivity, resulting in a constraint between Q factor and bandwidth. Moreover, AM sensors are also extremely sensitive to the value of the sense mode Q factor which will result in scale factor drifts caused by the ambient temperature and pressure. Even though an extensive variety of MEMS gyroscope designs and operation principles exists, achieving robustness against fabrication variations and imperfection as well as environmental fluctuations remain as one of the greatest challenges in high-performance MEMS gyroscope development. The limitations of the micromachining technologies define the performance and robustness of the device. Conventional gyroscopes design based on matching the drive and sense mode resonant frequencies are sensitive to variations in oscillatory system parameters, which affect device performance. Thus, realizing stable and reliable vibratory MEMS gyroscopes has proven extremely challenging, primarily due to the high sensitivity of the dynamical system response to fabrication and environmental variations. To overcome this challenge, a thorough understanding of all aspects of sensor production including MEMS fabrication, design, and backend operations is required. Moreover, these critical aspects must be mutually optimized to be universally adopted in the cost sensitive, high volume, consumer electronics market, which is the primary driver for MEMS gyroscope innovation.

In this study, we investigated frequency modulated MEMS gyroscopes that exploit changes in the natural frequency of the proof mass vibrations to measure rotation rate, which theoretically reduces the effect of noise. The FM technique measures the angular rate by detecting the difference between the frequencies of two closely spaced global vibration modes, as illustrated in Figure 1.7. The FM approach has already been implemented in other MEMS sensors including atomic force Microscopes (AFM), pressure sensors and mass sensors.

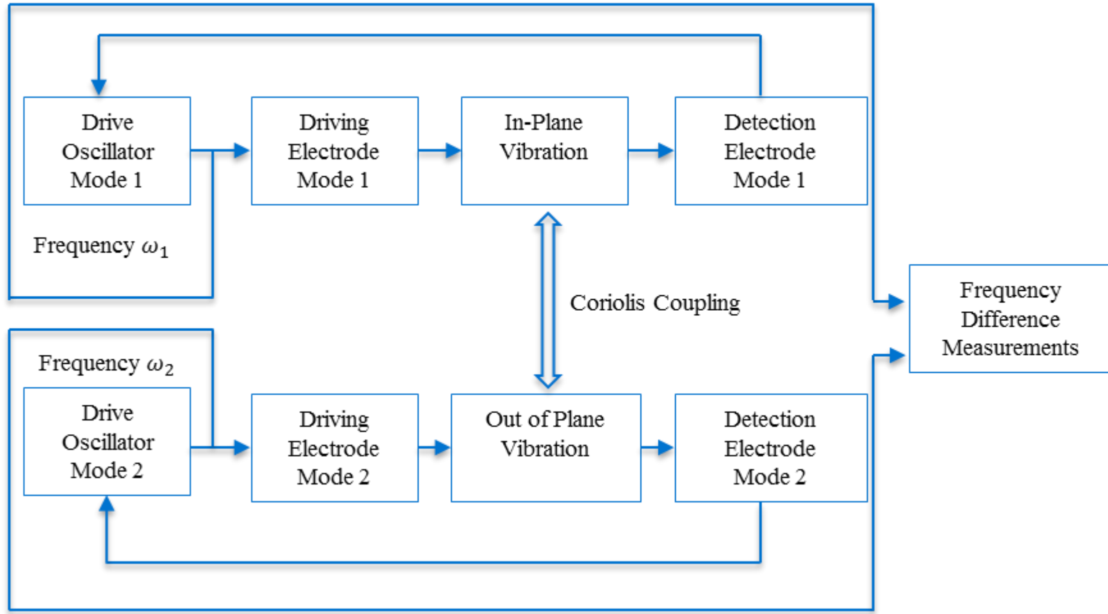


**Figure 1.8: FM vibrating MEMS gyroscope block diagram**

Although MEMS gyroscopes have been the subject of intensive research for several years and the frequency sensing approach has been shown to address some of the key limitations of existing MEMS sensors designs, the technique remains under-utilized in MEMS gyroscope research [16-18]. Seshia et al. reported an integrated microelectromechanical resonant gyroscope, but they did not give the dynamic characteristics of the resonant gyroscope in detail [20]. Moussa H. and Bourquin R [23] introduced the theory for direct frequency output vibratory gyroscopes, but they were concerned with gyroscope designs where the vibratory mode was out of the plane. Other studies have investigated the resonant gyroscope, but they all focus on improving the quality factor (for higher sensitivity), the driving control, or the fabrication process [26-28].

Zotov et al. proposed an angular rate sensor based on mechanical frequency modulation (FM) of the input rotation rate to solve the contradiction between the gain–bandwidth and dynamic range, [29]. The sensor consists of a symmetric, ultra-high Q, silicon micromachined Quadruple Mass Gyroscope (QMG) and a new quasi-digital signal processing scheme which takes advantage of a mechanical FM effect. The input angular rate is only proportional to the frequency split. The gyroscope comprises four identical symmetrically decoupled tines with linear coupling flexures as well as a pair of anti-phase synchronization lever mechanisms for both the x- and the y-modes. The complete x-y symmetrical structure improves robustness against the fabrication imperfections and frequency drifts.

Li et al. proposed a double-ended tuning fork (DETF) gyroscope, which utilizes resonant sensing as the basis for Coriolis force detection instead of displacement sensing [30]. The device is fabricated by the silicon on glass (SOG) micro fabrication technology. The gyroscope consists of two proof masses, a pair of DETF resonators and two pairs of lever differential mechanisms. The lever differential mechanism is responsible for the transmission of the differential Coriolis forces into one common force acting in the longitudinal direction of the DETF. When the two masses move toward each other or away from each other, the opposite Coriolis forces from the two masses are transferred to one common force. The common mode acceleration error is cancelled because the transferred force is differential. The rotation rate applied to the device can be estimated by demodulating the DETF resonant frequency and detecting the resonant frequency difference.

However, the effect of temperature and packaging stress on device performance remains a major challenge in MEMS gyroscope design. The present study focused on addressing this issue by implementing a novel free end cantilever beam design and the FM sensing approach. The FM sensing method has proven to be highly sensitive, provide good linearity, low noise and low power in other applications [24]. We also investigated for the first time the cantilever beam implementation and single port excitation and sensing scheme. The cantilever structure was designed to provide good control over the thermal, mechanical, and electrical characteristics, thereby dramatically improving bias stability.

The free end cantilever structure minimizes the effects of packaging and thermal stresses. Specifically, the design helps eliminate thermally induced strain between the supporting beam and the substrate, and reduces the impact of packaging sensitivity. The cantilever beam gyroscope could also be aligned in an orthogonal direction to develop a multi-axis device, which helps to reject external vibrations since the cantilever beam does not move in response to linear acceleration in the beam’s longitudinal axis. The single port sensing design also eliminates any cross talk between the drive mode and sense modes of the gyroscope caused by manufacturing misalignment (i.e., the design minimizes cross-axis sensitivity). The single-port MEMS FM gyroscope (signal processing) design could also be simplified and the electronics, signal processing electronics (IC architecture) and backend operations improved. The single port cantilever beam gyroscope design minimizes the error sources that corrupt the Coriolis signal and simplifies the IC architecture.

## 1.5 Motivation and Objectives of the Thesis

There is a growing demand for high-performance MEMS gyroscopes which can't be satisfied with either optical or currently existing gyroscope technologies. The need for smaller and lighter gyroscopes has been partly met by advances in MEMS design and fabrication. To maximize the device performance in conventional AM MEMS gyroscopes, resonance is used to enhance the response gain, and hence the sensitivity of the device, by matching the resonant frequencies of the drive and the sense-mode. However, bias stability, reliability, and other performance metrics remain major concerns as designers look to expand MEMS gyroscopes into a broader range of applications, such as navigation, which require an extended time use of the sensor.

In view of the above-mentioned issues, the current state of vibratory rate MEMS gyroscopes requires an order of magnitude improvement in performance and robustness. Hence, more research is needed to investigate angular rate sensing mechanisms including the feasibility of frequency modulated gyroscopes. Industries and academic research groups developing gyroscopes often focus on fabricating devices or theoretical work on control algorithms and lack the expertise to implement effective readout and control hardware.

The aim of this work is to design thermally stable and robust MEMS gyroscopes using a frequency modulation method, and by means of theoretical and experimental approaches. Two major design concepts, a novel cantilever beam design and traditional crab leg configuration, are explored to achieve a dynamical system with a wide bandwidth frequency response, Figure 1.8. We aim to develop, for the first time, a cantilever beam gyroscope that employs a transfer of energy identification technique to estimate the natural frequency deviation with the angular velocity input. The design goals of our cantilever MEMS gyroscope are to build a small sensor with a very low angle drift and bias instability, which requires devices with low stress and high-quality factors, wide dynamic range (capable of accurate measurements at both low and high rotation rates), and wide bandwidth to match the maneuverability of small vehicles.

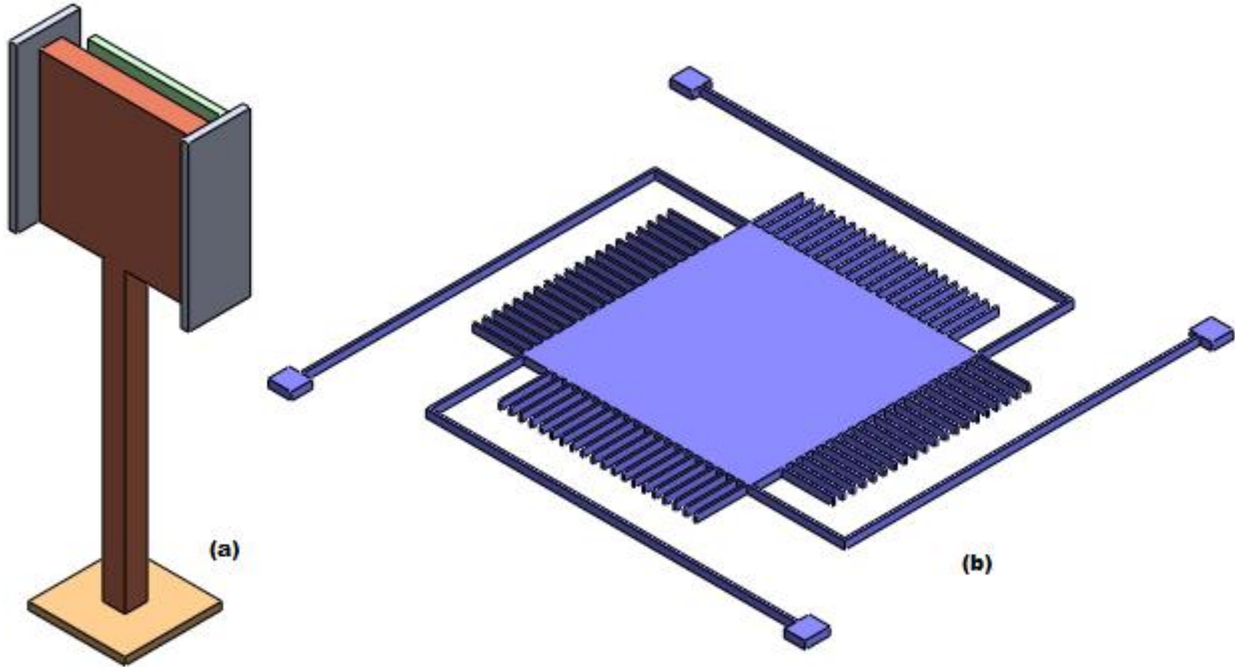


**Figure 1.9: Isometric view of (a) cantilever beam (b) crab leg gyroscope**

The general approach pursued in this research is to explore the possibility of achieving high device performance by reducing thermal and packing stress effects. We also aim to develop experimental parametric bandwidth frequency responses in the drive and sense modes. The work has two areas of focus. First, a system-level design of a MEMS angular velocity sensor is developed, to provide a general-purpose analysis of potential and selected aspects. Second, an integrated implementation and design of the electronics required by the angular velocity sensor is produced.

As illustrated in Figure 1.8, the cantilever beam MEMS gyroscope consists of clamped-free beams and a microplate that are driven into flexural out of plane or in-plane vibration. Then, in response to rotation force applied along the beam longitudinal axis, it starts to vibrate along an orthogonal direction. This motion can be used to compute the angular rate input. The drive axis actuation is provided by electrostatic force and the Coriolis-induced vibration is electrostatically detected by measuring the capacitance changes between the microplate and fixed electrode and dedicated sensing electrodes. The cantilever beam structure is designed to have out of plane drive mode and in plane sensing modes. A vibrating crab-leg beam structure is also investigated, primarily as a direct comparison against the cantilever beam design under the same test conditions.

### 1.5.1 Research Contribution

The objective of this research is to develop new dynamical sensing systems and structural designs for resonant MEMS vibratory gyroscope technologies using standard, low-cost, commercially available MEMS processes. The proposed research objectives are to:

- Demonstrate the MEMS gyroscope operation in the frequency modulation mode and investigate the modal frequencies of the MEMS gyroscope,
- Derive the mathematical model of the beam-rigid body gyroscope considering the static behavior of the beam-rigid body MEMS gyroscope and study the reduced-order nonlinear behavior of the system,
- Analyze the nonlinear behavior using Finite Element software (ANSYS) and compare the results of the method with the analytical and numerical results,
- Develop the mechanical-thermal noise analysis for a frequency modulated MEMS gyroscope
- Design and fabricate a prototype MEMS gyroscope to demonstrate the frequency modulated MEMS gyroscope concept,
- Develop a characterization method that measures the frequency of the MEMS gyroscope's two modes

## 1.6 Research Outline

This work is organized into six chapters to provide the scope of work. In chapter one, the working principles, types and applications of vibratory MEMS gyroscopes are introduced and comprehensively described. A review of MEMS gyroscope sensing methods along with the prior research work carried out by academic and industrial research groups are provided. Following the literature review, the research method is presented, including an overview of the research problems, as well as research objectives and the research motivation.

Chapter two covers the basics of the FM MEMS gyroscope concept and analysis of frequency modulated mathematical modeling. A detailed review of frequency modulated MEMS sensor implementation is given. The principles of operation and benefits of the FM gyroscope design is introduced along with related design parameters and characteristics. Throughout the FM sensing approach review, the frequency sensing method is proved to have better sensitivity and higher accuracy on micro-displacement measurement compared to the AM method. This provides the development background

and methods to significantly improve the performance of MEMS gyroscope systems. Towards the end of the chapter, the frequency excitation and detection approach, as well as gyroscope testing and characterization, are briefly discussed.

Chapter three comprehensively covers the dynamics of the cantilever beam MEMS gyroscope, taking into account its systematic design implementation. A comprehensive theoretical description is provided, and relevant dynamics and mechanical design considerations of the cantilever beam models are discussed in detail. Optimization, as well as simulation methodology in ANSYS, are also developed. The main emphasis of this work is to demonstrate the optimization of gyroscopes within the design rules of standards for Teledyne Dalsa MEMS Integrated Design for Inertial Sensors (MIDIS™), where we fabricate prototype device.

In chapter four, the noise analysis for frequency modulated MEMS gyroscope structures and noise-based optimization are briefly discussed. Chapter five discusses fabrication methods for MEMS vibration structures, including a cantilever beam and crab leg MEMS gyroscope fabrication process. These vibration structures are further described based on operation principles and functions introduced in chapter two. Prototype fabrication using the MIDIS™ process is also investigated. Finally, a testing methodology along with the electrical circuit, control, and sensing design is devised and test result presented.

The last chapter provides a list of major contributions and some suggestions for improving the performance of MEMS gyroscope design. To sum up the structure of this thesis, it defines a problem and discusses alternative methods to fine tune the final structure of the gyroscope.

# CHAPTER II

# Frequency Modulated MEMS Gyroscope

## 2.1 Resonance and Resonant Sensing

The resonance sensing concept is fundamental to understanding the operation of frequency modulated MEMS gyroscope systems. Resonance is a term used to describe a system's enhanced response at a certain characteristic natural frequency determined by parameters of the system. The specific frequency is one where the system retains input energy with minimum loss. Resonance can be observed in mechanical, optical and electronic systems as well as in systems that interconvert energy between these energy domains. At a microscopic scale, operating systems at resonance enhances the effects of small forces and the device's signal to noise ratio. A general functional block diagram of the resonant sensing approach is illustrated in Figure 2.1.

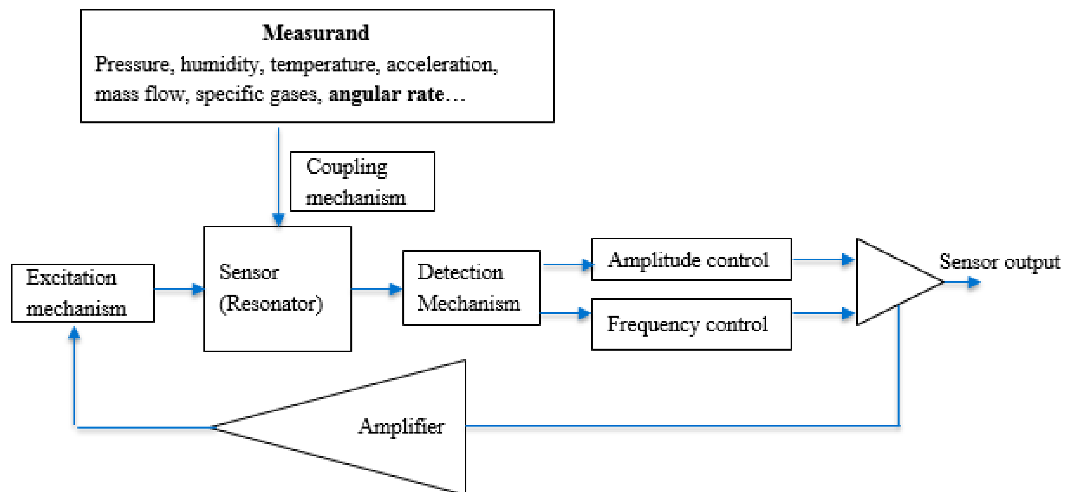


**Figure 2.1: Functional block diagram of resonant sensing**

The resonant characteristics of a mechanical system can be changed either by modulating the spring constant (stiffness) or the effective mass of the resonating system. Typically, a shift in either of these quantities can be monitored as a change in the resonant amplitude, frequency or phase [21-22]. A change in resonant characteristics can be monitored using several different techniques such as capacitive, optical and piezoresistive sensing. Generally, measuring the change in resonance frequency provides a highly

sensitive instrument and has the potential to address a large dynamic range [22-23]. The resonance frequency sensing approach has been implemented in numerous MEMS devices including Atomic Force Microscopy (AFM) and pressure sensors.

## 2.2 Frequency-Based Detection of Angular Rate

In conventional AM gyroscope designs, the primary mode drives at a constant amplitude and frequency along the drive axis. When the gyroscope is subjected to an angular rotation, a Coriolis force is generated along the sense axis, whose magnitude is proportional to the oscillation velocity of the drive axis and the magnitude of the input angular rate that is being measured. The sense direction motion magnitude is amplified according to the mechanical quality factor and the rate signal detected along the sense mode of vibration by reading the amplitude changes. In this work, we primarily focused on the FM approach, which tracks the instantaneous frequency of the drive and sense oscillation. The functional block diagram of the FM method is given in Figure 2.2.

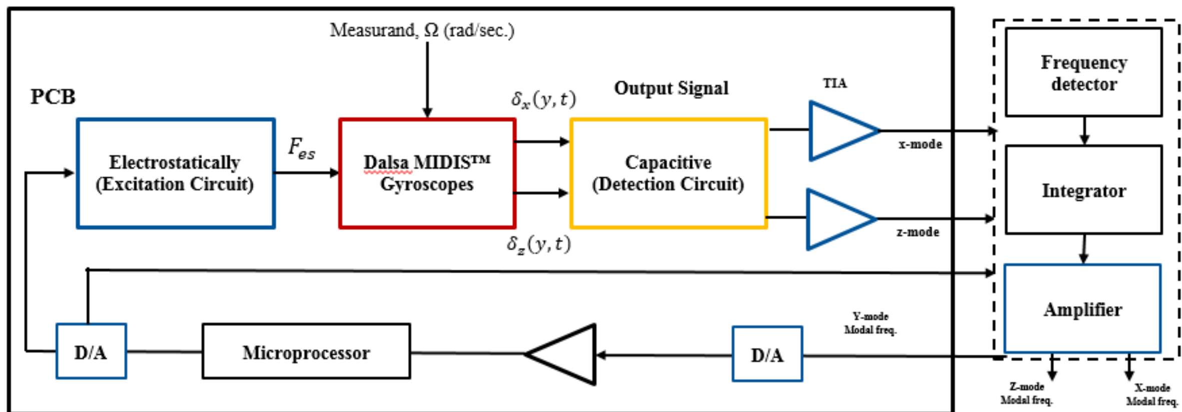


**Figure 2.2: Functional block diagram of FM MEMS gyroscope**

In this study, the FM approach was implemented, using cantilever beam and crab-leg MEMS gyroscope configurations, to detect the applied rotation rate using the shift in natural frequency of the first two close modes. A schematic of the Cantilever beam MEMS vibratory gyroscope is shown in Figure 2.3, which includes two parallel sidewall electrodes (the right side removed here for clarity) and the drive electrode. The cantilever beam is attached to a rotating base and it has a uniform cross section. At the free end, a proof mass (M) is attached, which is electrically coupled to the drive and sense electrodes. The suspended mass is driven to vibration along the z-axis by applying AC excitation and DC polarization voltage between the parallel plate (proof mass and stationary drive electrodes). When the cantilever beam gyroscope rotates around the y-axis, the Coriolis acceleration induced by the input

rotation rate causes the beam to transfer energy from the drive-mode (z-direction) to the sense-mode (x-direction). The input angular rate can be measured by analyzing the shift in the natural frequencies of these two modes.

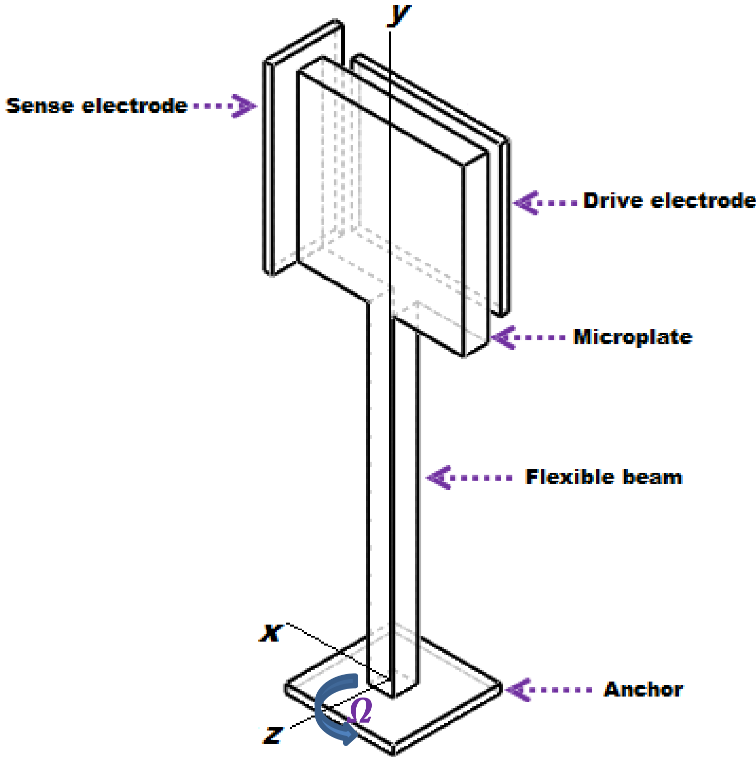


**Figure 2.3: Perspective view of the cantilever beam MEMS gyroscope**

A crab-leg MEMS gyroscope system was also developed and experimentally investigated to evaluate the performance advantage(s) of the new cantilever design. Traditional crab-leg flexure structures were designed within plane motion for both drive and sensing modes. In this design, we used a comb drive (set of parallel plates) for sensing and driving the gyroscope. In Figure 2.4, a schematic drawing of the crab-leg gyroscope is illustrated where the actuation takes place in the z-direction. When the angular rate is applied along the y-axis, the Coriolis force is induced and sensing happens in the x-direction.

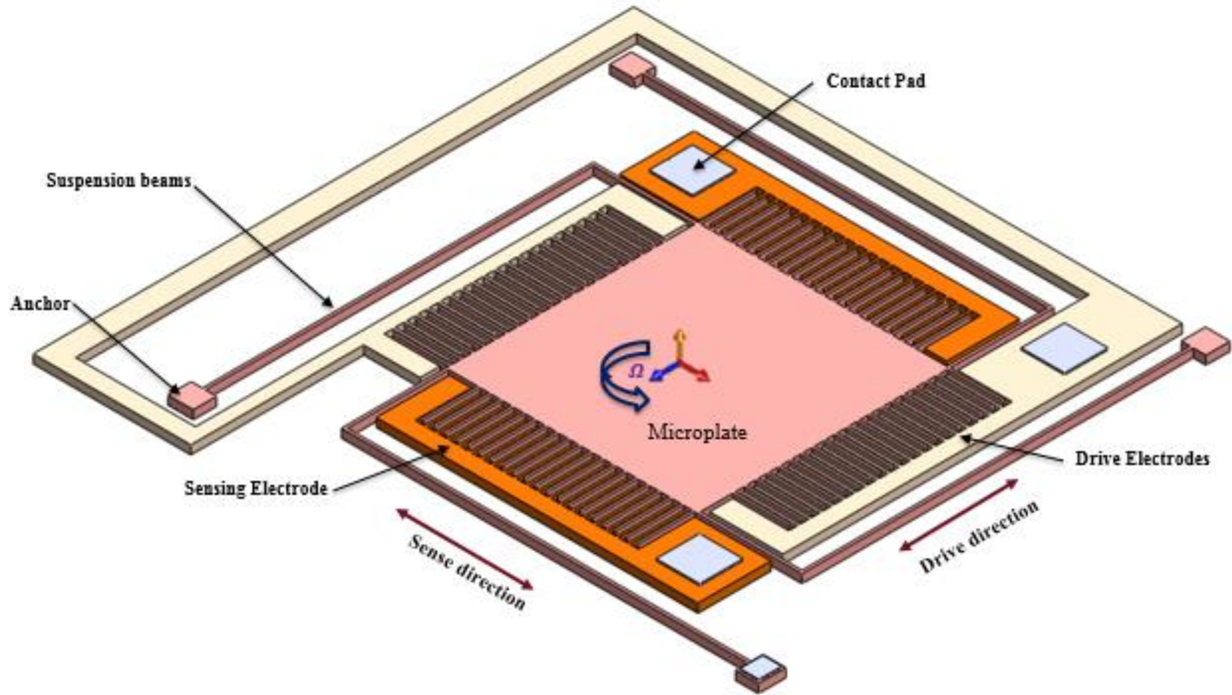


**Figure 2.4: Perspective view of the crab leg flexures**

## 2.3 Kinematics Analysis of the Cantilever Beam MEMS gyroscope

A mathematical model that represents the kinematics characteristics of the cantilever beam gyroscope, which is equally applicable to the crab leg dynamics, is presented in this section. The microplate proof mass ($\mathcal{M}$) is a rigid body and the center of the microplate can be assumed as a particle (O). Figure 2.5 shows the cantilever beam subjected to generalized electrostatic actuation ($F_{es}$) and Coriolis forces ($F_c$) at the tip.

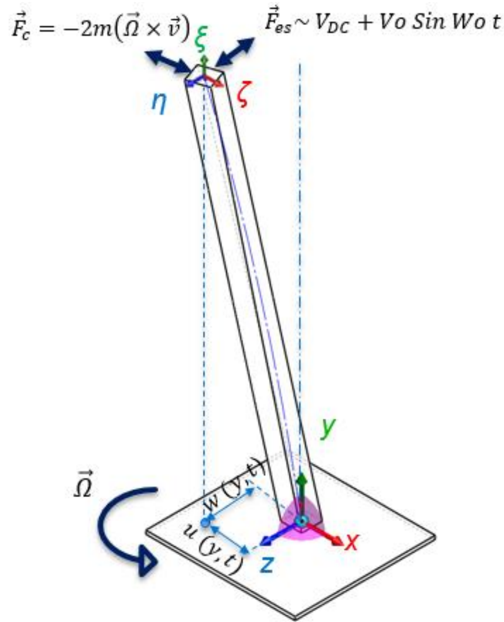


**Figure 2.5: Cantilever flexural- flexural displacements**

Although the cantilever beam has many modes of vibration, we consider here a model with two degrees of freedom with flexural displacements given by $\delta_x(y,t)$and $\delta_z(y,t)$ along the *x* and *z* directions that describe the in-plane and out-plane motion of the proof mass. The axis of rotation is along the beam axis (y-directions), as illustrated in Figure 2.5. Two coordinate systems are used to derive the kinematics characteristics of the cantilever beam gyroscope. The x-y-z axes define the inertial coordinate system (Frame A) with orthogonal unit vectors $i_x$, $j_y$, and $k_z$. The ξ-η-ζ axes define the base coordinate system (Frame B) with orthogonal unit vectors $i_\xi$, $j_\eta$ and $k_\varsigma$.

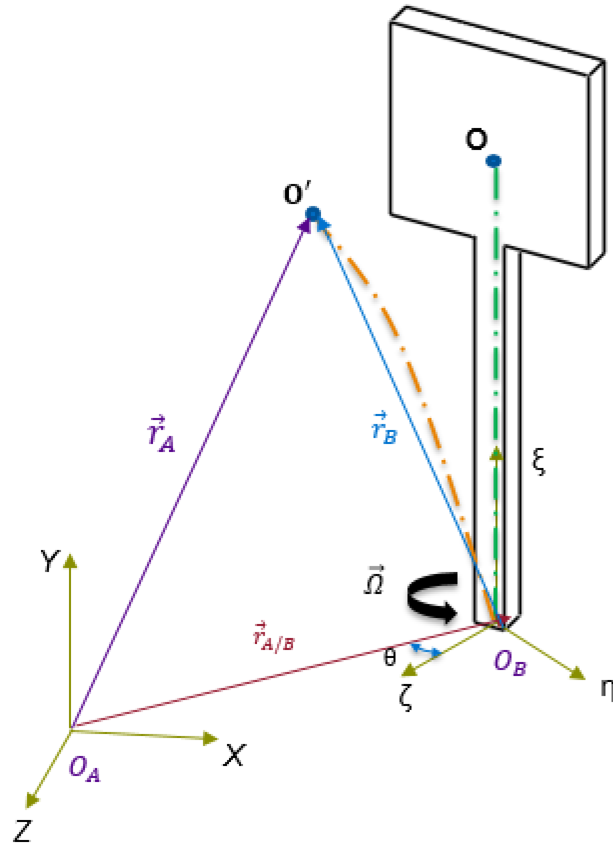


**Figure 2.6: Particle O moving in non-inertial Frame B with respect to inertial Frame A.**

In Figure 2.6, $\vec{\theta}$ is the orientation vector of base frame B relative to inertial Frame A. Hence, from the perspective of Frame A, the Particle O location can be expressed as:

$$\vec{r}_A(t) = \vec{r}_B(t) + \vec{r}_{A/B}(t) \tag{2.1}$$

$\vec{r}_A$: Position vector of particle O relative to inertial Frame A

$\vec{r}_B$: Position vector of particle O relative to base Frame B

$\vec{r}_{A/B}$: Position vector of particle O relative to rotating frame

When the system experiences constant angular velocity along the y-axis, the first derivatives of the position vector $\vec{r}_A(t)$ give the velocity of Particle O in the two reference frames. Hence, the absolute velocity of Particle O in Frame A can be derived by taking the time derivative of Eq. 2.1.

$$\dot{\vec{r}}_A(t) = \dot{\vec{r}}_B(t) + (\vec{\Omega} \times \vec{r}_{A/B}(t)) + \dot{\vec{r}}_{A/B}(t) \tag{2.2}$$

where $\vec{\Omega}$: Angular velocity of rotating Frame B given by $\vec{\Omega} = \dot{\vec{\theta}}$

The absolute acceleration of Particle O in the inertial reference frame A can be derived by taking second derivatives of Eq. (2.2).

$$\ddot{\vec{r}}_A(t) = \ddot{\vec{r}}_B(t) + (\dot{\Omega} \times \vec{r}_{A/B}) + \left(\vec{\Omega} \times (\vec{\Omega} \times \vec{r}_{A/B})\right) + (2\vec{\Omega} \times \dot{\vec{r}}_{A/B}(t)) \tag{2.3}$$

where $\ddot{\vec{r}}_A(t)$ is the linear acceleration of Particle O with respect to the inertial reference frame A,

$\ddot{\vec{r}}_B(t)$ is the acceleration of the particle with respect to the rotating Frame B

$(\dot{\Omega} \times \vec{r}_{A/B})$ is angular acceleration induced by tangential acceleration

$\left(\vec{\Omega} \times (\vec{\Omega} \times \vec{r}_{A/B})\right)$ is the centripetal acceleration

$(2\vec{\Omega} \times \dot{\vec{r}}_{A/B}(t))$ is the Coriolis acceleration

The Coriolis acceleration terms $(2\vec{\Omega} \times \dot{\vec{r}}_{A/B}(t))$ couple the drive and sense direction (z and x-axis) and allow the vibrating structure to act as a gyroscope. In Eq. 2.3, the Coriolis term states that an oscillating structure that undergoes a rotation will experience an acceleration that is proportional to the rotation rate in a direction that is orthogonal to both the rotation axis and the direction of motion. That is if the microplate moves along the z-axis and rotates about the y-axis, it will accelerate along the x-axis as observed in Frame B. Once that acceleration is detected and converted into a meaningful medium such as voltage, it is possible to determine the original rotation rate. The absolute acceleration vector for the x and z-acceleration components are then obtained as

$$\begin{aligned} \ddot{\vec{r}}_x(t) &= \ddot{x} - z\dot{\Omega} - x\Omega^2 - 2\Omega\dot{z} \\ \ddot{\vec{r}}_z(t) &= \ddot{z} - x\dot{\Omega} - z\Omega^2 - 2\Omega\dot{x} \end{aligned} \tag{2.4}$$

Equation 2.3 summarizes all the acceleration terms of a moving Particle O. The force terms of this acceleration can be along with the system damping and stuffiness can be written as:

$$\overrightarrow{F_A} = \left(m\ddot{\vec{r}}_B(t) + \left(m\dot{\Omega} \;\times \vec{r}_{A/B}\right) + \left(\vec{\Omega} \times m\left(\vec{\Omega} \times \vec{r}_{A/B}\right)\right) + 2m\left(\vec{\Omega} \times \dot{\vec{r}}_{A/B}(t)\right)\right) + \\ + c\dot{\vec{r}}_B(t) + k\vec{r}_B(t) \tag{2.5}$$

The fictitious force component in Eq. 2.5 includes

$$F_{fict} = \underbrace{\left(m\dot{\vec{\Omega}} \;\times \vec{r}_{A/B}\right)}_{\text{tangential force}} + \underbrace{\left(\vec{\Omega} \times m\left(\vec{\Omega} \times \vec{r}_{A/B}\right)\right)}_{\text{centripetal force}} + \underbrace{2m\left(\vec{\Omega} \times \dot{\vec{r}}_{A/B}(t)\right)}_{\text{Coriolis force}} \tag{2.6}$$

Hence, from Eq. 2.6 the Coriolis force is a part of the fictitious force used to describe the motion of objects observed in a rotating non-inertial reference frame. The tangential and centripetal force components which couple the two axes are undesirable and are a source of offset in a rate gyroscope and drift in a rate-integrating gyroscope. For a constant angular rate input $\dot{\vec{\Omega}} = 0$ and for very small angular rate, the centripetal force terms become negligible compared to the Coriolis force. Hence the Coriolis-induced motion is sensed for obtaining the angular rate; the corresponding rotation angle is obtained by integration.

A simple conceptual vibratory gyroscope is illustrated in Figure 2.7. A 2-DOF spring mass damper system is typically used to model the proof mass of the vibrating gyroscope. The governing equations of the vibratory gyroscope can be expressed as a second order spring mass damper system. The model includes a vibrating mass $\mathcal{M}$ and two spring-damper systems.

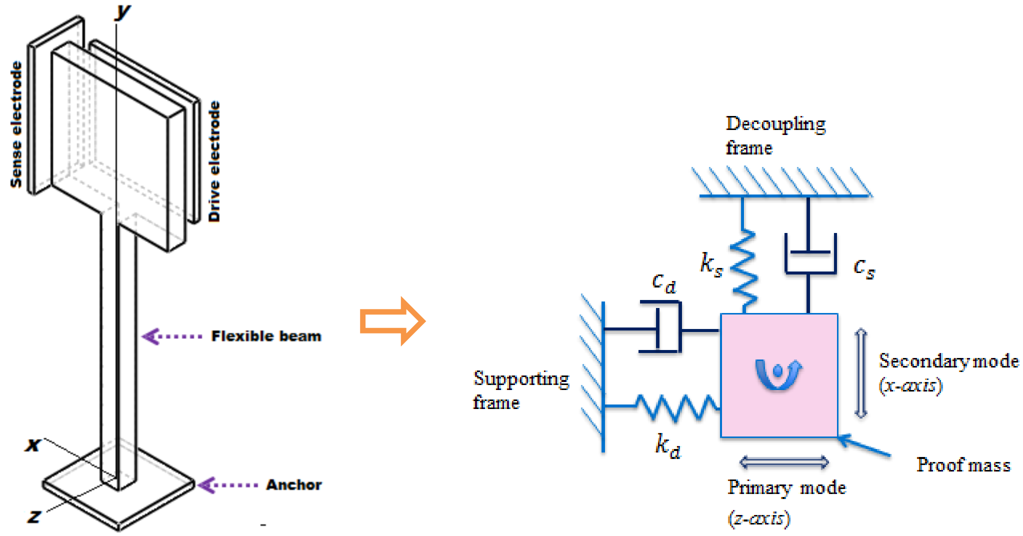


**Figure 2.7: Simplified lumped-mass model of a vibrating MEMS gyroscope**

Typically, MEMS vibratory gyroscope oscillations are excited using electrostatic actuation, which is proportional to the square of the applied voltage. The exciting force is sinusoidal with a drive frequency $\omega_{exc}$. In a simplest form, Newton's second law can be used to relate the accelerations in the x-axis and z-axis ($\ddot{\vec{r}}_x(t)$ and $\ddot{\vec{r}}_z(t)$) to the applied forces. By assuming small displacements relative to spring lengths with no cross coupling, the force balance equation of the spring-mass-damper system can be written thus:

$$m(\ddot{x} - z\dot{\Omega} - x\Omega^2 - 2\Omega\dot{z}) + c_x\dot{x} + k_x x + k_{xz}x = F_n$$
$$m(\ddot{z} - x\dot{\Omega} - z\Omega^2 - 2\Omega\dot{x}) + c_z\dot{z} + k_z z + k_{zx}z = F_{ex} + F_n \tag{2.7}$$

where $F_n$ force component due to Brownian noise

$k_{xz}x$, $k_{zx}x$ is quadrature force component

$F_{ex}$ is excitation electrostatic force

The spring stiffnesses ($k_x$ and $k_z$) are generally designed to be equal for maximum sensitivity. However, in the presence of structural imperfections during fabrication the two principal stiffness values do not match. This non-ideal behavior results in a frequency mismatch between the drive and the sense resonant frequencies and undesired coupling of the modes leading to errors in the sense output. Furthermore, the

fabrication imperfections of gyroscope such as non-symmetrical structures or the defect make anisoelasticity stiffness components ($k_{xz}$ and $k_{zx}$). Hence, this introduce extra motions on the sense axis without input rates applied. Thus, the Coriolis force and the extra motion which is coupled from the z-axis drive can be both observed on x-axis. This extra x-axis deflection is proportional with the z-axis displacement and it is named as quadrature coupling.

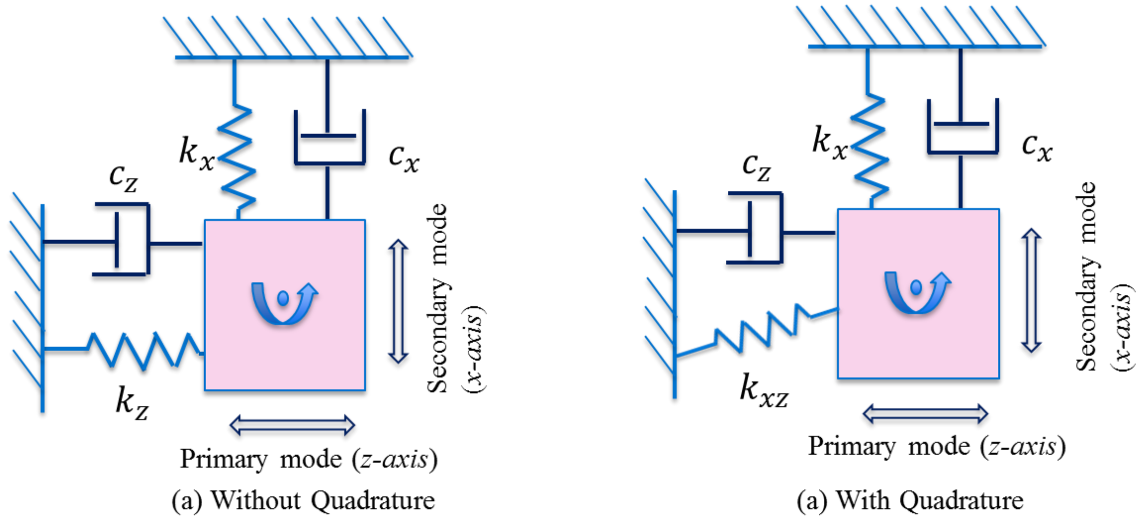


**Figure 2.8: lumped mass model without and with Quadrature coupling due to anisoelasticity terms**

Quadrature term included in the sense direction cannot be separated by amplitude detection only. To distinguish the Coriolis force and the quadrature term, the phase relationship between the two can be used since there is a 90-degree phase difference between the velocity and displacement on the drive axis. Equation 2.7 can be reformulated into a more convenient form, to emphasize the main parameters. If we divide by the mass of the movable structure, we get:

$$\begin{aligned} &\ddot{x} + 2\zeta_d\omega_{nd}\dot{x} \ + \left(\omega_{nd}^2 - \Omega^2\right)x \ - 2\Omega\dot{z} \ - z\dot{\Omega} \ = \omega_{ns}^2 X_d e^{j\omega t} \\ &\ddot{z} + 2\zeta_s\omega_{ns}\dot{z} \ + (\omega_{ns}^2 - \Omega^2)z \ - 2\Omega\dot{x} \ - x\dot{\Omega} = \omega_{nD}^2 Z_s e^{j\omega t} \end{aligned} \qquad (2.8)$$

where, $\omega_{nd}$ and $\omega_{ns}$ are the natural frequencies of the drive and sense direction,

$\zeta_d$ and $\zeta_s$ are the damping ratio of the drive and sense direction

$X_d$ and $Z_s$ are the excitation force amplitudes

Since the angular acceleration term ($\dot{\Omega}$) is usually small relative to the other terms in Eq. (2.8), it can be ignored. Although it can be difficult to confirm this conclusion through inspection, it may be motivated by the following reasoning: if the above-mentioned equations are non-dimensionalized by dividing both equations with $\omega_{nd}^2$ and $\omega_{ns}^2$ respectively, it would follow that $\frac{\dot{\Omega}}{\omega_n^2}$ is the dimensionless form of $\dot{\Omega}$. Since the natural frequencies of MEMS devices are in the order of kilohertz, it will follow that $\dot{\Omega} \ll \omega_n^2$, which confirms the resulting omission of $\dot{\Omega}$ from the ensuing equations. It should also be noted that it will take a harsh inertial environment to cause the angular acceleration term to become important [25].

### 2.3.1 MEMS Gyroscope Frequency Modulation Detection Approach

The natural frequency of a system is defined as the frequency at which a system oscillates freely after an initial disturbance has been applied to it, and is determined analytically by solving the system equations of motion without any applied forces. Hence, Eq. (2.7) can be solved by setting the right-hand side to zero, giving

$$\begin{aligned} &\ddot{x}(t) + 2\zeta_{\mathrm{d}}\omega_{nd}\dot{x}(t) \ + \left(\omega_{nd}^2 - \Omega^2\right)x(t) \ - 2\Omega\dot{z}(t) \ = 0 \\ &\ddot{z}(t) + 2\zeta_{\mathrm{s}}\omega_{ns}\dot{z}(t) \ + (\omega_{ns}^2 - \Omega^2)z\,(t) - 2\Omega\dot{x}(t) \ = 0 \end{aligned} \tag{2.9}$$

We assume the solution to the 2 DOF variety of the given as

$$\begin{aligned} &x\,(t) \ = \delta_x e^{j\theta_x(t)} \\ &z\,(t) \ = \delta_z e^{j\theta_z(t)} \end{aligned} \tag{2.10}$$

where $\delta_x$ and $\delta_z$ are the displacement amplitude of the x-mode and z-mode respectively. Differentiating (2.10) and substitution into (2.9) yields

$$\begin{aligned} &\mathrm{s}^2 + 2\zeta_{\mathrm{d}}\omega_{nd}s \ + (\omega_{n1}^2 - \Omega^2)C_{\mathrm{d}} \ - 2\Omega s\delta_x \ = 0 \\ &\mathrm{s}^2 + 2\zeta_2\omega_{n2}s \ + (\omega_{n2}^2 - \Omega^2)C_{\mathrm{s}} + 2\Omega \mathrm{s}\delta_z \ = 0 \end{aligned} \tag{2.11}$$

Both the cantilever beam and crab leg systems are designed to have equal natural frequencies in both senses and drive directions. Furthermore, because of the symmetrical geometries and configurations used in the design, damping will also be of the same order of magnitude in the $y$ and $z$ directions. Hence,

equal undamped natural frequencies and damping ratios could be assumed in Eq. (2.10), making $\omega_{nd}=\omega_{ns}=\omega_n$ and $\zeta_{\mathrm{d}}=\zeta_{\mathrm{s}}=\zeta$. The solution for Eq. (2.11) can be obtained by the following condition

$$\begin{vmatrix} s^2+2\zeta\omega_n s + (\omega_n^2-\Omega^2) & -2\Omega s \\ 2\Omega s & s^2+2\zeta\omega_n s + (\omega_n^2-\Omega^2) \end{vmatrix} = 0 \tag{2.12}$$

Hence

$$\begin{aligned} &[s^2+2\zeta\omega_n s + (\omega_n^2-\Omega^2)]^2 = -[2\Omega s]^2, \\ &s^2+2\zeta\omega_n s + (\omega_n^2-\Omega^2) = \pm j(2\Omega s), \\ &s^2+2(\zeta\omega_n \pm j\Omega)s + (\omega_n^2-\Omega^2) = 0 \\ &s_{1,2} = -(\zeta\omega_n \pm j\Omega) \pm \sqrt{\zeta^2\omega_n^2 \pm 2j\zeta\Omega\omega_n - \omega_n^2} \end{aligned} \tag{2.13}$$

The undamped natural frequencies for the system are obtained when $\zeta=0$, giving

$$s_{1,2} = \mp j\Omega \pm \omega_n = \pm j|\omega_n \pm \Omega| \tag{2.14}$$

Calculating the difference between the two natural frequencies gives the useful expression for the differential natural frequency. In turn, this gives the undamped natural frequencies $\omega_{1,2_\Omega}=|\omega_n \pm \Omega|$.

$$\Delta\omega_\Omega = \omega_{\mathrm{s}_\Omega} - \omega_{\mathrm{d}_\Omega} = 2\Omega \tag{2.15}$$

Equation (2.15) shows that the rotational velocity of the system directly affects the natural frequencies of the 2-DOF system. Therefore, we have a means of estimating the external rotation velocity by frequency demodulating the position signal in the drive and sense direction.

## 2.4 Electrical Excitation and Detection

MEMS vibratory gyroscope structure designed with two prime resonant modes, whose coupling is modulated by the external angular rate. To operate, the primary resonator needs to be driven into

vibration at a constant amplitude and frequency. The Coriolis force will be generated a vibration to the secondary resonator when the system subjected to angular velocity, which needs to be detected to determine the angular velocity. Hence, external access to the resonator is required to generate and sense movements in the drive and sense direction. In this study, we implemented a capacitive excitation and detection method using the two electrodes that form a parallel-plate capacitor for the cantilever beam design as shown in Figure 2.8.

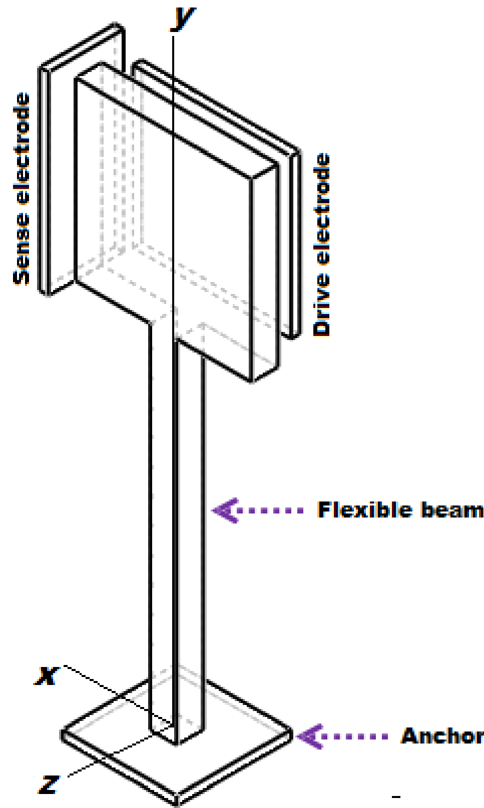


**Figure 2.8: A parallel-plate electrostatic actuator and detection electrodes**

The actuator needs to convert an electrical signal into an electrostatic force ($F_{es}$) to keep the drive axis at constant amplitude and frequency. The detection of the drive and sense motion requires a method to convert the position of the resonator ($\delta_z(y,t)$ and $\delta_x(y,t)$) to a quantity which can be measured with an electronic circuit as a voltage readout. Generally, the drive and sense electrodes on the substrate or side electrodes remain fixed, while the cantilever microplate electrode moves with the resonator. For excitation, an attractive electrostatic force can be generated between the electrodes by applying a voltage ($V_{exc}(t)$) between them. For detection, the structure forms a position-dependent capacitor as given in Eq. (2.16). Hence, the capacitance change corresponding to the gap change is measured and then converted to the desired quantity.

$$C = \frac{A\varepsilon_o\varepsilon_r}{g_o + \delta_x(y,t)} \quad (2.16)$$

where $\varepsilon_o$ and $\varepsilon_r$ is the absolute and relative permittivity of the insulator between the plates, $\varepsilon_r$ for vacuum or air is 1

$g_o$ is the initial gap between the electrodes (fixed and moving plates)

$A$ is the area of the sense electrode

The MEMS gyroscope control system must ensure that the amplitude and frequency remain constant in either the drive axis or in both the drive and sensing axes, depending on the operation modes. Excitation and detection can be designed to operate in either open-loop or closed loop modes. The main advantage of open-loop systems is that, by comparison with other modes, the circuitry used to operate the gyroscope is relatively simple (i.e., there is no control action in the sense axis) and, thus, easy to implement. However, under an open-loop mode of operation, the gyroscope's angular rate scale factor is very sensitive to fabrication defects and environment variations, and cannot be held constant over any appreciable bandwidth. Therefore, open-loop systems are limited to applications which require low-cost and low-performance gyroscopes.

In the closed-loop mode of operation, both the drive and sense direction amplitude and frequency are continuously monitored and amplitude driven to zero. Therefore, the bandwidth and dynamic range of the gyroscope can be greatly increased, extending far beyond what can be achieved with open-loop-based systems. However, under the conventional closed-loop mode of operation, it is difficult to ensure a constant noise performance in the face of environmental variations such as temperature changes. Moreover, there are practical difficulties in designing a feedback controller that keeps the closed-loop system both stable and sufficiently robust for gyroscopes with high-quality factors (Q). Therefore, the application areas for the conventional closed-loop mode of operation are those which allow for medium-cost and medium-performance (large bandwidth, but limited resolution) gyroscopes.

### 2.4.1 Primary Mode Excitation Method

There are many actuation methods available to MEMS technologies, including electrostatic, piezoelectric, thermal, and magnetic techniques. Among them, electrostatic actuation is the most common for MEMS resonator systems, owing to their easy integration and implementation. The cantilever beam parallel-plate electrostatic actuation comprises an attractive force generated by applying

voltage between two oppositely charged plates. For the cantilever beam MEMS gyroscope, electrostatic actuation can be modeled as a moving parallel plate capacitor that includes two sets of plates, as shown in Figure 2.9. Generally, the parallel plate design provides a large electrode area, which enables large forces, but only for small motions, due to rapid changes in force when the gap between the two plates varies [26]. Dramatic force changes cause instability in the drive mode.

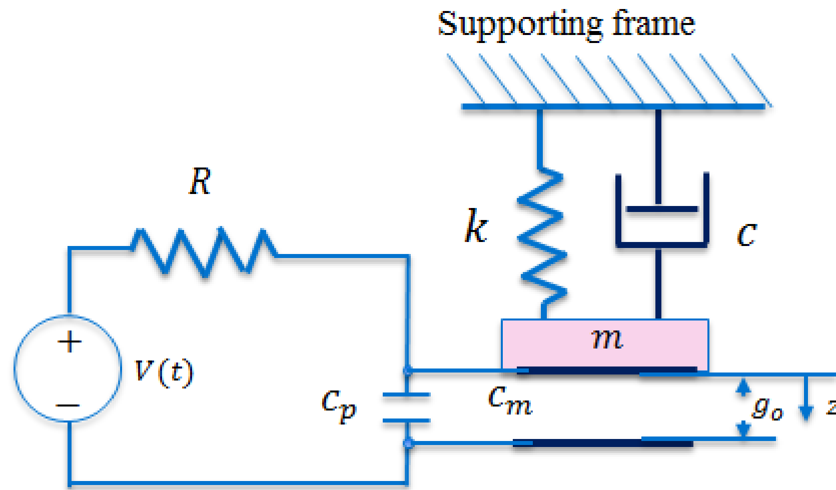


**Figure 2.9: A parallel plate electrostatic actuator**

The crab-leg design has a comb finger actuating and sensing electrode that operates perpendicular to the working plane to generate electrostatic forces or sense motion, as shown in Figure 2.10. By comparison with parallel plate actuators, comb drive devices are capable of larger displacements. One of the finger sets is connected to the movable part of the microplate, which is suspended by a spring, while the other is fixed on the substrate of the device. So, as an actuator, when a voltage is applied across the two sets of comb fingers, the electrostatic force attracts the plates to each other, generating motion.

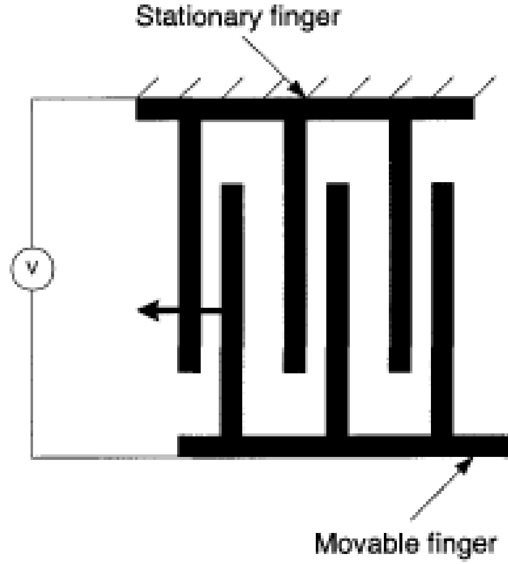


**Figure 2.10: Crab leg comb finger actuator and sensor electrodes**

The electrostatic force applied on the movable plate of the capacitor (while in drive mode) can be expressed as a partial derivative of the electrical energy with respect to the displacement as in Eq. (2.17).

$$F_{es} = \frac{\partial U_{es}}{\partial \delta_z(y,t)} \tag{2.17}$$

where $U_{es}$ and $\delta_z(y,t)$ are the total electrical energy and the displacement, respectively. When excitation voltage, $V_{exc}(t)$, is applied between the movable and fixed electrode, the electrical energy stored in the capacitor can be given as:

$$U_{es} = \frac{1}{2}C\big(V_{exc}(t)\big)^2 \tag{2.18}$$

Substituting Eq. (2.18) into Eq. (2.17), the electrostatic force can be written as

$$F_{es} = \frac{A\varepsilon_o\varepsilon_r\big(V_{exc}(t)\big)^2}{2(g_o + \delta_z(y,t))^2} \tag{2.19}$$

The electrostatic force is a nonlinear function of the actuation voltage, $V_{exc}(t)$, and the displacement, $\delta_z(y,t)$, as presented in Eq. (2.19). Generally, the displacement, $\delta_z(y,t)$, is small compared to the

initial gap ($g_o$), thus the force can be linearized by taking the first two terms of the Taylor series of Eq. (2. 19). Hence, the force can be written as:

$$F_{es} \approx \frac{A\varepsilon_o \varepsilon_r V_{exc}(t)^2}{2(g_o)^2} + \frac{A\varepsilon_o \varepsilon_r V_{exc}(t)^2}{(g_o)^3} . \delta_z(y,t) \tag{2.20}$$

The first term of the series can be interpreted as a displacement-independent attractive electrostatic force, which is used to excite the resonator, while the second term is a repulsive force with a linear dependency with the displacement. Equation (2.20) also indicates that the electrostatic force is proportional to the square of the excitation voltage, which may include DC and AC components [26].

$$V_{exc}(t) = V_{DC} + V_{AC}.Sin(\omega_{exc} t) \qquad 2.21$$

where $V_{DC}$ and $V_{AC}$ are the DC and AC components of the excitation voltage, respectively, and $\omega_{exc}$ is the frequency at which the excitation is performed. To achieve a maximum displacement with a given excitation force the excitation is normally performed at the mechanical resonance frequency of the MEMS structure. Hence, the resulting force is proportional to:

$$F_{es} \sim \left(V_{DC} + V_{AC}.Sin(\omega_{exc} t)\right)^2$$

$$F_{es} \sim (V_{DC})^2 + 2V_{DC}V_{AC}.Sin(\omega_{exc} t) + (V_{AC})^2 Sin^2(\omega_{exc} t) \qquad 2.22$$

$$F_{es} \sim (V_{DC})^2 + \frac{(V_{AC})^2}{2} + 2V_{DC}V_{AC}.Sin(\omega_{exc} t) - \frac{(V_{AC})^2}{2} Cos(2\omega_{exc} t)$$

From Eq. (2.22), it can be seen that there are forces generated at DC, $\omega_{exc}$, and $2\omega_{exc}$. In single-ended excitation schematically illustrated in Figure 2.11, the force generated at DC causes a static displacement of the gyroscope. The latter two of these forces can be used to excite the primary resonator of the gyroscope. If the excitation frequency is chosen to be equal to the natural frequency of the resonator, i.e $\omega_{exc} = \omega_{nd}$, then the resulting force component exciting the drive mode at its resonance frequency would be

$$F_{es} \sim 2V_{DC}V_{AC}.Sin(\omega_{nd}t) \qquad 2.23$$

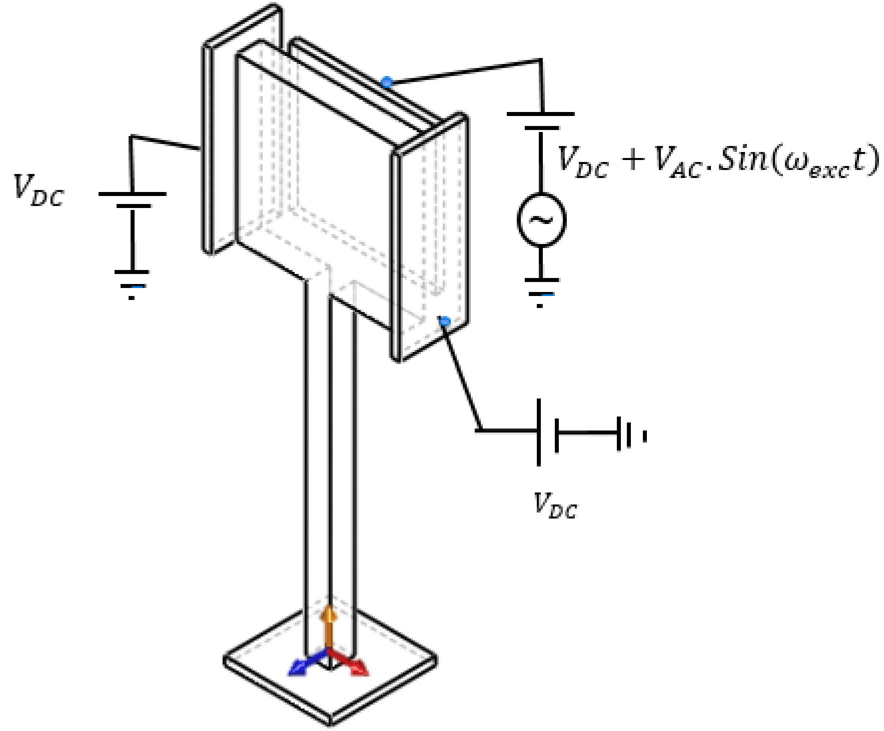


**Figure 2.11: Single Port actuation and sensing**

On the other hand, if the excitation frequency is chosen to be half of the natural frequency of the resonator, i.e that $\omega_{exc} = \frac{\omega_{nd}}{2}$, then the resulting force component exciting the primary resonator would be

$$F_{es} \sim -\frac{(V_{AC})^2}{2} Cos(\omega_{nd}t) \qquad 2.24$$

This result implies that excitation of the resonator can be performed either at the resonance frequency, in which case the force is proportional to the product of the DC and AC components of the excitation voltage or at half the resonance frequency, in which case the force is proportional to the AC component squared. In our experimental investigation, we have used both approaches depending on the excitation voltage requirement of a given prototype device.

If the resonator is excited differentially with voltage $\pm\frac{V_{exc}(t)}{2}$ as shown in Figure 2.12, the forces at DC and at $2\omega_{exc}$ are canceled. In that case, only the exciting force at $\omega_{nd}$ can be used to drive the resonator.

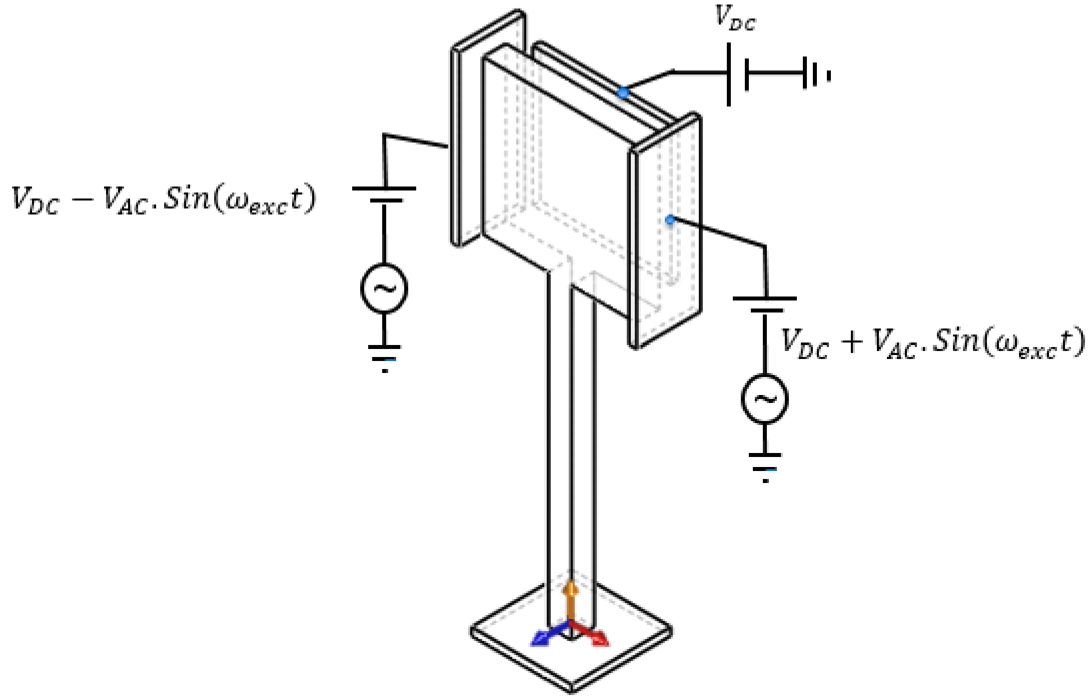


**Figure 2.12: Cantilever beam MEMS gyroscope actuation circuit**

### 2.4.2 Drive and Sense Motion Detection

The objective of MEMS gyroscope detection is to obtain an estimate of the angular rate (Ω) using the position signal ($\delta_x(y,t)$) along the sense directions, in the x-axis for the cantilever beam. Hence, the MEMS gyroscope readout converts the position information into a form suitable for electrical processing. The position information can be encoded in different forms, such as optical, capacitive and piezoelectric, depending on the sensing mechanism. Electrostatic capacitance sensing is a popular transduction technique for MEMS sensors. Physical variables that excite and move parallel plate capacitors can modify (via transverse motion) the gap between plates, thereby modifying the effective area of the capacitor. From the basic Eq. (2.16), if the gap between the two parallel plates changes, the capacitance will also change. The change in capacitance is inversely proportional to the square of the gap between the comb fingers. Therefore, both parallel plate and comb drive capacitors can be used as position sensors. This approach was implemented in the present study for Coriolis response detection [29-30].

For the cantilever MEMS gyroscope, parallel plate sense capacitors are formed using the fixed electrodes and the moving proof mass. As the proof mass moves in the sense direction in response to rotation-induced Coriolis force, the gap between the parallel plate electrodes changes and the resulting capacitance change is detected. These capacitances can be configured in different ways, as shown in Figure 2.13.

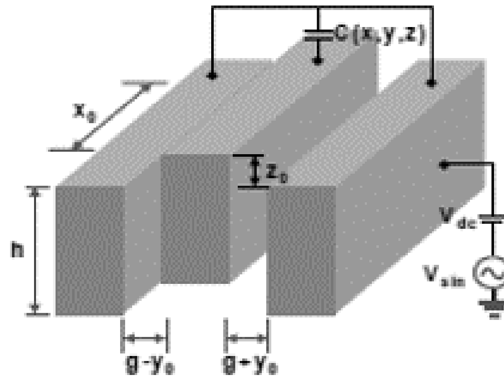


**Figure 2.13: Comb finger model for 3D electrostatic force analysis**

There are several circuit configurations used for capacitance measurements. To sense small capacitance changes, a high-performance readout circuit with high input impedance and very low noise is needed. In this work, the motional current is amplified and converted into a voltage signal by transimpedance amplifiers with a feedback resistor, and a lock in amplifier in sine-sweep mode.

Most of the conventional methods of actuation signal stabilization involve stabilizing of the signal amplitude using an automatic gain control (AGC) circuit while controlling the frequency with a phase-lock loop (PLL). Both of these control strategies involve comparing the drive signal with a reference signal. The result of the comparison is an error signal which is then used to control the drive signal. The capacitive signal can be measured using a transimpedance amplifier (TRA), which amplifies the output current to a detectable voltage. The signal from the CSA can be used as the reference signal for the PLL, which is then connected to the AGC loop. PLL trace a specific phase and frequency from a MEMS gyroscope. It comes with a phase (frequency) detector (PFD) to compare the reference signal with the voltage control oscillator (VCO) output. This comparison result would charge or discharge the charge pump (CP) in next stage. The CP output voltage will pass a designed low-pass filter (LF) to drive VCO. This loop will let VCO to generate the proper output to trace the resonator output until the frequency and phase difference is minimized and settled. Figure 2.14 shows the block diagrams MEMS gyroscope drive control.

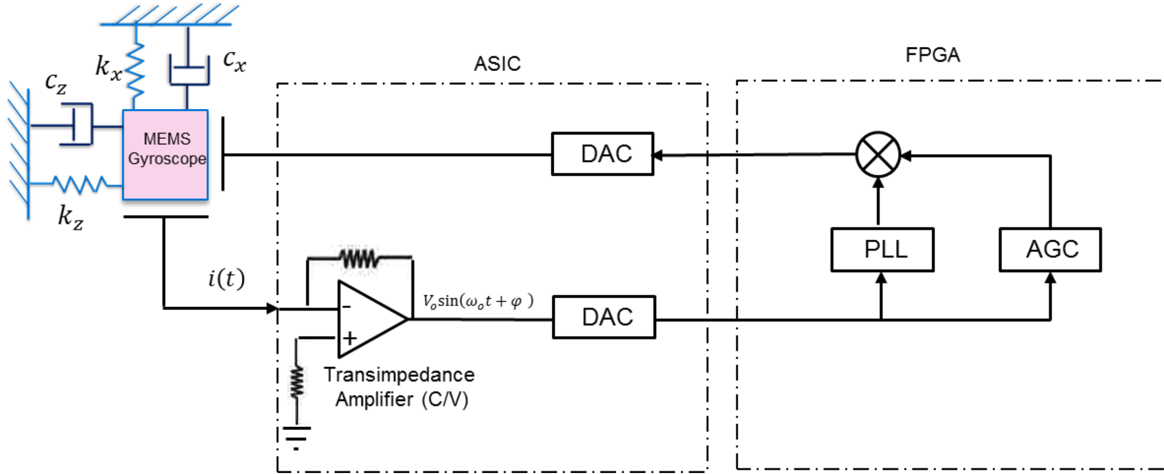


**Figure 2.14: Digital Drive mode control for MEMS gyroscope**

### 2.4.2.1 Single port actuation and detection with DC bias

When an electrostatic transducer is excited by a pure AC signal without DC bias at half of its natural frequency($\frac{1}{2}\omega_{nd}$), it resonates at its natural frequency, $\omega_{nd}$, and electrostatic force is proportional to the square of the applied voltage as presented in Eq. (2.24). While the excitation signal has only one frequency component, $\omega_{nd}$, the motion of the electrostatic transducer has a series of frequency components, DC, $2\omega_{nd}$, $4\omega_{nd}$, and higher harmonics due to the nonlinearity of electrostatic force. Then, the current induced by the motion of the transducer is up-converted by the frequency of the excitation signal $\omega_{nd}$; DC to $\omega_{nd}$, $2\omega_{nd}$ to $3\omega_{nd}$, and $4\omega_{nd}$ to $5\omega_{nd}$.

$$F_{es} \sim \left(V_{DC} + V_{AC}.Sin(\omega_{exc}t)\right)^2$$

$$= (V_{DC})^2 + 2V_{DC}V_{AC}.Sin(\omega_{exc}t) + (V_{AC})^2 Sin^2(\omega_{exc}t) \qquad 2.25$$

$$= (V_{DC})^2 + \frac{(V_{AC})^2}{2} + 2V_{DC}V_{AC}.Sin(\omega_{exc}t) - \frac{(V_{AC})^2}{2}Cos(2\omega_{exc}t)$$

While the current through the parasitic capacitance has only one frequency component $\omega_{nd}$, the motion induced current has different frequency components, $3\omega_{nd}$, $5\omega_{nd}$, and $7\omega_{nd}$. Using a transimpedance amplifier and a lock in amplifier, we can measure the total current and separate the current into a list of

frequency components: the current at $\omega_{nd}$ represents the sum of parasitic capacitance and static capacitance of the transducer; the current at $3\omega_{nd}$ represents the motion of the transducer at $2\omega_{nd}$ since we are interested in the resonant motion of the transducer at $\omega_o = 2\omega_{nd}$, we can easily determine its motion by measuring the magnitude of the current at $3\omega_{nd}$.

To derive the frequency components of the total current, we start with a general case when an electrostatic transducer is driven by an excitation voltage. The total current passing through the electrostatic transducer can be derived as thus:

$$i(t) = \frac{\mathrm{d}}{\mathrm{dt}}\left[\left(C_p + C_m\,(t)\right)V_{exc}(t)\right]$$
$$= \frac{\mathrm{d}C_m\,(t)}{\mathrm{dt}}V_{exc}(t) + \left(C_p + C_m\,(t)\right)\frac{\mathrm{d}V_{exc}(t)}{\mathrm{dt}} \quad 2.26$$

where $i(t)$, $C_m\,(t)$, $C_p$and $V_{exc}(t)$represents the total current; the capacitance of the electrostatic transducer; its parasitic capacitance; and the excitation voltage respectively. For a parallel plate electrostatic actuator, the capacitance of the transducer and its static pull-in voltage can be further simplified thus;

$$C_m\,(t) = \frac{A\varepsilon_o\varepsilon_r}{g_o - \delta_z(y,t)} = \frac{C_o}{1 - \delta_z(y,t)} \quad 2.27$$

$$V_{pi} = \sqrt{\frac{8kg_o^3}{27\varepsilon A}} \quad 2.28$$

where $\varepsilon$, $A$, $g_o$, $C_o$, $X(t)$, $x(t)$, $V_{pi}$ and k represent the permittivity of air, the area of the microplate, the original gap between the microplate and its bottom electrode. The original capacitance of the transducer at rest, the displacement of the microplate and its normized displacement with respect to the original gap, the static pull-in voltage of the transducer, and the mechanical stuffiness respectively.

To drive the transducer at its resonance, we define the executional signal either with a DC bias voltage or without a DC bias voltage as thus

$$V_{ex}(t) = V_{DC} + V_{AC}.Sin(\omega_a t), \left(V_{dc} \geq V_{ac},\ \omega_a = \frac{1}{2}\omega_o\right) \quad 2.29$$

$$V_{ex}(t) = V_{ac}.Sin(\omega_a t), \omega_a = \frac{1}{2}\omega_o \quad 2.30$$

where $V_{ex}(t)$, $V_{ac}$, $\omega_a$, $V_{DC}$ and $\omega_o$represent the actuation voltage, the peak amplitude of the harmonic signal, the frequency of the harmonic signal, the DC bias voltage, and the mechanical resonance of the electrostatic transducer. Figure 2.15 shows the block diagrams with the sensing circuit, demodulator and low pass filter.

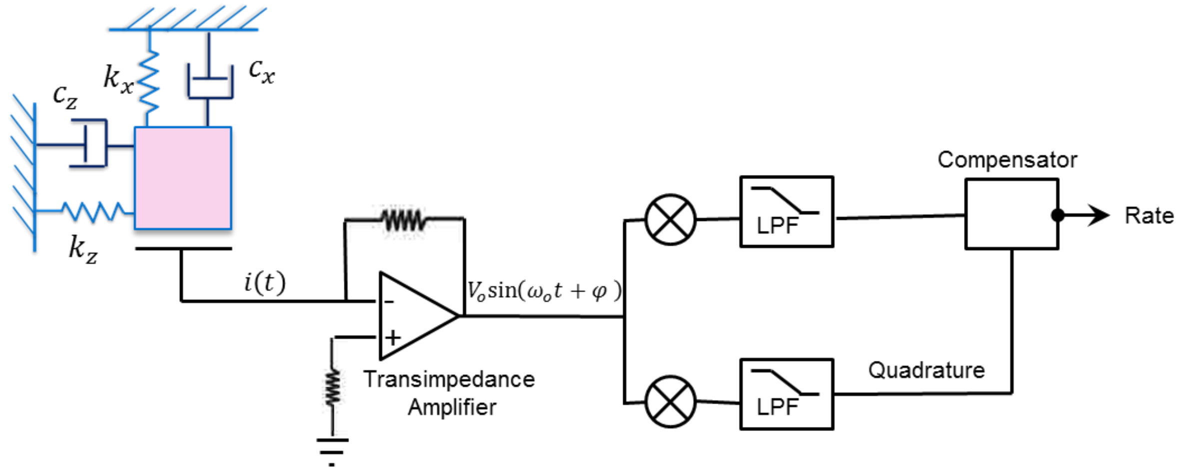


**Figure 2.15: Simplified circuit for sense direction with quadrature and Coriolis force output**

### 2.4.1.2 Single port detection with DC Bias

As presented earlier excitation and detection can be done with a DC bias or using pure AC signal. To explore the first approach, we can substitute Eq. (2.27, 2.28) into Eq. (2.26) we can derive the total current passing through the electrostatic transducer and its parasitic capacitance, when excited by $V_{ex}(t)$ as thus:

$$i(t) = \frac{C_o}{(1 - x(t))^2}\dot{x}(t)\ ASin(\omega_a t) + \left(C_p + \frac{C_o}{1 - x(t)}\right) A\omega_a cos(\omega_a t) \quad 2.31$$

Expanding Eq. (2.29) with respect to its frequency components we can simplify it as:

$$i(t) = \frac{C_o}{\left(1 - x(t)\right)^2}\dot{x}(t)\ \mathrm{A}Sin(\omega_a t) + \left(C_p + \frac{C_o}{1 - x(t)}\right)\ \mathrm{A}\omega_a cos(\omega_a t) \quad 2.32$$

Since the first term of Eq. (2.32) represents the current due to the parasitic capacitance. We can determine the parasitic capacitance by measuring the magnitude of the current at $\omega_a$. The second term of Eq. (2.32) represents the current induced by the displacement of the transducer; and the third term represents the current caused by the displacement and velocity of the transducer. Since the transducer is excited at its resonance, $x(t)$ can be assumed to be the harmonic motion at $\omega_a$ such as D. cos $(\omega_a t)$ the second term can be expanded using the Tayler series. The third term of Eq. (2.30) can be expanded into Eq. (2.32) as thus:

$$\begin{aligned}\frac{C_o}{\left(1 - x(t)\right)^2}\dot{x}(t) &= \left(C_o + 2C_o x(t) + 3C_o x^2(t) + Ox^3(t)\right)\dot{x}(t) \\ &= -C_o D\omega_o sin(\omega_o t) + 2C_o D^2\omega_o cos(\omega_o t)sin(\omega_o t) \\ &\qquad - 3C_o D^3\omega_o cos^2(\omega_o t)sin(\omega_o t) \\ &= -C_o D\omega_o sin(\omega_o t) + C_o D^2\omega_o sin(2\omega_o t) \\ &\qquad - \frac{3}{4}C_o D^3\omega_o\left(sin(\omega_o t) + sin(3\omega_o t)\right)\end{aligned} \quad 2.33$$

Substituting Eq. (2.31) and Eq. (2.32) into Eq. (30), we simplifying it

$$i(t) \approx \mathrm{A}\omega_o\left(C_p + C_o\right) \times \cos(\omega_o t) + \frac{3}{4}\mathrm{A}\omega_a C_o D \times \cos(3\omega_a t) + \frac{3}{4}\mathrm{A}\omega_a C_o D^2 \times \cos(5\omega_a t) \quad 2.34$$

As presented in Eq. (2.33), we can determine the parasitic capacitance of the electrostatic transducer by measuring the magnitude of the current at $\omega_a$. To determine the magnitude of the resonant motion at $2\omega_a$ we can measure the magnitude of the current at $3\omega_a$.

## 2.5 Effects of Capacitive Excitation and Detection

There are various undesired side effects related electrostatic excitation and detection methods including spring softening, parasitic capacitance and pull-in. To measure the capacitance between two electrodes, the structure needs to be biased, either with a known voltage or charge. This biasing then results in attractive electrostatic forces between the electrodes as discussed in the previous sections. These forces can affect the resonator parameters or even distort the capacitance being measured.

On the other hand, if the detection capacitance is formed by the parallel-plate structure as in the case of the cantilever beam parallel plate capacitor and if the structure is biased using a constant voltage, then the electrostatic forces are nonlinearly dependent on the displacement. This leads to electrostatic spring softening, and an effect which alters the resonance frequency of the resonator. Additionally, if the displacement is large compared to the initial gap, the nonlinearity of the electrostatic forces causes distortion to the displacement being measured.

### 2.5.1 Spring Softening

By adding $F_{es}$ to the right-hand side of the 1-D EoM given in Eq. (2.21) and reordering, the EoM can be written as

$$m\ddot{x} + c\dot{x} + \left(k - \frac{A\varepsilon_o\varepsilon_r V^2}{(g_o)^3}\right)y = \frac{A\varepsilon_o\varepsilon_r V^2}{2(g_o)^2} + F_{es} \qquad 2.35$$

Now, it can be seen that in an electrostatically excited mass-spring-damper system, the repulsive force acts as a negative electrostatic spring $k_{es}$, which reduces the effective spring constant $k_{eff}$. This phenomenon is known as electrostatic spring softening, and it is one of the most significant side effects of both capacitive excitation and detection. The electrostatic spring constant can be written as

$$k_{es} = -\frac{A\varepsilon_o\varepsilon_r V_{exc}(t)^2}{{g_o}^3} \qquad (2.36)$$

and the resulting effective spring constant as

$$k_{eff} = k + k_{es} = k - \frac{A\varepsilon_o\varepsilon_r V_{exc}(t)^2}{{g_o}^3} \tag{2.37}$$

As a result of the electrostatic spring softening, the resonance frequency is reduced to

$$\omega_0 = \sqrt{\frac{k_{eff}}{m}} = \sqrt{\frac{k - \frac{A\varepsilon_o\varepsilon_r V_{exc}(t)^2}{{g_o}^3}}{m}} \tag{2.38}$$

Therefore, the mechanical spring constant reduced by the square of the voltage applied to the electrodes. Because of the inherent nonlinearity of the parallel-plate actuator, its applicability may be limited when large relative displacements need to be generated.

# CHAPTER III

# MEMS Gyroscope Dynamic Behavior Modeling and Analysis

The kinematic principle discussed in previous chapter is a first-glance of the cantilever beam operation dynamics. In this chapter, a comprehensive model developed for the cantilever beam gyroscope to investigate the device dynamics and system characteristics. Particularly, studying the static and transient response of the cantilever beam structure under electrostatic actuation and Coriolis force would help to understand and explaining the behavior of the device and predict the overall system performance. As presented in the previous sections, the cantilever MEMS gyroscope system consists of a cantilever beam and suspended rigid mass at the free end [33]. A schematic of the beam is shown in Figure 3.1.

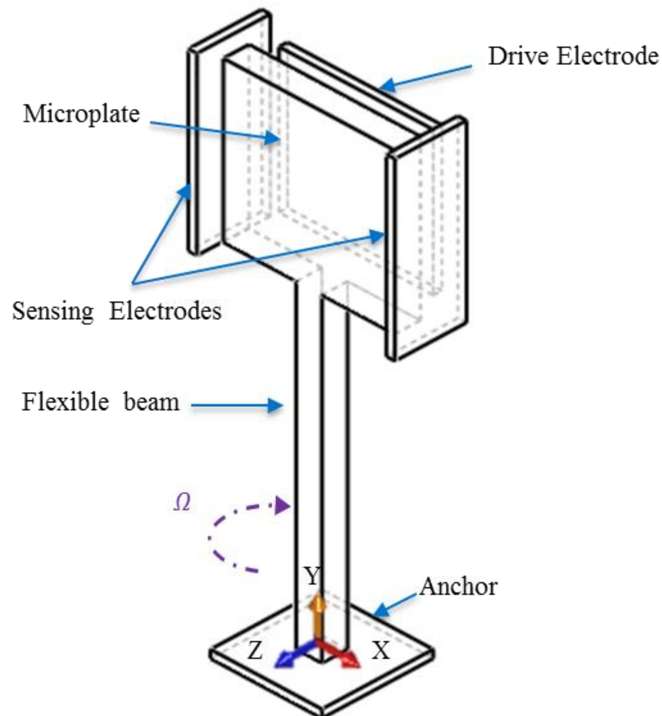


**Figure 3.1: Schematic of the cantilever beam**

The beam, which is attached to a rotating base, has a uniform width and thickness throughout its length. It has a mass per unit length $m$ and tip suspended microplate mass of M. A reduced order model implemented to describe device behavior as a function of design variables. The model considers the beam as a continuous medium and the suspended mass as a rigid body. As presented earlier, the electrostatic force is considered as a nonlinear function of the displacement and applied excitation voltages ($V_{ex}(t)$). The extended Hamilton principle is used to drive equations of motion and boundary conditions. The static and natural frequency of the cantilever beam gyroscope analyzed and the time and frequency response of the cantilever beam MEMS gyroscope are generated.

A major damping mechanism in MEMS vibrating structure is the viscous effects of the air surrounding the vibratory structure, and confined between the proof mass surfaces and the stationary surfaces. The damping of the structural material is usually orders of magnitude lower than the viscous damping, and is generally neglected. In our model, we ignored the viscous damping since the prototype was developed using Teledyne Dalsa MIDIS™ platform which provide vacuum packaged device. A number of prototype designed for cantilever and crab leg design using MIDIS™ platform with different mechanical characteristics. Result presented in this section refer to Cantilever 1 design which is partly constrained by the fabrication process, Figure 3.2.

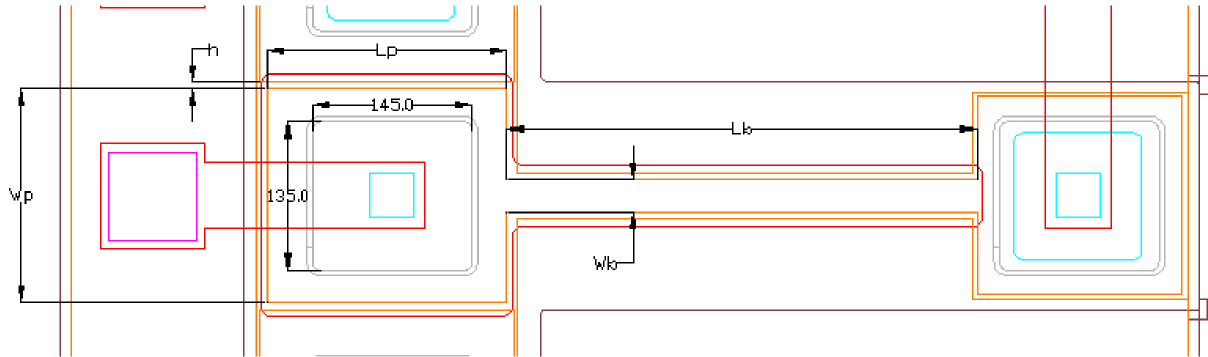


**Figure 3.2: Cantilever 1 design parameter**

The main design parameter for Cantilever 1 is provided in Table 3.1.

**Table 3.2: Cantilever 1 Gyroscope Parameters (Device 1)**

| | Description | Value |
|---|---|---|
| $L_b$ | Beam length | 427.5 $\mu m$ |
| $w_b$ | Beam width | 29.5 $\mu m$ |
| $t_b$ ($t_p$) | Beam (microplate) thickness | 30 $\mu m$ |
| $h$ | Initial capacitor gap | 2 $\mu m$ |
| $L_p$ | Microplate length | 218 $\mu m$ |
| $w_p$ | Microplate width | 194 $\mu m$ |
| $L_c$ | Length from beam tip to microplate | 109 $\mu m$ |
| M | Tip mass | $2.97 \times 10^{-6} g$ |
| m | Mass per unit length | $1.803 \times 10^{-11} g/\mu m$ |

## 3.1 Kinetics Modeling and Assumptions

The cantilever beam MEMS gyroscope subjected to electrostatic excitation forces ($F_{ex}$) ) at the free end and the rotating frame introduces Coriolis effects to the system dynamics. The dynamic behavior of a beam is described through two flexural components, $\delta_x(y,t)$ and $\delta_z(y,t)$, along the *x* and *z* directions, respectively, Figure 3.3. The beam flexural deformations in the two directions are coupled via the rotational speed of the base (Ω). Initially, we performed a preliminary FEA analysis to investigate the effects of varies forces including shear force. Effect of shear deformation found to be negligible hence, a differential beam element can be considered as a rigid body, whose motion is described by three translational and three rotational displacements. The deformation of the neutral axis of the cantilever beam can be determine and will be used to compute the deformation of any other point on the beam [34-36].

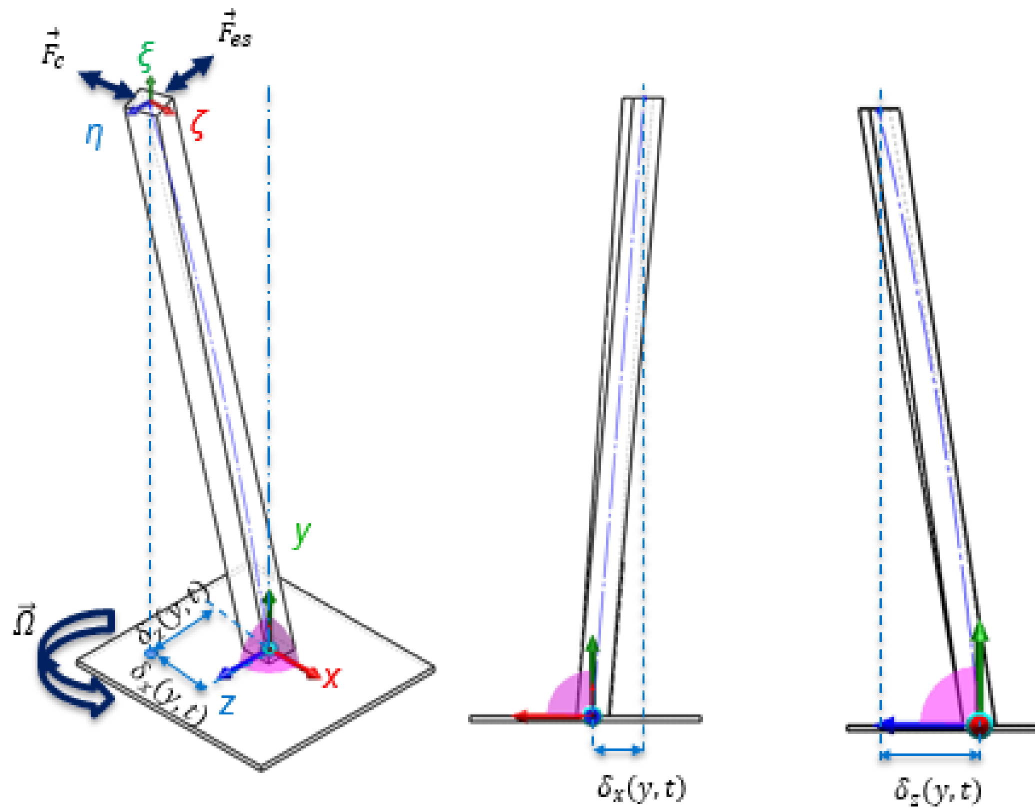

**Figure 3.3: Cantilever beam flexural-flexural deflection**

To model the dynamic behavior of the cantilever beam and suspended mass system, two coordinate systems are introduced, Figure 3.4. The inertial coordinate system (*x-y-z*) is aligned with the local curvilinear coordinate system (ξ-η-ζ) in the undeformed configuration. Three counter clockwise rigid body rotations are used to describe the motion of the beam's cross section at arc length $\ell$, from the undeformed to get to the deformed state. The Euler angles $\psi$, $\theta$, and $\phi$ are used to describe these rotations. First the *x-y-z* system is rotated about the *y*-axis, then about $\eta'$, the new position of the *y*-axis, and finally about the ξ-axis. The unit vectors of the ξ-η-ζ coordinate system are related to unit vectors of the *x-y-z* coordinate system through a transformation matrix [T], which is the product of three transformation matrices, one for each rigid body rotation [37-39].

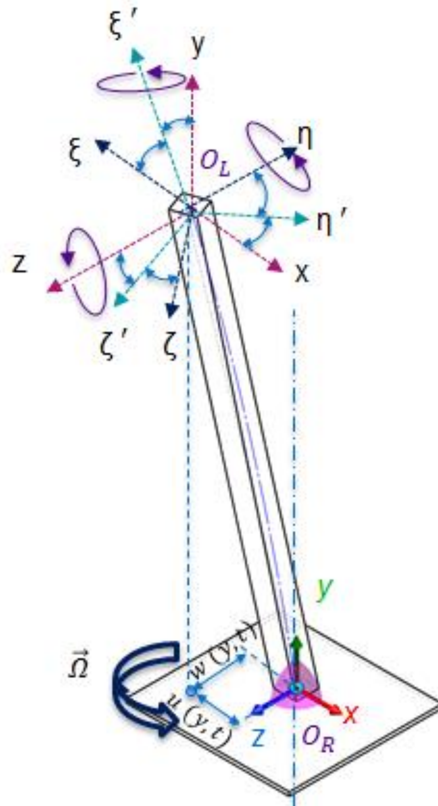


**Figure 3.4: Rigid body rotations of beam**

In general, each cross section of the beam experiences an elastic displacement of its centroid C and a rotation. The displacement components of the centroid C, with respect to the x, y, and z axes at the arc length $\ell$ and time t are denoted by $\delta_x(s,t)$, $\delta_y(s,t)$, and $\delta_z(s,t)$, respectively.

$$\begin{bmatrix} \hat{\imath}_x \\ \hat{\jmath}_y \\ \hat{k}_z \end{bmatrix} = [T] \begin{bmatrix} \hat{\imath}_\xi \\ \hat{\jmath}_\eta \\ \hat{k}_\varsigma \end{bmatrix} = [T_\psi][T_\theta][T_\phi] \begin{bmatrix} \hat{\imath}_\xi \\ \hat{\jmath}_\eta \\ \hat{k}_\varsigma \end{bmatrix} \quad (3.1)$$

The three individual transformation matrices and the transformation matrix $[T]$ are then

$$[T_\psi] = \begin{bmatrix} cos\psi & sin\psi & 0 \\ -sin\psi & cos\psi & 0 \\ 0 & 0 & 1 \end{bmatrix}, [T_\theta] = \begin{bmatrix} cos\,\theta & 0 & -sin\,\theta \\ 0 & 1 & 0 \\ sin\,\theta & 0 & cos\,\theta \end{bmatrix}, [T_\phi] = \begin{bmatrix} 1 & 0 & 0 \\ 0 & cos\phi & sin\phi \\ 0 & -sin\phi & cos\phi \end{bmatrix} \quad (3.2)$$

$$[T] = \begin{bmatrix} cos\psi\, cos\theta & cos\theta sin\psi & -sin\theta \\ -sin\psi cos\phi + sin\phi sin\theta cos\psi & cos\phi cos\psi + sin\phi sin\theta sin\psi & sin\phi cos\theta \\ sin\phi sin\psi + cos\phi sin\theta cos\psi & -sin\phi cos\psi + cos\phi sin\theta sin\psi & cos\phi cos\theta \end{bmatrix} \quad (3.3)$$

The absolute angular velocity of the local coordinate system $x'$-$y'$-$z'$ ~~is obtained from Figure 3.4~~

$$\omega(y,t) = \dot{\alpha} e_z + \dot{\beta} e_{y'} + \dot{\gamma} e_\xi \quad (3.4)$$

The expressions for $e_z$, and $e_{y'}$ are obtained from the transformation matrices in Eq. (3.2) and Eq. (3.3).

$$e_z = -sin\theta e_\xi + sin\phi cos\theta e_\eta + cos\phi cos\theta e_\varsigma \quad (3.5)$$

$$e_{y'} = cos\phi e_\eta - sin\phi e_\varsigma \quad (3.6)$$

Substituting Eq. (3.5) and (3.6) into Eq. (3.4) yields

$$\omega(\ell,t) = \left(\dot{\phi} - \dot{\psi} sin\theta\right) e_\xi + \left(\dot{\psi} sin\phi cos\theta + \dot{\theta} cos\phi\right) e_\eta + \left(\dot{\psi} cos\phi cos\theta - \dot{\theta} sin\phi\right) e_\varsigma \quad (3.7)$$

where the dots $(\dot{\ })$denotes the partial derivative with respect to time t and $e_i$ is a unit vector, and $i$ = x, y, z, ξ, θ, ζ indicates the direction of the unit vector. The curvature components can be obtained from the angular velocity components by replacing the time derivatives in Eq. (3.7) with spatial derivatives. Hence the curvature vector is given by

$$\rho(s,t) = (\phi' - \psi' sin\theta) e_\xi + (\psi' sin\phi cos\theta + \phi' cos\phi) e_\eta + (\psi' cos\phi cos\theta - \phi' sin\phi) e_\varsigma \quad (3.8)$$

The inextensibility condition expresses that the elongation of the neutral axis during the vibration is ignorable. Figure 3.5 shows a segment of the neutral axis of the cantilever beam. Segment CD is in the undeformed configuration while *C*D** is in the deformed configuration. The strain at point *C* is given by

$$e = \frac{ds^* - ds}{ds} = \sqrt{\left(1 + \delta_x{}'\right)^2 + \left(\delta_y{}'\right)^2 + \left(\delta_z{}'\right)^2} - 1 \tag{3.9}$$

Since the beam is assumed to be inextensional, the strain along the neutral axis is zero. Therefore Eq. (3.9) becomes.

$$1 = \left(1 + \delta_x{}'\right)^2 + \left(\delta_y{}'\right)^2 + \left(\delta_z{}'\right)^2 \tag{3.10}$$

Equation (3.10) is referred to as the inextensionality constraint.

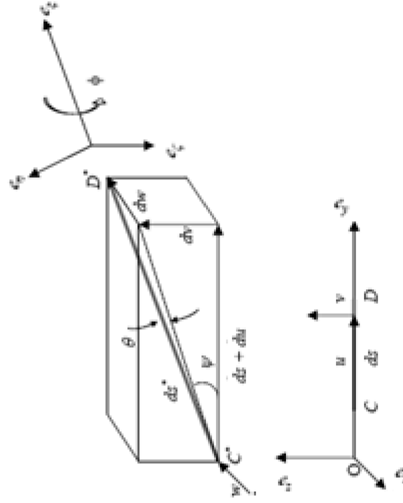

**Figure 3.5: A segment of the neutral axis local coordinate system**

Figure 3.4 can be used to determine the expressions for the angles ψ and θ in terms of the spatial derivatives of the transverse displacements. These expressions will be helpful in the simplification of the equations of motion later on. The relationships for $\psi$ and $\theta$ are then

$$tan\,\psi = \frac{\delta_y{}'}{1 + \delta_x{}'} \qquad tan\,\theta = \frac{-\delta_z{}'}{\sqrt{\left(1 + \delta_x{}'\right)^2 + \left(\delta_y{}'\right)^2}} \tag{3.11}$$

Equation (3.11) indicates $\psi$ and $\theta$ are dependent on the spatial derivatives of the displacement components $\delta_x$, $\delta_y$ and $\delta_z$. Therefore, there are only four independent variables for this problem, namely$\delta_x$, $\delta_y$, $\delta_z$, and $\phi$

### 3.1.2 Strain-Curvature Relations

Consider the cross section of the cantilever beam at the center of the suspended mass on the neutral axis, Figure 3.5. The figure shows the beam cross section at arclength s for both the deformed and undeformed configurations. An arbitrary point P in the undeformed beam cross section moves to point P* in the deformed cross section, with the displacement components of C being $(\delta_x, \delta_y, \delta_z)$ in the (x, y, z) system. The coordinates of P* relative to C* are still (η, ζ) because of the assumption of a rigid body motion where the shape of the cross section remains intact after bending. The position vectors of P and P∗ can be defined as

$$\vec{r}_P = \overrightarrow{OC} + \overrightarrow{CP} = se_x + \eta e_y + \zeta e_z \tag{3.12}$$

$$\vec{r}_{P^*} = \overrightarrow{OC^*} + \overrightarrow{C^*P^*} = (s+u)\, e_x + ve_y + we_z + \eta e_\eta + \zeta e_\zeta \tag{3.13}$$

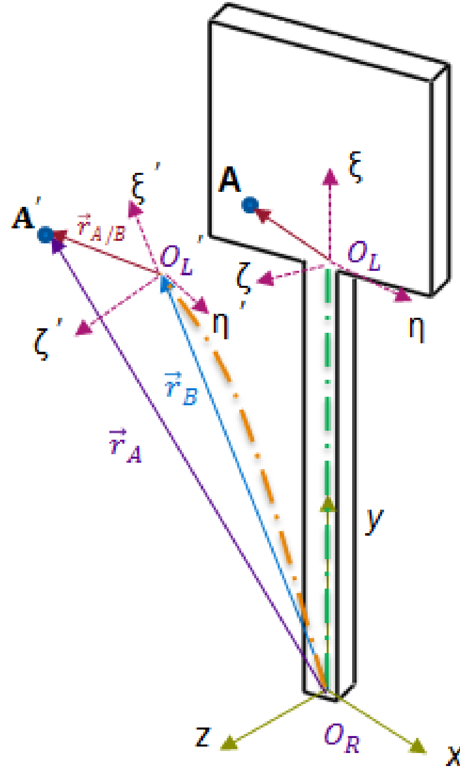


**Figure 3.6: Initial and deformed positions of an arbitrary point P**

The distance differentials for points $P$ and $P^*$ are given by

$$d\vec{r}_P = dse_x + d\eta e_y + d\zeta e_z \tag{3.14}$$

$$d\vec{r}_{P^*} = dse_\zeta + \eta de_\eta + d\eta e_\eta + \zeta de_\zeta + d\zeta e_\zeta \tag{3.15}$$

with the first term in Eq. (3.15) given by

$$dse_\zeta = \left(1 + {\delta_x}'\right)dse_x + {\delta_y}'dse_y + {\delta_z}'dse_z = C^* D^* \tag{3.16}$$

which is obtained directly from Figure 3.5. Eq. (3.14) and (3.15) are used to obtain

$$d\vec{r}_{P^*}.d\vec{r}_{P^*} - d\vec{r}_P.d\vec{r}_P = 2\left(\zeta\rho_\eta - \eta\rho_\xi\right)ds^2 - 2\zeta\rho_\xi ds d\eta + 2\eta\rho_\xi ds d\zeta \tag{3.17}$$

The difference of the squared distance differentials is related to the Green's strain tensor by

$$d\vec{r}_{P^*}.d\vec{r}_{P^*} - d\vec{r}_P.d\vec{r}_P = 2[ds \;\; d\eta \;\;\; d\zeta].\left[\varepsilon_{ij}\right].[ds \;\; d\eta \;\;\; d\zeta]^T \tag{3.18}$$

The components of the strain tensor in terms of the curvature are found by expanding the right-hand side of Eq. (3.18) and comparing it to the right-hand side of Eq. (3.17).

$$\varepsilon_{11} = \zeta\rho_\eta - \eta\rho_\xi, \gamma_{12} = 2\varepsilon_{12} = -\zeta\rho_\xi \;, \gamma_{13} = 2\varepsilon_{13} = \eta\rho_\xi, \;\; \varepsilon_{22} = \varepsilon_{23} = \varepsilon_{33} = 0 \tag{3.19}$$

## 3.2 Equations of Motion and Boundary Conditions

The extended Hamilton principle is used to derive the nonlinear partial-differential equations of motion. The equations describe the flexural-flexural motion of the cantilever beam. The Lagrangian of motion $l$ is given as:

$$\delta l = \mathrm{T} - \mathrm{U} \tag{3.20}$$

### 3.2.1 Kinetic Energy of the System

A schematic of the load applied on the cantilever beam is shown in Figure 3.7. The kinetic energy of the cantilever beam and suspended mass consists of two parts. The first part accounts the motion due to translation displacement and the second part account for motion due to rotation components.

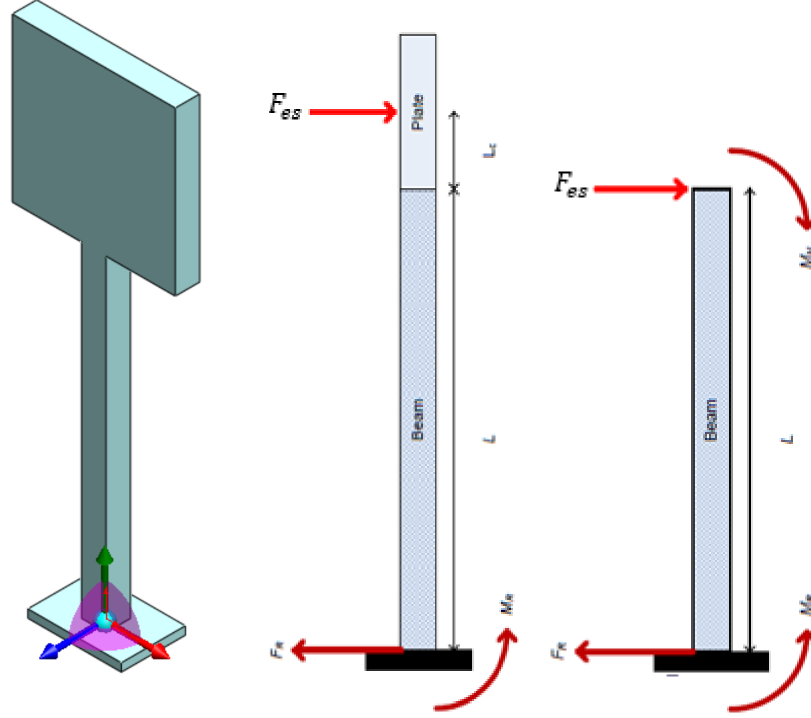


**Figure 3.7: Load acting on the cantilever beam**

The kinetic energy of the system can be expressed as:

$$T = T_{tr} + T_{rot} \tag{3.21}$$

The rotation angle of the microplate is the same as the cantilever beam slope at its tip, which can be given as

$$\delta_x(L,t)_y = \frac{\partial \delta_x(L,t)}{\partial L} \tag{3.22}$$

$$\delta_z(L,t)_y = \frac{\partial \delta_z(L,t)}{\partial L}$$

The angular speed of the microplate in the sense and drive direction can be expressed as $\dot{\delta}_x(L,t)_y$ and $\dot{\delta}_z(L,t)_y$, where the dot ( $\dot{}$ ) denote the partial derivatives with respect to time (*t*). Furthermore, the kinetic energy of the cantilever beam and microplate due to translation is given by

$$\begin{aligned} T_{tr} = \frac{1}{2}\rho A \int_0^l \left( \left(\dot{\delta}_x\,(y,t)\right)^2 + \left(\dot{\delta}_z(y,t)\,\right)^2 \right) dy \\ + \frac{1}{2}\rho A \Omega^2 \int_0^l ((\delta_x\,(y,t))^2 + (\delta_z(y,t)\,)^2) dy \\ + \rho A \int_0^l \Omega \left( \delta_x\,(y,t)\dot{\delta}_z\,(y,t) - \delta_z(y,t)\dot{\delta}_x\,(L,t) \right) dy \\ + \frac{1}{2} M \left( \left(\dot{\delta}_x\,(L,t)\right)^2 + \left(\dot{\delta}_z\,(L,t)\right)^2 \right) \\ + M\Omega \left( \delta_x(L,t)\dot{\delta}_z\,(L,t) - \delta_z(L,t)\dot{\delta}_x\,(L,t) \right) \\ + \frac{M\Omega^2}{2} \left( \left(\delta_x(L,t)\right)^2 + \left(\delta_z(L,t)\right)^2 \right) \end{aligned} \tag{3.23}$$

where $\delta_x$*(y, t)* and $\delta_z$ *(y, t)* be the differential beam element displacement at location *y* and time *t* in the x and z axis respectively

$\dot{\delta}_x\,(y,t)$ and $\dot{\delta}_z\,(y,t)$ are translational velocities of the differential beam element

$\Omega$ is the angular velocities

$\rho A$ is the $m$ass per unit length

$\delta_x(y,t)_y = \frac{\partial \delta_x(y,t)}{\partial y}$ and $\delta_z\,(y,t)\,_y = \frac{\partial \delta_z\,(x,t)}{\partial y}$ are the slope at location *y* and time *t*

$\delta_x(y,t)_{yy} = \frac{\partial^2 \delta_x(y,t)}{\partial y^2}$ and $\delta_z\,(x,t)\,_{yy} = \frac{\partial^2 \delta_z\,(y,t)}{\partial y^2}$ curvature at location *y* and time *t*

The kinetic energy also includes energy due to rotation of the differential element

$$T_{rot} = \frac{1}{2}\int_0^l \left[\omega_{\xi t}\,(y,t) + \omega_{\eta t}\,(y,t)\right][J]\left[\omega_{\xi t}\,(y,t) + \omega_{\eta t}\,(y,t)\right]^T dy$$

$$\begin{aligned} T_{rot} = \Omega^2 \int_0^l J\left[\left(\delta_x(y,t)_y\right)^2 + \left(\delta_z(y,t)_y\right)^2\right] dy \\ + \frac{1}{2}\int_0^l J\left[\left(\dot{\delta}_x\,(y,t)_y\right)^2 + \left(\dot{\delta}_z\,(y,t)_y\right)^2\right] dy \\ + \Omega\int_0^l J\left[\left(\delta_x\,(y,t)_y\dot{\delta}_z\,(y,t)_y - \delta_z\,(y,t)_y\dot{\delta}_x\,(y,t)_y\right)\right]dy + L_c J\Omega^2 \end{aligned} \tag{3.24}$$

where $[J]$ is the distributed inertia matrix.

In order to have matching natural frequency for the first two mode the cantilever beam is designed to have symmetrical cross-section. Furthermore, the product mass moments of inertia $J_{ij}$, $i \neq j$, are zero because a principal coordinate system is being used. Hence, using the notation $J_\xi = J_{11}$, $J_\eta = J_{22}$ and $J_\varsigma = J_{33}$, the inertia matrix $[J]$ is given by

$$[J] = \begin{bmatrix} J_\xi & 0 & 0 \\ 0 & J_\eta & 0 \\ 0 & 0 & J_\varsigma \end{bmatrix} = \rho \begin{bmatrix} \iint_A (\eta^2 + \zeta^2)\, d\eta d\zeta & 0 & 0 \\ 0 & \iint_A \zeta^2\, d\eta d\zeta & 0 \\ 0 & 0 & \iint_A \eta^2\, d\eta d\zeta \end{bmatrix} \tag{3.25}$$

Substituting Eq. (3.24) into Eq. (3.23), and adding Eq. (3.22) to the resulting expression provides the total kinetic energy of the system.

$$
\begin{aligned}
T = \frac{1}{2}\rho A \int_0^l \left( \left(\dot{\delta}_x\,(y,t)\right)^2 + \left(\dot{\delta}_z(y,t)\,\right)^2 \right) dy + \frac{1}{2}\rho A \Omega^2 \int_0^l \left( \left(\delta_y\,(y,t)\right)^2 + (\delta_z(y,t)\,)^2 \right) dy \\
+ \rho A \int_0^l \Omega(y\dot{z} - z\dot{y}) dy + \frac{1}{2} M \left( \left(\dot{\delta}_x\,(L,t)\right)^2 + \left(\dot{\delta}_x\,(L,t)\right)^2 \right) \\
+ M\Omega \left( \delta_x(L,t)\dot{\delta}_z\,(L,t) - \delta_z(L,t)\dot{\delta}_x\,(L,t) \right) + \frac{M\Omega^2}{2} \\
+ \Omega^2 \int_0^l J \left[ \left(\delta_x\,(y,t)_y\right)^2 + \left(\delta_z\,(y,t)_y\right)^2 \right] dy \\
+ \frac{1}{2} \int_0^l J \left[ \left(\dot{\delta}_x\,(y,t)_y\right)^2 + \left(\dot{\delta}_z\,(y,t)_y\right)^2 \right] dy \\
+ \Omega \int_0^l J \left[ \left( \delta_x\,(y,t)_y \dot{\delta}_z\,\,(y,t)_y - \delta_z\,(y,t)_y \dot{\delta}_x\,\,(y,t)_y \right) \right] dy + L_c J \Omega^2
\end{aligned} \tag{3.26}
$$

### 3.2.2 Potential Energy

The potential energy ($U$) of the system include the cantilever beam strain energy and the electrostatic potential energy of the electrostatic field between electrodes and the microplate. The strain energy of the beam is calculated using the strain tensor ($U_{st}$) components from Eq. (3.19). Hence, the total strain energy for the cantilever beam can be expressed as:

$$
U_s = \frac{1}{2} \int_0^l \left[ \iint_A \left( \sigma_{11}\varepsilon_{11} + \sigma_{12}{}^b \gamma_{12}{}^b + \sigma_{13}{}^b \gamma_{12}{}^b \right) d\eta d\zeta \right] d\ell \tag{3.27}
$$

Silicon wafer is used to fabricate the structural element of the sensor and a linear relationship between the stress and the strain is assumed. Therefore, Hooke's law can be used to relate the stress to the strain.

$$
\sigma_{11} \approx E\varepsilon_{11} \qquad \sigma_{12} \approx G\gamma_{12} \qquad \sigma_{13} \approx G\gamma_{13} \tag{3.28}
$$

$$
\varepsilon_{11} = \zeta\rho_\eta - \eta\rho_\xi
$$

Substituting the strain tensor components from the previous section into Eq. (3.27) and Eq. (3.28), and noting that the cross section is symmetric about the $\eta$ and $\zeta$ axes, the strain energy is written as

$$U_{st} = \frac{1}{2}\int_0^l \left(D_\xi \rho_\xi^2 + D_\zeta \rho_\zeta^2\right)_b d\ell \tag{3.29}$$

where $D_\xi$, and $D_\zeta$ are the flexural rigidities of the x and z axis respectively. The potential energy is then

$$\begin{aligned} U_{st} &= \frac{1}{2}\int_0^l \left(EI_\xi \delta_x(y,t)_{yy} + EI_\eta \delta_z(y,t)_{yy}\right) dy \\ U_{st} &= \frac{\mathrm{E}}{2}\int_0^l \left(I_y \delta_x(y,t)_{yy}{}^2 + I_z \delta_z(y,t)_{yy}{}^2\right) dy \end{aligned} \tag{3.30}$$

The electrostatic force applied underneath the microplate produces a potential energy that can be expressed

$$\begin{aligned} U_E &= -\frac{\varepsilon A_d}{2}\left(V_{DC} + V_{AC}(t)\right)_d{}^2 \int_0^{2L_C} \frac{1}{\mathrm{g}_d - \delta_x(L,t) - \delta_x(L,t)_y} dy \\ &\quad - \frac{\varepsilon a_s}{2}\left(V_{DC} + V_{AC}(t)\right)_s{}^2 \int_0^{2L_C} \frac{1}{\mathrm{g}_s - \delta_z(L,t) - \delta_z(L,t)_y} dy \\ &= \frac{\varepsilon A_p}{2\delta_x(L,t)_y}\left(V_{DC} + V_{AC}(t)\right)_d{}^2 \, ln\left[\mathrm{g}_d - \delta_x(L,t) - \delta_x(L,t)_y\right]\Big|_0^{2L_C} \\ &\quad + \frac{\varepsilon a_s}{2\delta_z(L,t)_y}\left(V_{DC} + V_{AC}(t)\right)_s{}^2 \, ln\left[\mathrm{g}_s - \delta_z(L,t) - \delta_z(L,t)_y\right]\Big|_0^{2L_C} \\ &= \frac{\varepsilon A_d}{2\delta_x(L,t)_y}\left(V_{DC} + V_{AC}(t)\right)_d{}^2 \; ln\left[\frac{\mathrm{g}_d - \delta_x(L,t) - 2L_C\,\delta_x(L,t)_y}{\mathrm{g}_d - \delta_x(L,t)}\right] \\ &\quad + \frac{\varepsilon a_s}{2\delta_z(L,t)_y}\left(V_{DC} + V_{AC}(t)\right)_s{}^2 \; ln\left[\frac{\mathrm{g}_s - \delta_z(L,t) - 2L_C\,\delta_z(L,t)_y}{\mathrm{g}_s - \delta_z(L,t)}\right] \end{aligned} \tag{3.31}$$

where ε is the permittivity of free space

$\left(V_{DC}+V_{AC}(t)\right)_d$ and $\left(V_{DC}+V_{AC}(t)\right)_s$ are the combination of DC and AC voltages applied between the drive and sense electrodes, respectively.

$A_d$ and $A_s$effective area of the drive and sense electrode direction respectively.

Here, the sensing axis also applied with a feedback voltage for closed loop design consideration. Then the total potential energy is given by

$$\mathrm{U} = U_{st} + U_E \tag{3.32}$$

$$\begin{aligned} &= \left(\frac{\mathrm{E}}{2}\int_0^l I_x\delta_x(y,t)_{yy}{}^2 + I_z\delta_z(y,t)_{yy}{}^2 dy\right) \\ &\quad + \left(\frac{\varepsilon a_d}{2\delta_x(L,t)_y}\left(V_{DC}+V_{AC}(t)\right)_d^{\;2}\; ln\left[\frac{\mathrm{g}_d-\delta_x(L,t)-2L_C\;\delta_x(L,t)_y}{\mathrm{g}_d-\delta_x(L,t)}\right]\right. \\ &\quad \left. + \frac{\varepsilon a_s}{2\delta_z(L,t)_y}\left(V_{DC}+V_{AC}(t)\right)_s^{\;2}\; ln\left[\frac{\mathrm{g}_s-\delta_z(L,t)-2L_C\;\delta_z(L,t)_y}{\mathrm{g}_s-\delta_z(L,t)}\right]\right) \end{aligned} \tag{3.33}$$

Equations (3.26) and (3.32) are substituted into Eq. (3.20) to obtain the final expression for the Lagrangian. The inextensionality constraint in Eq. (3.10) must be maintained during the variational process. The Lagrangian density is then

$$\delta\mathcal{L} = \frac{1}{2}\rho A\int_0^l \left(\left(\dot{\delta}_x\,(y,t)\right)^2 + \left(\dot{\delta}_z(y,t)\,\right)^2\right)dy + \frac{1}{2}\rho A\Omega^2\int_0^l ((\delta_x\,(y,t))^2 + (\delta_z(y,t)\,)^2)dy$$
$$+ \rho A\int_0^l \Omega(x\dot{z} - z\dot{x})dy + \frac{1}{2}M\left(\left(\dot{\delta}_x\,(L,t)\right)^2 + \left(\dot{\delta}_x\,(L,t)\right)^2\right)$$
$$+ M\Omega\left(\delta_x(L,t)\dot{\delta}_z\,(L,t) - \delta_z(L,t)\dot{\delta}_x\,(L,t)\right) + \frac{M\Omega^2}{2}\left(\left(\delta_x(L,t)\right)^2 + \left(\delta_z(L,t)\right)^2\right)$$
$$+ \Omega^2\int_0^l J\left[\left(\delta_x\,(y,t)_y\right)^2 + \left(\delta_z\,(y,t)_y\right)^2\right]dy$$
$$+ \frac{1}{2}\int_0^l J\left[\left(\dot{\delta}_x\,(y,t)_y\right)^2 + \left(\dot{\delta}_z\,(y,t)_y\right)^2\right]dy \tag{3.34}$$
$$+ \Omega\int_0^l J\left[\left(\delta_x\,(y,t)_y\dot{\delta}_z\,\,(y,t)_x - \delta_z\,(y,t)_y\dot{\delta}_x\,\,(y,t)_x\right)\right]dy + L_cJ\Omega^2$$
$$-\frac{1}{2}\int_0^l \left(EI_\xi\delta_y(y,t)_{yy}\right.$$
$$\left. + EI_\eta\delta_z(y,t)_{yy}\right)dy\frac{\varepsilon A_d}{2\delta_x(L,t)_y}\left(V_{DC}\right.$$
$$\left. + V_{AC}(t)\right)_d^{\;2}\;ln\left[\frac{\mathrm{g}_d - \delta_x(L,t) - 2L_C\;\delta_x(L,t)_y}{\mathrm{g}_d - \delta_y(L,t)}\right]$$
$$+ \frac{\varepsilon A_s}{2\delta_z(L,t)_y}\left(V_{DC} + V_{AC}(t)\right)_s^{\;2}\;ln\left[\frac{\mathrm{g}_s - \delta_z(L,t) - 2L_C\;\delta_z(L,t)_y}{\mathrm{g}_s - \delta_z(L,t)}\right]$$

### 3.3 Extended Hamilton's Principle

The MEMS cantilever beam gyroscope is subjected to non-conservative forces such as viscous damping and Coriolis forces. Therefore, the extended Hamilton's principle is used to derive the equations of motion. This approach permits the derivation of the equations of motion from a definite integral involving kinetic energy and the virtual work performed by the applied forces. Appropriate boundary conditions are also produced as part of the derivation. The extended Hamilton's principle can be stated as

$$\delta I = \int_{t_1}^{t_2} (\delta \mathcal{L} + \delta U_{nc}) dt = 0 \tag{3.35}$$

where $\delta \mathcal{L}$ is the virtual change in mechanical energy

$\delta U_{nc}$ is the virtual work done by non-conservative forces

$t_1$, $t_2$ are times at which the configuration of the system is assumed to be known

$\delta(\,)$ Symbol denoting the first variation, or virtual change, in the quantity in brackets

Replacing the Lagrangian components and taking the time integral, the overall dynamics can be expressed:

$$
\begin{aligned}
&\int_{t_1}^{t_2} \left\{ \frac{1}{2}\rho A \int_0^l \left( \left(\dot{\delta}_x\ (y,t)\right)^2 + \left(\dot{\delta}_z(y,t)\ \right)^2 \right) dy \right. \\
&\quad + \frac{1}{2}\rho A \Omega^2 \int_0^l ((\delta_x\ (y,t))^2 + (\delta_z(y,t)\ )^2) dy + \rho A \int_0^l \Omega(x\dot{z} - z\dot{x}) dy \\
&\quad + \ \frac{1}{2} M \left( \left(\dot{\delta}_x\ (L,t)\right)^2 + \left(\dot{\delta}_z\ (L,t)\right)^2 \right) \\
&\quad + M\Omega \left( \delta_x(L,t)\dot{\delta}_z\ (L,t) - \delta_z(L,t)\dot{\delta}_x\ (L,t) \right) \\
&\quad + \frac{M\Omega^2}{2} \left( \left(\delta_x(L,t)\right)^2 + \left(\delta_z(L,t)\right)^2 \right) \\
&\quad + \Omega^2 \int_0^l J \left[ \left(\delta_x\ (y,t)_y\right)^2 + \ \left(\delta_z\ (y,t)_y\right)^2 \right] dy \\
&\quad + \frac{1}{2} \int_0^l J \left[ \left(\dot{\delta}_x\ (y,t)_y\right)^2 + \ \left(\dot{\delta}_z\ (y,t)_y\right)^2 \right] dy \qquad (3.36) \\
&\quad + \Omega \int_0^l J \left[ \left( \delta_x\ (y,t)_y \dot{\delta}_z\ \ (y,t)_y - \delta_z\ (y,t)_y \dot{\delta}_x\ \ (y,t)_y \right) \right] dy + L_c J \Omega^2 \\
&\quad - \frac{1}{2} \int_0^l \left( EI_\xi \delta_x(y,t)_{yy} \right. \\
&\quad \left. + EI_\eta \delta_z(y,t)_{yy} \right) dy \frac{\varepsilon a_d}{2\delta_x(L,t)_x} \left( V_{DC} \right. \\
&\quad \left. + V_{AC}(t) \right)_d^{\ 2}\ ln \left[ \frac{\mathrm{g}_d - \delta_x(L,t) - 2L_C\ \delta_x(L,t)_y}{\mathrm{g}_d - \delta_x(L,t)} \right] \\
&\quad + \frac{\varepsilon a_s}{2\delta_z(L,t)_y} \left( V_{DC} \right. \\
&\quad \left. \left. + V_{AC}(t) \right)_s^{\ 2}\ ln \left[ \frac{\mathrm{g}_s - \delta_z(L,t) - 2L_C\ \delta_z(L,t)_y}{\mathrm{g}_s - \delta_z(L,t)} \right] \right\} dt = 0
\end{aligned}
$$

Utilizing the expressions for kinetic and potential energies, different components of Eq. (3.36) can be expressed as follows.

Kinetic energy is given by

$$
\begin{aligned}
\int_{t_1}^{t_2} \delta T dt = \int_{t_1}^{t_2} \Bigg\{ & \frac{1}{2}\rho A \int_0^l \left( \left(\dot{\delta}_x\,(y,t)\right)^2 + \left(\dot{\delta}_z(y,t)\,\right)^2 \right) dy \\
& + \frac{1}{2}\rho A \Omega^2 \int_0^l ((\delta_x\,(y,t))^2 + (\delta_z(y,t)\,)^2) dy + \rho A \int_0^l \Omega(x\dot{z} - z\dot{x}) dy \\
& + \frac{1}{2} M \left( \left(\dot{\delta}_x\,(L,t)\right)^2 + \left(\dot{\delta}_z\,(L,t)\right)^2 \right) \\
& + M\Omega \left( \delta_x(L,t)\dot{\delta}_z\,(L,t) - \delta_z(L,t)\dot{\delta}_x\,(L,t) \right) \\
& + \frac{M\Omega^2}{2} \left( \left(\delta_x(L,t)\right)^2 + \left(\delta_z(L,t)\right)^2 \right) \\
& + \Omega^2 \int_0^l J \left[ \left(\delta_x\,(y,t)_y\right)^2 + \left(\delta_z\,(y,t)_y\right)^2 \right] dy \\
& + \frac{1}{2} \int_0^l J \left[ \left(\dot{\delta}_x\,(y,t)_y\right)^2 + \left(\dot{\delta}_z\,(y,t)_y\right)^2 \right] dy \\
& + \Omega \int_0^l J\left[ \left( \delta_x\,(y,t)_y \dot{\delta}_z\,(y,t)_y - \delta_z\,(y,t)_y \dot{\delta}_x\,(y,t)_y \right) \right] dy \\
& + L_c J \Omega^2 \Bigg\} dt = 0
\end{aligned}
\tag{3.37}
$$

$$
\begin{aligned}
\int_{t_1}^{t_2} \delta U dt = \frac{1}{2} \int_0^l & \big( EI_\xi \delta_x(y,t)_{yy} \\
& + EI_\eta \delta_z(y,t)_{yy} \big) dy \, \frac{\varepsilon a_d}{2\delta_x(L,t)_y} \big( V_{DC} \\
& + V_{AC}(t) \big)_d^{\ 2} \; ln \left[ \frac{g_d - \delta_x(L,t) - 2L_C\,\delta_x(L,t)_y}{g_d - \delta_x(L,t)} \right] \\
& + \frac{\varepsilon a_s}{2\delta_z(L,t)_y} \left( V_{DC} + V_{AC}(t) \right)_s^{\ 2} \; ln \left[ \frac{g_s - \delta_z(L,t) - 2L_C\,\delta_z(L,t)_y}{g_s - \delta_z(L,t)} \right] dt
\end{aligned}
\tag{3.38}
$$

In order to simplify the solution approach, the equation of motion and boundary conditions are non-dimensionalized.

$$EI_x\delta_x(y,t)_{yyyy} + c\dot{\delta}_x(y,t) + \rho A\ddot{\delta}_x(y,t) - 2\rho A\Omega\dot{\delta}_z(y,t) - \rho A\dot{\Omega}\delta_z(y,t) - \rho A\Omega^2\delta_x(y,t) + 2j_x\Omega^2\delta_x(y,t)_{yy} - j_x\dot{\Omega}\delta_z(y,t)_{yy} - j_x\ddot{\delta}_x(y,t)_{yy} = 0$$

$$EI_z\delta_z(y,t)_{yyyy} + c\dot{\delta}_z(y,t) + \rho A\ddot{\delta}_z(y,t) - 2\rho A\Omega\dot{\delta}_x(y,t) - \rho A\dot{\Omega}\delta_x(y,t) - \rho A\Omega^2\delta_z(y,t) + j_z\Omega^2\delta_z(y,t)_{yy} + j_z\dot{\Omega}\delta_x(y,t)_{yy} - j_z\ddot{\delta}_z(y,t)_{yy} = 0 \tag{3.39}$$

$$\rho A\ddot{\delta}_x(y,t) + c\dot{\delta}_x(y,t) + D_\zeta\delta_x(y,t)_{yyyy} = 2\rho A\Omega\dot{\delta}_z(y,t) + \rho A\dot{\Omega}\delta_z(y,t) + \rho A\Omega^2\delta_x(y,t) - 2j_x\Omega^2\delta_x(y,t)_{yy} + j_x\dot{\Omega}\delta_z(y,t)_{yy} + j_x\ddot{\delta}_x(y,t)_{yy}$$

$$\rho A\ddot{\delta}_z(y,t) + c\dot{\delta}_z(y,t) + D_\zeta\delta_z(y,t)_{yyyy} = 2\rho A\Omega\dot{\delta}_x(y,t) + \rho A\dot{\Omega}\delta_x(y,t) + \rho A\Omega^2\delta_z(y,t) - 2j_z\Omega^2\delta_z(y,t)_{yy} + j_z\dot{\Omega}\delta_x(y,t)_{yy} + j_z\ddot{\delta}_z(y,t)_{yy} \tag{3.40}$$

The boundary conditions at the fixed end $(y = 0)$ are no deflection and zero slope as shown below respectively:

$$\delta_x(0,t) = 0 \qquad \delta_z(0,t) = 0$$

$$\delta_x(0,t)_y = 0 \qquad \delta_z(0,t)_y = 0 \tag{3.41}$$

The boundary conditions at the end of the cantilever beam $(y = L)$ are moment and shear balances as shown below, respectively.

$$EI_y\delta_y(L,t)_{yy} = -ML_C\,\ddot{\delta}_x(L,t) - \left(ML_C{}^2 + J\right)\ddot{\delta}_x(L,t)_y + \frac{\varepsilon a_d}{2\left(\delta_x(L,t)_y\right)^2}\left(V_{DC} + V_{AC}(t)\right)_d{}^2 \left[\frac{2L_C\delta_x(L,t)_y}{g_d - \delta_y(L,t) - 2L_C\delta_x(L,t)_y} - \ln\left[\frac{g_d - \delta_x(L,t)}{g_d - \delta_x(L,t) - 2L_C\delta_x(L,t)_y}\right]\right]$$

$$EI_z\delta_z(L,t)_{yy} = -ML_C\,\ddot{\delta}_x(L,t) - \left(ML_C{}^2 + J\right)\ddot{\delta}_x(L,t)_y + \frac{\varepsilon a_d}{2\left(\delta_x(L,t)_y\right)^2}\left(V_{DC} + V_{AC}(t)\right)_d{}^2 \left[\frac{2L_C\delta_x(L,t)_y}{g_d - \delta_y(L,t) - 2L_C\delta_x(L,t)_y} - \ln\left[\frac{g_d - \delta_x(L,t)}{g_d - \delta_x(L,t) - 2L_C\delta_x(L,t)_y}\right]\right]$$

(3.42)

$$EI_y\delta_y(L,t)_{yyy} = M\,\ddot{\delta}_x(L,t) - M\Omega^2\delta_x(y,t) - 2M\Omega\,\dot{\delta}_z(y,t) - M\dot{\Omega}\,\delta_z(y,t) + J_x\,\dot{\Omega}\delta_z(L,t)_x + 2J_x\Omega^2\,\delta_x(L,t)_y + J_x\,\ddot{\delta}_x(L,t)_y - \frac{\varepsilon a_d}{2\delta_x(L,t)_y}\left(V_{DC} + V_{AC}(t)\right)_d{}^2\left[\frac{1}{g_d - \delta_x(L,t) - 2L_C\delta_x(L,t)_y} - \frac{1}{g_d - \delta_x(L,t)}\right]$$

$$EI_z\delta_z(L,t)_{yyy} = M\,\ddot{\delta}_z(L,t) - M\Omega^2\delta_z(y,t) - 2M\Omega\,\dot{\delta}_x(y,t) - M\dot{\Omega}\,\delta_x(y,t) + J_z\,\dot{\Omega}\delta_x(L,t)_y + 2J_z\Omega^2\,\delta_z(L,t)_y + J_z\,\ddot{\delta}_z(L,t)_y - \frac{\varepsilon a_d}{2\delta_x(L,t)_y}(V_{DC})_s{}^2\left[\frac{1}{g_d - \delta_x(L,t) - 2L_C\delta_x(L,t)_y} - \frac{1}{g_d - \delta_x(L,t)}\right]$$

where the moment of inertia of the suspended mass about its point of connection with the microbeam is given by $ML_C{}^2 + J = \frac{3}{4}ML_C{}^2$

In non-dimensional forms of the equations of motion become

$$\delta_x(y,t)_{yyyy} + \hat{c}\dot{\delta}_x(y,t) + \ddot{\delta}_x(y,t) - 2\frac{1}{d}\Omega\dot{\delta}_z(y,t) - \frac{1}{d}\dot{\Omega}\delta_z(y,t) - \Omega^2\delta_x(y,t) + 2J_x\Omega^2\delta_x(y,t)_{yy} - \frac{J_x}{d}\dot{\Omega}\delta_z(y,t)_{yy} - J_x\ddot{\delta}_x(y,t)_{yy} = 0 \quad (3.43)$$

$$\delta_z(y,t)_{yyyy} + c\dot{\delta}_z(y,t) + \ddot{\delta}_z(y,t) - 2\Omega\dot{\delta}_x(y,t) - \dot{\Omega}\delta_x(y,t) - \Omega^2\delta_z(y,t) + 2J_z\Omega^2\delta_z(y,t)_{yy} - J_z d\,\dot{\Omega}\delta_x(y,t)_{yy} - J_z\ddot{\delta}_z(y,t)_{yy} = 0 \quad (3.44)$$

The cantilever beam dynamics depends on three factors: beam resistance to bending, inertia due to movement, and electrostatic force. For convenience, we introduce the following non-dimensional parameters:

$$\mathfrak{x} = \frac{y}{\mathrm{L}} \qquad \mathfrak{l} = \frac{L_c}{\mathrm{L}} \qquad \mathfrak{t} = \frac{t}{\mathrm{T}} \qquad \mathfrak{y} = \frac{\delta_x(y,t)}{g_y} \qquad \mathfrak{z} = \frac{\delta_z(y,t)}{g_y}$$

$$\mathfrak{t} = \mathcal{T}\mathrm{t} \qquad \omega_x = \frac{\Omega}{\mathcal{T}} \qquad \mathfrak{m} = \frac{\mathrm{M}}{\rho A\mathrm{L}} \qquad \mathbf{j} = \frac{\mathrm{j}}{\rho AL^2} \qquad \Omega = \frac{\Omega}{\mathcal{T}}$$

$$\mathfrak{c} = \mathrm{c}\frac{L^2}{\sqrt{\mathrm{EI}\rho A}} \qquad \Omega = \frac{\Omega}{\mathcal{T}} \qquad \mathfrak{t} = \mathcal{T}\mathrm{t} \qquad \Omega = \frac{\Omega}{\mathcal{T}} \qquad \Omega = \frac{\Omega}{\mathcal{T}}$$

$$\boldsymbol{\alpha_u} = \frac{\varepsilon a_d \mathrm{L}^4}{2EId^2}$$

Where T is a time constant defined by $\mathrm{T} = \sqrt{\frac{\rho AL^4}{\mathrm{EI}}}$.

We decompose

$$\mathfrak{y}_{yyyy} + \hat{c}\dot{\mathfrak{y}} + \ddot{\mathfrak{y}} = 2\frac{1}{d}\Omega\dot{\delta}_z(y,t) + \frac{1}{d}\dot{\Omega}\delta_z(y,t) + \Omega^2\delta_x(y,t) - 2J_x\Omega^2\delta_x(y,t)_{yy} + \frac{J_x}{d}\dot{\Omega}\delta_z(y,t)_{yy} + J_x\ddot{\delta}_x(y,t)_{yy} \quad (3.45)$$

$$\mathfrak{z}_{yyyy} + c\dot{\mathfrak{z}} + \ddot{\mathfrak{z}} = 2\Omega\dot{\delta}_x(y,t) + \dot{\Omega}\delta_x(y,t) + \Omega^2\delta_z(y,t) - 2J_z\Omega^2\delta_z(y,t)_{yy} + J_z d\,\dot{\Omega}\delta_x(y,t)_{yy} + J_z\ddot{\delta}_z(y,t)_{yy} \tag{3.46}$$

Subject to the following boundary conditions:

At $\mathfrak{x} = 0$

$$\mathfrak{y}\,(0,\mathfrak{t}) = 0 \tag{3.47}$$

$$\left(\mathfrak{y}\,(0,\mathfrak{t})\right)_y = 0$$

At $\mathfrak{x} = 1$

$$\mathfrak{y}\,(1,\mathfrak{t})_{yy} = M_N \frac{\alpha_1 {(V_{DC})_d}^2}{\left(\delta_z(1)_y\right)^2}\left[\frac{\gamma\delta_z(1)_y}{1-\delta_z(1)-\gamma\delta_z(1)_y} - ln\left(\frac{1}{1-\delta_z(1)-\gamma\delta_z(1)_y}\right)\right] \tag{3.48}$$

$$\mathfrak{y}\,(1,\mathfrak{t})_{yyy} = \frac{\alpha_1 {(V_{DC})_d}^2}{\left(\delta_z(1)_y\right)^2}\left[\frac{\gamma\delta_z(1)_y}{1-\delta_z(1)-\gamma\delta_z(1)_y} - \frac{1}{1-\delta_z(1)}\right]$$

The microbeam deflection due to electric force include the sum of a static component as a result of the DC voltage, denoted by $\hat{\delta}_{z_s}(\hat{y})$ and a dynamic component because of the AC voltage, denoted by $\hat{\delta}_{z_d}(\hat{y},\hat{t})$; that is

$$\hat{\delta}_z(\hat{y},\hat{t}) = \hat{\delta}_{z_s}(\mathrm{y}) + \hat{\delta}_{z_d}(\hat{y},\hat{t}) \tag{3.49}$$

### 3.3.1 Static Deflection Analysis

The static analysis aims at computing the static deflection of the center of the microplate as the MEMS gyroscope is actuated using a constant voltage ( $V_{dc}$) dropping the AC voltage. Hence, there will not be a dynamic behaviour in this situation and the beam is at static equilibrium. Furthermore, the angular rate is set to zero ($\Omega = 0$) to uncouple the equation of motions in the sense and drive direction. Therefore, the static analysis in both drive and sense direction would have the same approach. Here, we present the static deflection in the drive direction is governed by

$$(\hat{\delta}_{z_S}(\hat{y},t))_{yyyy} - \Omega^2\delta_z(\hat{y},t) + 2J_z\Omega^2\delta_z(\hat{y},t)_{yy} = 0$$

(3.50)

$$(\mathfrak{y}_S(\mathfrak{x},\mathrm{t}))_{yyyy} - \omega_x{}^2\mathfrak{y}(\mathfrak{x},\mathrm{t}) + 2\mathbf{j}_y\omega_x{}^2\mathfrak{y}(\hat{\mathfrak{x}},\mathrm{t})_{yy} = 0$$

Subject to the following boundary conditions:

At $\mathfrak{x} = 0$ $\quad \mathfrak{y}_{zs}\,(0,\mathrm{t}) = 0$ (3.51)

$$\left(\mathfrak{y}_{zs}(0,\mathrm{t})\right)_y = 0$$

At $\mathfrak{x} = 1$ (3.52)

$$\left(\mathfrak{y}_{zs}\,(1,\mathrm{t})\right)_{yy} = -\mathrm{M}_N\frac{\alpha_1(V_{DC})_d{}^2}{\left(\delta_z(1)_y\right)^2}\left[\frac{\gamma\delta_z(1)_y}{1-\delta_z(1)-\gamma\delta_z(1)_y} - ln\left(\frac{1}{1-\delta_z(1)-\gamma\delta_z(1)_y}\right)\right]$$

$$\left(\mathfrak{y}_{zs}\,(1,\mathrm{t})\right)_{yyy} = \frac{\alpha_1(V_{DC})_d{}^2}{\left(\delta_z(1)_y\right)^2}\left[\frac{\gamma\delta_z(1)_y}{1-\delta_z(1)-\gamma\delta_z(1)_y} - \frac{1}{1-\delta_z(1)}\right]$$

Dropping all terms related to time variation, the general solution to the modified Eq. (1) is a third-degree polynomial:

$$\hat{\delta}_{z_S}(\hat{y}) = A\hat{y}^3 + B\hat{y}^2 + C\hat{y} + D \tag{3.53}$$

where $\hat{\delta}_{z_S}(\hat{y})$ is the normalized static deflection at the normalized position $\hat{y}$ along the beam. We also drop any time variation terms in the BC's;

Using the fixed end boundary conditions Eq. (3.51) in Eq. (3.53), the constants C and D vanish. Since both $\hat{\delta}_{z_S}(1)$and $\left(\hat{\delta}_{z_S}\right)_y(1)$ and are actually functions of A and B, then the BCs will yield two non-linear algebraic equations for every $V_{DC}$.

$$\begin{cases} 6A+2B=\dfrac{\alpha_1 V_{DC}^2}{(3A+2B)^2}\left[\dfrac{\gamma(3A+2B)}{1-A-B-\gamma(3A+2B)}-ln\left(\dfrac{1-A-B}{1-A-B-\gamma(3A+2B)}\right)\right] \\ 6A=\dfrac{\alpha_1 V_{DC}^2}{3A+2B}\left[\dfrac{1}{1-A-B-\gamma(3A+2B)}-\dfrac{1}{1-A-B}\right] \end{cases} \tag{3.54}$$

Equation (3.54) can be solved numerically for A and B to provide the static deflection as function of voltage. For the cantilevers 1 geometric and physical parameters described earlier in this chapter, the result is shown in Figure 3.8. The result displays variation of the static deflection of the cantilevers beam and microplate system with the applied DC voltage. It is composed of two branches: a lower branch corresponds to stable equilibria, whereas the upper branch corresponds to unstable equilibria. Figure 3.8 also shows that beyond a critical voltage $V_P$, there are no equilibria. This critical point, known as the pull-in point, corresponds to $V_P$ = 45.295 Volts and a maximum deflection of 0.2837 nm. We prepared a mathematic reduced order model to simulate the cantilever beam gyroscope and the result is presented in the next section, Appendix B.

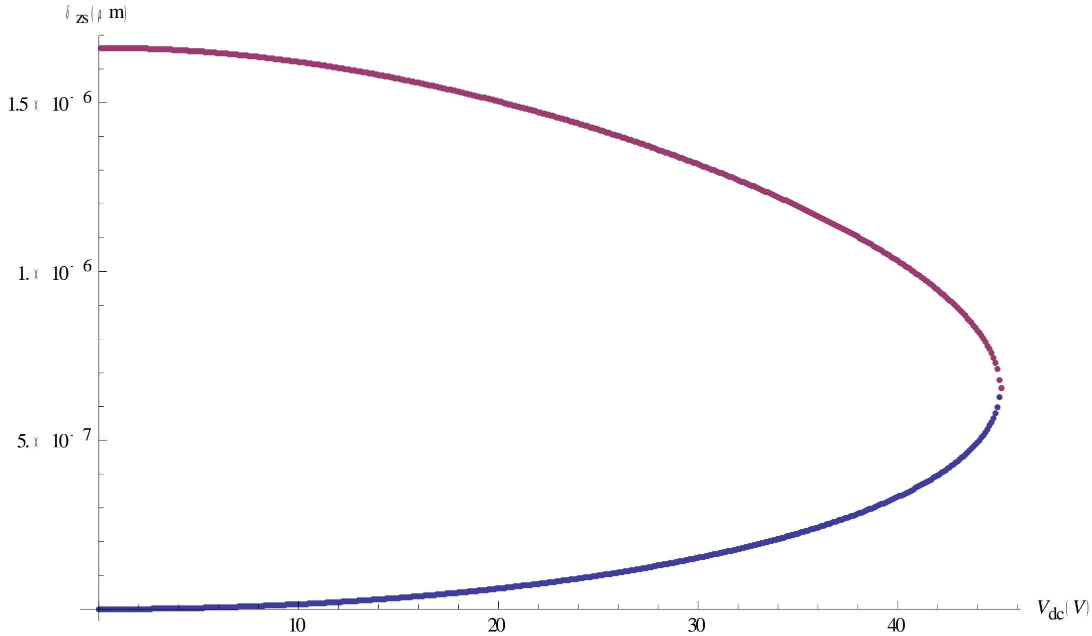


**Figure 3.8: Variation of the static deflection in the drive with the DC voltage**

$V_{DC} \neq V_{pi}$, the solution to system (4.22) yields two distinct values for A and B

Figure 3.9 displays the maximum static deflection ($\hat{\delta}_{x_s}(\hat{y})$) in the sense directions with the DC voltage. The resulting curve is typical for electrostatic actuators with lower and upper branches of solutions corresponding, respectively, to stable and unstable equilibria of the micro-beam. The pull-in voltage is 45.61V and the associated deflection 0.24 nm. For our application, one needs to avoid the occurrence of pull-in and then select an operating voltage less than 45.61V.

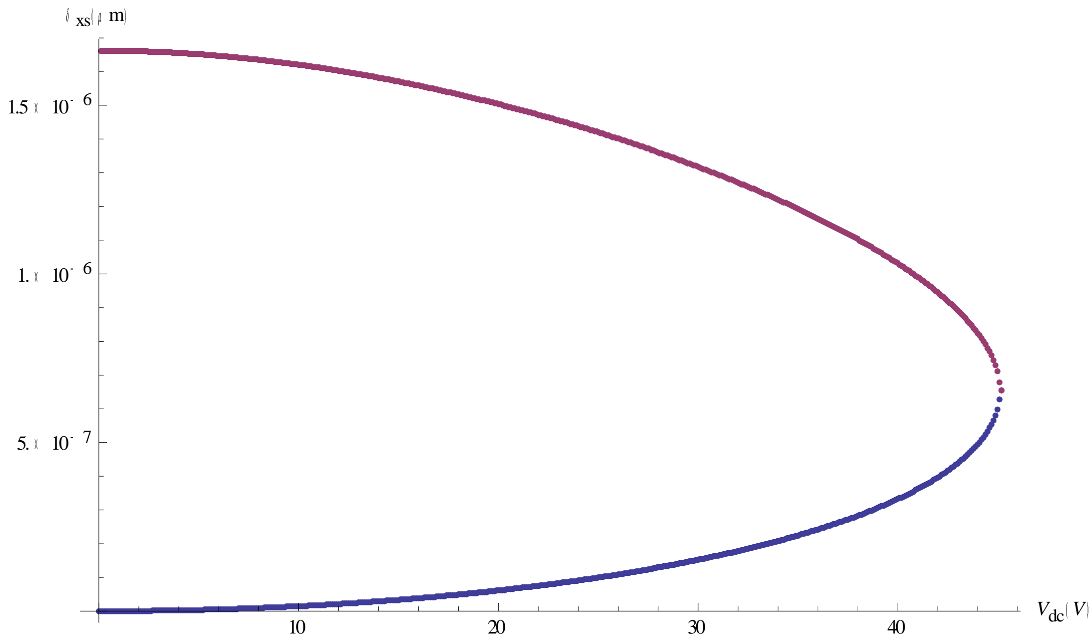


**Figure 3.9: Variation of the static deflection in the sense direction with the DC voltage**

Very close pull-in voltage and deflection was attained using FEA analysis. Also, we note that the symmetric configuration considered here results in the static deflection in the drive and sense directions being identical $\hat{\delta}_{x_s}(\hat{y}) = \hat{\delta}_{z_s}(\hat{y})$ for the same DC voltage. From a design standpoint, this presents a desirable outcome since a match between the DC forces and static deflections on the sense and drive directions can be obtained. This would eliminate spurious torsional motions and leads to a match between the natural frequencies in the sense and drive directions.

### 3.3.2 Natural Frequencies and Mode Shapes

The modal analysis transforms the general motions equations of the beam from a Partial Differential Equation (PDE) to an Ordinary Differential Equation (ODE) problem. The dynamic behaviour of the beam is analyzed around a static operating point as the sum of several mode shapes, where each shape represents the typical response of the beam to an excitation at a given frequency. The effect of each

mode on the general motion of the beam decreases with the increase of the frequency associated to the mode. In this particular case, it is sufficient to consider the first three modes to have a good knowledge of the displacement of the beam. The first two modes are desired to have very close natural frequency to each other whereas the third mode is intended to have a wider different from the two to avoid energy transfer.

Initially, the general motion equations need to be linearized around a given static operating point, that is, around a constant input voltage $V_{DC}$. Substituting Eq. (3.20) into Equations (3.18 - 3.19) and expanding the nonlinear electrostatic force using Taylor series about $\delta_z(y,t) = 0$ yields the dynamics of the cantilevers beam and microplate system about its static equilibrium:

$$\ddot{\delta}_z(y,t) + \hat{c}\dot{\delta}_z(y,t) + \hat{\delta}_z(y,t)_{yyyy} - J_z\ddot{\delta}_z(y,t)_{yy} = 0 \tag{3.55}$$

We drop the nonlinear forcing and damping terms in Equations (3.55), (3.26), and (3.27) and obtain the following linear eigenvalue problem

$$\left(\hat{\delta}_{\hat{z}}\right)_{\hat{t}\hat{t}} + \left(\hat{\delta}_{\hat{z}}\right)_{\hat{y}\hat{y}\hat{y}\hat{y}} = 0 \tag{3.56}$$

Subject to the following boundary conditions:

$$\hat{\delta}_{\hat{z}}\,(0,\hat{t}) = 0$$
$$\hat{\delta}_{\hat{z}}\,(0,\hat{t}) = 0 \tag{3.57}$$

$$\hat{\delta}_{\hat{z}_d}(1,\hat{t})_{xx} = -\hat{L}_C\widehat{M}\ddot{\delta}_y(1,\hat{t}) -$$
$$\frac{4}{3}\hat{L}_C{}^2\widehat{M}\ddot{\delta}_y(1,\hat{t})_x + \alpha_1 V_{CD}^2\left(\frac{\gamma^2}{\left(1-\hat{\delta}_{\hat{y}}\,(1,\hat{t})\right)\left(1-\hat{\delta}_{\hat{y}}\,(1,\hat{t})\right)}\hat{\delta}_y\,(1,\hat{t})\right) \tag{3.58}$$

$$\hat{\delta}_{\hat{z}z\hat{z}_d}\,(1,\hat{t}) =$$

We solve Eq. (3.29) and (3.30) for the mode shapes and corresponding natural frequencies for a given static deflection$w_s\,(\hat{x})$. To this end, we let

$$\hat{\delta}_z(y,t)_{yyyy} + \hat{c}\dot{\delta}_z(y,t) + \ddot{\delta}_z(y,t) - 2\frac{1}{d}\Omega\dot{\delta}_z(y,t) - \frac{1}{d}\dot{\Omega}\delta_z(y,t) - \Omega^2\delta_z(y,t) + 2J_z\Omega^2\delta_z(y,t)_{yy} - \frac{J_z}{d}\dot{\Omega}\delta_z(y,t)_{yy} - J_z\ddot{\delta}_z(y,t)_{yy} = 0 \tag{3.59}$$

$$\hat{\delta}_z\,(\hat{y},\hat{t}) = \xi(\hat{y})e^{i\omega\hat{t}} \tag{3.60}$$

where $\xi(\hat{y})$ is the mode shape and $\omega$ is its corresponding non-dimensional natural frequency. Substituting Equation (3.32) into Equations (3.29) and (3.30) yields the following eigenvalue problem:

$$\xi^{iv}(\hat{y}) + \xi^{ii}(\hat{y}) - \omega\xi(\hat{y}) = 0 \tag{3.61}$$

and the associated boundary conditions are

$$\begin{aligned}
&\xi(0) = 0\\
&\xi'(0) = 0\\
&\xi''(1) = \hat{L}_c\widehat{M}\omega^2\xi(1) + \frac{4}{3}\hat{L}_c{}^2\widehat{M}\omega^2\xi'(1) + \alpha_1 V_{DC}^2\big(C_1\xi(1) + C_2\xi'(1)\big)\\
&\xi'''(1) = -\widehat{M}\omega^2\xi(1) - \hat{L}_c\widehat{M}\omega^2\xi'(1) - \alpha_1 V_{DC}^2\big(C_3\xi(1) + C_4\xi'(1)\big)
\end{aligned} \tag{3.62}$$

The general solution of Eq. (4.33) can be expressed as

$$\xi(y) = \lambda_1 cos\beta y + \lambda_2 sin\beta y + \lambda_3 cosh\beta y + \lambda_4 sinh\beta y \tag{3.63}$$

where the coefficients $\lambda_i$are functions of the applied voltage and $\beta = \sqrt{\omega}$ . Using the first two boundary conditions in Eq. 3.34, we eliminate two of the unknowns, say $\lambda_3$ and $\lambda_4$ . This yields two linear algebraic equations in $\lambda_1$ and $\lambda_2$, which can be written in the following matrix form:

$$[N]\begin{Bmatrix}\lambda_1\\ \lambda_2\end{Bmatrix} = 0 \text{ with } [N] = \begin{bmatrix} n_{11} & n_{12} \\ n_{21} & n_{22}\end{bmatrix} \tag{3.64}$$

and

$$\begin{aligned}
n_{11} &= \beta^2(cos\beta + cosh\beta) + (cos\beta - cosh\beta)\left(\hat{L}_c\widehat{M}\beta^4 + \alpha_1 V_{DC}^2 C_1\right) \\
&\quad - \beta(sin\beta + sinh\beta)\left(\frac{4}{3}\hat{L}_c{}^2\widehat{M}\beta^4 + \alpha_1 V_{DC}^2 C_2\right) \\
n_{12} &= \beta^2(sin\beta + sinh\beta) + (sin\beta - sinh\beta)\left(\hat{L}_c\widehat{M}\beta^4 + \alpha_1 V_{DC}^2 C_1\right) \\
&\quad + \beta(cos\beta + cosh\beta)\left(\frac{4}{3}\hat{L}_c{}^2\widehat{M}\beta^4 + \alpha_1 V_{DC}^2 C_2\right) \\
n_{21} &= -\beta^2(sin\beta + sinh\beta) + (cos\beta - cosh\beta)\left(\widehat{M}\beta^4 + \alpha_1 V_{DC}^2 C_3\right) \\
&\quad + \beta(sin\beta + sinh\beta)\left(\hat{L}_c\widehat{M}\beta^4 + \alpha_1 V_{DC}^2 C_1\right) \\
n_{22} &= \beta^3(cos\beta + cosh\beta) - (sin\beta - sinh\beta)\left(\widehat{M}\beta^4 + \alpha_1 V_{DC}^2 C_3\right) \\
&\quad + \beta(cos\beta - cosh\beta)\left(\hat{L}_c\widehat{M}\beta^4 + \alpha_1 V_{DC}^2 C_1\right)
\end{aligned} \tag{3.65}$$

Setting the determinant of the two by two matrix equal to zero leads to the characteristic equation det(N)=0 of the cantilever and microplate system. Solving the characteristic equation, we obtain an infinite number of natural frequencies for a given DC voltage. In Figure 3.10 show variation of the first natural frequency $\omega$ with the applied voltage

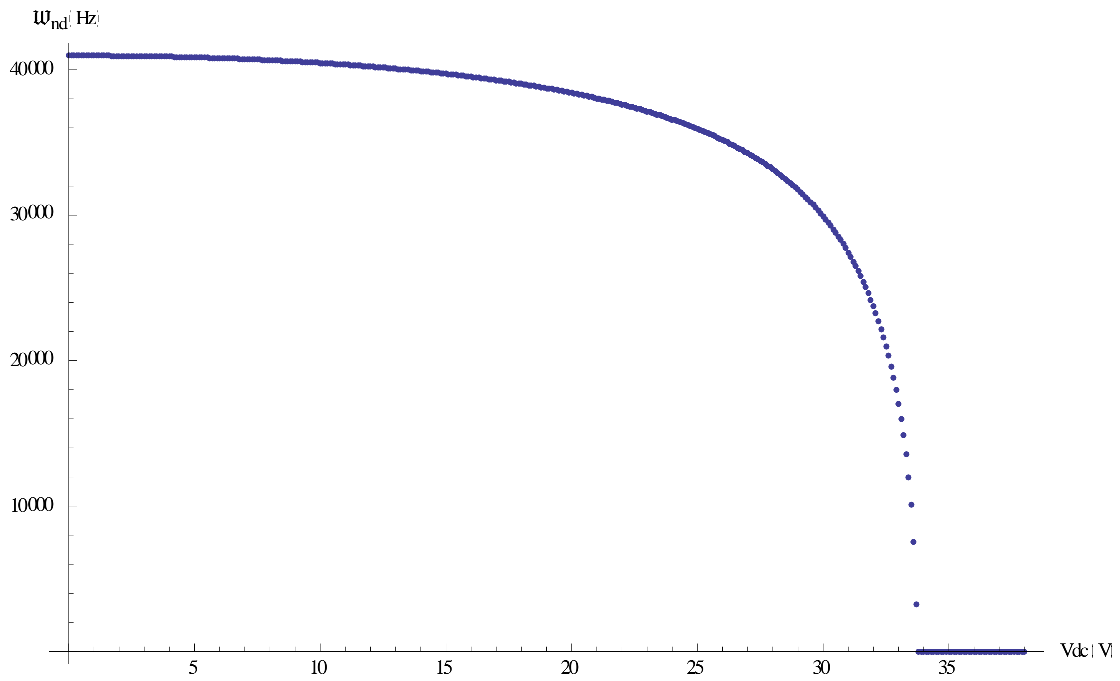


**Figure 3.10: Variation of the first natural frequency with the DC voltage for cantilever 1 gyroscope (drive)**

Similarly, the solution in the sense direction provides

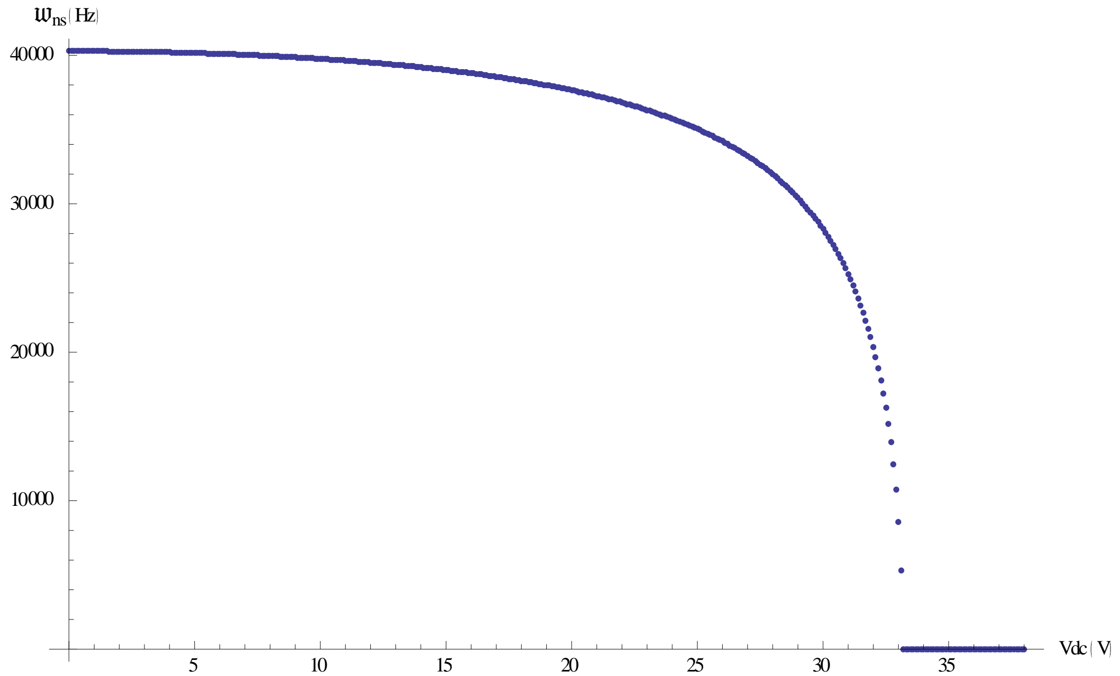


**Figure 3.11: Variation of the first natural frequency with the DC voltage for Cantilever 1 gyroscope (sense)**

It follows from Figure 3.10 and 3.11 that increasing the applied DC voltage leads to a sharp drop in the first natural frequency followed by the pull-in instability. A numeral model also developed and implemented to study the dynamic behavior of the cantilever beam. The equations of motion derived in the previous section is simplified to include nonlinear effects up to order three. This is accomplished by expanding each term in the equations into a Taylor series and discarding terms of order greater than three. The simplification is necessary to enable the use of the equations to study the motion of the beam using numerical techniques. The simplification process begins by obtaining the order three Taylor series expansions of $u'$, ψ, and θ. These are derived using the Taylor series expansion of *arctan (x)*

$$tan^{-1}y = y - \frac{1}{3}y^3 + \cdots \tag{3.66}$$

which is combined with Eq. (3.10) and (3.11) to get

$$\delta_x(y,t)_{yyyy}$$

$$\left(\delta_x(y,t)_y\right)^2$$

$$\begin{aligned}\delta_x(y,t)_y &= \left[1 - \left(\delta_x(y,t)_y\right)^2 - \left(\delta_z(y,t)_y\right)^2\right]^{\frac{1}{2}} - 1 \\ &= \frac{1}{2}\left[\left(\delta_x(y,t)_y\right)^2 - \left(\delta_z(y,t)_y\right)^2\right] + \cdots\end{aligned} \tag{3.67}$$

$$\begin{aligned}\psi = tan^{-1}&\frac{\delta_x(y,t)_y}{1+\delta_x(y,t)_y} \\ &= tan^{-1}\left\{\delta_x(y,t)_y\left[1 - \left(\delta_x(y,t)_y\right)^2 - \left(\delta_z(y,t)_y\right)^2\right]^{-1/2}\right\} \\ &= \delta_x(y,t)_y\left[1 + \frac{1}{6}\left(\delta_x(y,t)_y\right)^2 + \frac{1}{2}\left(\delta_z(y,t)_y\right)^2\right] + \cdots\end{aligned} \tag{3.68}$$

$$\begin{aligned}\theta = tan^{-1}&\frac{\delta_z(y,t)_y}{\left[1 - \left(\delta_y(y,t)_y\right)^2 - \left(\delta_x(y,t)_y\right)^2\right]^{1/2}} \\ &= tan^{-1}\left\{-\delta_z(y,t)_y\left[1 - \left(\delta_z(y,t)_y\right)^2\right]^{-1/2}\right\} \\ &= \delta_z(y,t)_y\left[1 + \frac{1}{6}\left(\delta_z(y,t)_y\right)^2\right] + \cdots\end{aligned} \tag{3.69}$$

The order three expansions for the angle of twist is obtained from the twisting curvature $\rho_\xi$. The order three equations of motion for the flexural-flexural-torsional vibration of a cantilever beam.

$$
\begin{aligned}
& m\ddot{\delta}_x(y,t) - c_x\dot{\delta}_z(y,t) - D_\zeta\left(\delta_x(y,t)_{yyyy}\right)^2 \\
&= Q_v + \Bigg\{ +\left(D_\eta - D_\zeta\right)\left[\delta_z(y,t)_{yy}\int_l^s \delta_z(y,t)_{yy}\delta_x(y,t)_{yy}\, ds \right. \\
&\quad \left. - \delta_z(y,t)_{yyy}\int_0^s \delta_z(y,t)_y\delta_x(y,t)_{yy}\, ds\right] \\
&\quad - \frac{\left(D_\eta - D_\zeta\right)^2}{D_\xi}\left(\delta_z(y,t)_{yy}\int_l^s\int_0^s \delta_x(y,t)_{yy}\delta_z(y,t)_{yy} ds\, ds\right)'\Bigg\}' \qquad (3.70) \\
&\quad - D_\zeta\left\{\delta_z(y,t)_{yy}\left(\delta_x(y,t)_y\delta_x(y,t)_{yy} + \delta_z(y,t)_y\delta_z(y,t)_{yy}\right)'\right\}' \\
&\quad - \frac{1}{2}m\left\{\delta_x(y,t)_y\int_l^s \frac{\partial^2}{\partial t^2}\left[\int_0^s \left[\left(\delta_x(y,t)_y\right)^2 + \left(\delta_z(y,t)_y\right)^2\right] ds\right] ds\right\}' \\
&\quad - \left(\delta_x(y,t)_y\int_l^s Q_y ds\right)'
\end{aligned}
$$

$$
\begin{aligned}
& m\ddot{\delta}_z(y,t) - c_z\dot{\delta}_z(y,t) - D_\eta\delta_z(y,t)_{yyyy} \\
&= Q_z \\
&\quad + \Bigg\{ +\left(D_\eta - D_\zeta\right)\left[\delta_x(y,t)_{yy}\int_l^s \delta_z(y,t)_{yy}\delta_x(y,t)_{yy}\, ds \right. \\
&\quad \left. - \delta_x(y,t)_{yyy}\int_0^s \delta_x(y,t)_y\delta_z(y,t)_{yy}\, ds\right] \\
&\quad - \frac{\left(D_\eta - D_\zeta\right)^2}{D_\xi}\left(\delta_x(y,t)_{yy}\int_l^s\int_0^s \delta_x(y,t)_{yy}\delta_z(y,t)_{yy} ds\, ds\right)'\Bigg\}' \qquad (3.71) \\
&\quad - D_\eta\left\{\delta_z(y,t)_y\left(\delta_x(y,t)_y\delta_x(y,t)_{yy} + \delta_z(y,t)_y\delta_z(y,t)_{yy}\right)'\right\}' \\
&\quad - \frac{1}{2}m\left\{\delta_z(y,t)_y\int_l^s \frac{\partial^2}{\partial t^2}\left[\int_0^s \left[\left(\delta_x(y,t)_y\right)^2 + \left(\delta_z(y,t)_y\right)^2\right] ds\right] ds\right\}' \\
&\quad - \left(\delta_z(y,t)_y\int_l^s Q_y ds\right)'
\end{aligned}
$$

The boundary conditions for Eq. (3.70) and (3.71) are given by

$$\delta_x(0,t) = 0, \quad \delta_z(0,t) = 0, \quad \delta_x(0,t)_y = 0, \quad \delta_z(0,t)_y = 0$$
$$\delta_x(l,t)_{yy} = 0, \quad \delta_z(l,t)_{yy} = 0, \quad \delta_x(l,t)_{yyy} = 0, \quad \delta_z(l,t)_{yyy} = 0 \qquad (3.72)$$

Numerical algorithm used to solve the equation of motion for the planar flexural forced vibration of the cantilever beam. The partial differential equation is first discretized in the spatial coordinate using Galerkin's weighted residual method. Then, the equation is discretized in the time domain using the Newmark technique. Finally, a numerical algorithm is used to calculate the nonlinear response of the beam. Therefore, an approximate solution is sought by discretizing the spatial coordinate using Galerkin's weighted residuals method, and then in the time domain using the Newmark technique. The discretization in the spatial coordinate is carried out in three steps: mesh generation and function approximation, element equation, and assembly and implementation of boundary conditions.

The cantilever beam MEMS gyroscope design parameter provided in Table 3.1 is used to simulate the device characteristics. An AC harmonic excitation voltage ($f^*{}_d = V_{AC}\cos(\omega_{ex}t)$) was tuned to excite the gyroscope near the natural fundamental frequency $\omega_{ex}$ =40.56 kHz. Figures 3.12 and 3.13 show the time-response curves corresponding to $f^*{}_d = 15\ \cos(\omega_{ex}t)$ Volt in the drive and sensing mode, respectively. The gyroscope behavior for a time varying angular rate ($\Omega = \Omega_0 \sin(\beta t)$) were also investigated.

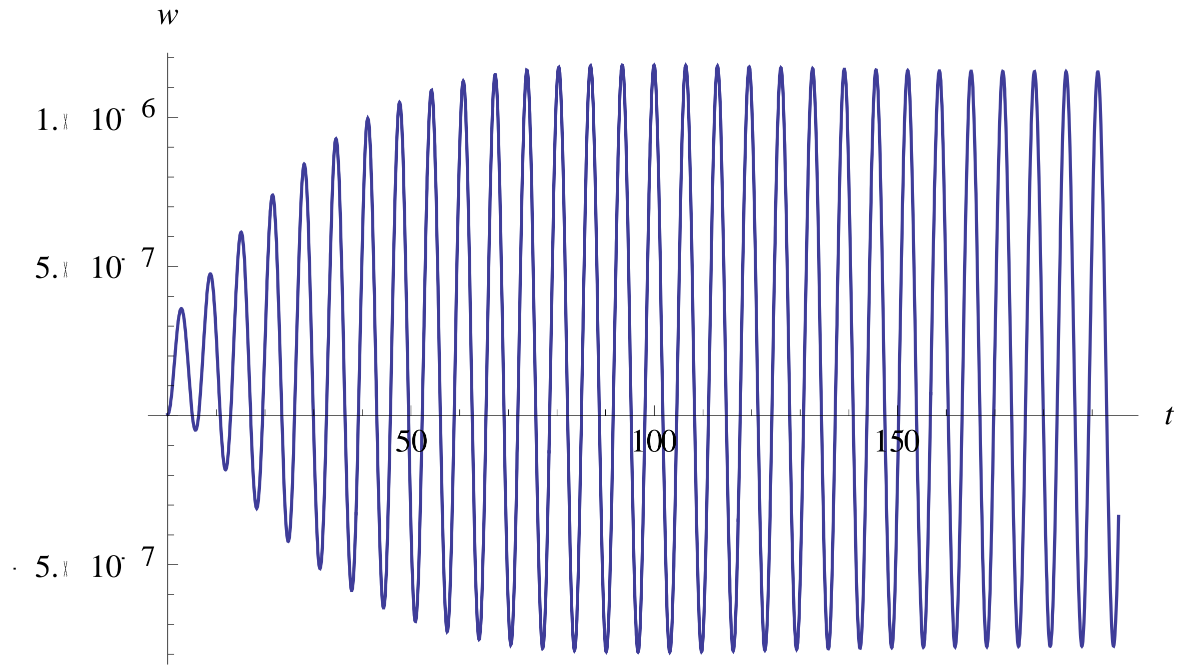


**Figure 3.12: System output response plot for the drive mode**

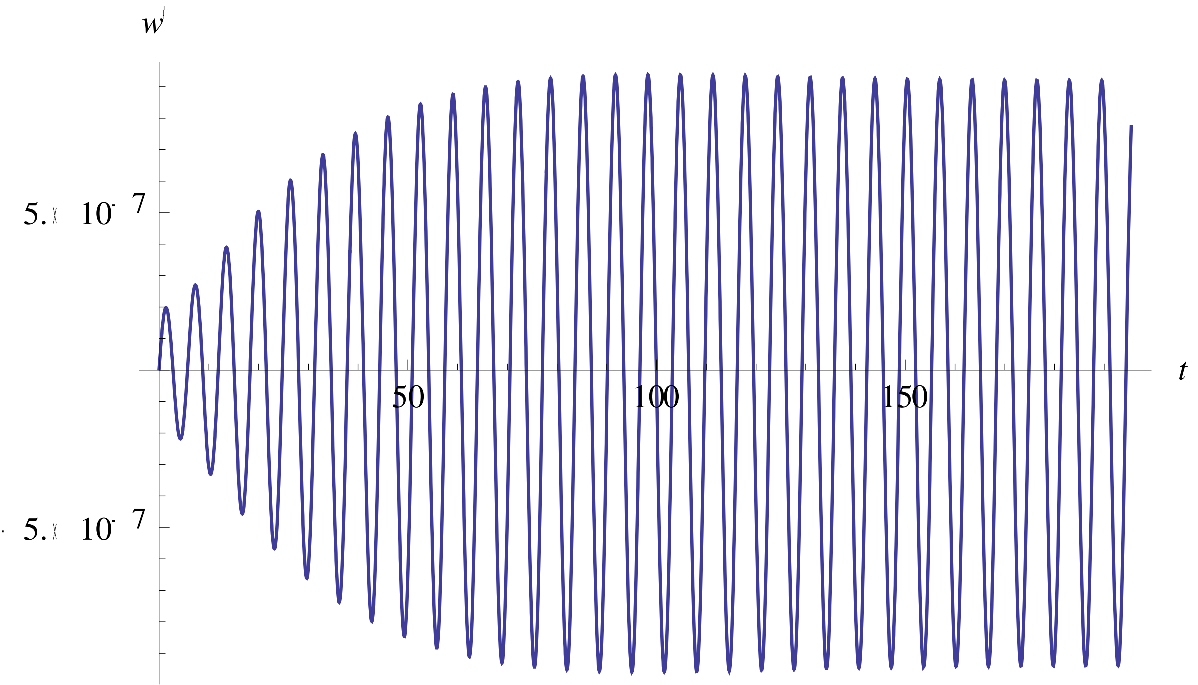


**Figure 3.13: System output response plot for the Sense mode**

## 3.6 Finite Element Simulations and Results

The gyroscope dynamic analysis for the cantilever beam gyroscope in previous section established the relationship between device characteristic such as device resonant frequency, displacement and capacitance sensitivity with various design parameters such as material properties of the beam structure and beam geometry (length, width and beam thickness).

In this section, a finite element model developed for the cantilever beam and crab leg design presented. A commercial CAD software, SolidWorks was used to develop the 3D model. For parametric finite element model of the cantilever beam and crab leg, Parametric Design Language of ANSYS (APDL) is used. For static and modal analysis, a number of parameters (geometric, material, analysis options, etc) can easily, change to account for different prototype sample developed, Appendix G. variables are taken as parameters and they can be changed interactively. Boundary and loading conditions are described for each analysis in the other subsections. In the next section analysis and result preformed for Cantilever 1 and Crab leg 2 is presented.

### 3.6.1 Cantilever Beam Gyroscope FEA Analysis

In this section, Finite Element Analysis (FEA) for the cantilever beam MEMS gyroscope design is presented. As the MEMS structure moves due to electrostatic excitation force, the electrostatic field distribution will change. Hence, a coupled electrostatic-structural analysis was implemented that allows the actual electrostatic actuation of a MEMS device to be simulated, capturing the interdependencies of these two physics.

The full cantilever beam model was used for static and modal analysis since the model is small enough to run with available computational resource and does not need simplification. The FEA analysis presented here does not take into account the effect of gravity condition. Both the cantilever beam and crab leg 3D model developed using SolidWork and imported to ANSYS. In this analysis, shell elements were used for the microplate. A shell element is the combination of the bending element and the membrane element. At each node, the shell element has both translational DOFs and rotational DOFs in each direction. When the structure's thickness is far less than the other dimensions, shell elements can usually give more accurate results than solid elements. A tetrahedral solid element were also used for the cantilever beam, Figure 3.14.

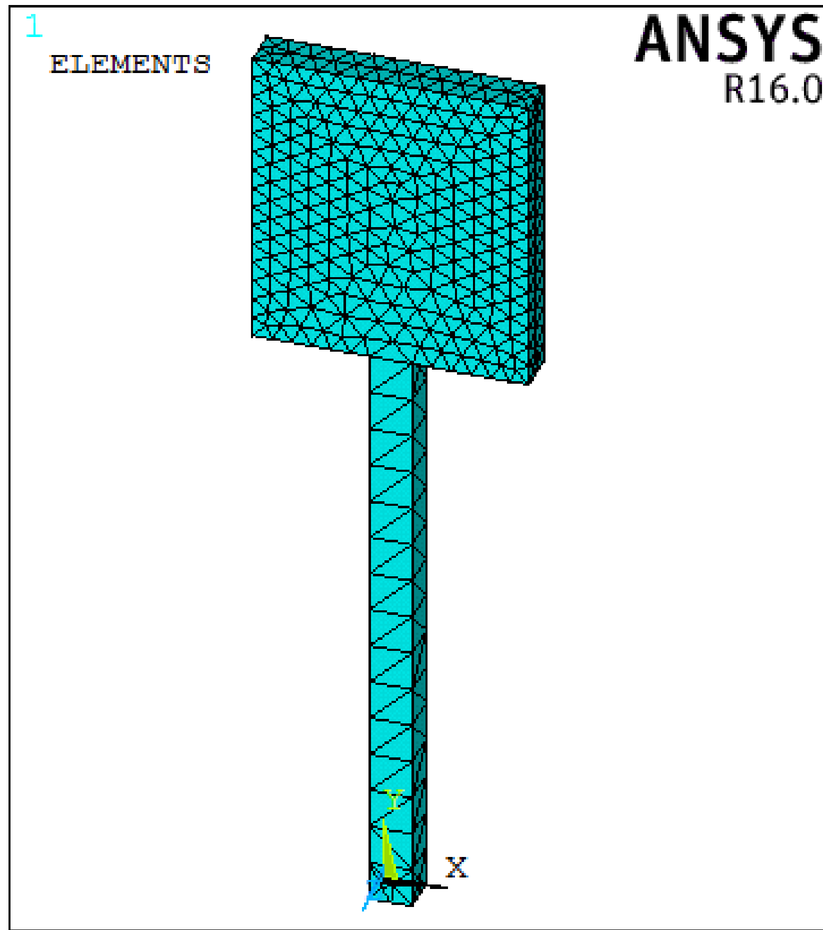


**Figure 3.14: Meshed element of the cantilever beam gyroscope**

First, the FEM static analysis is required to estimate the cantilever beam deflection in response to the electrostatic force in the drive and sense direction, respectively. The beam is mechanically constrained at the fixed base and voltages are applied to the microplate which is used as a parallel plate electrodes. Furthermore, a static simulation was performed to identify the pull-in voltage. A DC input voltage is swept and we observe the voltage value at which the results failed to converge which resembles an abrupt increase in the deflection corresponding to the pull-in Figure 3.15. This critical point, corresponds to the pull-in voltage has a value of $V_P = 45.295$ Volts which is in perfect agreement for the numerical model presented earlier. This result is also verified by other method that requires defining convergence tolerance criteria using the CNVTOL command, this allows the solver to converge and the result is available in the nodal solution.

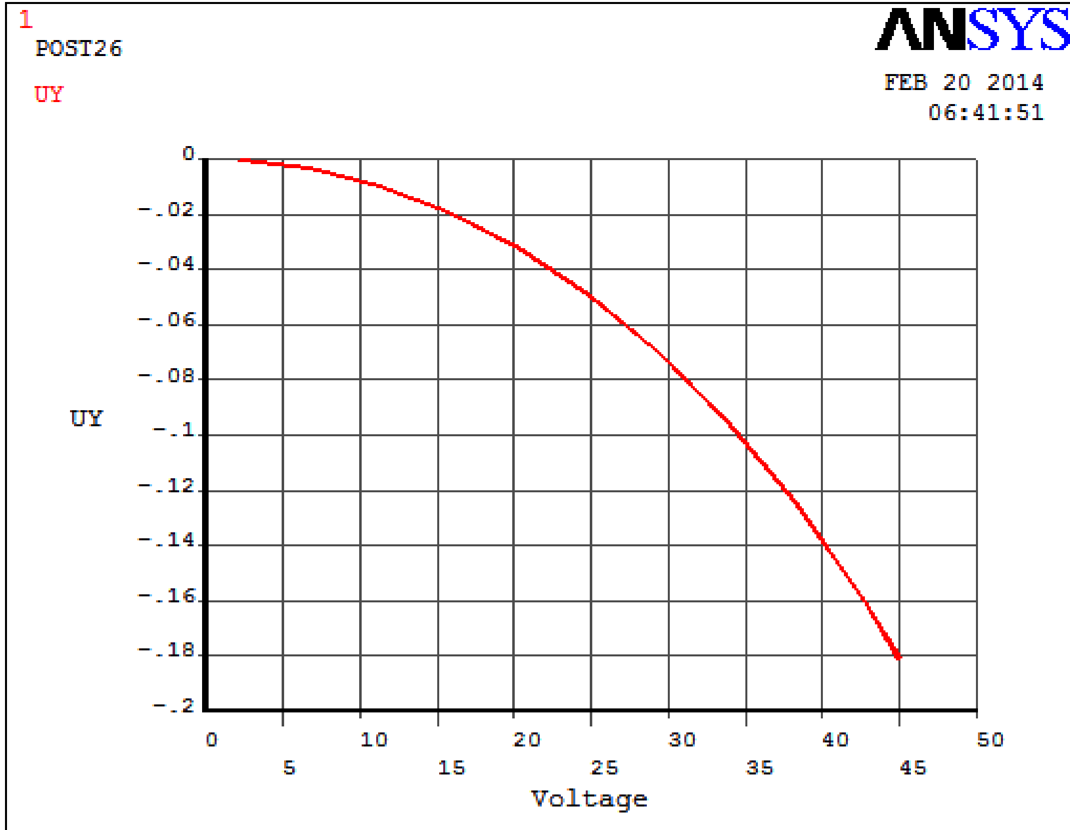


**Figure 3.15: Variation of the static deflection with the DC voltage**

The distribution of the structural deformations obtained from the FEM simulations for the MEMS gyroscope for an applied voltage of 15 V is shown in Figures 3.16. The contour plot demonstrates that the microplate is displaced at the center approximately 0.7 n$m$. This demonstrates that the MEMS gyroscope section displaces without experiencing significant bending, which is in line with the expected behavior of a rigid body structure.

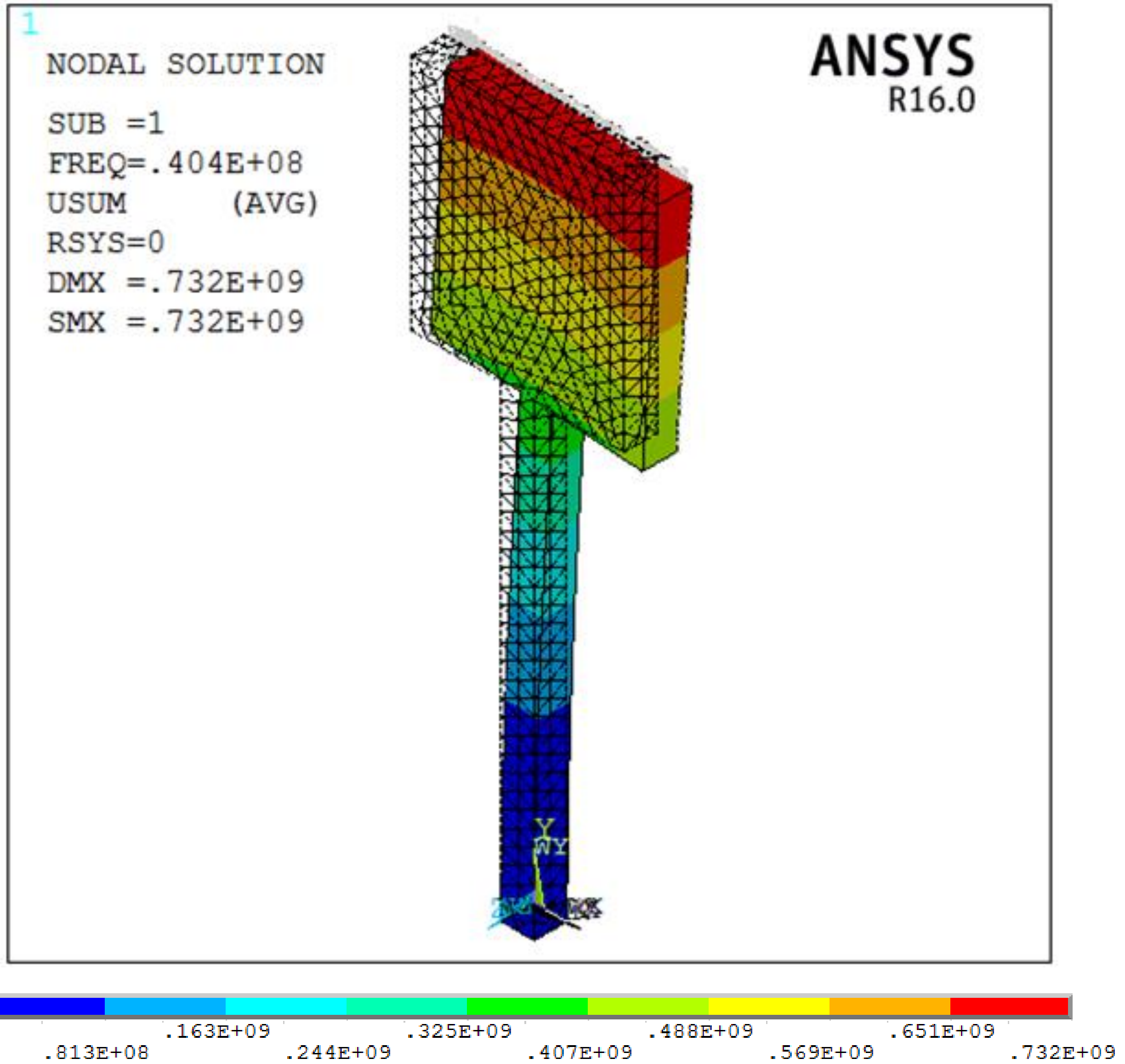


**Figure 3.16: Deformed shape of the cantilever beam gyroscope**

The modal solution is followed by mode extraction to provide the full modal solution. Several extraction methods are available in ANSYS software for mode extraction from the reduced solution; each is suitable for a range of models. Block Lanczos method is typically used for large symmetric Eigenvalue problems utilizing a sparse matrix solver. The Block Lanczos Eigenvalue solver uses the Lanczos algorithm where the Lanczos recursion is performed with a block of vectors. This method is as accurate as the subspace method and less time consuming. It uses the sparse matrix solver, overriding any solver specified via the EQSLV command and is especially powerful when searching for Eigenfrequencies in a given part of the Eigenvalue spectrum of a given system. The convergence rate of the Eigenfrequencies

will be about the same when extracting modes in the midrange and higher end of the spectrum as when extracting the lowest modes.

The application of DC bias voltage at the device electrodes produces electrostatic forces which creates stresses in the beam and affects the natural frequencies. The prestressed modal analysis was performed in two steps: The first step was a static analysis with the DC bias voltage applied and prestressing active (PSTRES, ON) as preformed in the previous section. The second step was a modal analysis with the prestressing still active. The DC bias voltage was applied using the distributed array of TRANS126 elements. With a 0V bias, the problem is solved without the inclusion of "spring softening" effects. For the static prestress analysis, a DC bias voltage ranging from 0-45 Volts was applied across the TRANS126 elements.

A modal analysis is used to determine the structure vibration characteristics of natural frequencies and mode shapes. We extracted the first 3 vibration modes of this gyroscope to decide which two modes are the driving modes and sensing mode of the gyroscope. The shape and values of the mode frequency versus voltage curves are approximately the same over the course up to the pull in voltage. The deformed shapes of the first three modes are shown in Figures 3.17 through 3.19 for the cantilever beam gyroscope. These include the first out of plane mode shapes and frequencies, second in plan mode and the third torsional mode. From the simulated results, the first two set frequencies are 40.4 kHz and 40.8 kHz. Therefore, the resonant frequency of the driving mode is 40.4 kHz; and the resonant frequency of the sensing mode is 40.8 kHz. In general, ANSYS predicts a slight higher modal frequency than reduced order model solution in the drive direction. This slight difference can be explained by the effect of pre-stress consideration including in our ANSYS simulation.

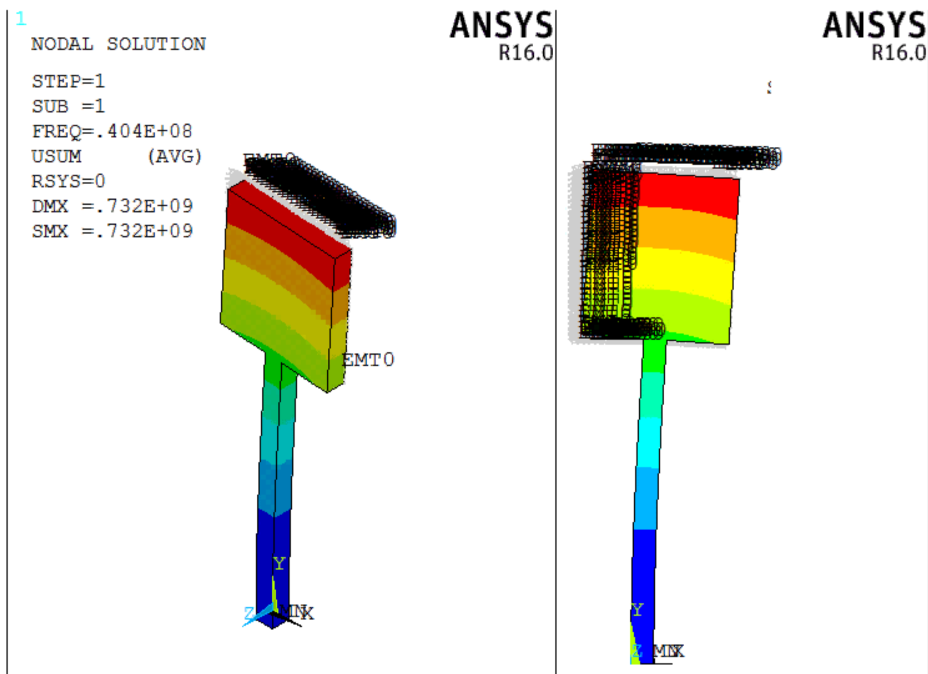


**Figure 3.17: First mode shape of the cantilever beam**

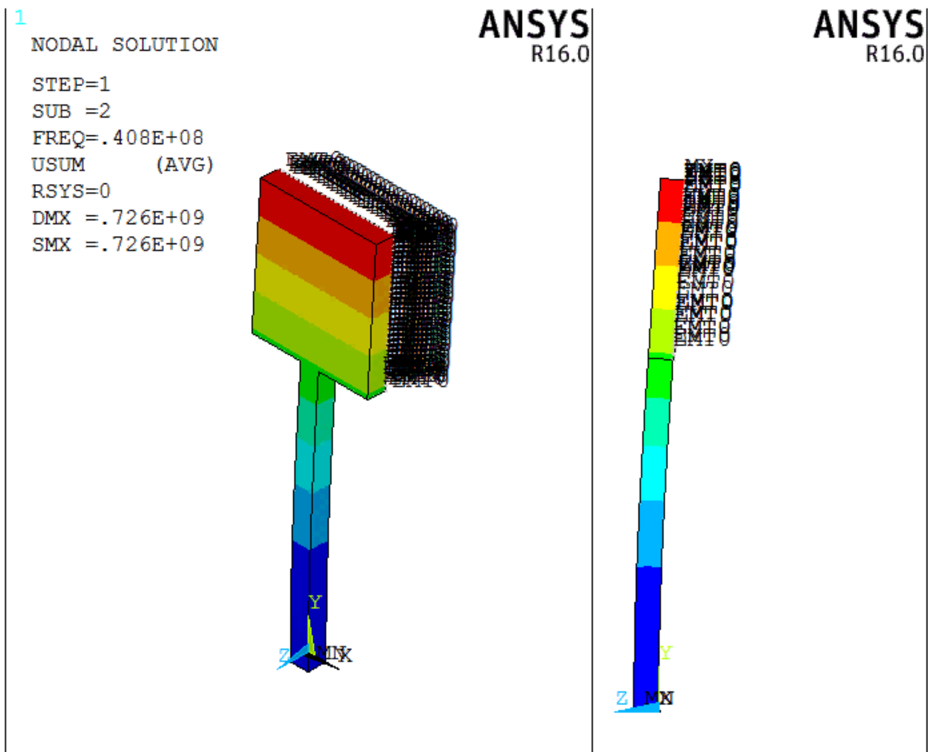


**Figure 3.18. Second mode shape of the cantilevered beam.**

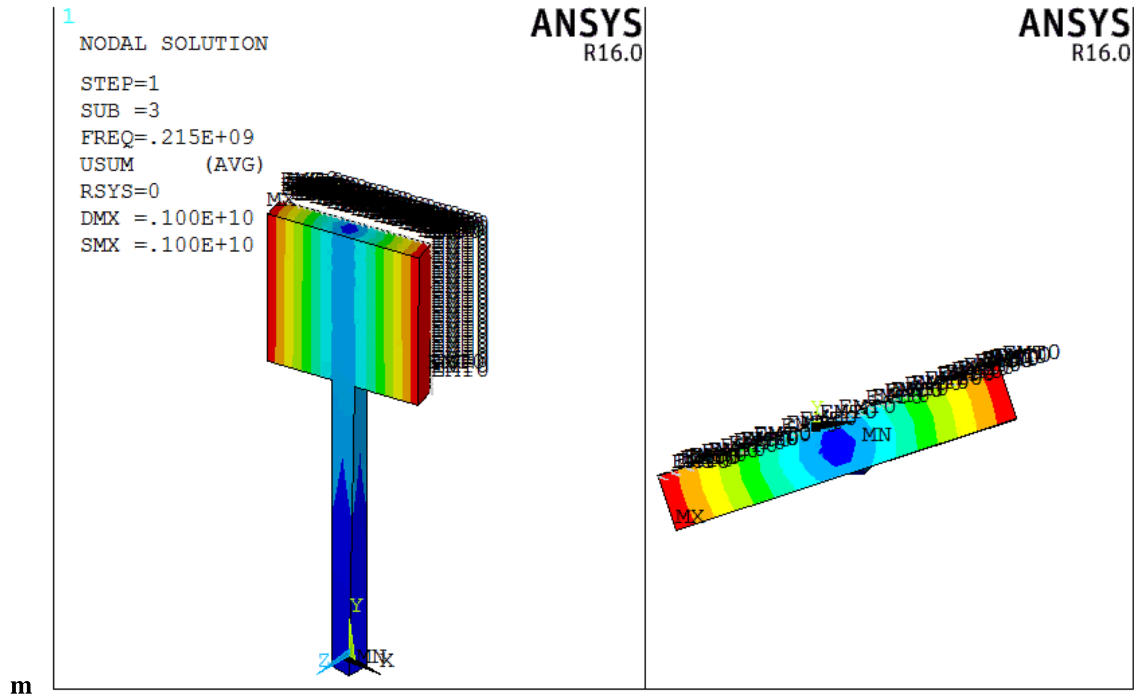


**Figure 3.19. Third mode shape of the cantilevered beam.**

As shown in Figure 3.19, the third mode has a frequency an order of magnitude larger than the first two mode which good to avoid energy transfer between the first two mode and the third mode.

### 3.6.2 Crab Leg FEA Analysis (Device 2)

FEA simulation for the crab-leg MEMS gyroscopes were also developed using ANSYS finite element analysis software. In the same way, a 3D modal analysis of the crab leg gyroscope was performed to predict the modal frequencies. Similar procedure was implemented for the crab leg gyroscope design. The layout of the gyroscope is shown in Figure 3.20 indicating the basic feature dimension and a complete list is presented in Table 3.2. The suspension beam provide equal compliance in both lateral directions (modes). Due to the presence of several comb finger, the analysis requires a large computing power and time than the cantilever beam presented earlier.

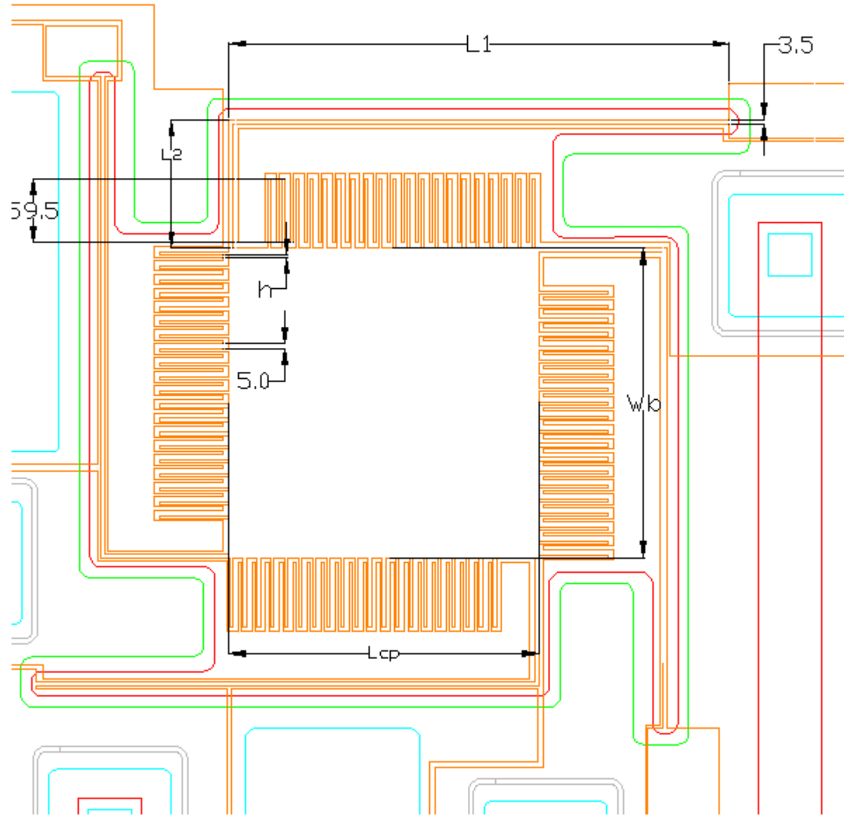


**Figure 3.20: Crab leg gyroscope design parameter**

**Table 3.2: Crab Leg Gyroscope Parameters (Device 2)**

| | Description | Value |
|---|---|---|
| $L_1$ | Beam length 1 | $468\ \mu m$ |
| $L_2$ | Beam length 2 | $120\ \mu m$ |
| $w_b$ | Beam width | $3.5\ \mu m$ |
| $t_b\ (t_p)$ | Beam thickness | $30\ \mu m$ |
| $h$ | Initial capacitor gap | $2\ \ \mu m$ |
| $L_{cp}$ | Microplate length | $290\ \mu m$ |
| $w_p$ | Microplate width | $290\ \mu m$ |
| M | Tip mass | $5.88 \times 10^{-6} g$ |

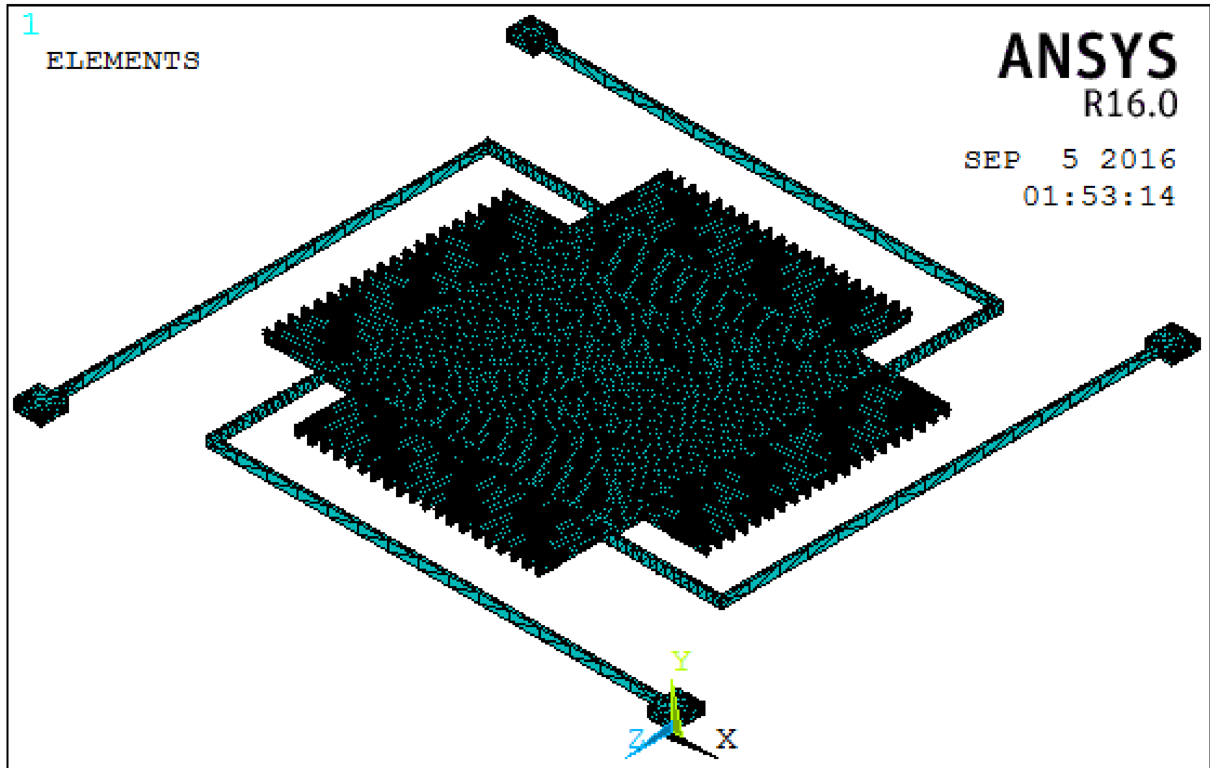


**Figure 3.21: Meshed crab leg gyroscope**

Shell elements were used for the microplate and a 3D tetrahedral solid elements were also used for the suspension beam. Figure 3.21 shows the 3D solid model mesh generated by ANSYS. The distribution of the structural deformations of the crab leg FEM simulations for an applied voltage of 15 V is shown in Figures 3.22. The maximum deflection occur at the microplate along with the comb figures with a displacement of approximately 28 n$m$.

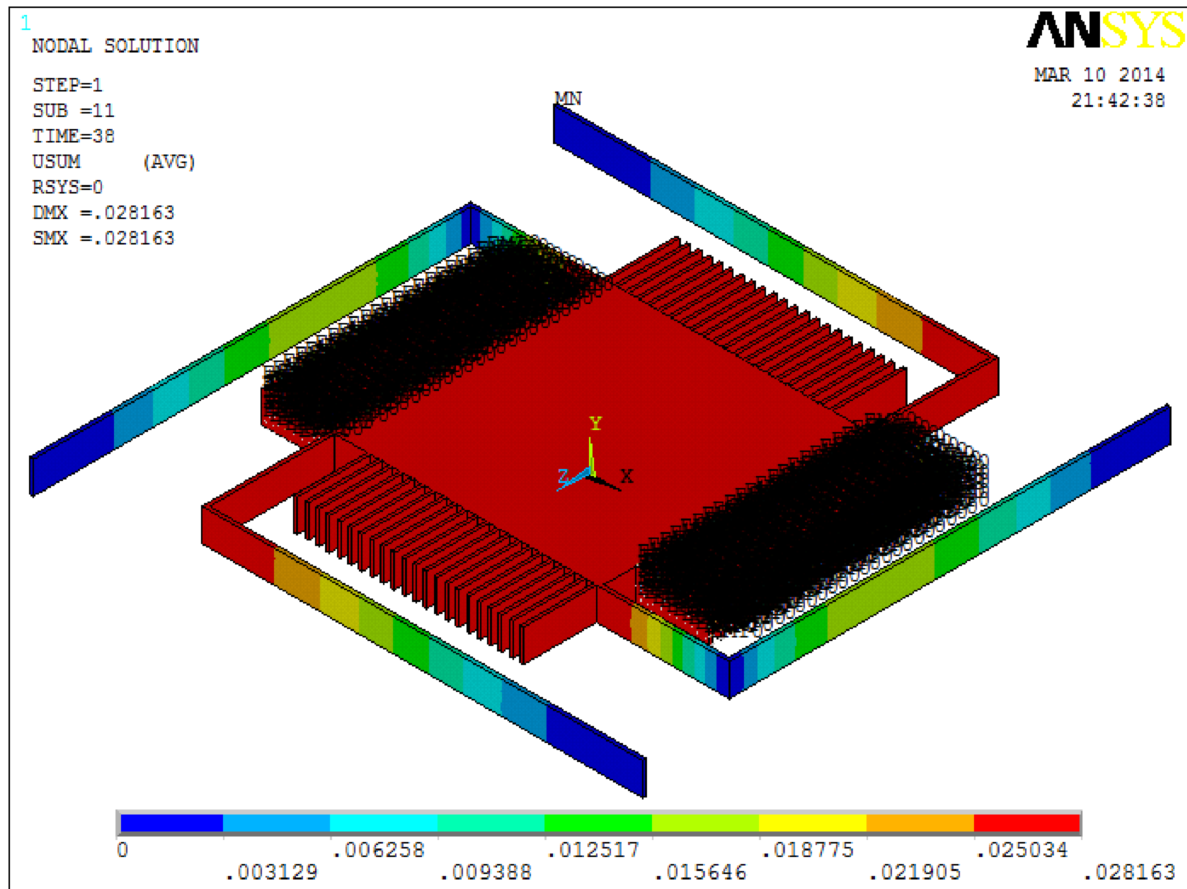


**Figure 3.22: Static deflection and deformed shape of the crab-leg gyroscope**

The modal solution is followed by mode extraction using similar procedure outline for the cantilever beam analysis. The primary drive and sense modes are 19.8 kHz and 20.1 kHz, respectively. The out of plan mode y axis has resonance that is only 2% higher than the z-axis sense mode. The z-axis (drive) and x-axis (sense) modes are designed to be 25% higher than the y-axis drive mode. The intent is that neither the z-sense mode nor the y-sense mode will be excited when the device operates at the x-axis drive resonance. The first three mode shapes are shown in Figure 3.23 through 3.25.

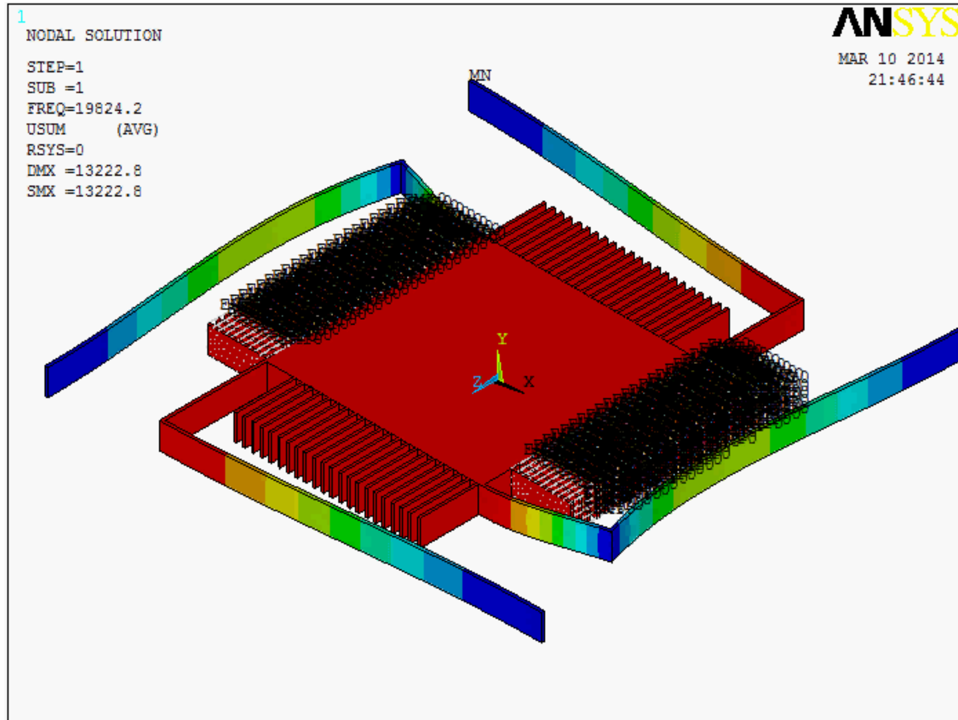


**Figure 3.23: The first mode shape of crab-leg gyroscope (z-axis)**

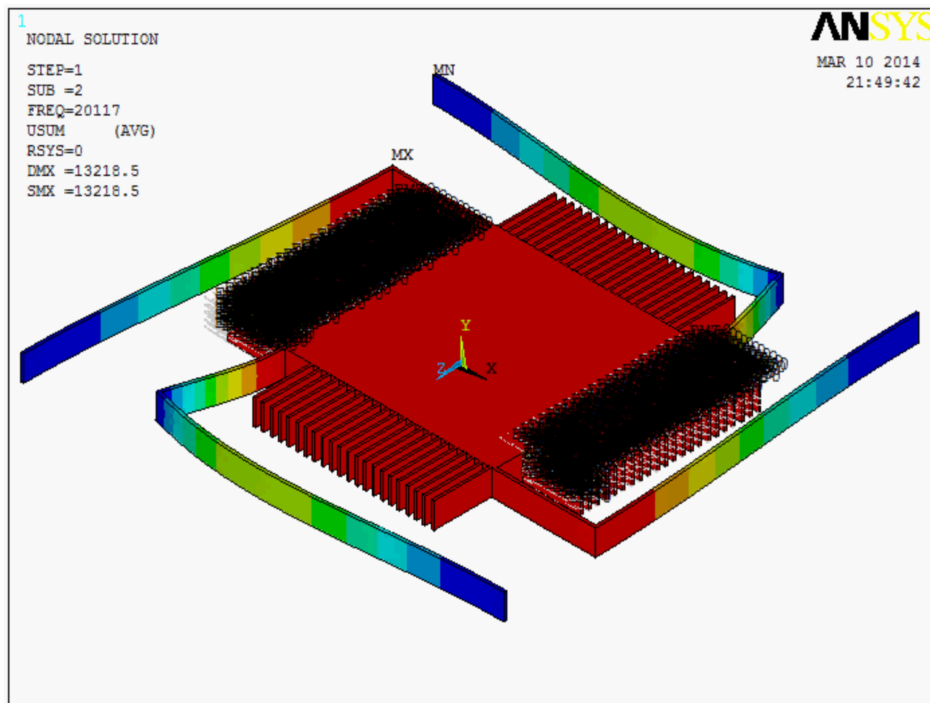


**Figure 3.24: The second mode shape of crab-leg gyroscope (x-axis)**

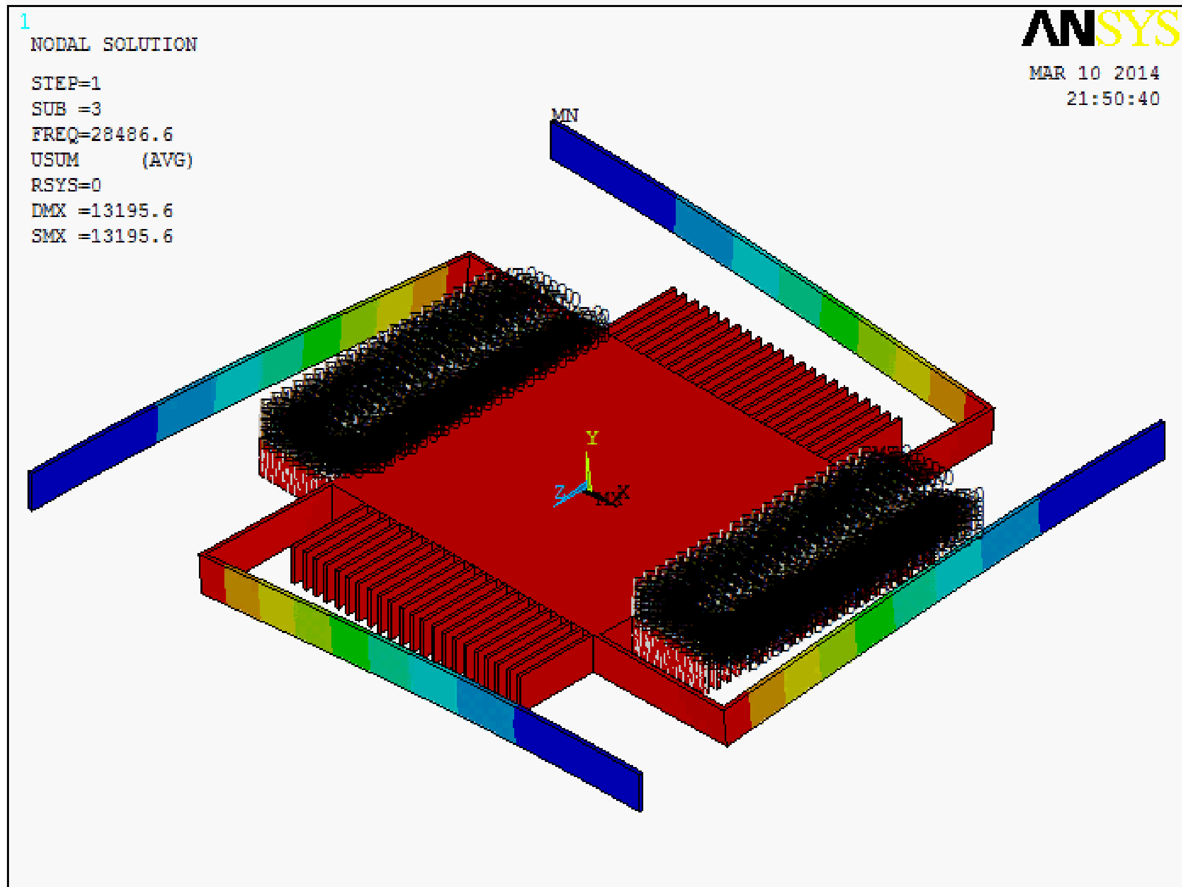


Figure 3.25: The third mode shape of crab-leg gyroscope (y-axis)

# CHAPTER IV

# Analysis of Thermal Noise in Frequency-Modulated Gyroscopes

Noise in MEMS gyroscopes can be introduced from electrical and mechanical sources. Mechanical noise is usually more significant and presented as Brownian motion and is analyzed extensively for AM modulated gyroscope. A MEMS gyroscope, the mass-spring-damper system is dissipative systems exhibits thermal noise. Thermal noise in MEMS gyroscopes arise due to molecular agitation inside beam springs, actuation and sense structures, suspended mass and the surrounding environment. The cantilever fluctuates with respect to the rest position due to the random impacts of the surrounding molecules. In the same way, the cantilever dissipates the stored mechanical energy through its interaction with the surrounding thermal bath. This relationship between the thermal forces and the dissipation of mechanical energy is described by the fluctuation-dissipation theorem, which is usually applied to determine the electrical noise across a resistor. Thermodynamics sets the ultimate sensitivity of beam springs based MEMS devices in general.

The fluctuation-dissipation theorem in statistical physics for predict the behavior of non-equilibrium thermo-dynamical systems. These systems involve the irreversible dissipation of energy into heat from their reversible thermal fluctuations at thermodynamic equilibrium. The fluctuation-dissipation theorem applies both to classical and quantum mechanical systems. The fluctuation-dissipation theorem relies on the assumption that the response of a system in thermodynamic equilibrium to a small applied force is the same as its response to a spontaneous fluctuation. Therefore, the theorem connects the linear response relaxation of a system from a prepared non-equilibrium state to its statistical fluctuation properties in equilibrium. Often the linear response takes the form of one or more exponential decays.

Previously research has been done on thermal noise for amplitude modulated MEMS gyroscope [28]. This chapter presents analysis of thermal noise for frequency modulation MEMS gyroscope. Hence, we investigate the effect of thermal noise on the natural frequency of the MEMS gyroscope since the rotation rate is measured by detecting the shift in the natural frequencies of two closely spaced global

vibration modes. We analyzed analytical expressions for the effect of thermal noise on the frequency modulation MEMS gyroscope and compare the output signals due to both the rotation rate and thermal noise.

## 4.1 Thermal Noise in MEMS Gyroscope

Temperature fluctuation generate noise in electrical or mechanical system. Commonly in large-scale sensors this kind of noise is usually neglected. However, as a device size reduced, thermal noises become significant and cause performance degradation [45]. Generally, MEMS gyroscopes are limited by electrical noise and systematic errors, but for such small mechanical structures and low values of displacement in the sensing direction, thermal noise should be considered as the theoretical sensitivity limiting factor. Mechanical thermal noise occurs due to vibrations of atoms in the materials from which a device is made and the environment in which the device operates.

There are three primary works that investigated the thermal noise properties of amplitude modulated MEMS gyroscope [51-52]. The first studied the effect of mechanical thermal fluctuations on a vibrating-mass surface-micromachined gyroscope [53]. It was found that the mechanical–thermal noise source represents a practical sensitivity limit in the gyroscope and is likely to restrict their performance [54].

In chapter two, we modeled the MEMS gyroscope as a 2-DOF spring-mass-damper. The mechanisms that couple these thermal vibrations to the mechanical of interest are the energy dissipation mechanisms. The interaction of molecules with flexible parts of the sensing elements immersed in a gaseous or a liquid medium can be described by the equation of a harmonic oscillator as follows

$$
\begin{aligned}
&m\left(\ddot{x} - y\dot{\Omega} - x\Omega^2 - 2\Omega\dot{y}\right) + (c+\delta)\dot{x} + (k+\varphi)x = F_{ext}(t) + F_{th}(t) \\
&m\left(\ddot{y} - x\dot{\Omega} - y\Omega^2 - 2\Omega\dot{x}\right) + c\dot{y} + ky = F_{th}(t)
\end{aligned}
\tag{4.1}
$$

where $F_{ext}(t)$ is the deterministic excitation force, $F_{th}(t)$ is the stochastic force excited from the surrounding molecules on the flexible part of the sensor, m is the mass, $c$ is the damping constant, and $k$ is the spring constant. $\delta$ and $\varphi$ are the variation of the damping and spring constant due to imperfection of micro-fabrication.

The magnitude of $F_{ext}(t)$ in the drive direction is sufficiently large enough to neglect the thermal noise effect in this direction. Therefore, our investigation focuses the thermal noise effect in the sense

direction. The natural frequencies of the system are defined as $\omega_n = \sqrt{\frac{k}{m}}$, and the damping ratio are $\zeta = \frac{c}{2\sqrt{mk}}$. Using these expressions, the equations of motion can be written as

$$\ddot{y} + 2\zeta\omega_n\dot{y} + (\omega_n^2 - \Omega^2)y - 2\Omega\dot{x} - x\dot{\Omega} = F_{th}(t) \tag{4.2}$$

Assuming that the mean of the stochastic force is zero, $F_{th}(t) = 0$ and no external force in the sense direction is applied, the mean velocity $\bar{v} = \frac{d\bar{x}}{dt}$ vanishes. On the other side, the instantaneous velocity $v(t) = \frac{dx}{dt}$ is not zero as the sensor is excited constantly by the surrounding molecules. The Brownian force is given by the following equation:

$$F_{th}(t) = \sqrt{4k_BT\zeta} \tag{4.3}$$

which causes Brownian motion of the harmonic oscillator $y_{th}$ and can be solved by combining Eq. (4.1) and [53]. Solving the Laplace domain results in

$$y_{th} = \frac{\sqrt{4k_BT\zeta}\,(\omega_n^2 m)}{\left(\frac{s}{\omega_n}\right)^2 + \frac{1}{Q}\frac{s}{\omega_n} + 1} \tag{4.4}$$

where $Q$ is the quality factor, $k_B$ is the Boltzmann constant, and $\omega_n$ is the natural resonance frequency. Recalculating the equivalent acceleration originating from the Brownian force gives the following equation:

$$a_{th} = \sqrt{\frac{4k_BT\omega_n}{mQ}} \tag{4.5}$$

Previous studies [53, 54] have shown that the minimum detectable force gradient for amplitude modulated gyroscope is given by According to

$$\delta F'_{min} = \sqrt{4k_L k_B TB/\omega_o Q\langle y_{th}^2\rangle} \quad (4.6)$$

where $(y_{th}^2)$ is the mean-square amplitude of the driven cantilever vibration, B is the measurement bandwidth, Q is the quality factor of the cantilever resonance, and $k_B$, T is the thermal energy at the ambient temperature.

Equation [4.6] shows that a high-quality factor (Q) and a huge mass are desirable to reduce the influence from the thermal noise. A huge mass can be achieved by bulk micromachining being carved out of a full wafer. Careful design and suspending the proof mass in vacuum further reduce the thermal noise by increasing the Q factor. However, with amplitude modulated gyroscope, increasing the quality factor (Q) restricts the bandwidth of the system. Therefore, there is always a trade-off between the bandwidth and the sensitivity of amplitude modulated gyroscope.

## 4.2 Thermal Noise in Frequency-Modulated Gyroscopes

The equipartition theorem states that energy is shared equally amongst all energetically accessible degrees of freedom of a system. Hence, the thermal energy in the cantilever results in cantilever motion described by [52]

$$\begin{aligned} \frac{1}{2}m\omega_o\langle x_{th}^2\rangle &= \frac{1}{2}k_B T \\ \frac{1}{2}m\omega_o\langle z_{th}^2\rangle &= \frac{1}{2}k_B T \end{aligned} \quad (4.7)$$

where $\langle x_{th}^2\rangle$ and $\langle z_{th}^2\rangle$ is the mean-square displacement of the end of the cantilever due to thermal excitation in the x and z-axis. The spectral noise density $N_{th}(\omega)$ and $\langle x_{th}^2\rangle$ are related by [50]

$$\langle x_{th}^2\rangle = \frac{1}{2\pi}\int_0^\infty N_{th}(\omega)d\omega \quad (4.8)$$

$$\langle z_{th}^2 \rangle = \frac{1}{2\pi}\int_0^\infty N_{th}(\omega)d\omega$$

and $N_{th}(\omega)$ can be further described by

$$N_{th}(\omega) = |G(\omega)|^2 \Psi_{th}(\omega) \tag{4.9}$$

where $|G(\omega)|^2$ is the response function of the cantilever (damped harmonic oscillator) given by

$$|G(\omega)|^2 = \frac{1/m^2}{(\omega_0^2 - \omega^2)^2 + (\omega_0\omega/Q)^2} \tag{4.10}$$

and $\Psi_{th}(\omega)$is the thermal white noise drive given by

$$\Psi_{th}(\omega) = 4m\omega_0 k_B T/Q \tag{4.11}$$

If we ignore noise components with a modulation frequency on the order of the oscillator linewidth and less, we may write an approximate expression for the spectral noise density $N^{th}$ in each sideband in terms of the modulation frequency as follows:

$$N_{th}(\omega_{mod}) = \mathrm{K}_B T/m\omega_o Q{\omega_{mod}}^2 \tag{4.12}$$

The phase noise energy is given by $N_{op}(\omega_{mod})$ $=k_l N_{th}(\omega_{mod})/2)$ and the mean-square frequency modulation due to this noise source is given by

$$\langle(\delta\omega_{\mathrm{d}})^2\rangle = \int_{\omega_{mod}} \frac{2E_p(\omega_{mod})}{E_C} f_{mod}^2 df_{mod} \tag{4.13}$$

This is in case where it is necessary to calculate the effective frequency deviation over some finite baseband bandwidth say

where $\delta f$ is the mean-square frequency modulation due to this noise source C, is the oscillator energy (carrier power) given by C = $E_C$ = $k_l x_{osc}^2$) over the bandwidth of measurement

Integrating Eq. (12) over the bandwidth of measurement, the minimum detectable frequency shift of a cantilever beam oscillator incorporated in a self-oscillating system with positive feedback has been estimated.

$$\delta\omega_{\mathrm{s}} = \sqrt{\frac{\omega_{\mathrm{s}_\Omega} k_B T B}{kQ\langle x_{osc}^2 \rangle}}$$
$$\delta\omega_{\mathrm{d}} = \sqrt{\frac{\omega_{\mathrm{d}_\Omega} k_B T B}{kQ\langle z_{osc}^2 \rangle}} \tag{4.14}$$

As presented in chapter two, we can determine input angular rate by taking the difference between the two natural frequencies i.e $\omega_{\mathrm{d}_\Omega} - \omega_{\mathrm{s}_\Omega} = 2\Omega$.. Since similar design parameter were used for the drive and sense direction, the two mode will have the same shift in resonance frequency due to thermal effect. The thermally induced change in resonance frequency therefore cancel each other with not output effect on the output reading. Therefore, the frequency modulated detection method allows the sensitivity to be increased by using a very high Q without sacrificing bandwidth or dynamic range. With very low damping, noise in the amplitude modulated can play a significant role in reducing system sensitivity.

## 4.2 Analysis of Stability and Device Performance of the Cantilever Gyroscopes

Two main parameters representing the performance of MEMS gyroscope is the angle random walk and the bias instability. These two parameters can be obtained by the Allan variance method or by power spectral density. In the following section, the Allan variance method describe for ARW and bias stability analysis.

### 4.2.1 Allan variance

Allan variance is a statistical measurement used to characterize and identify noise related error sources and their contribution to the overall noise statistics. It is defined as one half of the time average of the squares of the differences between successive readings of the frequency deviation sampled over a given sampling period. This is a time-domain analysis method of the stochastic process of the sensor measurements which investigates the errors as a function of averaging times. Allan variance analysis is

always performed for zero input to the sensor. In this situation, any sensor output is due to noise arising from the sensor. Allan variance analysis of a time domain signal Ω (t) consists of computing its root Allan variance for different integration time constants τ and then analyzing the characteristic regions and log-log scale slopes of the $\sigma(\tau)$ curve to identify different noise modes, i.e., random components of the signal with different autocorrelation power laws [6].

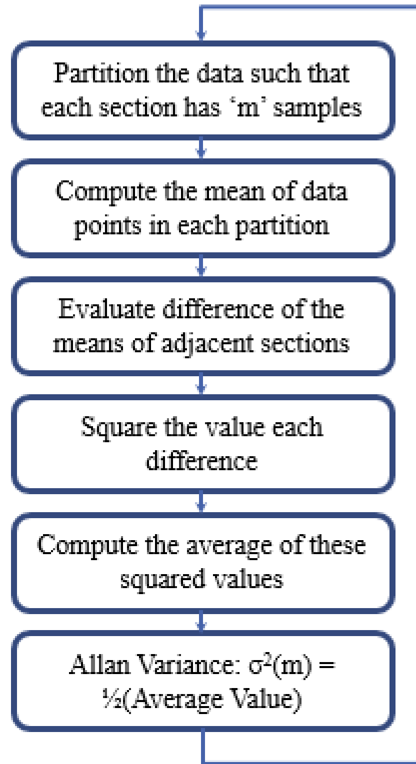


**Figure 4.1: Allan Variance flow chart**

The first step of Allan variance analysis is to acquire a time history Ω (t) of the gyroscope's output using an experimental setup. The measurement is performed in a stable climate without exciting the system. Assume that $\Omega_{1:k} = \{\Omega_k\}_1^k$ is a dataset of K consecutive measurements recorded with sample time T. Averaging over clusters of n samples, with a cluster time $\tau$ = nT, we obtain

$$\bar{\Omega}_{1:L}(n) = \{\bar{\Omega}_l\}_{l=1}^{k}, \tag{4.15}$$

The Allan variance for cluster time $\tau$ = nT is now defined as

$$\sigma^2(\tau) = \frac{1}{2}\langle(\bar{\Omega}_{\mathrm{k+m}} - \bar{\Omega}_k)^2\rangle \tag{4.16}$$

The Allan variance can be related to the power spectral density $S_X(f)$ of the measurements y using [6]

$$\sigma^2(\tau) = 4\int_0^{\infty} \frac{\sin^4(\pi f\tau)}{(\pi f\tau)^2} S_X(f)df \tag{4.17}$$

Hence, the Allan variance can be interpreted as the energy of the spectral density passed through a filter. The bandwidth of the filter depends on the cluster time Tc. The Allan variance can therefore be used to identify various noise sources present in the measurements. Typically it is presented as the Allan standard deviation (Tc) versus cluster time Tc in a log–log plot, as shown in Figure 4.2.

$$\sigma^2(\tau) = \frac{1}{2}\langle(\bar{\Omega}_{\mathrm{k+m}} - \bar{\Omega}_k)^2\rangle \tag{4.18}$$

The Allan variance is an easy tool to study and compare the noise characteristics of inertial sensors. However, it does not consider factors such as linearity, temperature stability and other calibration parameters related to dynamic accuracy. These effects are also very relevant for sensor quality and price. Therefore, the Allan variance should never be relied on exclusively when deciding which sensor to use in an application.

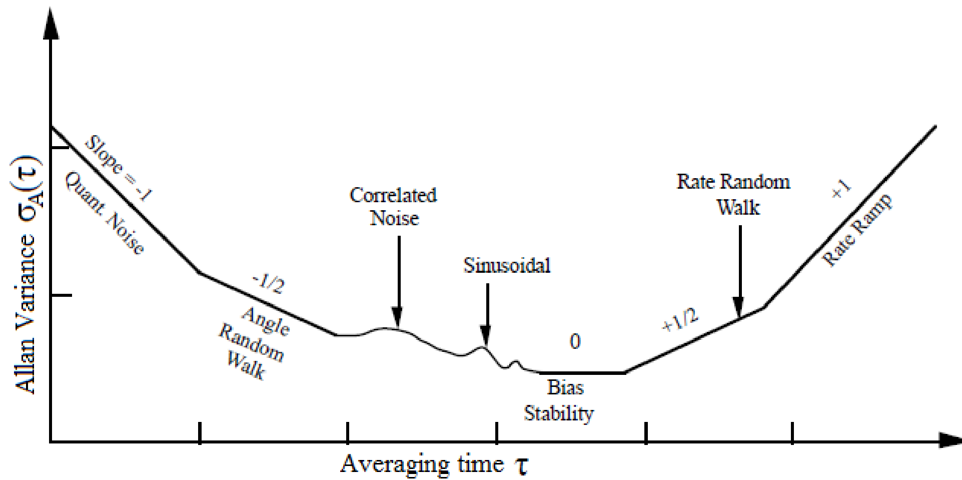


**Figure 4.2: Sample Plot of Allan Variance Analysis Results [5]**

# CHAPTER V

# Prototypes Fabrication and Device Characterization

A cantilever and crab-leg MEMS gyroscopes prototype was fabricated to experimentally investigate the presented hypothesis. During the course of this Ph.D. two fabrication platform were used to fabricate the prototype MEMS gyroscope, viz. SOIMUMPS and Teledyne Dalsa MEMS Integrated Design for Inertial Sensors (MIDIS™) process. SOIMUMPS prototypes primary used to study the mechanical characteristics of the device. In this chapter a brief description of the MIDIS™ process, characterization method and the test results for the prototype MEMS gyroscopes fabricated are covered. The MIDIS™ process is used to fabricate both the cantilever beam and the crab-leg designs. The Process distinctively capable of creating a fixed electrode underneath the cantilever beam microplate as well as the sidewalls electrode.

The overall die sizes of the fabricated gyroscope chips are 4.0 mm x 4.0 mm that enables us to put fourteen (14) different designs for both cantilever beam and crab leg gyroscope. The entire MEMS gyroscope structure is made of a single crystal silicon wafer which is good to avoid problems caused by thermal mismatch of materials. The bulk silicon device layer also allows for thicker MEMS structures (30µm) which provides inherently better noise and sensitivity due to larger masses, larger capacitances and higher frequencies operation.

As partially illustrated in Figure 5.1, there are several layers of material employed in MIDIS™ process, however the only design variation affecting the resonant frequency of the different design is the structural layer including the gyroscope length, width and suspended mass plate dimensions. This variations in the dimensions of the cantilever and crab leg design intended to allow for different natural frequency operation range that should result in different device sensitivities. Appendix G provide summary of different design parameters and device characterization results. A resonant frequency in the

range between 38 kHz to 45 kHz designed for the cantilever beam gyroscope. The cantilever beam MEMS gyroscope design uses side wall as well as a bottom parallel plate electrode to drive and sustained oscillation and to sense the Coriolis oscillation. In Figure 5.1 different colors are used for the structural layer for visibility of the different structural parts.

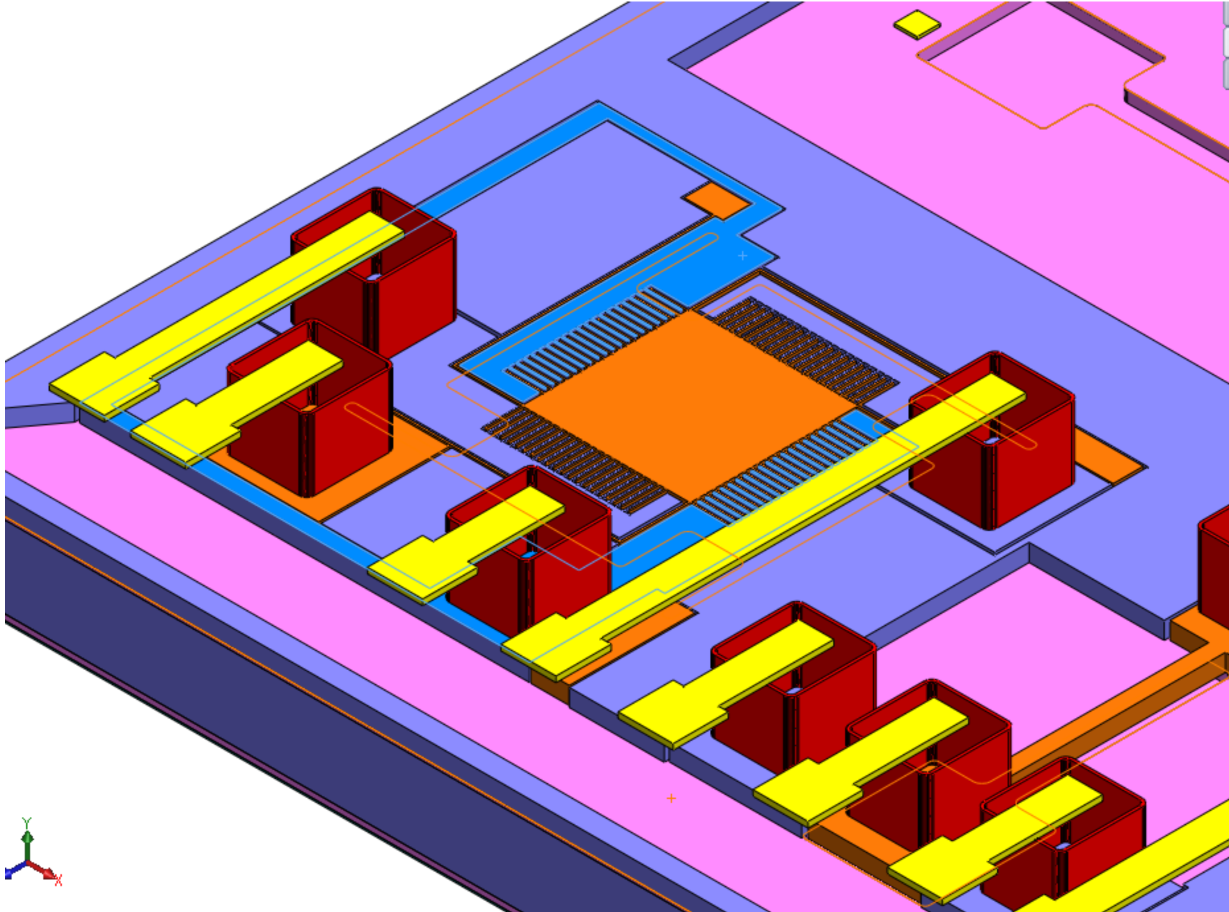

**Figure 5.1: A 3D model of the structure of the cantilever beam element**

For the crab leg design a comb drive and sensing electrode constructed from an array of two side by side beams. Figures 5.2 represent the structure of the drive and sense electrode and other features for the cantilever and crab leg design.

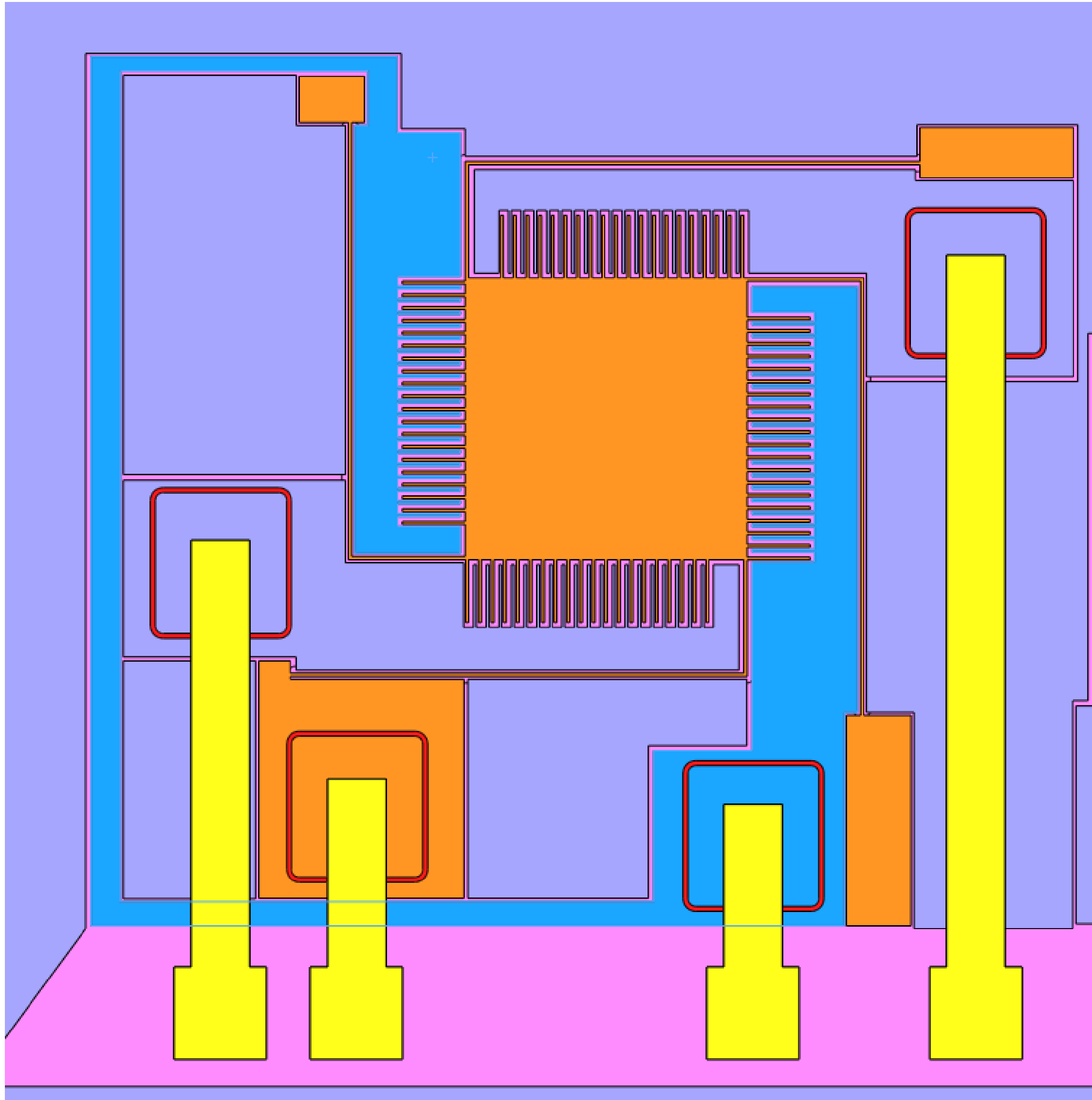

**Figure 5.2: A comb finger electrode and other structural parts for the crab leg beam element**

## 5.1 Prototypes Fabrication MIDIS™ Process

Teledyne Dalsa MIDIS™ platform is mixed micromachining process for manufacturing inertial sensors which is capable of integrating the MEMS device with CMOS. In this process, major micromachining techniques includes surface and bulk machining, Through Silicon Via (TSV) with metal plugs (ISDP), anhydrous HF Release, thick polymers, and wafer bonding. The MIDIS™ platform also provides wafer level packaging with high-vacuum sealing that allows a high quality factor (Q) for the MEMS inertial sensors. The process makes use of three starting silicon substrates that includes Handle, Membrane, and TSV as shown in Figure 5.3.

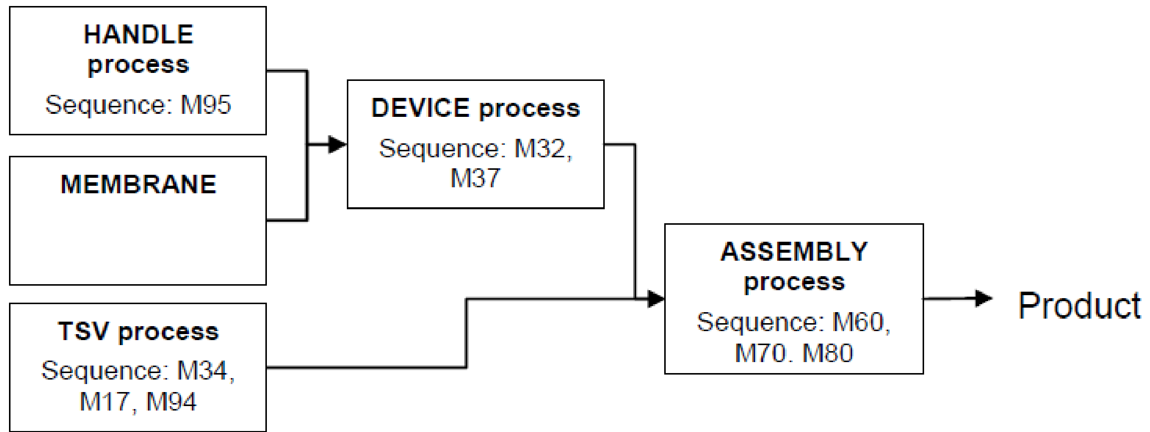


**Figure 5.3: Substrates assembly process**

The overall fabrication process requires twelve (12) masks as listed in Table 6.1. The design rule imposes a number of constraints which is not discussed here.

**Table 5.1: Design Mask Summary**

| **Design layer description** | **Mask number** | **Functional description** |
|---|---|---|
| CELLBND | NA | Design support layer (used for data generation during mask data preparation) indicating the intended die dimensions. This layer must be used in all submitted top cells. |
| BOTTOM DEEP CAVITY | 95 | Used to define deep cavity bellow STRUCT of the HANDLE wafer. |
| STRUCTURE | 32 | Used to define areas for the sensing STRUCT on front side of the Device wafer. |
| BUMPER | 32 | Used to define lateral stoppers/SBUMPs for mobile STRUCTs. |
| COMB TOP RECESS | 37 | Combs teeth to be thinned on the front side of the DEVICE wafer. |
| CAVITY SEAL | 34 | Used to define bonding plan area between of the TSV and MEMBRANE wafers dedicated to define volume of same pressure. |

| CONDUCTIVE ANCHOR | 34 | Used to define bonding plan areas dedicated to STRUCT features anchoring and electrical connectivity between of the TSV and MEMBRANE wafers. |
|---|---|---|
| ISOLATION TRENCH | 17 | Used to define trenches and equipotential areas in the TSV wafer. |
| TOP_CAVITY | 94 | Used to define regions for top cavity of the TSV wafer. |
| CONTACTS | 60 | Used to define CONT (though the Isolation Oxide) on the ASSEMBLY wafer. |
| METAL | 70 | Used to define bond pad STRUCTs and routing on the ASSEMBLY wafer. May be used for die labelling. |
| PADS | 80 | Used to define bond pad openings through passivation layers on the ASSEMBLY wafer. |

The major fabrication process steps are summarized below and further information provided in Appendix F.

1. The handle substrate (wafer) is machined using deep reactive ion etching (DRIE) process to form the bottom cavity for both cantilever and crab-leg gyroscopes.
2. The device structural (membrane) layer is bonded on the handle substrate.
3. The membrane wafer is used to create the structural parts over the bottom deep cavity after bonding and grinding.
4. Device wafer is formed by wafer bonding of handle to membrane and then machined to form sensing structure of the MEMS gyroscope.
5. Additional process is used to create deep recess and other features on one side before the device bonding to TSV substrate.
6. TSV is micro-machined to form a standoff between the MEMS structural part and the top cavity.
7. Assembly wafer is formed by wafer bonding of the TSV wafer to Device wafer.
8. The front side of the Assembly wafer is then processed to define various functions (contacts, metal routing, and bond pads).
9. Once bonded, the device and TSV wafer bonded, they form the assembly substrate which goes through the final processing steps.

Figure 5.4 to 5.12 illustrate an overview of the major process steps.

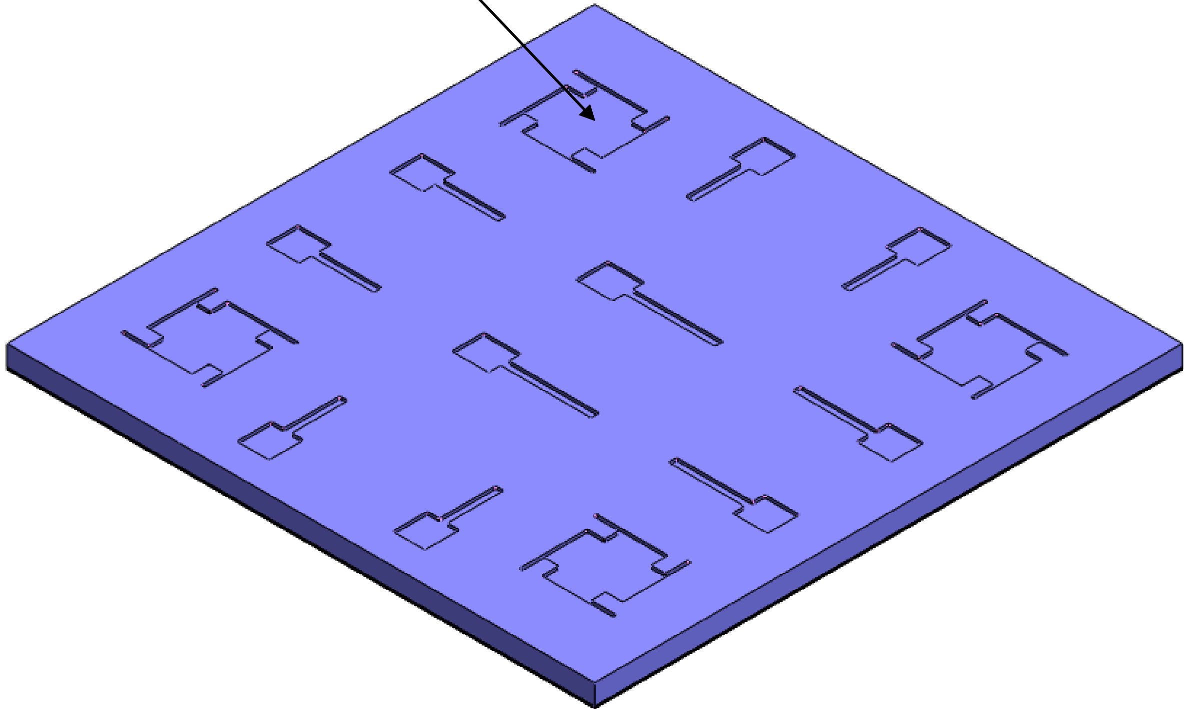


**Figure 5.4: Handle wafer patterning to a depth of 20µm using mask 95 cavity**

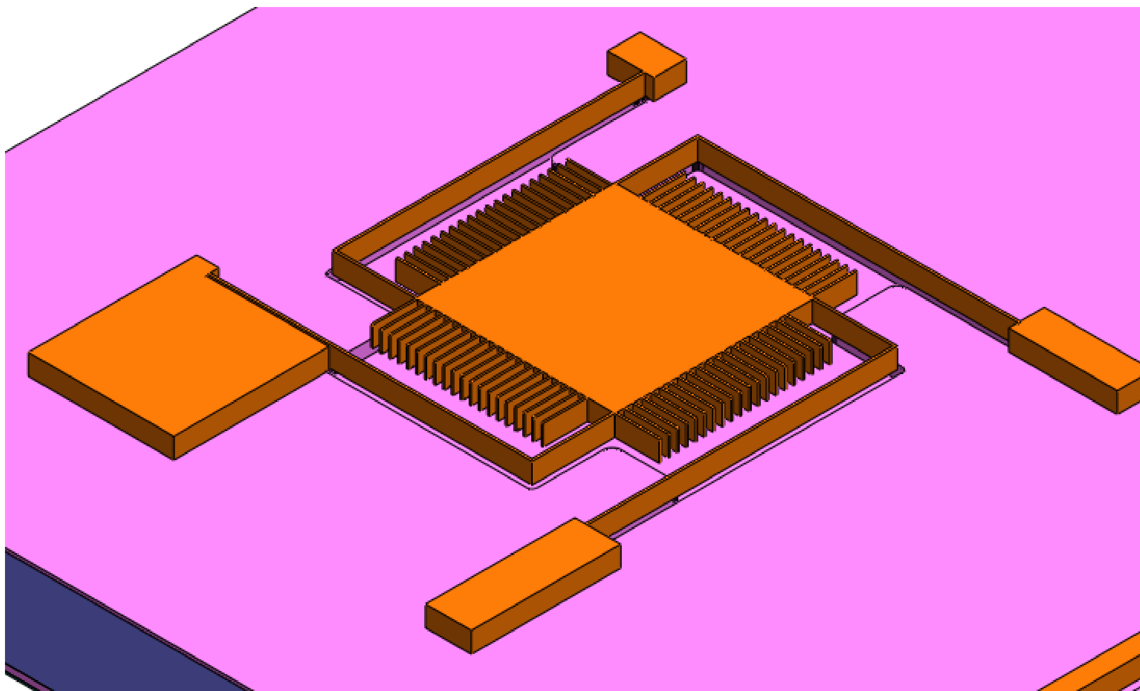

**Figure 5.5: Device layer is patterned using a combination of mask 32 and 37**

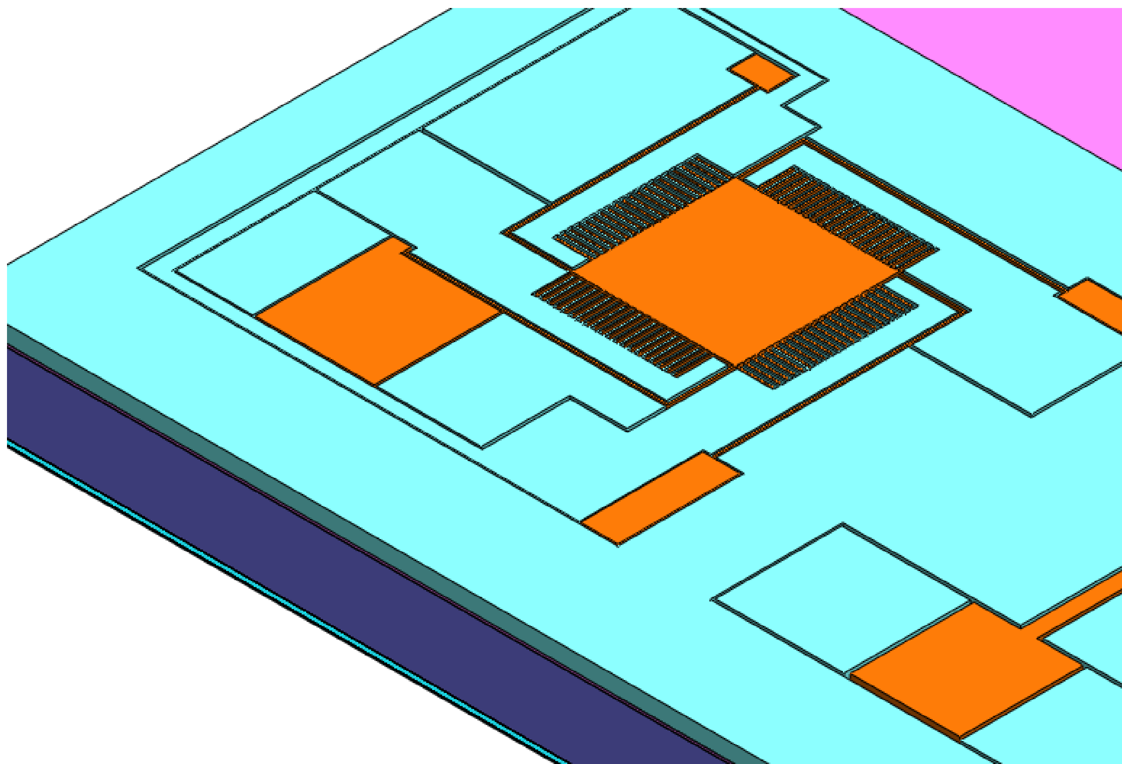

**Figure 5.6: crab-leg sense and drive electrodes defined using mask 32 and 37**

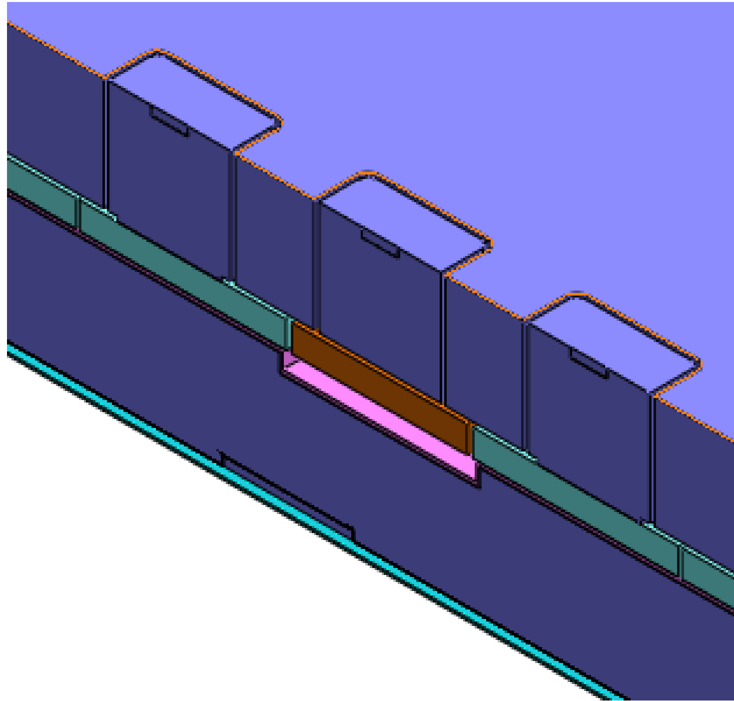

**Figure 5.7: Second bonding plane definition using mask 34 to creates a 2μm deep spacer between device TSV wafers**

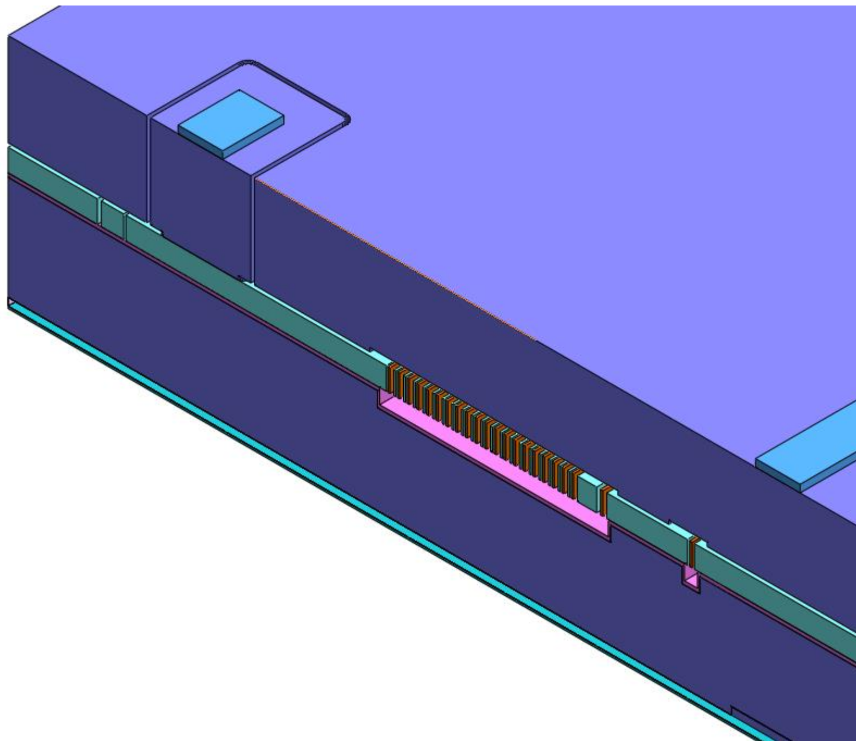

**Figure 5.8: Second bonding plane definition using mask 34**

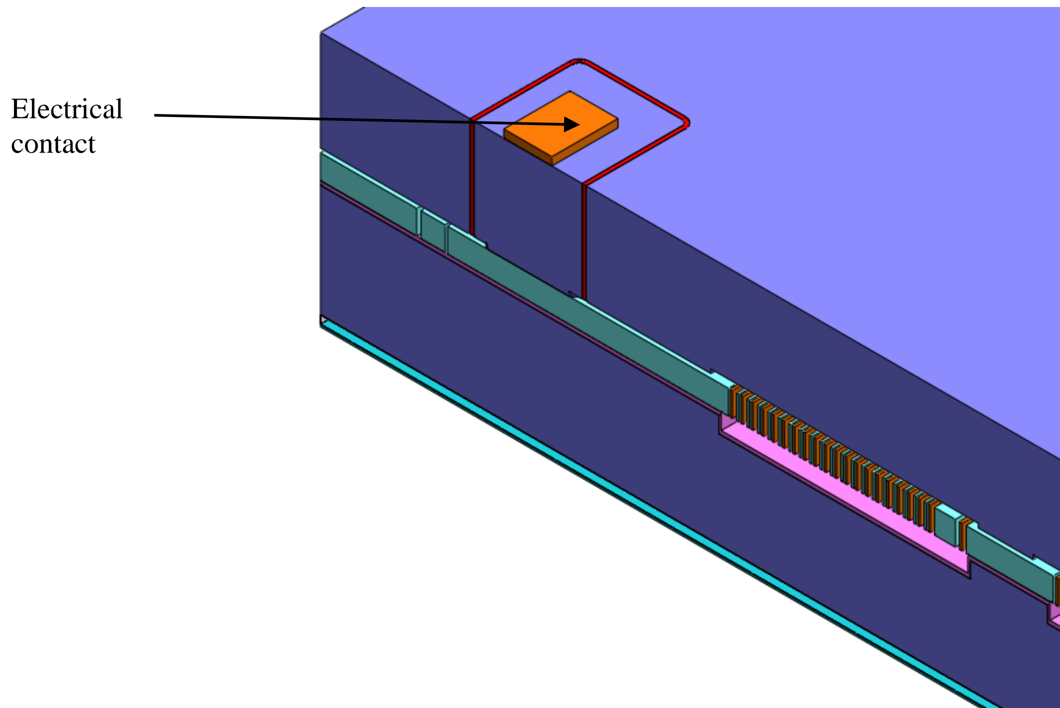


**Figure 5.9: Cross-section view of final stack**

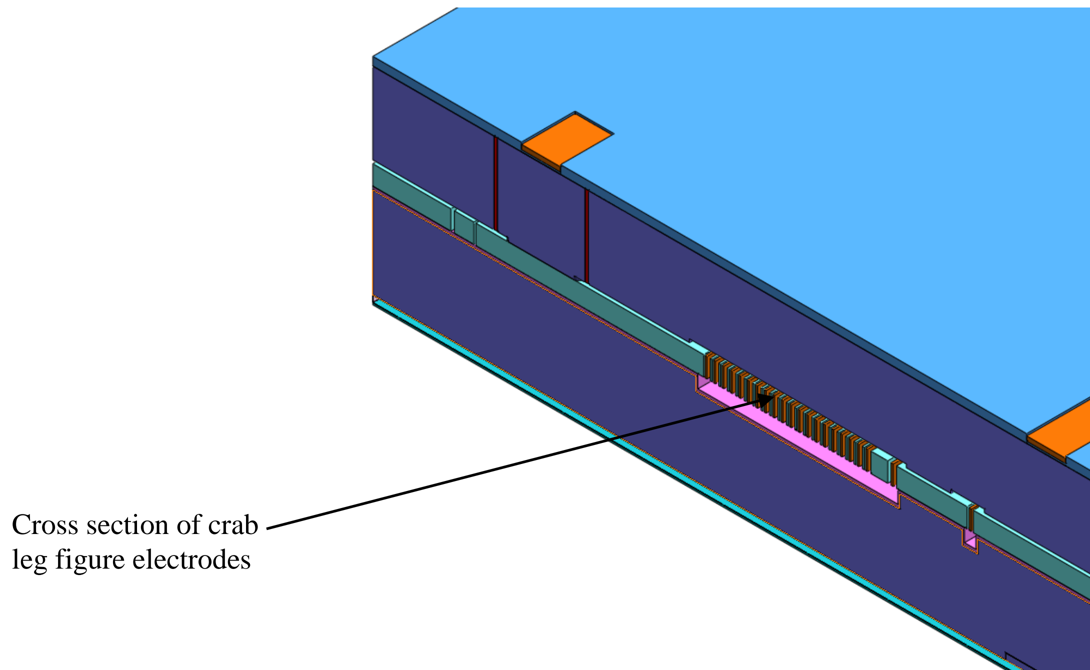


.

**Figure 5.10: Second bonding plane definition using mask 34**

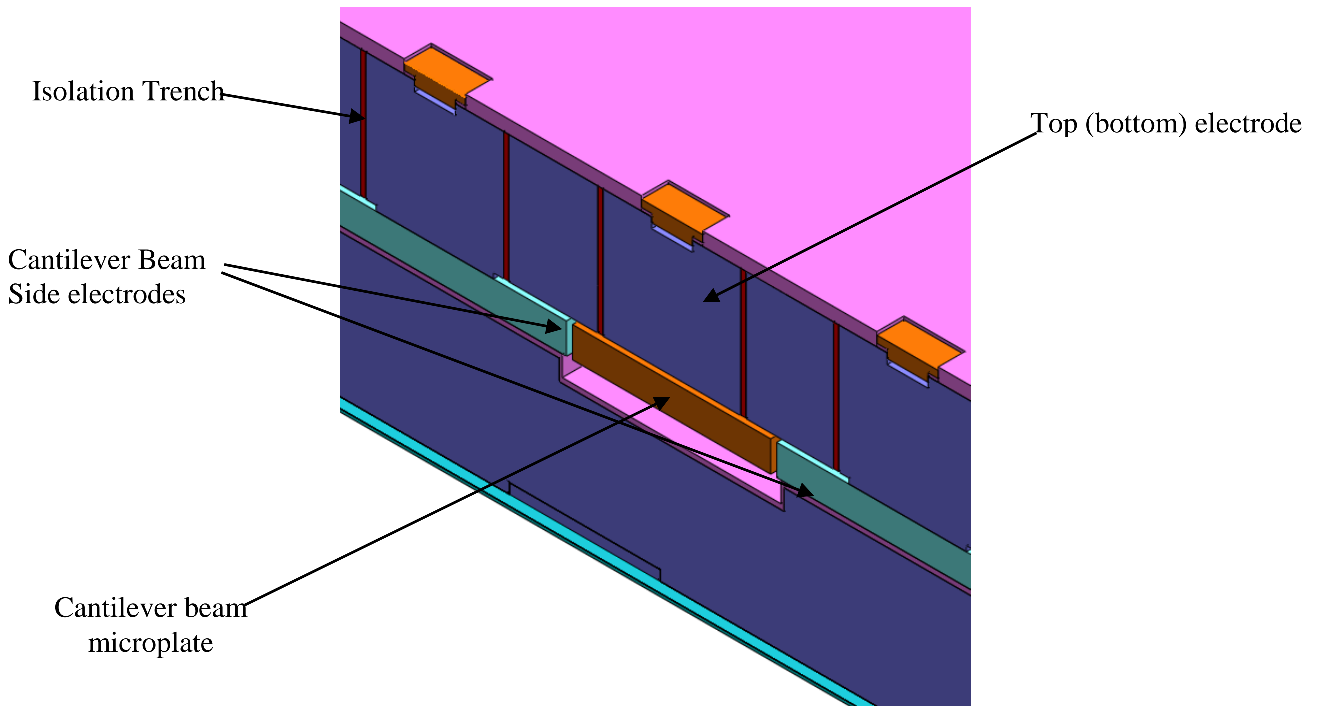


**Figure 5.11: Second bonding plane definition using mask 34**

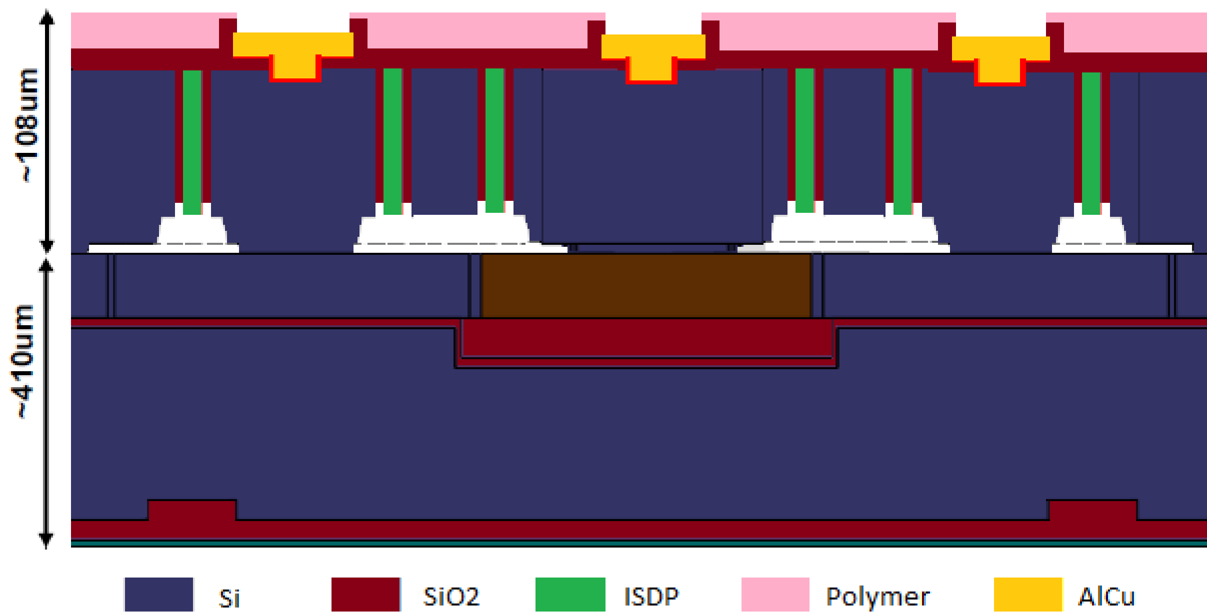


**Figure 5.12: Process cross-section with substrates and masks identification**

The final assembled model cross section for the cantilever beam is provided in Figure 5.12. After fabrication and dicing, the devices were attached to a ceramic DIP-48 package and wire bonded.

Figure 5.xx shown the Elec the cantilever and crab-leg structures after using mask 32 and 37 as illustrated in Figure 5.6:

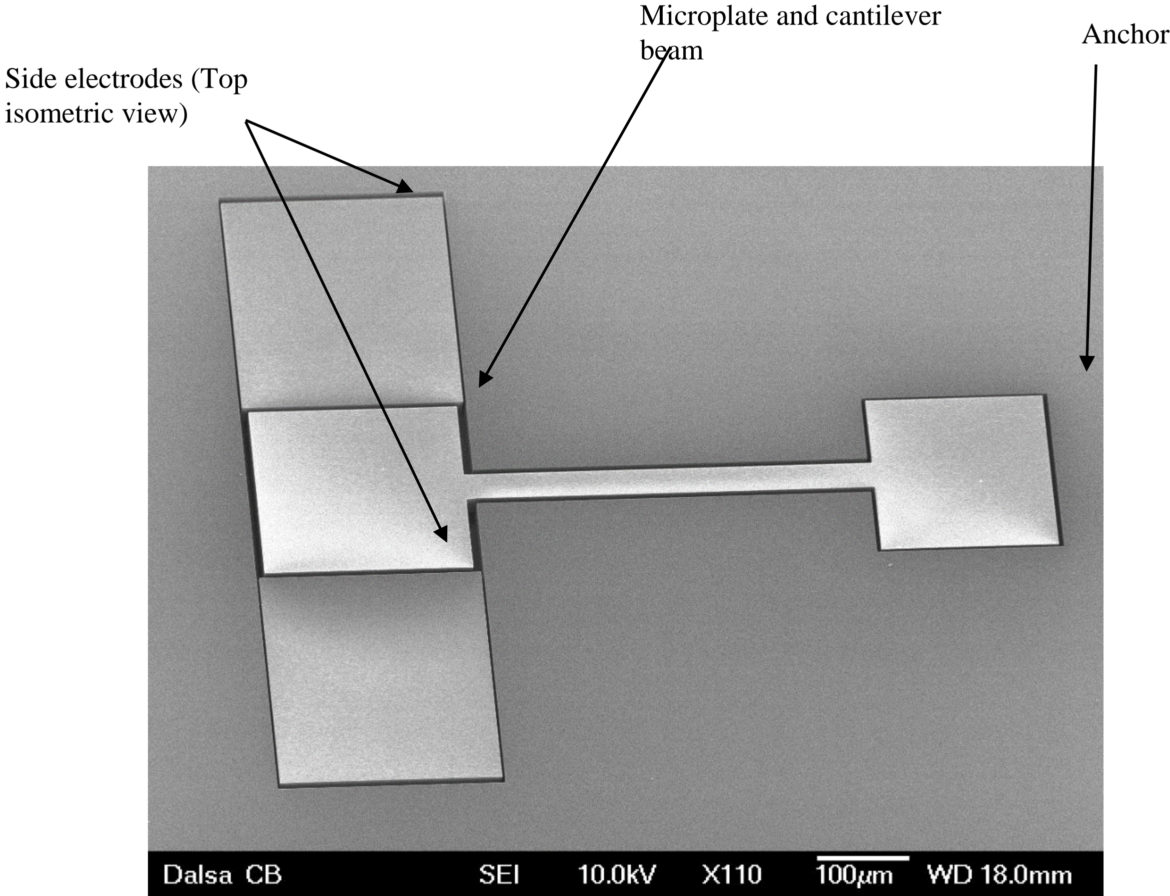


**Figure 5.13: SEM image for Cantilieiver 1 MEMS gyroscope structure (Handle and TSV wafer not shown)**

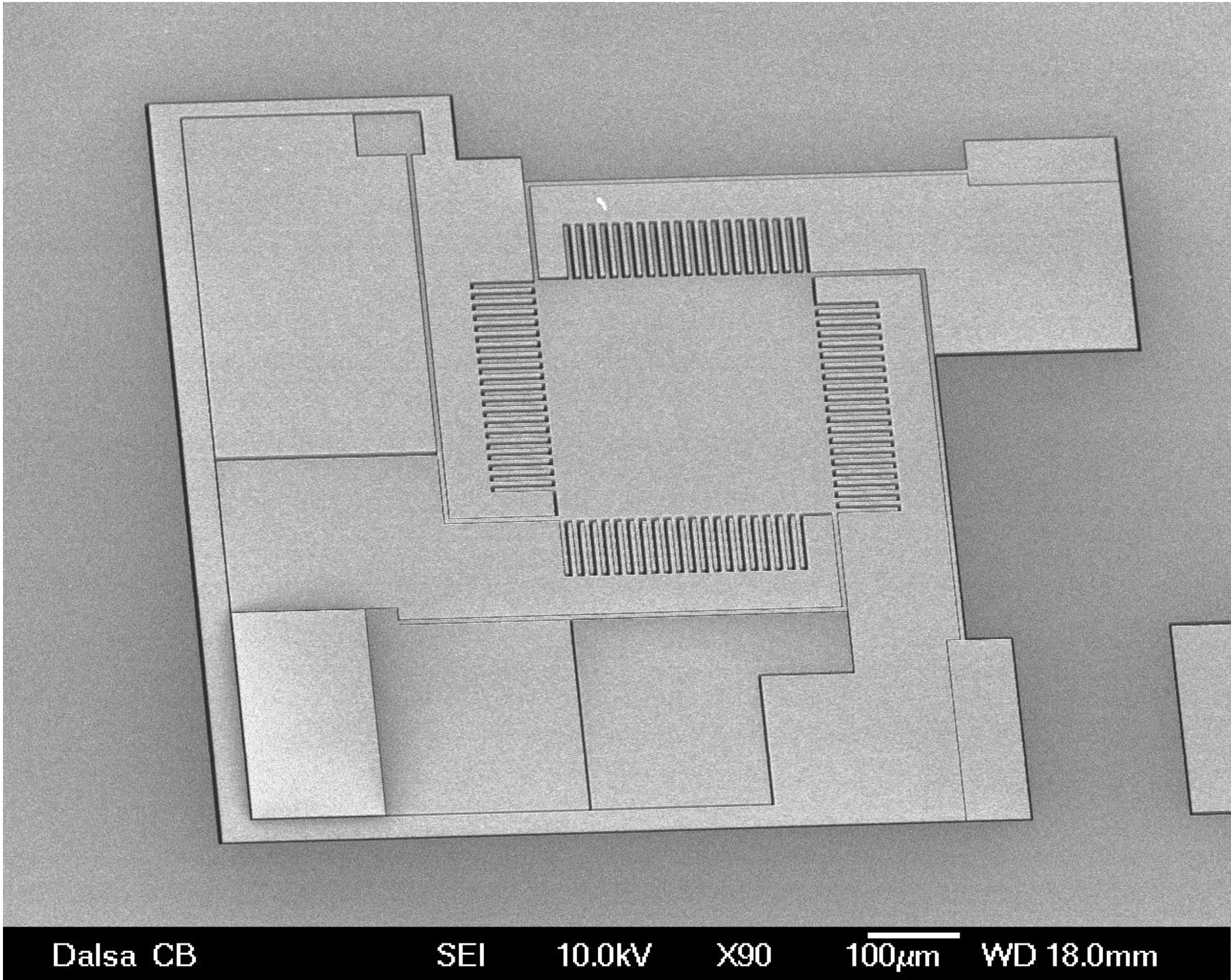


**Figure 5.14: SEM image for crab-leg MEMS gyroscope structure (Handle and TSV wafer not shown)**

Figure 5.15 shows a picture of one of the wire bonded gyroscopes chip. The chip carrier is further assembled onto a breadboard, where it is combined with sensor electronics with readout to the lock in amplifier.

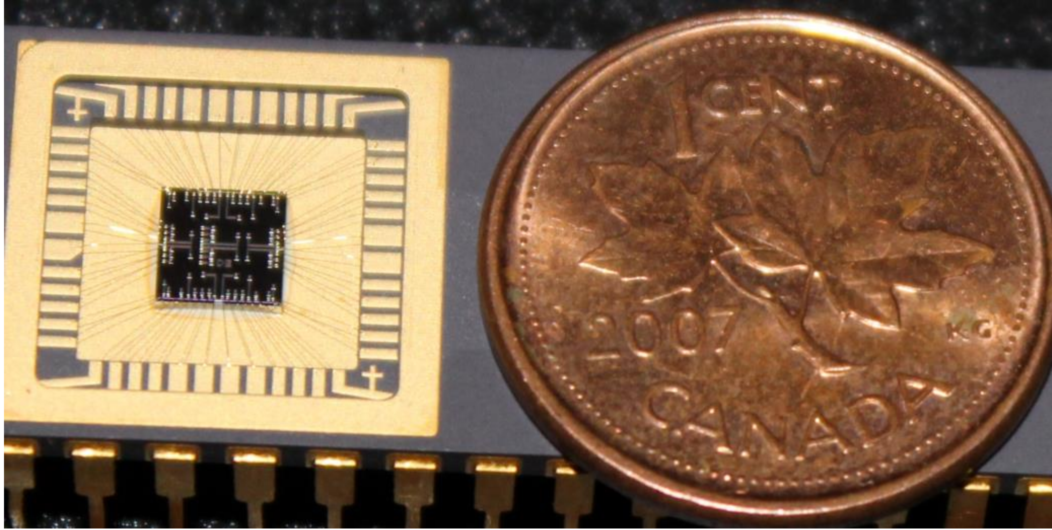


**Figure 5.15: Photograph of vacuum packaged test chip along with a 1 cent coin**

## 5.2 Experimental Characterization

Experimental characterization and testing for the prototype cantilever beam and crab leg MEMS gyroscopes includes resonant frequencies, quality factors, zero-rate output drift, and resonant frequencies relation of the first two modes, the Coriolis signal in responses to rotation, and temperature dependence of the resonance frequency. In order to verify the feasibility of the frequency modulated technique, some relevant dynamic frequency measurement methods are investigated and implemented. In all the investigated technique, the motional current is amplified and converted into a voltage signal by transimpedance amplifiers with a feedback resistor along with a lock in amplifier in sine sweep mode. Based on this approach, three different characterization setup were developed and employed to extract device characterization. Figure 5.14 illustrate the customized transimpedance amplifier implementation.

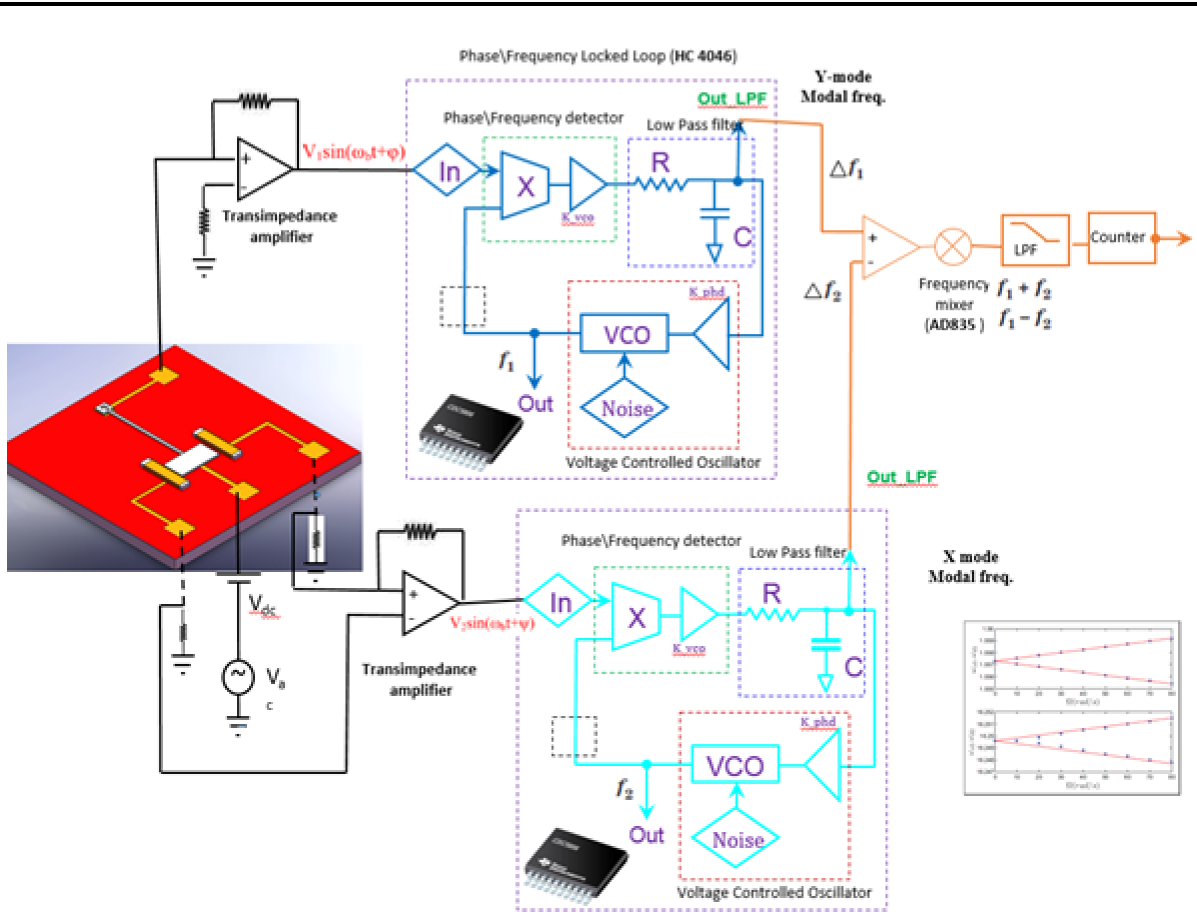


**Figure 5.16: Sensing circuit to detect the frequency difference between driving and sensing side resonance**

Parasitic capacitances and electromagnetic interference suppression approached were adapted at various level of the test to obtain correct results. The different characterization approach implemented during the course of this study provided very close results but we obtained the most stable results using the HF2TA current amplifier along with the HF2LI lock in amplifier to measure the spectrum of current fluctuations induced by excited vibrations of the MEMS gyroscope. The basic gyroscope drive-mode amplitude and frequency control is performed by using the HF2LI lock amplifier in-built phase locked loops (PLL) and automatic gain control (AGC). A PLL consists of three components: a phase detector, a VCO and a Loop Filter. The phase of the input and output signals is compared and the difference is converted to a voltage input to a voltage-controlled oscillator whose frequency tracks the input voltage.

### 5.2.1 Single port Actuation and Detection

The single port excitation and detection technique discussed in chapter 2 is implemented to characterize the natural frequency, quality factor and rate table test of the prototype devices. Hence, the frequency response measurement is performed for the drive and sense modes by electrostatically exciting the system with a sine wave in frequency sweep mode, and capacitive detecting the response simultaneously using a single port. Swept frequency gain phase analysis was performed using a lock in amplifier which sweeps the source frequency and records both the amplitude and phase of the received signal. The excitation and detection are both performed through the electrodes patterned on the structural and TSV wafers. Figure 5.15 and 5.16 show illustration of the characterization setup and pictures of the experimental setup for measuring the frequency response.

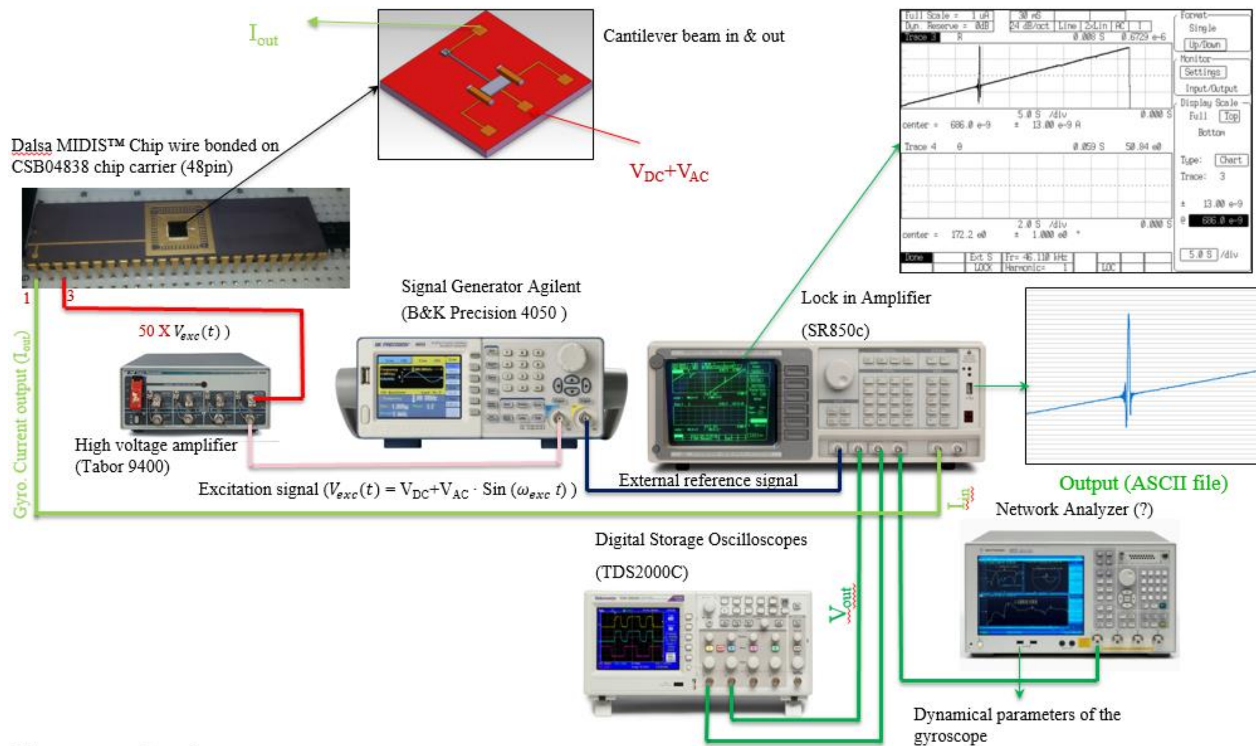


**Figure 5.17: Illustration of the device characterization setup**

First characterization was performed to determine the natural frequency for all prototypes developed. The designed natural frequency values together with the actual device character provide a reference value where we measure the frequency fluctuation to relate with the input angular rate. The test results also provide an insight about the process variations and the quality factor of the resonator.

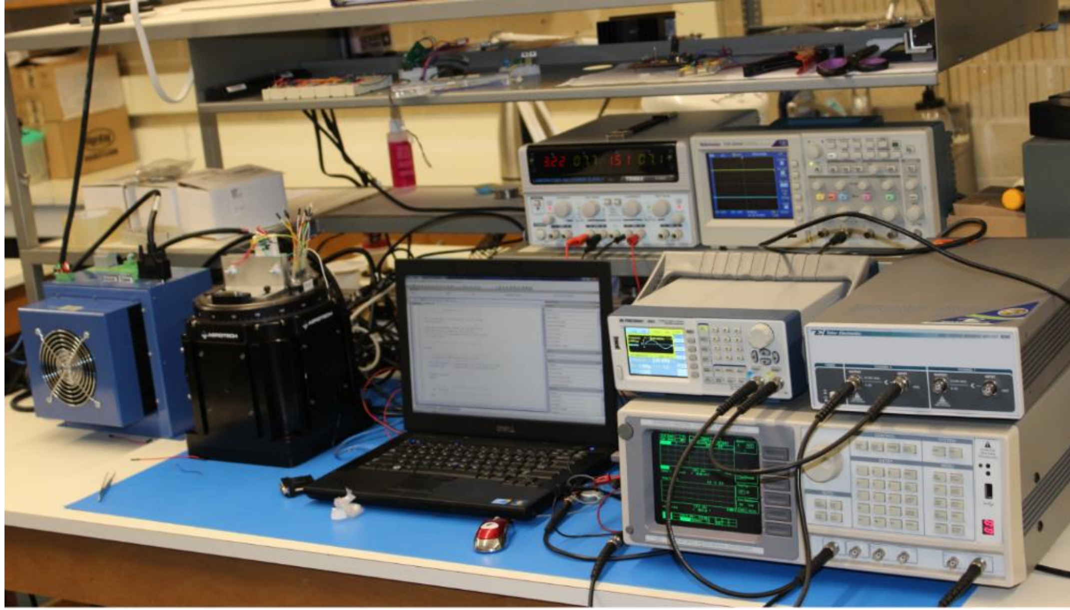

**Figure 5.18: The experimental setup for device characterization using SR850c lock amplifier**

In next sections we primarily reported result for the cantilever 1 (device 1) and crab leg 2 (device 2). First, for the cantilever design 1, the proof mass is driven in the direction perpendicular to the surface of the substrate using the bottom electrode and then the electrical gain of the mechanism is extracted by the transimpedance amplifier and HF2LI lock in amplifier. The HF2LI lock in amplifier has sufficient sensitivity to measure a frequency shift of 0.001 Hz up to 100 kHz. By means of electrostatically to drive the MEMS gyroscope, a combination of AC and DC voltage as well as by pure AC excitation signal without DC bias at an half of its mechanical resonance, $\omega_{ex} = \frac{1}{2}\omega_o$. The cantilever beam gyroscope is also driven in the in-plan direction (x-axis) using the two sidewall electrode to characterize the secondary (sense) mode, Figure 5.17. The result obtained from these different actuation approach provide similar results and the next section provide result for pure AC excitation.

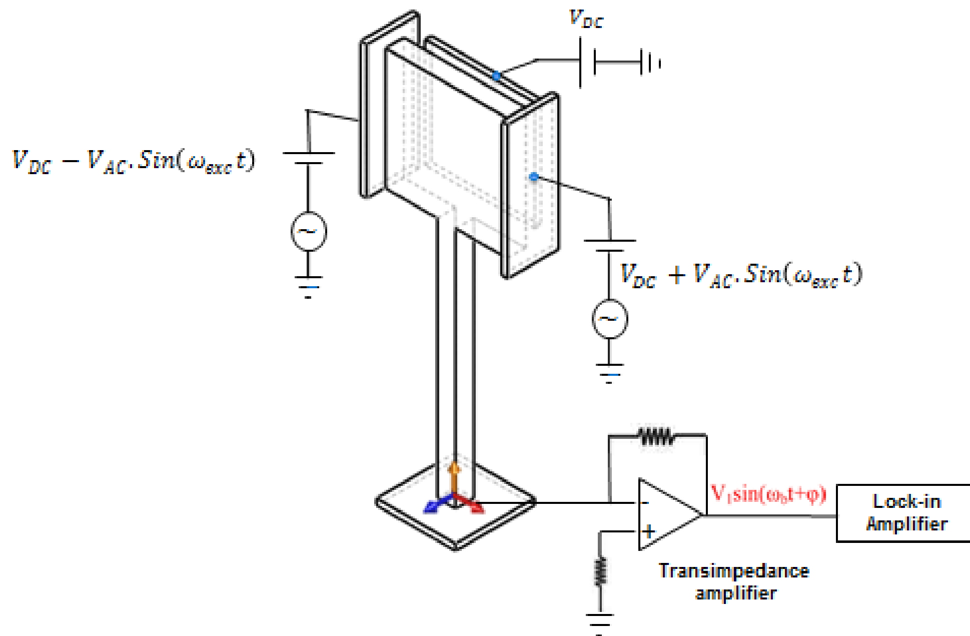


**Figure 5.19: Actuation and Sensing circuit for device characterization in the in-plan direction (x-axis)**

The current caused by the resonant motion of the MEMS gyroscope actuator using pure AC signal consist of a list of frequency components $2\omega_{ex}$, $4\omega_{ex}$ and higher harmonics due to nonlinearity of electrostatic force. Since these frequency components are converted by the excitation frequency,$\omega_{ex}$, the amplitude of current at $3\omega_{ex}$ and higher harmonics is measured by a transimpedance amplifier and the HF2LI lock in amplifier to determine the amplitude of the resonant motion of the gyroscope.

Initially, the drive mode (z-axis) resonance of the cantilever beam gyroscope (device 1) was investigated by analyzing the frequency at the maximum amplitude and -90° phase. The natural frequency of the cantilever was measured to be 40.189 kHz which is in good agreement with the result obtained from the reduced order model and FEM simulation (ANSYS), which are 40.8 kHz and 40.4 kHz respectively. Similarly, the sense mode (x-axis) characterized and the natural frequency measured to be 40.198 KHz. The experimental resonant frequencies of the sense and drive mode slightly lower than the designed values. For the reduced order model and finite element analysis, temperature dependency of the Young's modules was not included. Nonetheless, the experimental value provided very close result with the design values. This could be partly due to the fact that the cantilever beam is free at one end and thermal stress that might be induced during fabrication or packaging will not remain permanent to affect the structure stiffness and its resonance properties. Figure 5.18 provide the frequent response test results of the drive modes for the cantilever 1 and Table 5.2 summarized the measured results.

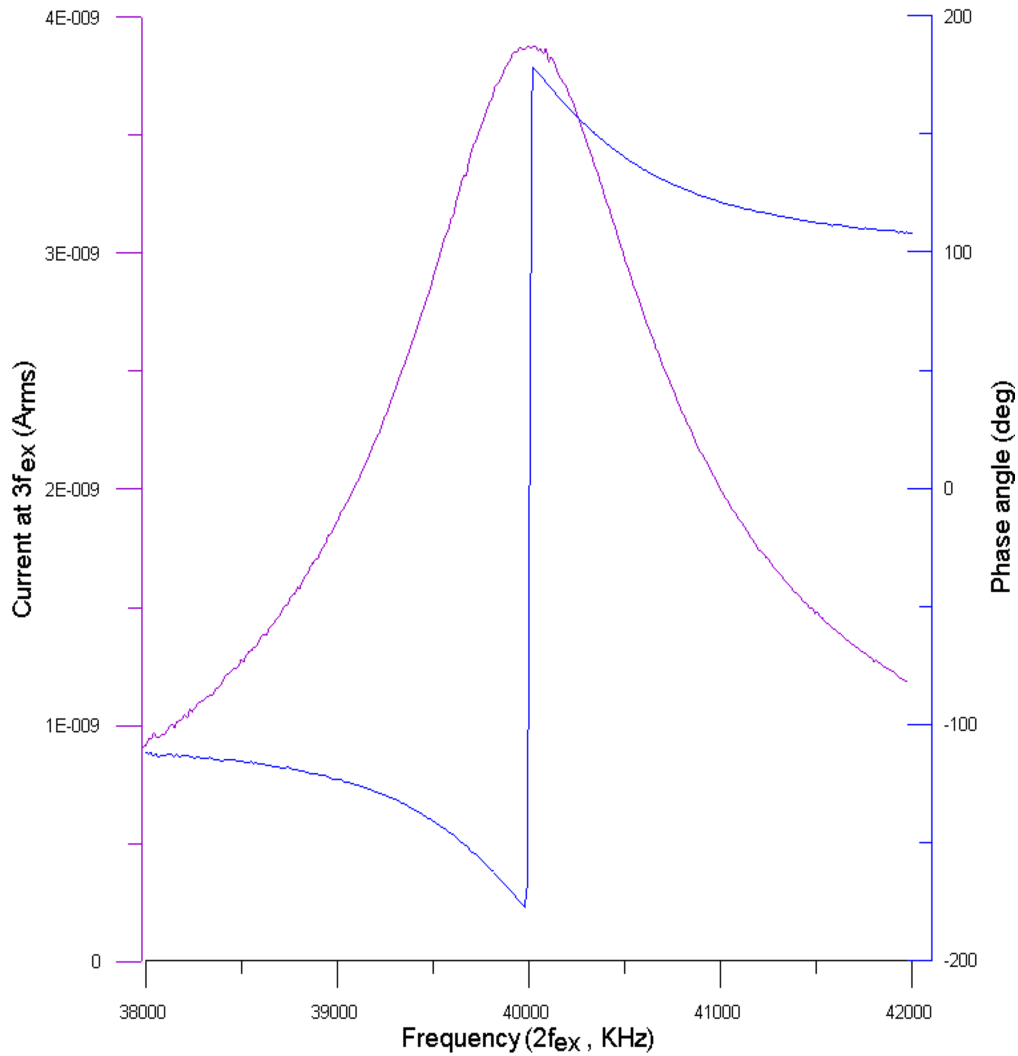


**Figure 5.20: Measured frequency response for Cantilever 1 gyroscope in the drive direction**

**Table 5.2: Testing and simulation results of the fundamental parameters of cantilever 1**

| **Test Parameter** | **Drive mode** | | **Sense mode** | |
|---|---|---|---|---|
| | | ROM/FEA | | ROM/FEA |
| Actuation Voltage | 15 $V_{pp}$ | | 15 $V_{pp}$ | |
| Sweep frequency | 38 kHz to 42 kHz | | 38 kHz to 42 kHz | |
| Parasitic capacitance | 3.5 pF | | 3.5 pF | |
| Natural frequency | 40.189 kHz | 40.8/40.4 kHz | 41.191 KHz | 40.8/40.4 kHz |
| Qaulity factor | ~1850 | | ~1800 | |
| Pull-in voltage | 45.0 V | 45.25 /45.2 V | 41.191 V | 45.25 /45.2 V |

The quality factor characterization provided different results through the course of the test due to potential device leaking or outgassing. Initially, the cantilever drive mode quality (Q) factors found to be above 1850 and start to decrease as the time progress. In order to investigate the quality factor issue a second version of both the cantilever and crab leg design is currently in fabrication.

A series of other cantilever prototype designs were also tested and the first to mode natural frequencies in the z and x directions are well matched with less than 0.1% deviation with the design values. All the other cantilever beam gyroscope design characterized and test results are summarized in Appendix G. The measured natural frequencies are in good agreement with simulated result using the reduced order model. Figure 5.19 show the zicontrol software screen shot for cantilever beam device #3 which has the same geometric dimension as device #1 except its length, which is $388\mu m$. The resonance frequent measured to be 45.050 kHz in a good agreement with the design values, Appendix G. The zicontrol software conveniently used to setup test parameters for the HF2TA current amplifier and HF2LI lock in amplifier using the graphical window interface, as shown in Figure 5.19.

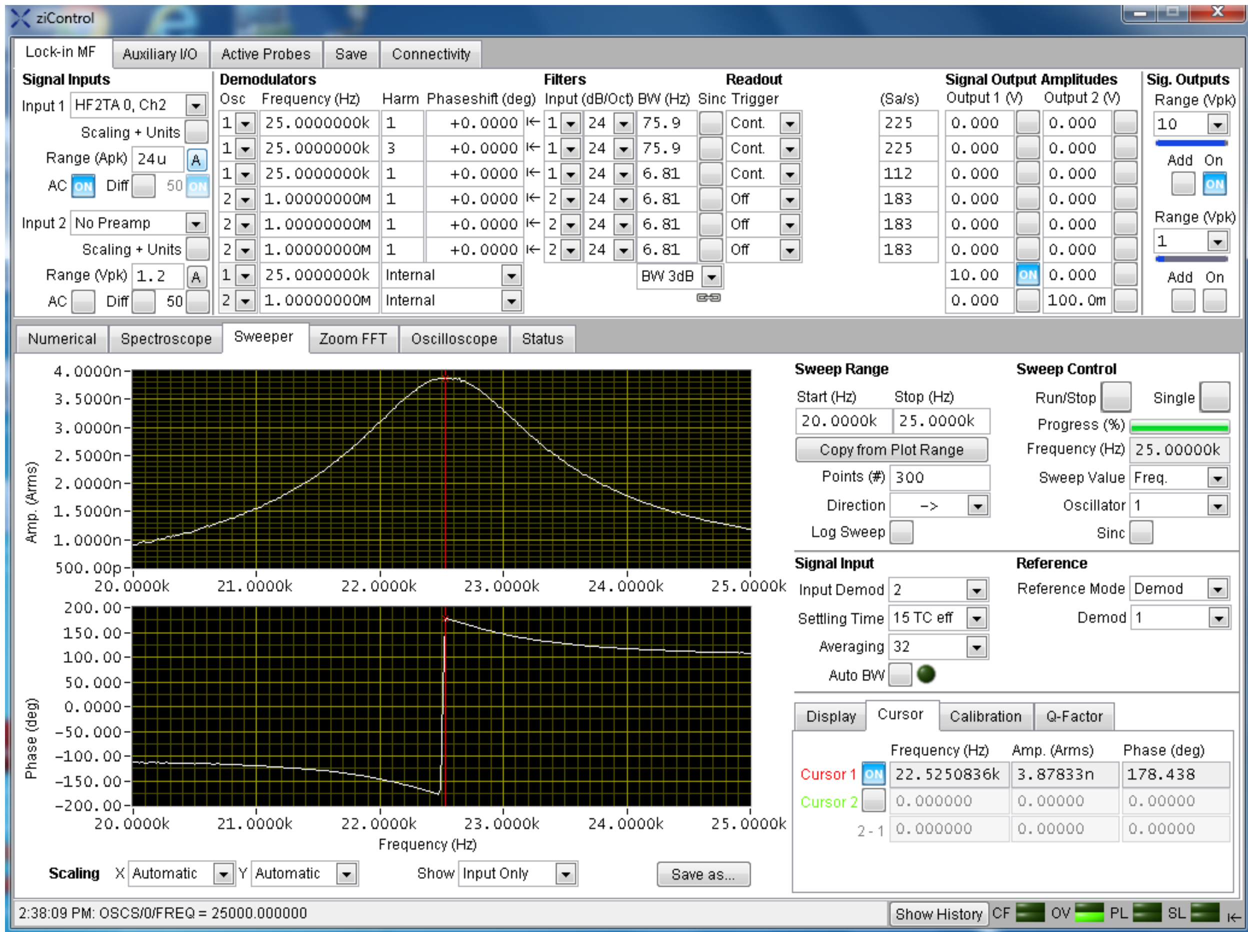


**Figure 5.21: zicontrol screen shot for the cantilever beam design 3**

### 5.2.2 Crab-Leg Characterization

A similar single port test setup and procedure was adapted for the crab leg characterization. The crab-leg gyroscopes natural frequencies and quality factor were characterized in the sense and drive direction using the comb finger drive and sense electrodes. The drive mode was electrostatically excited with an actuation voltage, $V_{es}(t) = V_{pp} \cdot \text{Sin}(\omega_{exc}\ t)$, in a swept mode, produced by HF2LI lock in amplifier internal signal generator. This is done exciting the crab-leg gyroscopes with a pure AC signal over a range of sweep frequencies and recording the amplitude vs. frequency and phase vs. frequency curves, Figure 5.20.

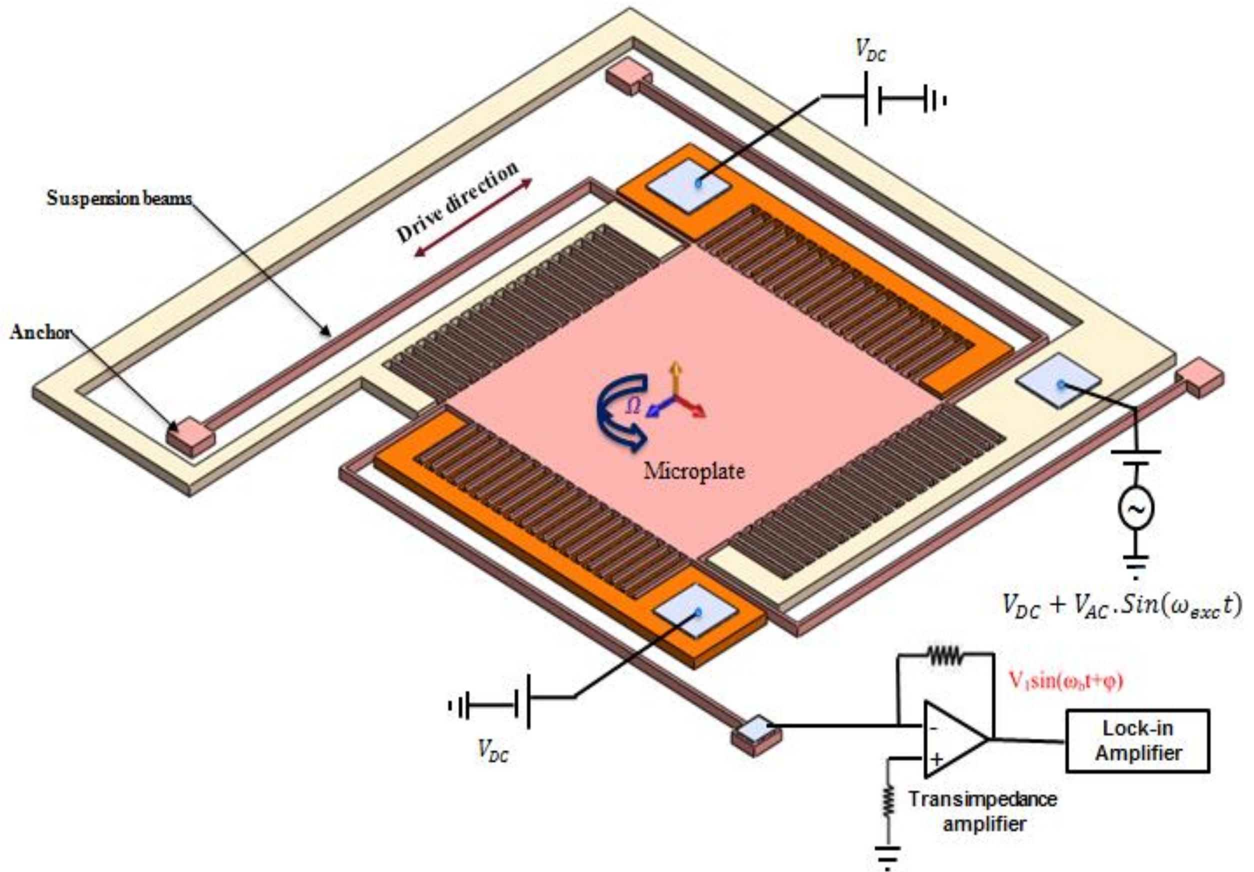


**Figure 5.22: Electrical connection for frequency response test for Device #2**

Figure 5.21 presents the drive mode resonance characteristics measured using the HF2LI lock in amplifier while the gyroscope is excited by a pure harmonic signal. The response is acquired by connecting the transimpedance amplifier output to the input of the lock in amplifier in sine-sweep mode. The drive-mode resonant frequencies measured to be 17.293 kHz and the sense-mode resonant frequencies are in between 17.262 kHz.

The figure show the frequency response for the drive mode both current amplitude and phase shift, where there is cross coupling with the sense mode. This is common issue regarding MEMS resonance design that degreed device performance which is not observed in the cantilever beam design.

During the design process, the beam length and width are optimized to make the two modes close to each other however the test result provide a wider separation between the first two mode mode. This could be due to fabrication imperfection that result a stiffness component that couple the two axis and it cause a major challenge for existing fixed-fixed architect MEMS sensor and actuator design. The initial

quality factor of the drive mode is measured to be 3000 and as in the case of the cantilever beam the quality factor degrade over the course of this work.

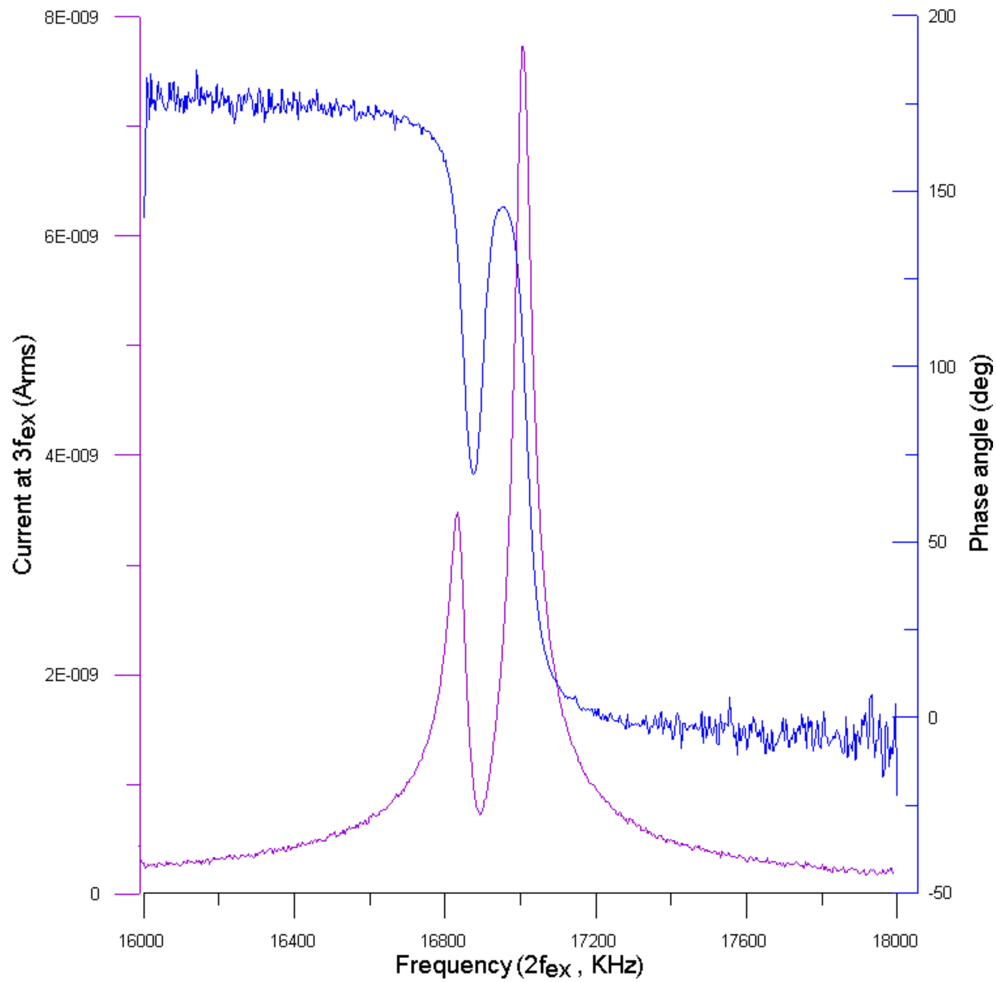


**Figure 5.23: Measured frequency response for Crab leg (Device #2) drive mode**

Figure 5.22 show the zicontrol software screen shot for crab leg Device #2, which is also plotted in figure 5.21. As shown in Figure 5.21, the quality factor degraded to 313 indicating an order of magnitude reduction.

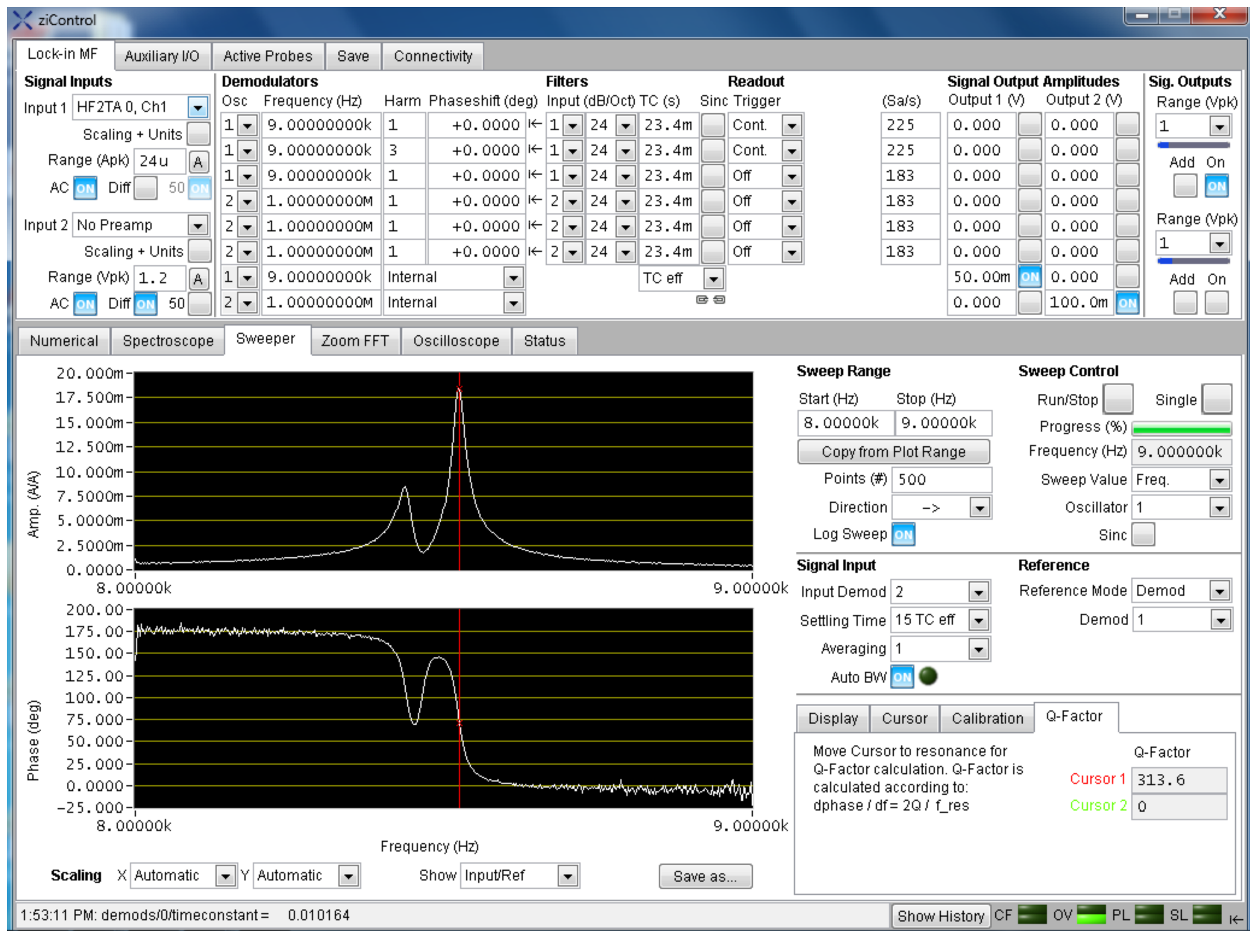


**Figure 5.24: zicontrol screen shot of the test device #2**

**Table 6.2: Testing results of the fundamental parameters of crab leg design (Device #2)**

| **Test parameter** | **Drive mode** | | **Sense mode** | |
|---|---|---|---|---|
| | | FEA | | FEA |
| Actuation Voltage | 10 $V_{pp}$ | | 10 $V_{pp}$ | |
| Sweep frequency | 16 kHz to 18 kHz | | 16 kHz to 18 kHz | |
| Parasitic capacitance | 5.6 pF | | 5.6 pF | |
| Natural frequency (drive) | 17.283 kHz | 19.824kHz | 17.271 KHz | 20.117kHz |
| Qaulity factor | ~3000 | | ~3000 | |
| Pull-in voltage | - | 15V | - | 15V |

Similarly for the finite element analysis, temperature dependency of the Young's modules was not included. However, the experimental result provided a slightly more variation with the design result compared with the cantilever beam. This could be due to packaging or thermally induced stress that occurred in fixed-fixed MEMS structure that we initially outline to address. The reduced order model and FEM analysis result verified using the other twelve (12) other cantilever and crab leg designs and the result are summarized in Appendix G.

## 5.3 Rate Table Test

Similarly, single port excitation and sensing approach were used for the prototype gyroscope rate table test. The prototype gyroscope and signal detecting electronics were mounted on an ARMS-200 Rotary Motion Simulator which is controlled by Soloist HLe controller. HF2LI used for single and double mode detection which offers key features including a built-in signal modulation and demodulation at several frequencies in parallel and incorporate PLLs and PID for frequency amplitude control an. Single port connection of the HF2LI is illustrated in Figure 5.23. A series of test were performed both for the cantilever and crab leg MEMS gyroscope input rate ranging from 0 to 1500 deg/sec, limited by ARMS-200 Rotary Motion rate table.

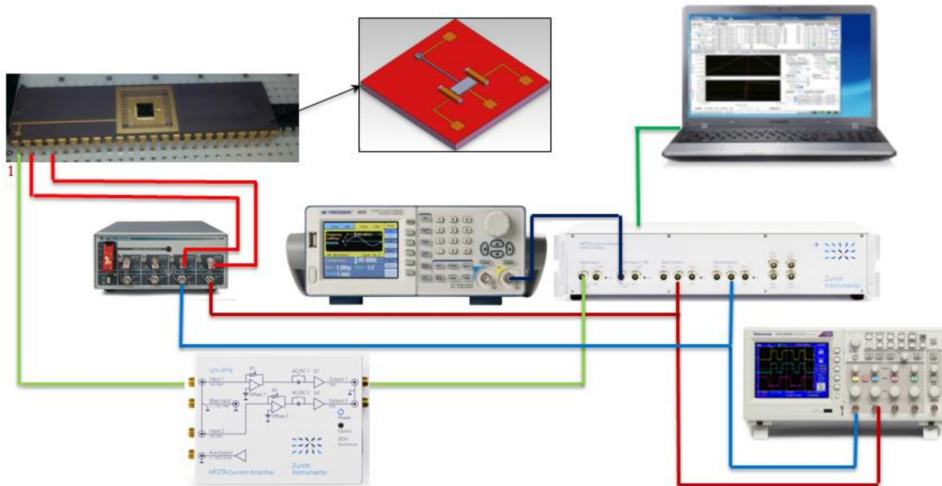

**Figure 5.25: The experimental illustration for rate table (rate table not shown here)**

For the drive-mode control, the oscillation of the vibratory gyroscope is maintained at resonance by means of a PLL. The drive-mode of the gyroscope is connected to input and output of the HF2LI. Furthermore, the mechanical amplitude is kept constant using a PID controller. For electrostatic actuation, an offset ($V_{Offset}$) is applied to the drive signal. This offset was added with function generator

or by using the Add connector on the HF2LI front panel, depending on the voltage requirement for the cantilever beam gyroscope.

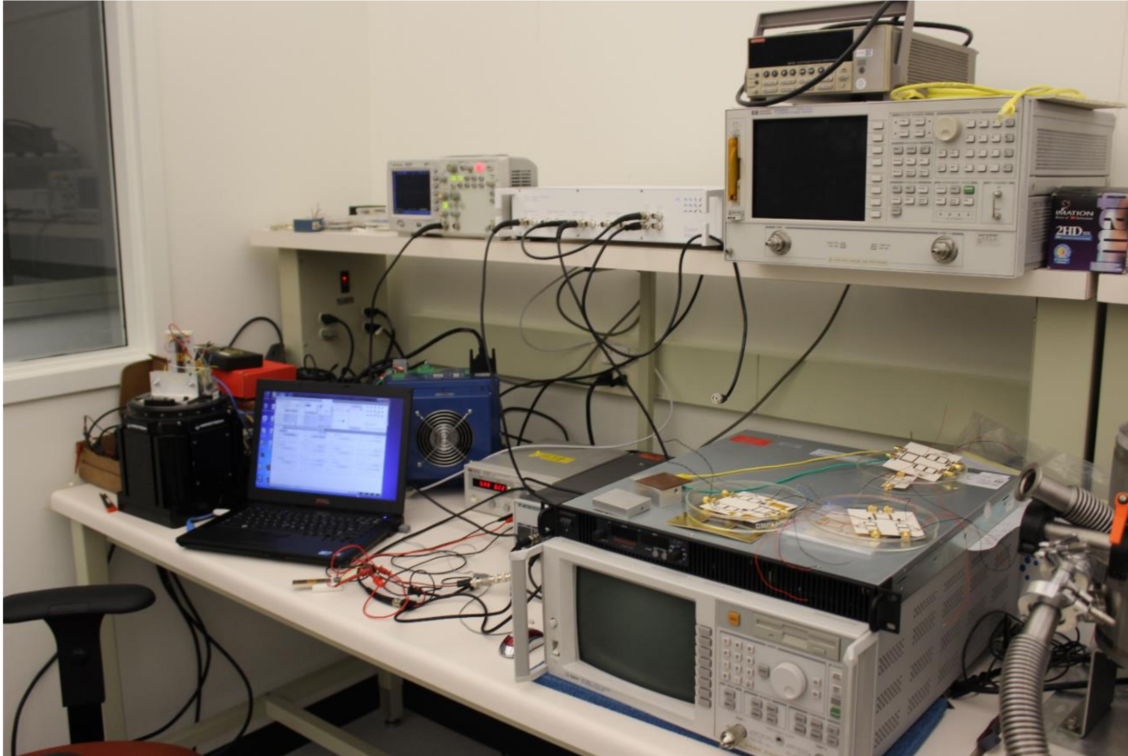

**Figure 5.26: The experimental setup for rate-table characterization**

In this test results, the microplate is driven by a pure AC signal without DC bias, which is amplified by the high voltage amplifier, Tabor 9400. While both sidewall electrodes are grounded, its bottom electrode is connected to the virtual ground of the transimpedance amplifier to measure the current flowing through the microplate and the bottom electrode. The amplitude of the current and phase shift measured by the lock in amplifier, Zurich Instrument HF2LI. The spectrum analyzer, Agilent N9010A, is also used to observe the frequency components of the measured current in real time.

Current signal output from the device was processed in real-time using the HF2TA current amplifier along with HF2LI lock in amplifier. The shift in the resonant frequency of the cantilever-based gyroscope due to angular speed is measured. As theoretically expected for a single-axis gyroscope, the shift in the natural frequency for both the drive and sense axis measured to be linearly proportional to the input rate, Figure 5.25. At the rotational speed of 1500 deg/sec along the drive axis, the shift in the resonant frequency was found to be 4.2 Hz. The FM gyroscope demonstrates less than 0.05 % nonlinearity throughout the entire range.

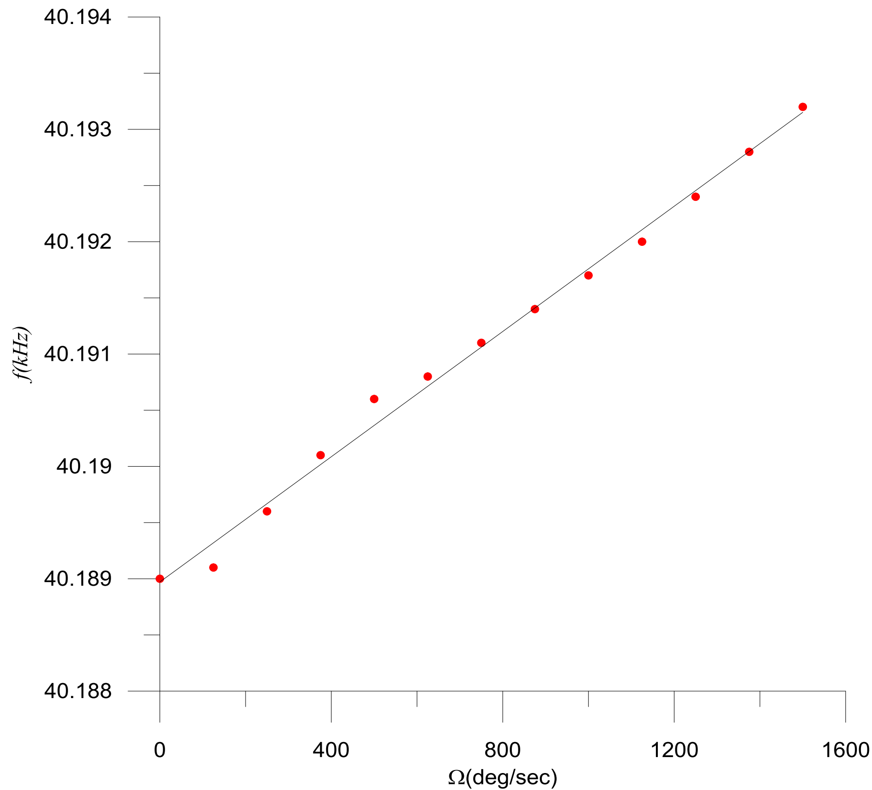


**Figure 5.27: Measured frequency response for Cantilever beam (Device #1)**

Rate table experimental results demonstrate the FM detection approach outlined in the previous sections for both cantilever and crab-leg design. The cantilever MEMS gyroscope provided a table test result over the course of time. The scale factor is confirmed to be equal to the angular gain factor of the gyroscope.

## 5.4 Temperature Effects on Cantilever vs Crab Leg

Change in resonance frequency and quality factor for the MEMS structure could be potential induced by either change in Young's modules due to temperature variation or strain between the supporting beams and substrate [42]. The temperature effect test was preformed to determine influence on the performance of a gyroscope by analyze the effects of temperature on the resonance frequency of cantilever and crab leg gyroscopes. The two port in-put and output of the HF2LI lock in amplifier is used to test the crab leg and cantilever beam gyroscopes simultaneously to observe thermal effect under the same test condition. The test was performed for zero bias (zero angulate rate) changes by measuring drift of the natural frequency due to thermal effect. The test was also performed to verify the need for thermal compensation for the cantilever beam design.

The actuation and sense method implemented in the previous section were used to drive the gyroscope for testing its resonant frequency and the quality factor under the temperature change from 22 °C (room temperature) to 110 °C using the open loop testing scheme using the following procedure

1. The gyroscope and the circuit are statically mounted on the hot plate during the course of measurement
2. The temperature value of the hot plate raised from 22 °C to 110 °C in 10 °C increment
3. The temperature at each sampling point is maintained for 25 minutes before testing to ensure that the temperature on the hotplate and the gyroscope is fully heated uniformly.
4. Additional external temperature measurement was done using Infrared thermal measurement unit to insure uniform thermal distribution
5. The lock in amplifier (or function generator) provides the sinusoidal signal to drive the gyroscope, as in the previous cases.
6. Both the crab-leg and cantilever beam gyroscope current output is connected to the current and lock in amplifier.
7. By sweeping the frequency of excitation signal, the frequency response of vibrating amplitude and frequency recorded, so its peak of the frequency response is just the resonant frequency ($\omega_n$) and its quality factor $Q$ can be measured directly from the HF2LI lock in amplifier

Test result provided in Table 5.4 indicate that the natural frequency shift. Experiment data analyzed while the sample gyroscope excited with a pure harmonic signal at 10 $V_{peak}$. We used a $5^{th}$ order polynomial to fit the measurement data in order to find the resonant frequencies and the quality factors of cantilever and crab-leg gyroscope at different temperature ºC. So, based on these experiment data, the mechanical resonance and the quality factor of the gyroscope slightly decrease as its temperature increases.

**Table 6.4: Cantilever and crab leg test result**

| Temperature (°C) | Cantilever beam (Device 1) | | Crab Leg Design (Device 2) | |
|---|---|---|---|---|
| | Resonance Frequency (Hz) | Quality factor | Resonance Frequency (Hz) | Quality factor |
| 22 | 40195.437 | 14.7 | 17293.882 | 315.6 |
| 30 | 40194.892 | 14.7 | 17292.931 | 315.0 |
| 40 | 40194.375 | 14.6 | 17292.228 | 314.2 |
| 50 | 40193.863 | 14.6 | 17291.738 | 313.5 |
| 60 | 40193.258 | 14.5 | 17290.654 | 311.8 |
| 70 | 40192.713 | 14.4 | 17288.027 | 310.6 |
| 80 | 40191.461 | 14.3 | 17286.781 | 310.2 |
| 90 | 40190.955 | 14.2 | 17285.354 | 309.7 |
| 100 | 40190.276 | 14.0 | 17284.479 | 308.8 |
| 110 | 40189.954 | 13.9 | 17283.846 | 307.2 |

Thermal effect on resonance frequency is significant for the crab leg design compared to the cantilever beam design. The frequency increased with increasing the operating temperature for the crab leg but slightly decrease for the cantilever beam design. Based on the test data analysis the natural frequencies change with temperature. The both the cantilever beam and the crab leg resonant frequencies descend while the temperature increases. However, the comparison between the two designs indicate that temperature effect on MEMS gyroscope can be improved using free suspended structure to decrease thermal stress there by improving the device performance.

## 5.5 Noise Analysis

In this section, the Allan Variance method is applied to data captured from the cantilever beam and crab leg. Two sets of where acquired by sampling the cantilever beam and crab leg gyroscopes for 3 hours in a frequency sweep mode. Fluctuation of the natural frequency measured and converted into deg/sec is plotted in Figure 5.28 and 5.29 for the crab leg and cantilever beam design respectively.

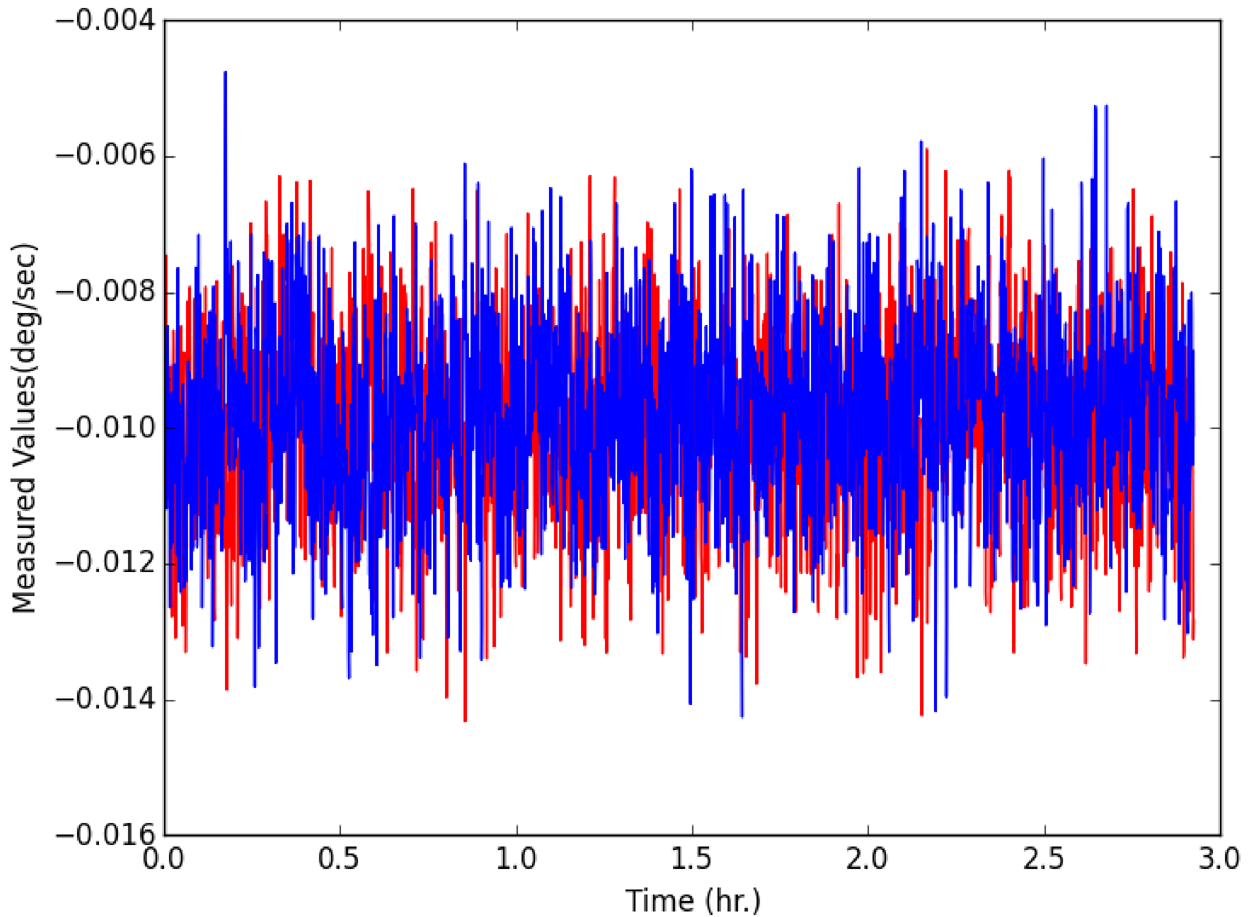


**Figure 5.28: Measured frequency shift as a function of time for the cantilever beam gyroscopes**

Since the observed natural frequency fluctuation value was small and it was necessary to work on window small part of raw measurements close to the estimated natural frequency was analyzed. For stochastic analysis of the gyroscope, the whole data of about three hour datasets have been used. Two test measurement was taken for the cantilever beam design (Device 1) and crab leg MEMS gyroscope (Device 2). A combination of Matlab and Python is used for the data analysis.

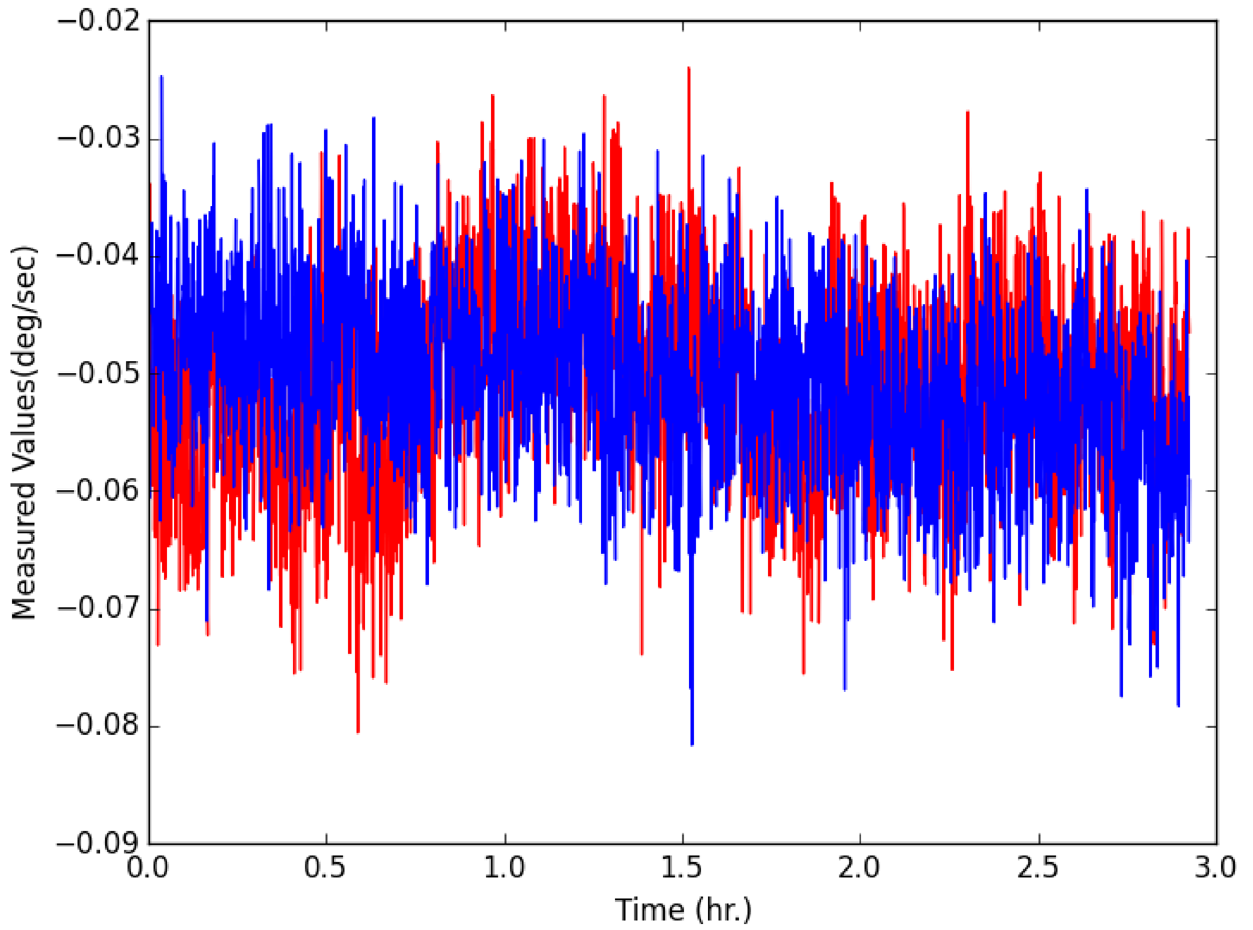


**Figure 5.29: Measured frequency shift as a function of time for the crab leg gyroscopes**

Figure 5.30 shows the measured Allan deviation plot generated from the acquired data using the method presented in the previous chapter 4. The plot provide insight regarding the type and magnitude of random noise captured data in the acquired data.

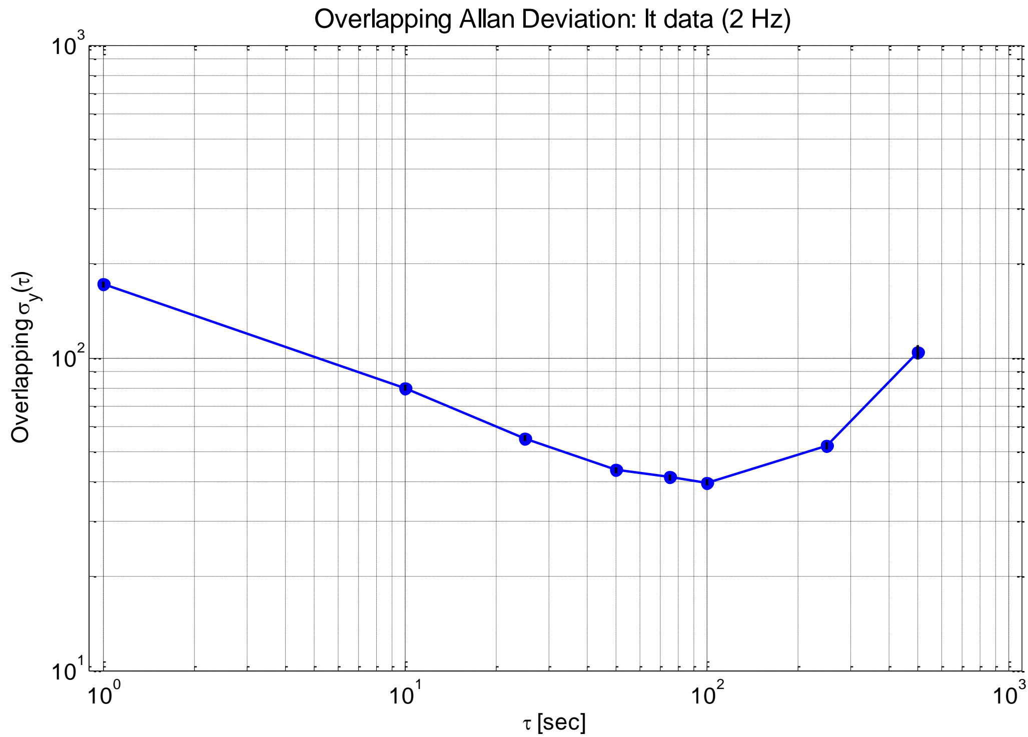


**Figure 5:30: Measured Allan variance comparison between cantilever beam FM gyroscopes**

From figure 5.30 the Angular Radom Walk (ARW) and the bais instability identifiable by a slope of $-1/2$ and the graph low point respectively. The ARW of the cantilever beam and crab leg gyroscopes are is 0.24 and 1.25 deg/h/$\sqrt{\text{Hz}}$, respectively. The bias stabilities of the cantilever beam and crab leg gyroscopes are 30 and 69 ∘/hr at 100 and 27 s averaging time, respectively. Noise performance of the FM sensor is limited by the frequency stability of the two modes of vibration in the gyroscope. The cantilever beam measured with better ARW as well as bias stabilities providing further advantage over the fixed-fixed type of the crab leg design.

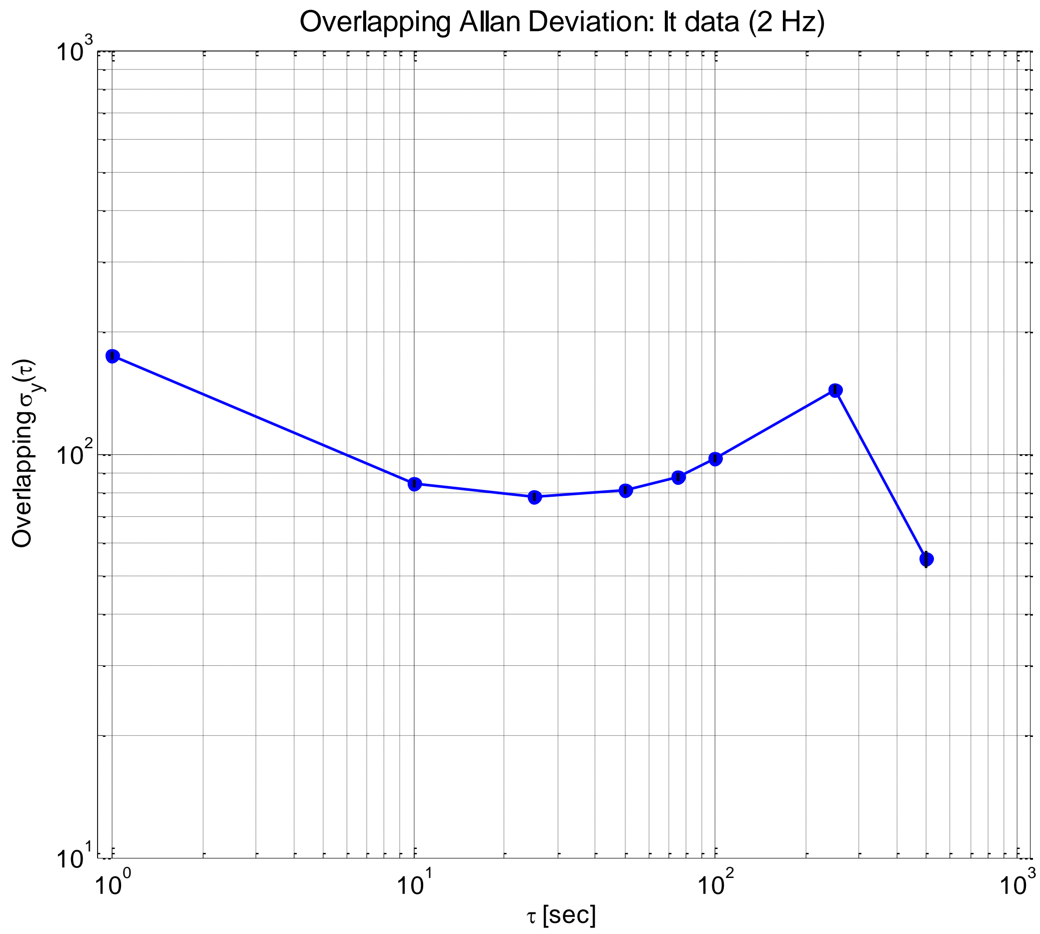


**Figure 5.31: Measured Allan variance comparison between crab leg FM gyroscopes**

# CHAPTER VI

## Summary and Conclusions

Two MEMS gyroscope devices were developed based the FM detection method, one a novel cantilever beam design and the other a traditional crab-leg technology. The crab-leg gyroscope served as a direct comparison against the cantilever beam design, providing baseline performance data under the same test conditions. A new methodology for the design and analysis of FM MEMS gyroscopes was formulated and applied to the design and fabrication of both prototypes. The design emphasis was on the investigation of device dynamics and demonstration of the proof of concept. The working principle and dynamic output characteristics of the FM detection method for MEMS gyroscope devices were introduced, providing a theoretical basis for analyzing the dynamic frequency output characteristics of resonant vibratory gyroscopes.

The cantilever beam and a crab-leg designs were modeled and analyzed, along with suspended mass. A nonlinear model of the cantilever beam MEMS gyroscope was presented, considering electrostatic and Coriolis forces. The system governing equations were solved using a reduced order model, and FEM simulation was performed to verify the result. The effects of changing input excitation parameters on the performance of the gyroscope were investigated.

Based on the design, a prototype device was fabricated using the Teledyne Dalsa MEMS Integrated Design for Inertial Sensors (MIDIS™) Process. Furthermore, three different characterization and test setups were investigated and implemented for resonance operation of the drive and sense mode resonator. A frequency measurement method based on dynamic output characteristics was implemented to investigate the modulated output signal of the resonant vibratory gyroscope. A characterization and control system for MEMS gyroscopes was performed mainly using commercially available hardware and software.

The results of the proof of concept analysis and the advantages of cantilever beam gyroscopes over traditional fixed-fixed designs are discussed in chapter five. The resulting benefits include simpler dynamics and control, improved scale factor stability over micromechanical gyroscopes utilizing open-

loop displacement sensing, and large dynamic range. The cantilever beam MEMS gyroscope also demonstrated lower angular random walk and bias instability, which helps minimize error sources that corrupt the Coriolis signal. Thermal testing of the sample device demonstrated that the amplitude and frequency fluctuant for both cantilever and crab leg design. However, the cantilever beam gyroscope performed much better and was less affected by thermal change to the environment. Addressing thermal effects in MEMS gyroscope design could potentially yield reliable, robust and high-performance devices, leading to a wide range of applications including dynamic vehicle control, automotive safety systems, navigation/guidance systems, and interactive consumer electronics.

While it was not experimentally verified, the cantilever beam MEMS gyroscope design is expected to reject vibrations (by sensing the orthogonally arranged secondary gyroscope), which is one of the major sources of error for MEMS devices. This is mainly because the cantilever cannot vibrate along the longitudinal direction, a phenomenon that can be used to improve device performance by measuring orthogonally arranged cantilever gyroscopes and adapt sensor fusion. The single port detection FM detection method was reported for the first time in this work, and showed a clear benefit to determining the input rate angle (by observing a single axis (drive) motion output), which could potentially solve cross-axis sensitivity (a common MEMS gyroscope error source).

## 6.1 Contributions and Outcome of This Work

This study explored novel sensing and design concepts for MEMS gyroscopes that provide inherent robustness against structural and thermal parameter variations, and require less demanding active compensation schemes. This work focuses on system level contributions to the characterization and control of MEMS gyroscopes. The primary contributions include:

- Investigation of the natural frequency shift sensing method for MEMS cantilever beam gyroscopes. The mathematical model of the cantilever beam carrying a rigid body is developed. To derive the mathematical model, the kinetic energy of the structure under spatial rotation and deformation is computed.

- Demonstration of MEMS gyroscope operation in frequency modulation mode and investigation of the MEMS gyroscope modal frequencies. The application of the proposed system in the frequency-modulation mode is demonstrated by experimental method the input rotation rate as the function of the modal frequencies. In practice, the modal frequencies are measured and the rotation rate is computed from the equation.

- Mathematical models for the beam-rigid body gyroscope, considering the static behaviour of the beam-rigid body MEMS gyroscope and study the reduced-order nonlinear behaviour of the system,

- Analysis of the device's nonlinear behaviour using Finite Element software (ANSYS) and comparison to the results of the method with the reduced order model results. A finite element analysis of the structure provides an insight to the performance and design of the MEMS sensor and result in a better design before going to the experimentation phase.

- The impact of mechanical-thermal noise effects on frequency modulated MEMS gyroscopes was studied.

- The fabrication and experimental verification of the cantilever beam MEMS gyroscope, demonstrating the frequency modulated MEMS gyroscope concept. The results provide a basis for further improvement of the design and performance of the beam-based rotation rate sensors.

- Development of a characterization method that measures the frequency of the MEMS gyroscope's two modes

## 6.2 Recommendations for Future Work

We implemented the single port FM detection and control system using commercially available hardware and software. An off the shelf HF2TA current amplifier and HF2LI lock in amplifier were used to measure the spectrum of current fluctuations, allowing us to obtain the most stable test results. The characterization setup could potentially be improved by using PCB board design with a stable transimpedance amplifier with a similar gain as the HF2TA current amplifier. Furthermore, future research must be undertaken to develop FM detection circuitry using CMOS-based single mode detection architecture for commercialization and batch fabrication.

Temperature remains one of the major challenges impeding MEMS inertial sensor performance. While the cantilever design demonstrated improved performance for thermal fluctuation, additional innovative structural designs, operational principles and fabrication processes could be explored to ultimately develop a navigation-grade MEMS gyroscope unit. During the course of this study various fabrication techniques were explored, including those for cantilever beam designs with large suspended masses, to enhance the sensor robustness and increase capacitive sensitivity (by increasing area). We also

developed a microfabrication process for the new design architecture, but could not implement it due to limited fabrication access. This work could be significantly advanced in collaboration with industry, enabling realization of a robust design that could potentially provide inherently better noise and sensitivity due to larger masses and larger capacitances.

A thorough design optimization was performed to find the best parameters for selecting a fabrication platform for our cantilever gyroscope, ensuring the best system performance is obtained. This work could benefit with a system level optimization study, taking broader gyroscope performance metrics into account. In conclusion, this study presents one possible method to improve MEMS gyroscope performance using structural design and sensing approach technical.

## References


[1] N. Yazdi, F. Ayazi, and K. Najafi "Micromachined Inertial Sensors" Proceeding of IEEE, Vol. 86, No. 8, August 1998, pp. 136-147.

[2] C. Acar and A. M. Shkel "Structural design and experimental characterization of torsional micromachined gyroscopes with non-resonant drive mode" Journal of micromechanics and microengineering, 14 (2004) 15-25.

[3] H. Xie and G. K. Fedder "Integrated Microelectromechanical Gyroscopes" Journal of Aerospace Engineering, Vol. 16, No. 2, April 2003, pp. 65-75.

[4] N. Barbour, and G. Schmidt "Inertial Sensor Technology Trends" IEEE Sensors Journal, Vol. 1, No. 4, Dec 2001, pp. 332-339.

[5] IEEE-952 "IEEE Standard Specification Format Guide and Test Procedure for Single-Axis Interferometric Fiber Optic Gyros" December 2008.

[6] P. Greiff, B. Boxenhorn, T. King, and L. Niles "Silicon monolithic micromechanical gyroscope" Tech. Dig. 6th Int. Conf. Solid-State Sensors and Actuators, San Francisco, CA, June 1991, pp. 966-968.

[7] G. B. Malykin "The Sagnac effect: correct and incorrect explanations" Physics-Uspekhi 43, 1229–1252 (2000).

[8] E. Alper and T. Akin "A symmetric surface micromachined gyroscope with decoupled oscillation modes" Sensors and Actuators, (2004) 347-358.

[9] Y. S. Hong, J. H. Lee and S. H. Kim "A lateraly driven symmetric micro resonator for gyroscopic applications" Journal of Micromachining and Microengineering, 10 (2000) 452-458.

[10] C. Jeong "A study on resonant frequency and Q factor tunings for MEMS vibratory gyroscopes" Journal of micromechanics and microengineering, 14 (2004) 1530-1536.

[11] M. Esmaeili, N. Jalili, and M. Durali "Dynamic modeling and performance evaluation of a vibrating beam microgyroscope under general support motion" Journal of Sound and Vibration 301 (2007) 146–164

[12] G.L. Anderson "Natural frequencies of a cantilever with an asymmetrically attached tip mass" AIAA Journal 16 (1978) 281–282.

[13] M.R.M. Crespo da Silva and C.C. Glynn "Nonlinear Flexural-Flexural-Torsional Dynamics of Inextensional Beams: I. Equations of Motion" Journal of Structural Mechanics, 6(4), 437-448.

[14] Bhadbhade V. and Jalili N "Modeling and Vibration Analysis of Cantilever-based Rocking Mass Gyroscope" Proceedings of 2006 ASME International Mechanical Engineering Congress & Exposition, Chicago, IL.

[15] Takaway T., Fukudaz T. and Takadaz T "Flexural–Torsion Coupling Vibration Control of Fiber Composite Cantilevered Beam by Using Piezoceramic Actuators" Smart Materials and Structures, 6, 477-484.

[16] M. W. Putty and K. Najafi "A micromachined vibrating ring gyroscope" Tech. Dig. Solid-State Sens. Actuator Workshop, Hilton Head Island, SC, June 1994, pp. 213-220.

[17] Hopkin, I. D. "Vibrating gyroscopes (automotive sensors)". IEEE Colloquium on Automotive Sensors. Digest No. 1994/170. Solihull, UK, Sept. 1994, pp. 1-4.

[18] Tanaka, K., Mochida, Y., Sugimoto, S., Moriya, K., Hasegawa, T., Atsuchi, K., and Ohwada, K. "A micromachined vibrating gyroscope". Proc., Eighth IEEE Int. Conf. on Micro Electro Mechanical Systems (MEMS ’95), Amsterdam, Netherlands, Jan. 1995, pp. 278-281.

[19] Clark, W. A., Howe, R. T., and Horowitz, R. "Surface micromachined Z-axis vibratory rate gyroscope" Technical Digest. Solid-State Sensor and Actuator Workshop, Hilton Head Island, S.C., June 1996, pp. 283-287.

[20] A. Seshia, R. Howe, and S. Montague, “An Integrated Microelectromechanical Resonant-Output Gyroscope” IEEE MEMS 2002, Las Vegas, NV, pp. 722-726, 2002.

[21] Juneau, T., Pisano, A. P., and Smith, J. H. "Dual axis operation of a micromachined rate gyroscope" Proc., IEEE 1997 Int. Conf. on Solid State Sensors and Actuators (Tranducers ’97), Chicago, June 1997, pp. 883-886.

[22] Lutz M., Golderer W., Gerstenmeier J., Marek J., Maihofer B., Mahler S., Munzel H., and Bischof U. "A precision yaw rate sensor in silicon micromachining" Transducers 1997, Chicago, IL, June 1997, pp. 847-850.

[23] Moussa, H. and Bourquin, R.: "Theory of direct frequency output vibrating gyroscopes" IEEE Sensors Journal, vol. 6, pp. 310-315, 2006.

[24] Albrecht T. R., Gru¨tter P., Horne D., and Rugar D., "Frequency modulation detection using high-Q cantilevers for enhanced force microscope sensitivity" Journal of Applied Physics. 69(2), 668 (1991).

[25] Abe, M., Shinohara, E., Hasegawa, K., Murata, S. and Esashi, M. "Trident-type tuning fork silicon gyroscope by the phase difference detection. In: Proceedings of the 13th IEEE International Conference on Microelectromechanical Systems" pp. 508- 513. 2000.

[26] Sangtak Park, Mahmoud Khater, David Effa, Eihab Abdel-Rahman, and Mustafa Yavuz "Detection of Cyclic-Fold Bifurcation in Electrostatic Transducers by Motion-Induced Current" Journal of Micromechanics and Microengineering, Volume 27, Number 8, 2017.

[27] John, J., Jakob, C., Vinay, T. and Qin, L. "Phase differential angular rate sensor concept and analysis" IEEE Sensors Journal, vol. 4, pp. 471-478, 2004.

[28] Yang, H., Bao, M., Yin, H. and Shen, S. "Two-dimensional excitation operation mode and phase detection scheme for vibratory gyroscopes" Journal of Micromechanics and Microengineering, vol. 12, pp. 193-197, 2002.

[29] S.A. Zotov, I.P. Prikhodko, A.A. Trusov, and A.M. Shkel, “Frequency Modulation Based Angular Rate System” Proc. IEEE MEMS, Cancun, Mexico, January 23 - 27, 2011.

[30] Xie, L.; Xiao, D.; Wang, H.; Wu, X.; Li, S. Sensitivity Analysis and Structure Design for Tri-Mass Structure Micromachined Gyroscope. In Proceedings of the 2009 4th IEEE International Conference on Nano/Micro Engineered and Molecular Systems, Shenzhen, China, 5–8 January 2009; pp. 126–129.

[31] D. R. Sparks, S. R. Zarabadi, J. D. Johnson, Q. Jiang, M. Chia, O. Larsen, W. Higdon, and P. Castillo-Borelley. "A CMOS integrated surface micromachined angular rate sensor: It’s automotive applications" Tech. Dig. 9th Int. Conf. Solid-State Sensors and Actuators (Transducers’97), Chicago, IL, June 1997, pp. 851-854.

[32] Y. Oh, B. Lee, S. Baek, H. Kim, J. Kim, S. Kang, and C. Song. "A surface micromachined tunable vibratory gyroscope" Proc. IEEE Micro Electro Mechanical Systems Workshop (MEMS’97), Japan, 1997, pp. 272-277.

[33] D. Effa, Eihab Abdel-Rahman, and Mustafa Yavuz, "Cantilever Beam Microgyroscope Based on Frequency Modulation" IEEE/ASME International Conference on Advanced Intelligent Mechatronics, July 9-12, 2013 Wollongong, Australia.

[34] K. Y. Park, C. W. Lee, Y. S. Oh, and Y. H. Cho. "Laterally oscillated and force-balanced micro vibratory rate gyroscope supported by fish hook shape springs" Proceeding IEEE Micro-Electro Mechanical Systems Workshop (MEMS'97), Japan, 1997, pp. 494-499.

[35] Kourepenis, J. Bernstein, J. Connely, R. Elliot, P. Ward, and M. Weinberg. "Performance of MEMS inertial sensors" Proceeding IEEE Position Location and Navigation Symposium, 1998, pp. 1-8.

[36] Mochida, Y., Tamura, M., and Ohwada, K. "A micromachined vibrating rate gyroscope with independent beams for the drive and detection modes" Proceeding Twelfth IEEE Int. Conf. on Micro Electro Mechanical Systems (MEMS '99), Orlando, FL, Jan. 1999, pp. 618-623.

[37] Funk, K., Emmerich, H., Schilp, A., Offenberg, M., Neul, R., and Larmer, F. "A surface micromachined silicon gyroscope using a thick polysilicon layer" Proceeding Twelfth IEEE Int. Conf. on Micro Electro Mechanical Systems (MEMS '99), Orlando, FL, Jan. 1999, pp. 57-60.

[38] Park, K. Y., Jeong, H. S., An, S., Shin, S. H., and Lee, C. W. "Lateral gyroscope suspended by two gimbals through high aspect ratio ICP etching" Proceeding IEEE 1999 Int. Conf. on Solid State Sensors and Actuators (Tranducers '99), Sendai, Japan, June 1999, pp. 972-975.

[39] S. Lee, S. Park, J. Kim, and D. Cho. "Surface/bulk micromachined single crystalline-silicon micro-gyroscope" IEEE/ASME Journal of Microelectromechanical Systems, Vol.9, No.4 Dec. 2000, pp. 557-567.

[40] Jiang, X., Seeger, J. I., Kraft, M., and Boser, B. E. "A monolithic surface micromachined Z-axis gyroscope with digital output" Digest of Technical Papers, 2000 Symposium on VLSI Circuits, Honolulu, June 2000, pp. 16-19.

[41] H. Xie and G. K. Fedder. "A CMOS-MEMS lateral-axis gyroscope" Proceeding 14th IEEE Int. Conf. Microelectromechanical Systems, Interlaken, Switzerland, Jan. 2001, pp. 162-165.

[42] H. Luo, X. Zhu, H. Lakdawala, L. R. Carley, and G. K. Fedder. "A copper CMOS- MEMS z-axis gyroscope" Proceeding 15th IEEE Int. Conf. Microelectromechanical Systems, Las Vegas, NV, Jan. 2001, pp. 631-634.

[43] D. Effa, Eihab Abdel-Rahman, and Mustafa Yavuz, "Analysis of Thermal Noise in Frequency-Modulated Gyroscopes" IEEE/ASME International Conference on Advanced Intelligent Mechatronics, November 9-12, 2014 Montreal, Canada.

[44] W. Geiger, W.U. Butt, A. Gaisser, J. Fretch, M. Braxmaier, T. Link, A. Kohne, P. Nommensen, H. Sandmaier, and W. Lang. "Decoupled Microgyros and the Design Principle" Sensors and Actuators A (Physical), Vol. A95, No.2-3, Jan. 2002, pp. 239-249.

[45] J. A. Geen, S. J. Sherman, J. F. Chang, and S. R. Lewis. "Single-chip surface micromachining integrated gyroscope with 50 deg/hour root Allan variance" Dig. IEEE Int. Solid-State Circuits Conf., San Francisco, CA, Feb. 2002, pp.426-427.

[46] Seshia, A. A., Howe, R. T., and Montague, S. "An integrated microelectromechanical resonant output gyroscope" Proc., The Fifteenth IEEE Int. Conf. on Micro Electro Mechanical Systems (MEMS 2002), Las Vegas, Jan. 2002, pp. 722-726.

[47] G. He and K. Najafi. "A single crystal silicon vibrating ring gyroscope" Proceeding the Fifteenth IEEE Int. Conf. on Micro Electro Mechanical Systems (MEMS 2002), Las Vegas, Jan. 2002, pp. 718-721.

[48] H. Xie and G. K. Fedder. "Fabrication, Characterization, and Analysis of a DRIE CMOS-MEMS Gyroscope" IEEE Sensors Journal, Vol. 3, No. 5, 2003, pp. 622-631.

[49] T. J. Brosnihan, J. M. Bustillo, A. P. Pisano, and R. T. Howe. "Embedded interconnect and electrical isolation for high-aspect-ratio, SOI inertial instruments" Transducers 1997, Chicago, IL, June 1997, pp. 637-640.

[50] W.A. Clark, R.T. Howe, and R. Horowitz. "Surface Micromachined Z-Axis Vibratory Rate Gyroscope" Proceedings of Solid-State Sensor and Actuator Workshop, June 1994.

[51] Shkel, R. Horowitz, A. Seshia, S. Park and R.T. Howe. "Dynamics and Control of Micromachined Gyroscopes" American Control Conference, CA, 1999.

[52] S. Park and R. Horowitz. "Adaptive Control for Z-Axis MEMS Gyroscopes" American Control Conference, Arlington, VA, June 2001.

[53] R.P. Leland. "Adaptive Tuning for Vibrational Gyroscopes" Proceedings of IEEE Conference on Decision and Control, Orlando, FL, Dec. 2001.

[54] C.W. Dyck, J. Allen, and R. Hueber. "Parallel Plate Electrostatic Dual Mass Oscillator" Proceedings of SPIE SOE, CA, 1999.

[55] X. Li, R. Lin, and K.W. Leow. "Performance-Enhenced Micro-Machined Resonant Systems with Two-Degrees-of-Freedom Resonators" Journal of Micromech, Microeng, Vol. 10, 2000, pp. 534-539.

[56] T. Usada. "Operational Characteristics of Electrostatically Driven Torsional Resonator with Two-Degrees-of-Freedom" Sensors and Actuators A, Vol. 64, 1998, pp. 255-257.

## Appendix A: MEMS Gyroscope Model Using MATLAB / Simulink

MEMS gyroscope was modeled in Matlab/SIMULINK which performance of the proposed processing chain has been simulated. The general view of MEMS gyroscope Simulink model includes value input boxes representing geometrical dimensions, material properties and load acceleration and measured properties. The input to the system is the rotation rate which was given in terms of degree/sec. The input is given to the MEMS module. The MEMS block is designed with the help of gyro specifications natural frequency and damping, which generates the amount of motion in the sense direction producing sensed angular rate. The model includes a bias error block to compensate deterministic or stochastic noise factors. The signal is introducing with white noise that generate random drift error. This would have added Angular Random Walk (ARW) and The Rate Random Walk (RRW). The simulation also contains several blocks including sensitivity and digital low pass filter. Sample signal output plotted blow for 0 rate inputs.

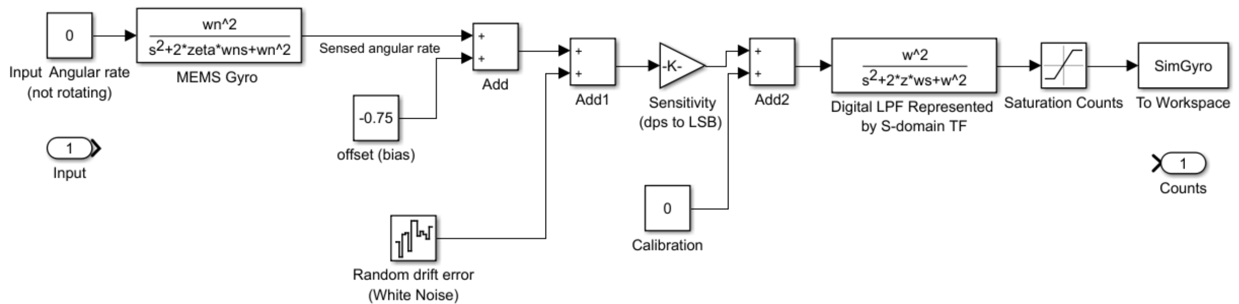

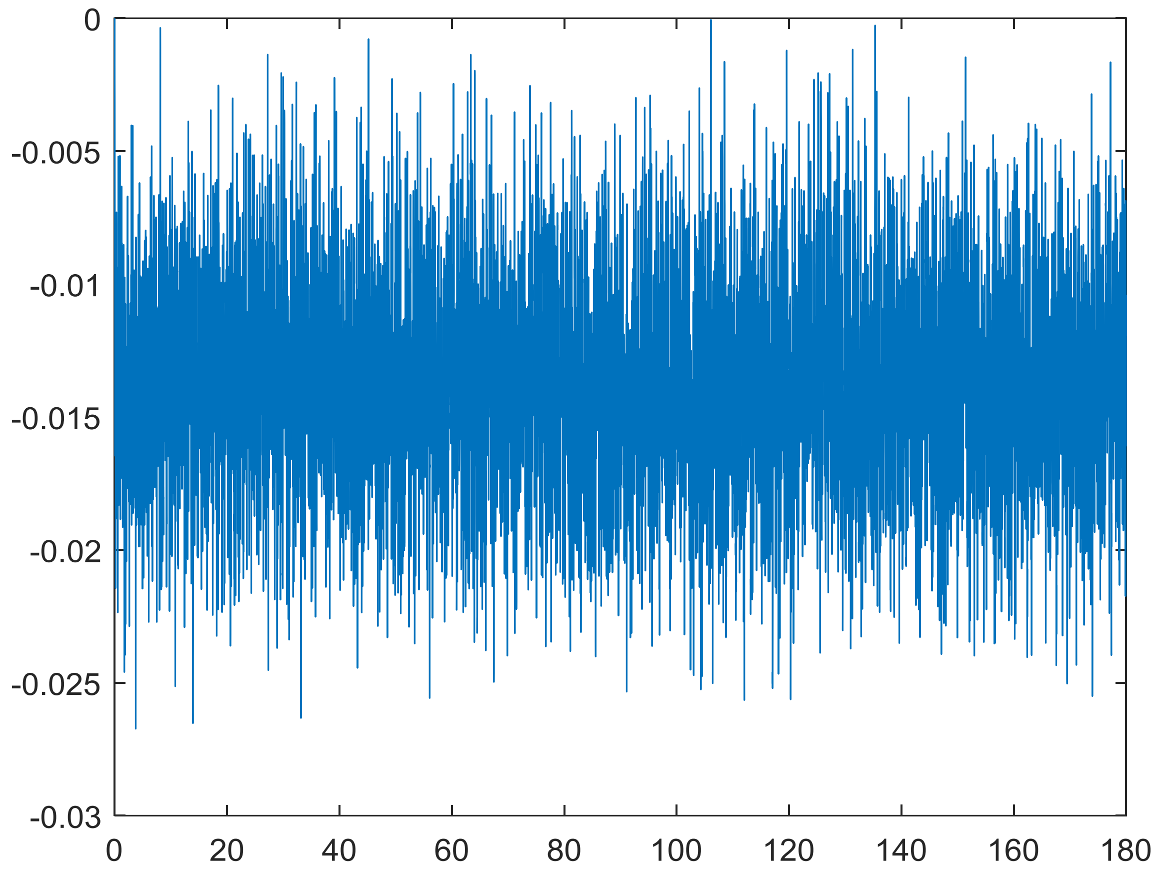
0
-0.005
-0.01
-0.015
-0.02
-0.025
-0.03
0
20
40
60
80
100
120
140
160
180

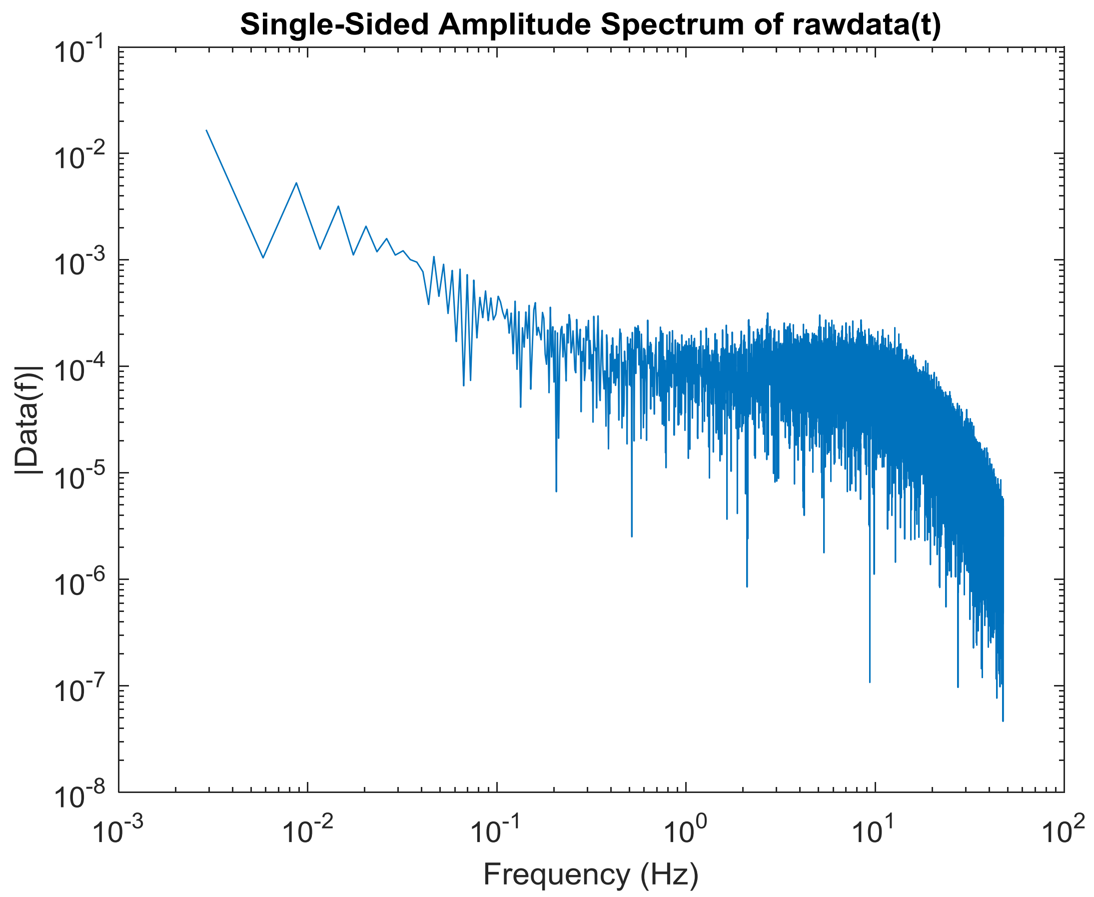
Single-Sided Amplitude Spectrum of rawdata(t)
|Data(f)|
Frequency (Hz)
10-1
10-2
10-3
10-4
10-5
10-6
10-7
10-8
10-3
10-2
10-1
100
101
102

## Appendix B: Fabrication process flow

Design Layer Cell Boundary (M83): Design support layer (used for data generation during mask data preparation) indicating the intended die dimensions.

Design Layer Bottom Deep Cavity (M95) Used to define deep cavity bellow structure of the handle wafer.

Design Layer Structure (M32) Used to define areas for the sensing structure on front side of the DEVICE wafer.

Design Layer Comb Top Recess (M37) Combs teeth to be thinned on the front side of the Device wafer.

Design Layer Bumper (M34) Used to define lateral stoppers/SBUMPs for mobile STRUCTs.

Device top cavity is defined using mask 94 (20µm head space). Mask 17 is used to define connection vias (TSVs) followed my mask 60 for contacts (not shown) and mask 70 to define interconnects. TSV wafer upper cavity (30µm high) using M94 Fabrication of TSV using M17 followed by contacts using M60 (not shown) Handle/Device wafer + TSV wafer bond. Interconnects using M70 & M80

Design Layer Conductive Anchor (M155) Used to define bonding plan areas dedicated to structure features anchoring and electrical connectivity between of the TSV and Membrane wafers.

Design Layer Isolation Trench (M56) Used to define trenches and equipotential areas in the TSV wafer.

Design Layer Top Cavity (M96) used to define regions for top cavity of the TSV wafer.

Design Layer Contacts (M60) used to define CONT (though the Isolation Oxide) on the assembly wafer.

Design Layer Metal (M70) used to define bond pad structure and routing on the assembly wafer. May be used for die labelling.

Design Layer PADS (M80) used to define bond pad openings through passivation layers on the assembly wafer.

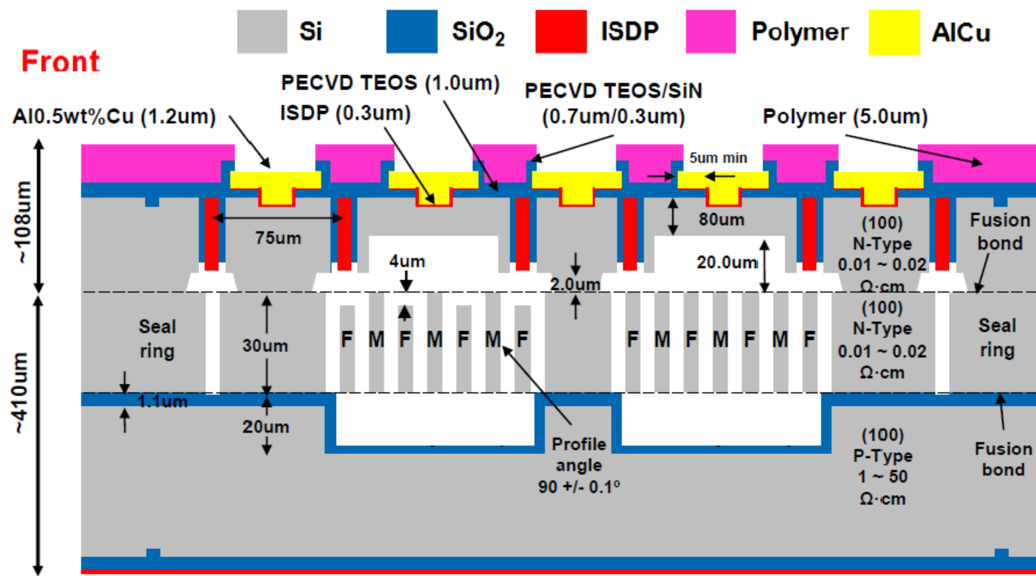


Process cross-section view of the developed includes the material legend (Crab leg).

## Appendix C: Mask Design Layouts of MIDIS™

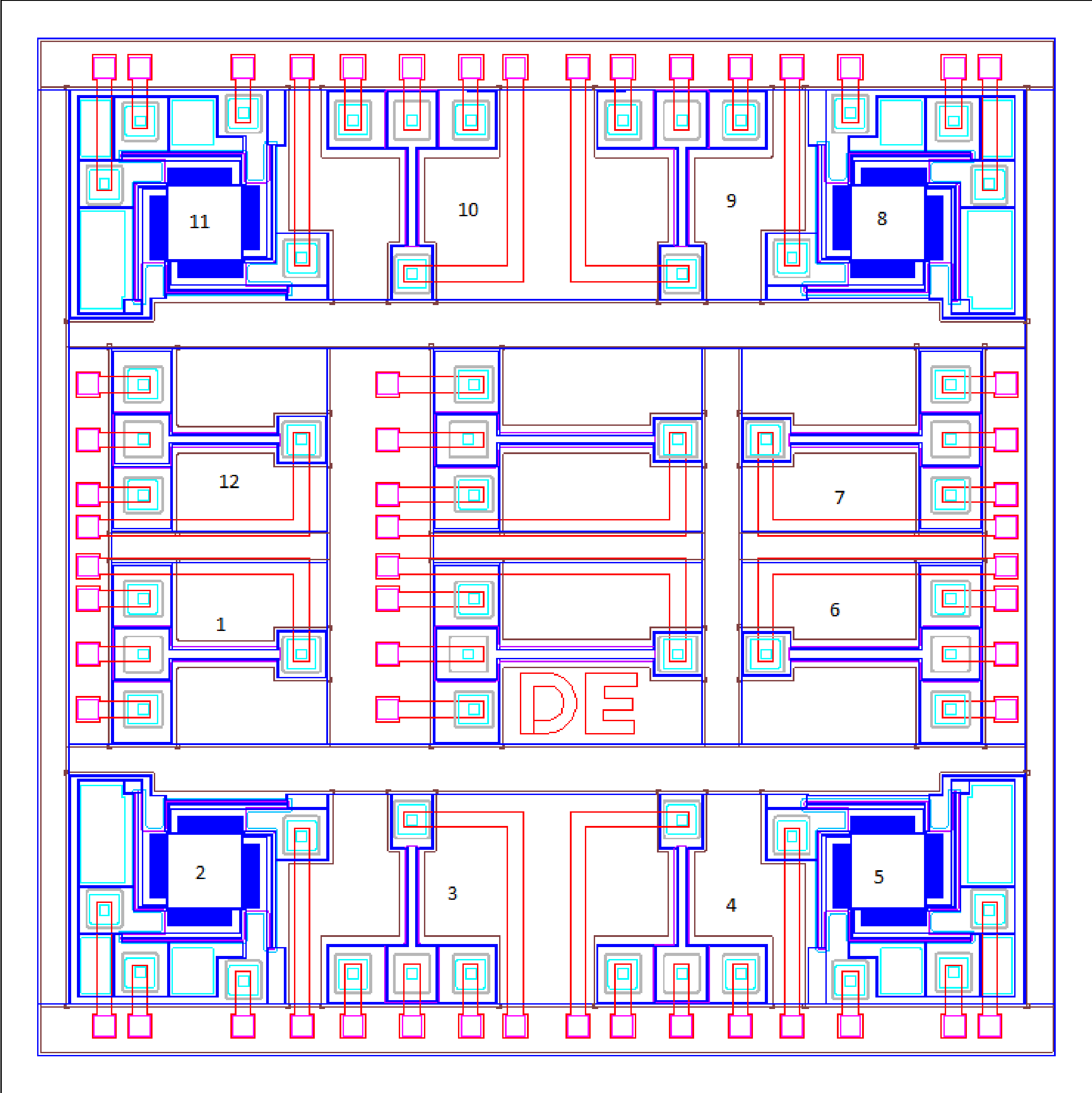

## Appendix D: Device Design Parameter and Test Results

### Device 1 & 12: Cantilever Beam Gyroscope

| Description | | Value |
|---|---|---|
| $L_b$ | Beam length | $427.5\ \mu m$ |
| $w_b$ | Beam width | $29.5\ \mu m$ |
| $t_b\ (t_p)$ | Beam (microplate) thickness | $30\ \mu m$ |
| $h$ | Initial capacitor gap | $2\ \ \mu m$ |
| $L_p$ | Microplate length | $218\ \mu m$ |
| $w_p$ | Microplate width | $194\ \ \mu m$ |
| $L_c$ | Length from beam tip to microplate | $109\ \mu m$ |
| M | Tip mass | $2.97 \times 10^{-6} g$ |

### Test Parameters and Results

| **Test Parameter** | **Drive mode** | | **Sense mode** | |
|---|---|---|---|---|
| | | ROM/FEA | | ROM/FEA |
| Actuation Voltage | 15 $V_{pp}$ | | 15 $V_{pp}$ | |
| Sweep frequency | 38 to 42 kHz | | 38 to 42 kHz | |
| Parasitic capacitance | 3.5 pF | | 3.5 pF | |
| Natural frequency | 40.189 kHz | 40.8/40.4 kHz | 41.191 KHz | 40.8/40.4 kHz |
| Qaulity factor | ~1850 | | ~1800 | |
| Pull-in voltage | 45.0 V | 45.25 /45.2 V | - | 45.25 /45.2 V |

**Device 2, 5, 8 & 11: Crab leg Gyroscope**

| Description | | Value |
|---|---|---|
| $L_1$ | Beam length 1 | 468 $\mu m$ |
| $L_2$ | Beam length 2 | 120 $\mu m$ |
| $w_b$ | Beam width | 10$\mu m$ |
| $t_b$ ($t_p$) | Beam thickness | 30 $\mu m$ |
| $h$ | Initial capacitor gap | 2 $\mu m$ |
| $L_{cp}$ | Microplate length | 290 $\mu m$ |
| $w_p$ | Microplate width | 290 $\mu m$ |
| M | Tip mass | $5.88 \times 10^{-6} g$ |

**Test Parameters and Results**

| **Test parameter** | **Drive mode** | | **Sense mode** | |
|---|---|---|---|---|
| | | FEA | | FEA |
| Actuation Voltage | 10 $V_{pp}$ | | 10 $V_{pp}$ | |
| Sweep frequency | 16 to 18 kHz | | 16 to 18 kHz | |
| Parasitic capacitance | 5.6 pF | | 5.6 pF | |
| Natural frequency (drive) | 17.283 kHz | 19.824kHz | 17.271 KHz | 20.117kHz |
| Qaulity factor | ~3000 | | ~3000 | |
| Pull-in voltage | - | 15V | - | 15V |

**Device 3 & 10: Cantilever Beam Gyroscope**

| Description | | Value |
|---|---|---|
| $L_b$ | Beam length | $388\ \mu m$ |
| $w_b$ | Beam width | $29.5\ \mu m$ |
| $t_b\ (t_p)$ | Beam (microplate) thickness | $30\ \mu m$ |
| $h$ | Initial capacitor gap | $2\ \mu m$ |
| $L_p$ | Microplate length | $218\ \mu m$ |
| $w_p$ | Microplate width | $194\ \mu m$ |
| $L_c$ | Length from beam tip to microplate center | $109\ \mu m$ |
| M | Tip mass | $2.97 \times 10^{-6} g$ |

**Test Parameters and Results**

| **Test Parameter** | **Drive mode** | | **Sense mode** | |
|---|---|---|---|---|
| | | ROM/FEA | | ROM/FEA |
| Actuation Voltage | 15 $V_{pp}$ | | 15 $V_{pp}$ | |
| Sweep frequency | 40 to 50 kHz | | 40 to 50 kHz | |
| Parasitic capacitance | 3.2 pF | | 3.4 pF | |
| Natural frequency | 46.32 kHz | $\mathbf{46.01}$/46.2 kHz | 46.32 KHz | $\mathbf{46.01}$/46.12 kHz |
| Qaulity factor | ~1842 | | ~1842 | |
| Pull-in voltage | - | 52.63 V | - | 52.63 V |

**Device 4 & 9: Cantilever Beam Gyroscope**

| | Description | Value |
|---|---|---|
| $L_b$ | Beam length | $400\ \mu m$ |
| $w_b$ | Beam width | $29.5\ \mu m$ |
| $t_b\ (t_p)$ | Beam (microplate) thickness | $30\ \mu m$ |
| $h$ | Initial capacitor gap | $2\ \mu m$ |
| $L_p$ | Microplate length | $230\ \mu m$ |
| $w_p$ | Microplate width | $215\ \mu m$ |
| $L_c$ | Length from beam tip to microplate | $109\ \mu m$ |
| M | Tip mass | $2.97 \times 10^{-6} g$ |

**Test Parameters and Results**

| **Test Parameter** | **Drive mode** | | **Sense mode** | |
|---|---|---|---|---|
| | | ROM/FEA | | ROM/FEA |
| Actuation Voltage | 15 $V_{pp}$ | | 15 $V_{pp}$ | |
| Sweep frequency | 38 to 42 kHz | | 38 to 42 kHz | |
| Parasitic capacitance | 3.7 pF | | 3.8 pF | |
| Natural frequency | $\mathbf{44.648}$ kHz | $\mathbf{44.37/44.24}$kHz | $\mathbf{44.652}$ kHz | $\mathbf{44.37/44.24}$kHz |
| Qaulity factor | ~1665 | | ~1665 | |
| Pull-in voltage | | 50.4/51.2 V | - | 50.4/51.2 V |

**Device 6 & 7: Cantilever Beam Gyroscope**

| Description | | Value |
|---|---|---|
| $L_b$ | Beam length | 621 $\mu m$ |
| $w_b$ | Beam width | 29.5 $\mu m$ |
| $t_b$ ($t_p$) | Beam (microplate) thickness | 30 $\mu m$ |
| $h$ | Initial capacitor gap | 2 $\mu m$ |
| $L_p$ | Microplate length | 239.5 $\mu m$ |
| $w_p$ | Microplate width | 196 $\mu m$ |
| $L_c$ | Length from beam tip to microplate center | 119.75 $\mu m$ |
| M | Tip mass | $3.28 \times 10^{-6} g$ |

**Test Parameters and Results**

| **Test Parameter** | **Drive mode** | | **Sense mode** | |
|---|---|---|---|---|
| | | ROM/FEA | | ROM/FEA |
| Actuation Voltage | 15 $V_{pp}$ | | 15 $V_{pp}$ | |
| Sweep frequency | 35 to 40 kHz | | 35 to 40 kHz | |
| Parasitic capacitance | 4.2 pF | | 4.0 pF | |
| Natural frequency | 37.53 kHz | - | 37.53 KHz | - |
| Qaulity factor | ~1850 | | ~1800 | |
| Pull-in voltage | - | 40.26 V | - | 40.26 V |

**Device 13 & 14: Cantilever Beam Gyroscope**

| Description | | Value |
|---|---|---|
| $L_b$ | Beam length | $517\ \mu m$ |
| $w_b$ | Beam width | $29\ \mu m$ |
| $t_b\ (t_p)$ | Beam (microplate) thickness | $30\ \mu m$ |
| $h$ | Initial capacitor gap | $2\ \mu m$ |
| $L_p$ | Microplate length | $250\ \mu m$ |
| $w_p$ | Microplate width | $200\ \mu m$ |
| $L_c$ | Length from beam tip to microplate center | $119.75\ \mu m$ |
| M | Tip mass | $3.28 \times 10^{-6} g$ |

**Test Parameters and Results**

| **Test Parameter** | **Drive mode** | | **Sense mode** | |
|---|---|---|---|---|
| | Test result | ROM/FEA | **Test result** | ROM/FEA |
| Actuation Voltage | 15 $V_{pp}$ | | 15 $V_{pp}$ | |
| Sweep frequency | 38 to 42 kHz | | 38 to 42 kHz | |
| Parasitic capacitance | 3.82 pF | | 3.75 pF | |
| Natural frequency | 39.73 kHz | - | 39.73 kHz | - |
| Qaulity factor | ~1850 | | ~1850 | |
| Pull-in voltage | - | 42.34 V | - | 42.34 V |